# Single Cell Biomechanical Phenotyping using Microfluidics and Nanotechnology

**Hesam Babahosseini**

Dissertation submitted to the faculty of the Virginia Polytechnic Institute and State University in partial fulfillment of the requirements for the degree of

**Doctor of Philosophy**

In

**Mechanical Engineering**

Masoud Agah, Chair
Lissett R. Bickford,
Chang Lu,
Jeannine S. Strobl,
Chenming (Mike) Zhang,
Xiaoyu (Rayne) Zheng,

**9th December 2015**
**Blacksburg, Virginia**

**Keywords:** MicroElectroMechanical Systems (MEMS), Biomechanics, Microfluidics, Atomic Force Microscopy (AFM), Drug Screening, Tumor Initiating Cells, Fractional Zener Model, Generalized Maxwell Model, Single Cell Analysis, Pulsed Stress, Iterative Mechanical Characteristics (iMECH), Cancer,

# Single Cell Biomechanical Phenotyping using Microfluidics and Nanotechnology

**Hesam Babahosseini**

## ABSTRACT

Cancer progression is accompanied with alterations in the cell biomechanical phenotype, including changes in cell structure, morphology, and responses to microenvironmental stress. These alterations result in an increased deformability of transformed cells and reduced resistance to mechanical stimuli, enabling motility and invasion. Therefore, single cell biomechanical properties could be served as a powerful label-free biomarker for effective characterization and early detection of single cancer cells. Advances and innovations in microsystems and nanotechnology have facilitated interrogation of the biomechanical properties of single cells to predict their tumorigenicity, metastatic potential, and health state.

This dissertation utilized Atomic Force Microscopy (AFM) for the cell biomechanical phenotyping for cancer diagnosis and early detection, efficacy screening of potential chemotherapeutic agents, and also cancer stem-like/tumor initiating cells (CSC/TICs) characterization as the critical topics received intensive attention in the search for effective cancer treatment. Our findings demonstrated the capability of exogenous sphingosine to revert the aberrant biomechanics of aggressive cells and showed a unique, mechanically homogeneous, and extremely soft characteristic of CSC/TICs, suitable for their targeted isolation. To make full use of cell biomechanical cues, this dissertation also considered the application of nonlinear viscoelastic models such as Fractional Zener and Generalized Maxwell models for the naturally complex, heterogeneous, and nonlinear structure of living cells.

The emerging need for a high-throughput clinically relevant alternative for evaluating biomechanics of individual cells led us to the development of a microfluidic system. Therefore, a high-throughput, label-free, automated microfluidic chip was developed to investigate the biophysical (biomechanical-bioelectrical) markers of normal and malignant cells.

Most importantly, this dissertation also explored the biomechanical response of cells upon a dynamic loading instead of a typical transient stress. Notably, metastatic and non-metastatic cells subjected to a pulsed stress regimen exerted by AFM exhibited distinct biomechanical responses. While non-metastatic cells showed an increase in their resistance against deformation and resulted in strain-stiffening behavior, metastatic cells responded by losing their resistance and yielded slight strain-softening. Ultimately, a second generation microfluidic chip called an iterative mechanical characteristics (iMECH) analyzer consisting of a series of constriction channels for simulating the dynamic stress paradigm was developed which could reproduce the same stiffening/softening trends of non-metastatic and metastatic cells, respectively. Therefore, for the first time, the use of dynamic loading paradigm to evaluate cell biomechanical responses was used as a new signature to predict malignancy or normalcy at a single-cell level with a high (~95%) confidence level.

*To my sweetheart wife and my dearest parents*

*And to students in Iran*

## Acknowledgments

In the Name of God, the Most Gracious, the Most Merciful,

Throughout my 4 years PhD journey between years 2011 and 2015, a lot of people helped me accomplish this dissertation and definitely, it would not have been possible without them.

I start with Prof. Masoud Agah, my PhD advisor and the director of the VT MEMS lab who I owe the most for completing this dissertation. I express my most sincere and gratitude to him who trusted me and provided me with this opportunity to achieve one of my life dream. His creative advice and guidance helped me a lot throughout this research. The best thing about him was his truth and patience during this research which allowed me to achieve successful outcomes. He will be remained forever one of my role models in life.

After him, I am extremely grateful of Dr. Jeannine S. Strobl, a member of my PhD dissertation committee who had a major contribution in this dissertation. Her endless favors and help especially in biological aspects of this research are greatly appreciated. Then, I should extend my thanks to my PhD dissertation committee members; Dr. Lissett Bickford (Biomedical Engineering and Mechanics), Dr. Chang Lu (Chemical Engineering), Dr. Mike Zhang (Biological System Engineering), and Dr. Rayne Zheng (Mechanical Engineering) as well as Dr. Raffaella De Vita (Biomedical Engineering and Mechanics) for accepting this role, putting their precious time, and providing valuable insight in my research. I would like to especially thank Dr. Mike Zhang; advisor of my second MSc in Biological System Engineering at Virginia Tech.

I am grateful to Dr. Eva M. Schmelz (Human Nutrition, Food and Exercise) and Dr. Paul C. Roberts (NIH) who collaborated with our lab and majorly contributed in the studies presented in two first chapters. I also express my gratitude to Dr. Nima Mahmoodi (University of Alabama) and his former student, Ben Carmichael (Southern Research Institute) for our successful collaborations in the studies presented in Chapter 3 and 4.

I extend my gratitude for technical assistance and support provided throughout my dissertation to Mr. Stephen McCartney (ICTAS, Nanoscale Characterization and Fabrication Laboratory), Mr. Don Leber (Micron Clean Room), Dr. Kristi Decourcy (Fralin Life Science Institute, Confocal Microscopy Laboratory), and Ms. Kathy Low (Virginia College of Veterinary Medicine, Morphology Laboratory).

I would like to specially thank three alumni of VT MEMS lab: Dr. Vaishnavi Srinivasaraghavan (Intel) who was my colleague in the microfluidic project and had a major contribution in the progress of this project, Mr. Alperen Ketene (Boeing), and Dr. Mehdi Nikkhah (Arizona State University) who initiated the AFM project in the lab and paved this hard way for current achievements. I also would like to appreciate friendship of my other VT MEMS colleagues; Dr. Yahya Hosseini (MIT), Dr. Muhammad Akbar (Penn State), Dr. Hamza Shakeel (NIST), Dr. Shree Narayanan (Intel), Dr. Phillip Zelner (Department of Defense), Ms. Sepeedah Soltanian-Zadeh (TI), Mr. Mohammad Mehdi

Alemi, Ms. Diana Nakidde (Intel), Ms. Sarah El-Helw, Mr. Apoorva Garg (Bloomberg), and Mr. Michael Restaino.

Most importantly, my sincere thanks go to my beloved and beautiful wife, Hasti for her love, support, and patience. She stood by my side during this journey as my true best friend. She always supported me with her great encouragements and was always happier than me for my every single success. I hope I can return these favors. Words cannot express my gratitude to my dearest parents, Ali and Fatemeh who set me on this journey early on in life by their encouragements and dedications. I inherently gained a strong faith and work ethic from them. I wish them a long healthy blessed life. I also have to thank my family and my precious siblings; Hamed, Hamideh, and Hamid and their families as well as my in-laws.

Finally, I have been fortune to find numerous true friends in Blacksburg who were our family here. Their names are too numerous to mention, but I want to thank all of them. I also need to thank all of my former teachers who dedicated their lives for teaching me. All the people I appreciated above are divine gifts from God. I have felt his help at every stage of my life and I am immensely thankful for all the blessings.

This research was financially supported by the National Science Foundation (NSF) under award CBET-1403304 and ECCS-0925945 and the Institute of Critical Technology and Applied Science (ICTAS) at Virginia Tech.

Hesam Babahosseini,
December 2015,
Blacksburg, VA

# Table of Contents

# List of Figures

# List of Tables

# 1 Introduction

## *1.1 Cell components and structure*

The cell is the most basic functional unit of life. The cell can be classified into two types of eukaryotic and prokaryotic. Eukaryotic cells contain nucleus and many other organelles which are encapsulated by a membrane. The cell membrane is a lipid bilayer that controls the flow into and out of the cell through ion channels by maintaining an electrical potential difference between the intra- and extracellular environment. The eukaryotic cells are of complex organisms including animals and plants. While the prokaryotes cells are the simple organisms such as bacteria that lack the cell membrane-surrounded nucleus. Instead, prokaryotes have a cell wall and their genetic material is carried in a single circular chromosome. Figure 1.1 shows a schematic drawing of a typical eukaryotic cell. The internal structure of a eukaryotic cells includes components such as nucleus, endoplasmic reticulum, mitochondria, Golgi apparatus and cytoskeleton.

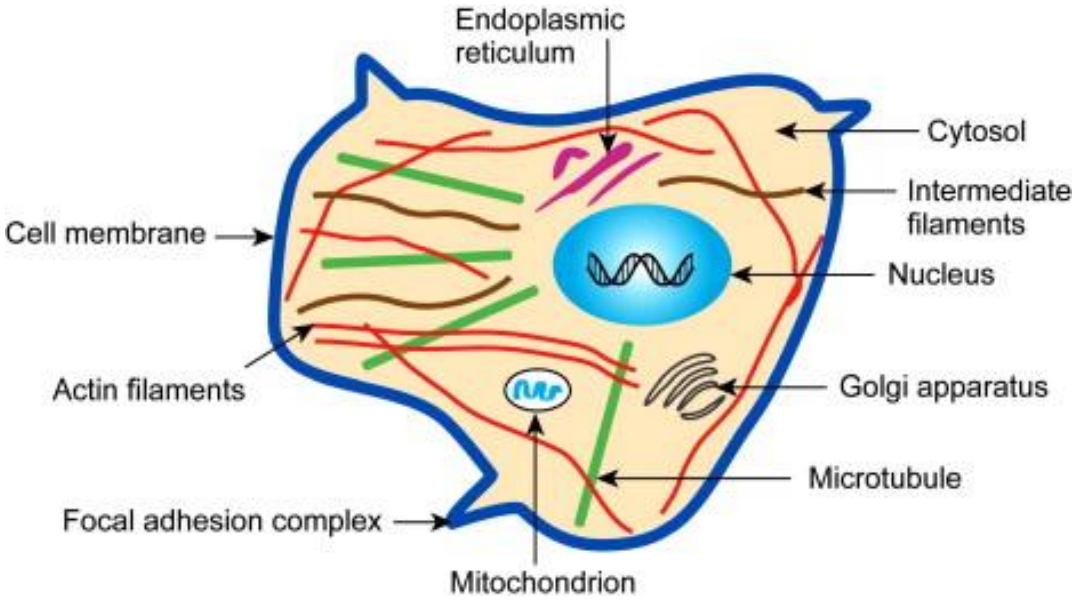


**Figure 1.1 The content of a eukaryotic cell including nucleus, endoplasmic reticulum, golgi apparatus, mitochondria, cytosol, membrane, and cytoskeleton [1]. S. Suresh. Biomechanics and biophysics of cancer cells. Acta Biomaterialia. 2007;3:413-38. Used under fair use, 2015.**

The cell is a dynamic structure which can sense microenvironmental changes and stimuli and convert them into biological responses and adapt its cytoskeleton [2, 3]. The

cell cytoskeleton contains a complex network of protein fibers and biopolymers embedded within the cytoplasm. The cell cytoskeleton supports cell shape, structure, and internal organization [1]. It also has a major contribution in many fundamental cellular processes such as cell mitosis, division, migration, and signaling. Moreover, it is the primary determinant of the cell integrity and mechanical properties [4]. The cytoskeleton is made of three major fibers including microtubules, intermediate filaments, and actin filaments. The eukaryotic cell assembles a wide variety of structures using these three basic filaments. Figure 1.2 shows a fluorescence image of a eukaryotic cytoskeletal structure.

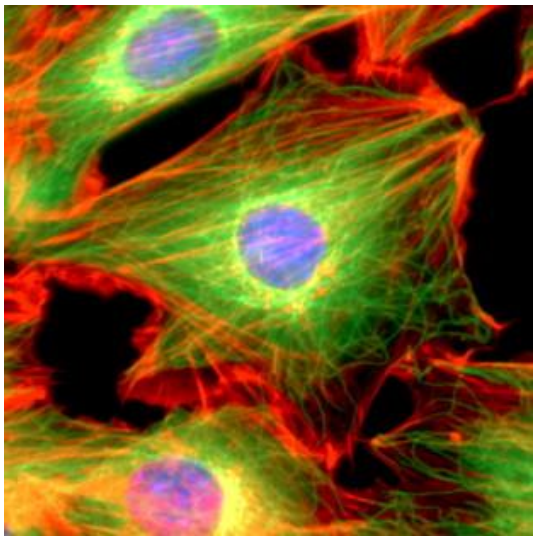

**Figure 1.2 The eukaryotic cytoskeleton including actin microfilaments shown in red and microtubulin shown in green is an intracellular matrix that supports cell shape and function [1]. S. Suresh. Biomechanics and biophysics of cancer cells. Acta Biomaterialia. 2007;3:413-38. Used under fair use, 2015.**

Actin filaments shown in Figure 1.3.A are reversible assemblies made of two actin chains (F-actin and G-actin) that are twisted around one another. F-actins are linear strand with about 7 nm diameter and 15 μm length, and have a barbed end and pointed end. Monomeric G-actin is polymerized into F-actin at the barbed (positive) end while depolymerized at the pointed (negative) end. Actin filaments are mostly concentrated beneath the cell membrane. Actin filaments are stiff with the Young's modulus of 1.3-2.5 GPa [5]. Microfilaments constitute the main part of proteins in the cell (1-10%) and are found in almost every cell. They are numerous in muscle cells (up to 20%) and in cells that move by changing shape such as phagocytes. Actin filaments keep cellular shape and allow movement of certain cells by forming cytoplasmatic extensions and protrusions including sheet-like lamellipodia, spike-like filopodia, and finger-like microvilli. The actin interacts

with myosin to cause contraction in muscle cells plays a major role in the cell migration process [6].

Microtubules shown in Figure 1.3.A are the thickest of the cytoskeleton structures with an outer diameter of 25 nm, inner diameter of 14 nm, and a persistence length of 6 mm. Alpha and beta tubulin are two subunit proteins that form dimers (pairs) which come together to form hollow cylinders. The cylinders are twisted around each other to form the microtubules. Microtubules have a Young's modulus around 1.9 GPa and a persistence length of 6 mm [5]. Microtubules determine cell shape especially during mitosis and have a dynamic structure with a half-life of only several minutes. Microtubules help the cell keep its shape. They hold organelles in place and allow them to move around the cell, and they form the mitotic spindle during cell division [6].

Intermediate filaments shown in Figure 1.3.C consist of alfa helical rod domain. The rods coil another filament to form a dimer. The assembly of dimers form staggered tetramers followed by formation of protofilaments. The final intermediate filament contains approximately eight protofilaments around each other in a rope-like structure. The naming of intermediate filament is because their diameter (10 nm) falls between the diameters of actin filaments (6 nm) and microtubules (25 nm) [5]. Their Young's modulus is 1-5 GPa and have a persistence length of approximately 1-3 μm. Intermediate filaments made of the protein lamin, vimentin, keratin which are found in skin, hair, and nails cells. Intermediate filaments organize cell shape and the position of organelles in cytoplasm [6].

Among the three major components of cytoskeleton, the actin filaments have the dominant role in cell deformability and structural integrity at a certain strain range. Intermediate filaments are compliant to deform to some reasonable extent while are engaged into the shear stress at large strains. Microtubules have a minor shear or tensile resistance and do not have a significant contribution in mechanical integrity of the cell body, but provide stability to the cytoskeletal structure in concert with other filaments.

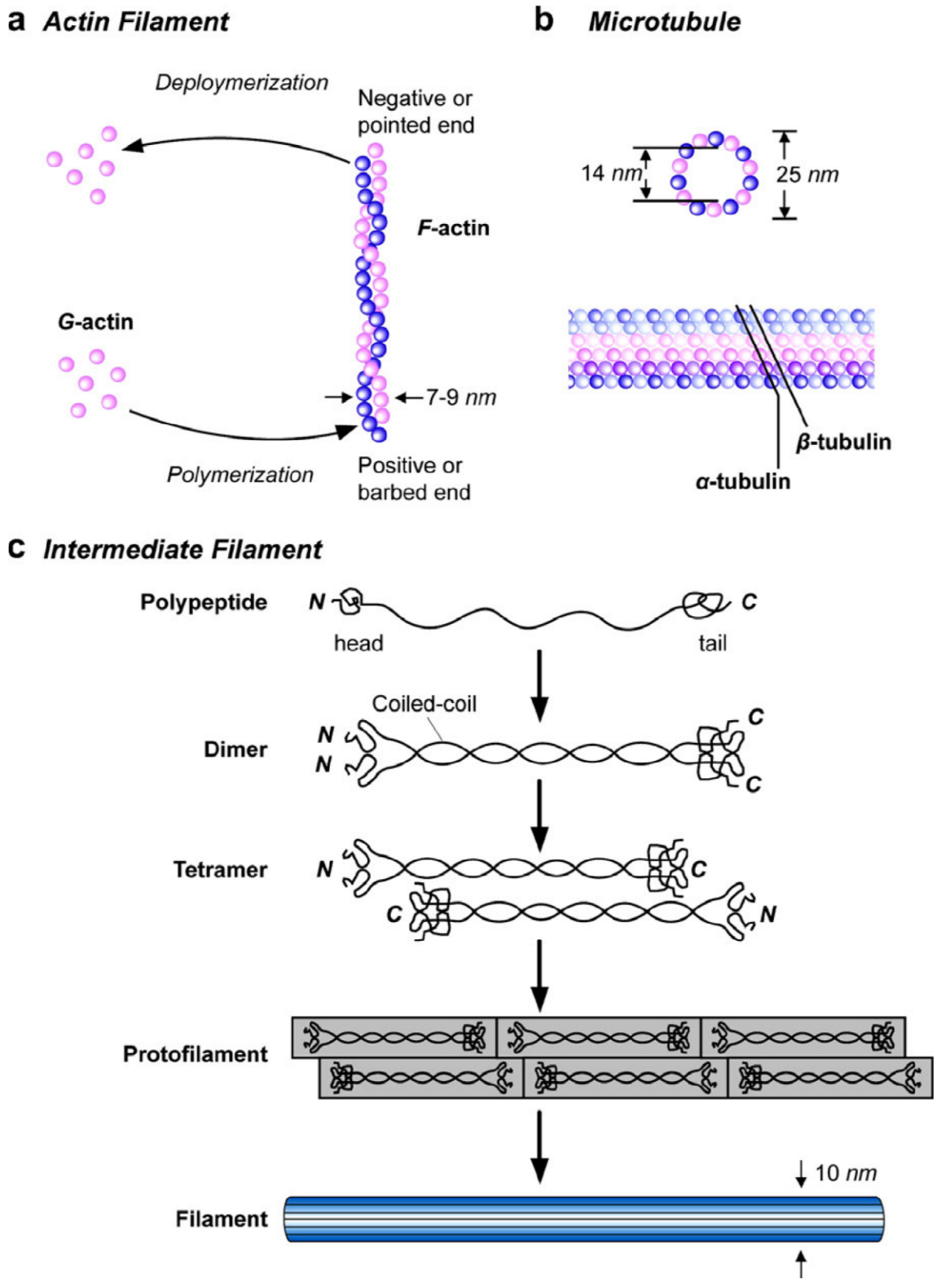


**Figure 1.3 The cytoskeletal components, (a) Actin microfilaments, (b) Microtubules, (c) Intermediate filaments [7]. R.D. Kamm, M.R.K. Mofrad. Introduction, with biological basis for cell mechanics. Cytoskeletal mechanics: models and measurements. Cambridge University Press, Cambridge. 2006;1-17 Used under fair use, 2015.**

In an attempt to analyze the cell cytoskeleton structure and its mechanical behavior, the Tensegrity theory [8] was proposed by Donald E. Ingber and has been significantly employed among biologists and engineers [4, 9-11]. This model classifies the actin filaments as tensional and microtubules as compressive components and hypothesizes that the cell structure stabilizes itself using a "prestress" cytoskeletal lattice within the body [11]. The rigidity of the structure is proportional to the level of prestress, which is dependent on the density of tensional and compressive components [12].

## *1.2 Cell biomechanics*

The study of cell mechanics has gained great significance in the past decades because mechanical loading of cells induces deformation and remodeling, which can influence many aspects of a living cell. The collective mechanical interactions of multiple filamentous proteins in the cell cytoskeleton are responsible for overall cell biomechanical behavior [13]. The cell cytoskeleton not only provides mechanical support to the cell [14] but has been shown to play a pivotal role in transducing mechanical stimuli in the microenvironment into intracellular signaling events and changes in gene expression, [15] regulating differentiation [16], adhesion [17, 18], contractility, migration [19, 20] and other processes. These are mechanically-oriented processes that are of critical importance in developmental biology [21], tissue homeostasis and processes such as wound healing [22], but also contribute to diseases such as cancer [23]. The progression of cancer is associated with an alteration of the cytoskeleton [24]: metastatic cancer cells become softer to facilitate motility [25, 26]. In fact, aggressive cancer cells have acquired the ability to deform and squeeze through tissue matrix and access the circulatory systems and subsequently adhere to and extravasate blood or lymph vessels to establish secondary tumors [27, 28] suggesting that the metastatic potential of cancer cells is related to their mechanical properties. Therefore, the ability to characterize the mechanical nature of a cell could provide insight into how cells receive and integrate regulatory signals from the surrounding environment and the impact on normal development and disease progression.

A wide variety of established transformed and non-transformed cell lines have been studied including prostate [29], breast [30, 31], bladder [32], ovary [33], lung [34], mesothelial [35], blood [36], osteoblast cells [37, 38]. The first study comparing cancerous

and normal cells is reported by Lekka et al., where they analyzed cells extracted from the human bladder [32]. The group reported that normal bladder cells had an elastic modulus of 7.5±3.6 kPa (n=20) while cancer bladder cells had an elastic modulus of 0.3±0.2 kPa (n=20). Overall, there is an agreement that transformed cells are "softer" and more deformable than their healthier counterparts by means of measuring their Elastic Moduli [1]. Nevertheless, cell viscoelasticity has been assessed qualitatively in some studies [39, 40], but not sufficiently enough [37].

In previous studies at VT MEMS Lab, first, Nikkhah et al. [41] attempted to investigate the mechanical responses of human breast epithelia cells using Atomic Force Microscopy (AFM). They showed that MDA-MB-231 metastatic cells are significantly softer with an averagely smaller elastic modulus comparing to MCF10A non-invasive cells. Using AFM analyses, they also showed that the growth media composition has a pronounced effect on cells elasticity. Later, Ketene et al. [33] investigated the mechanical responses of mouse ovarian surface epithelial (MOSE) cells, a developed mouse cell line that can represent the early, intermediate, and late stages of human ovarian cancer. With the use of AFM, they showed the results pertaining to the rate of change in cell viscoelasticity during the gradual progression of cancer disease. Another study on MOSE cells was devoted to cytoskeleton component analysis in the determination of their exact roles in the cell's mechanical behavior. The results introduced actin filaments as the primary player in structural integrity and viscoelastic responses in cells [42].

## *1.3 Tools for measuring single cell biomechanics*

### 1.3.1 Atomic Force Microscopy (AFM)

A variety of methods have been developed to interrogate cellular mechanical properties, such as viscoelasticity and deformability, mainly at the single cell level [43-47]. The parameters typically used to describe the mechanical properties are the elastic modulus, which relates applied stresses and cell deformation [32, 48] and the viscosity modulus, which corresponds cell time-dependency stress relaxation response to a step displacement [39, 49]. As shown in Figure 1.4, to date, several conventional experimental techniques have been developed to probe and quantify cell deformation characteristics, namely micropipette aspiration [50], parallel microplate devices [51], magnetic cytometry

[52, 53], optical tweezers [54], optical stretching rheometry [55], and most notably AFM [56, 57].

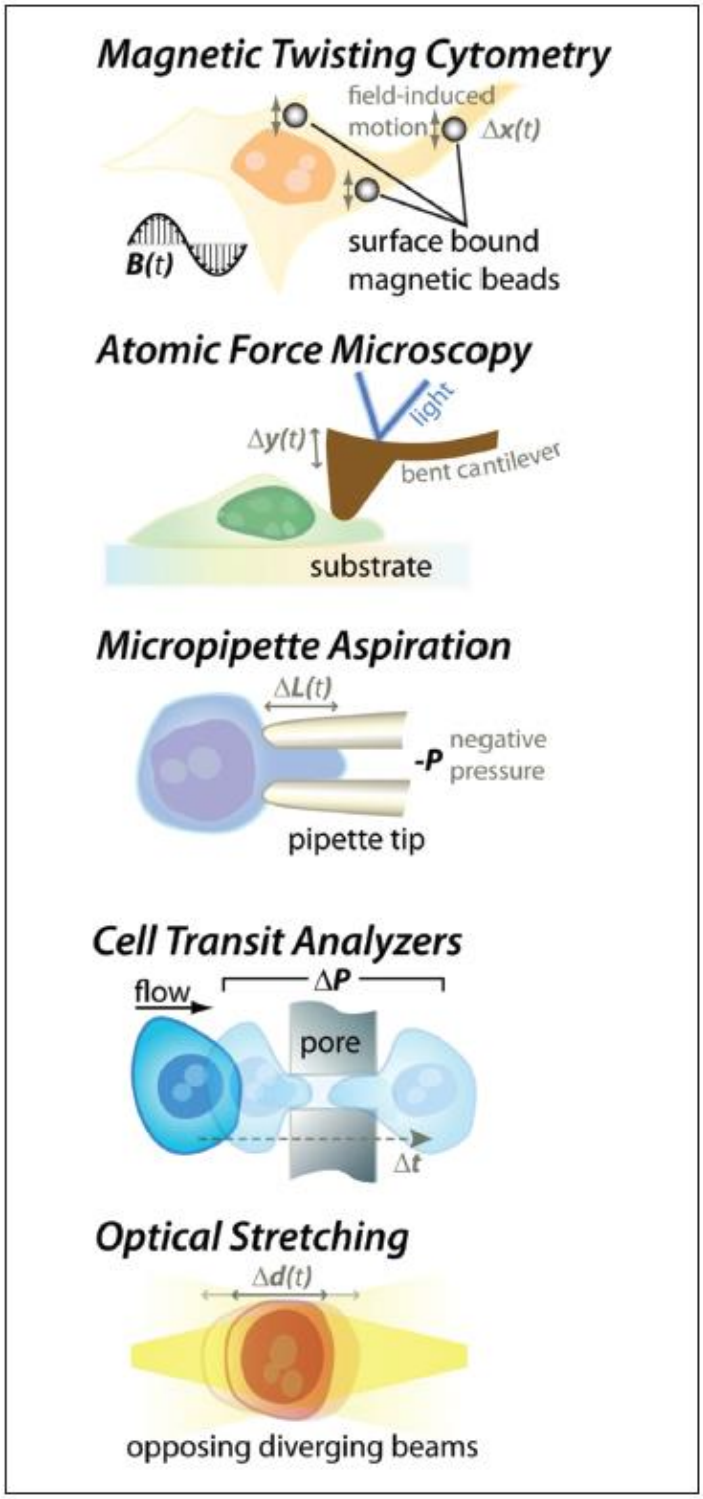


**Figure 1.4 Schematic illustration of various conventional experimental techniques for cell biomechanical measurement. [58]. D. Di Carlo. A mechanical biomarker of cell state in medicine. J Lab Autom. 2012;17:32–42. Used under fair use, 2015.**

AFM invented in 1980 has been at the forefront of cell structure characterization because of its precise force load application and ability to analyze live samples under more suitable real time conditions (*in vitro* cell culture) [59-62]. AFM [63] can be used for atomic and nanoscale surface characterization in both air and liquid environments. AFM is basically used to measure the mechanical properties of the biological sample under investigation [64]. AFM consists of a tip mounted on a micro-beam and is close to the specimen surface. In most of the cases, cantilevers are made of silicon or silicon nitride with a tip radius of curvature in the orders of few nanometers. As the tip moves on the surface to be investigated, the interacting force between the tip and the surface induces the transverse displacement of the tip. The cantilever motion can either be measured optically or by using sensing elements built into the cantilever itself. In optical approach, a laser beam is transmitted to the tip of the cantilever and allowed to reflect back. The reflected laser beam is detected using a photosensitive detector located few centimeters away. The output of this photosensitive detector is provided to the computer for processing the motion of the probe and deflection of the cantilever with sub-nanoscale sensitivity. AFM can measure forces as small as $10^{-18}$ N.

There are three basic operating modes of AFM: (i) contact mode, (ii) noncontact mode, and (iii) tapping mode. Specifically, in contact mode, the tip of the cantilever is always in contact with the sample surface. The cantilever beam acts as a spring, so the tip is always pushing very lightly against the sample. Any motion of the probe, any change in the deflection of the cantilever, and consequently, the interacting force between the sample of interest and the probe can be detected.

### 1.3.2 Microfluidic-based analyzers

AFM and other techniques suitable for single-cell analysis such as micropipette aspiration, optical tweezers, and magnetic tweezers have extremely low throughput (1cell per 2-10min). The emerging need for a high-throughput clinically relevant alternative technique for evaluating deformability of individual cell has led to the development of microfluidic-based analyzers [65]. Microfluidic-based analyzers are high-throughput tools (up to 1000 cells per 1min) for determining biophysical signatures at single-cell resolution. For characterizing the biomechanical properties of a cell, the cell must be deformed.

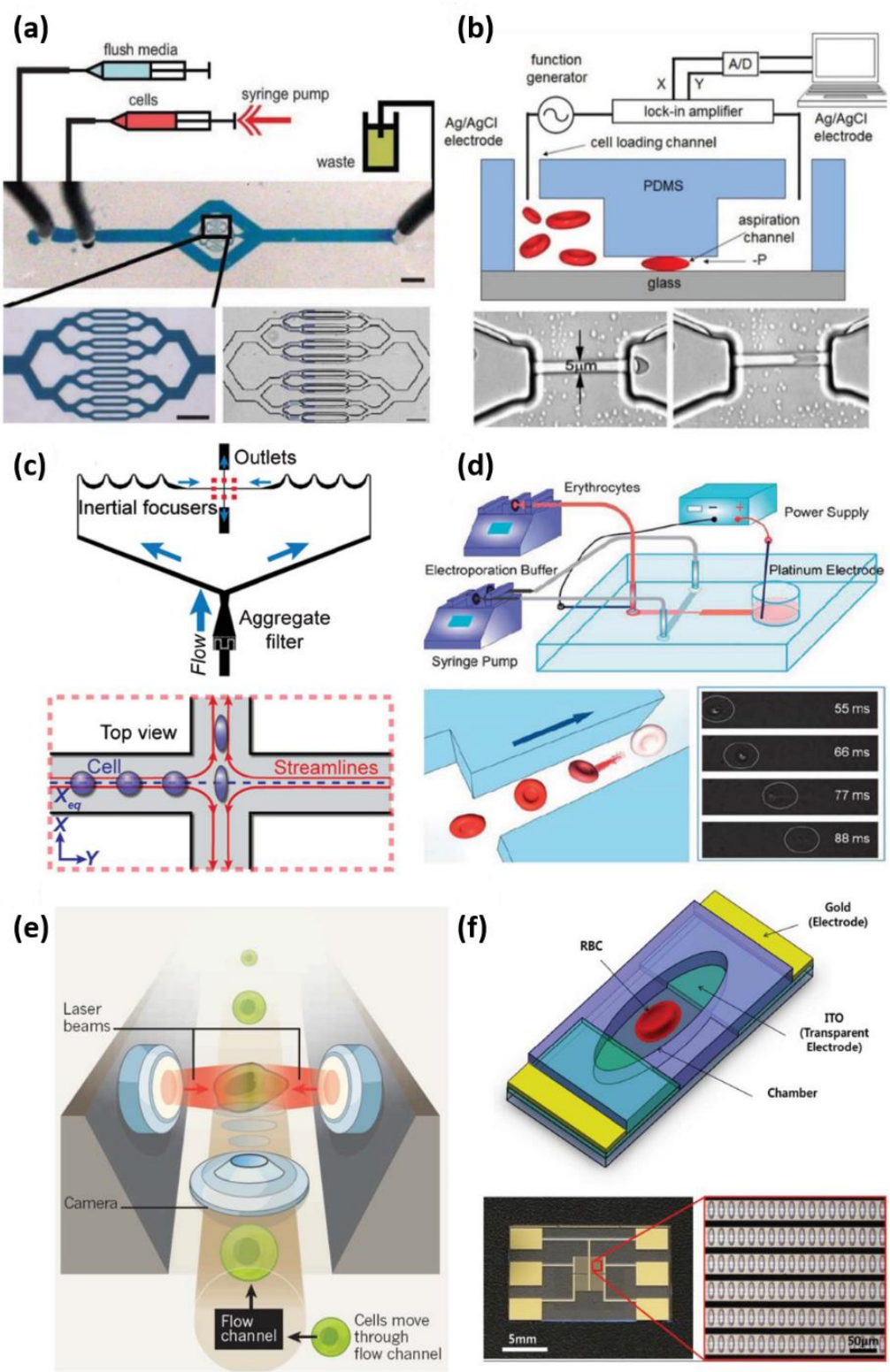


**Figure 1.5 (a) A microfluidic biophysical flow cytometer device including a network of 64 parallel capillary-like microchannels for blood cell deformability measurement using a high speed camera [66]. M. J. Rosenbluth, W. A. Lam, D. A. Fletcher. Analyzing cell mechanics in hematologic diseases with microfluidic biophysical flow cytometry. Lab Chip. 2008;8:1062-70. Used under fair use, 2015. (b) A**

**microfluidic system for characterizing the bioelectrical and biomechanical properties of RBCs (Red Blood Cells) at 100–150 cells/s. The transit time measurements are made using electrical impedance changes when an RBC passes through the constriction channel [67]. Y. Zheng, E. Shojaei-Baghini, A. Azad, C. Wang, Y. Sun. High-throughput biophysical measurement of human red blood cells. Lab Chip. 2012;12:2560-7. Used under fair use, 2015. (c) Hydrodynamic stretching microfluidic cytometry device that focuses cells to the center lines of the test channel by inertial effects and then stretches them by fluid pressure and finally analyzes their deformability by high-speed imaging at a high-throughput of 2,000 cells/s [68]. D. R. Gossett, H. T. K. Tse, S. A. Lee, Y. Ying, A. G. Lindgren, O. O. Yang, et al. Hydrodynamic stretching of single cells for large population mechanical phenotyping. Proc Natl Acad Sci USA. 2012;109:7630-5. Used under fair use, 2015. (d) An electroporation-induced microfluidic device for lysing RBCs at the single-cell level in the narrow section by applying a constant DC voltage. RBCs lysis time obtained by high-speed time-lapse imaging is correlated to their deformability [69]. N. Bao, G. C. Kodippili, K. M. Giger, V. M. Fowler, P. S. Low, C. Lu. Single-cell electrical lysis of erythrocytes detects deficiencies in the cytoskeletal protein network. Lab Chip. 2011;11:3053-6. Used under fair use, 2015. (e) An optical stretcher uses two laser beams to trap and deform cells travelling along a flow channel. The cell deformation images are recorded and analyzed to assess their elasticity and contractility [70]. E. Jonietz. Mechanics: The forces of cancer. Nature. 2012;491:S56-S7. Used under fair use, 2015. (f) A microchamber array integrated with electrodes for electro-deformation of individual trapped RBCs by applying a DEP force [71]. I. Doh, W. C. Lee, Y. H. Cho, A. P. Pisano, F. A. Kuypers. Deformation measurement of individual cells in large populations using a single-cell microchamber array chip. Appl Phys Lett. 2012;100:173702. Used under fair use, 2015.**

Thus, microfluidic-based analyzers for cell deformability measurements can be classified based on the mechanical stimuli applied to deform the cell [65] into structure-induced deformation (Figure 1.5.a [66] and 1.5.b [67]), fluid-induced deformation (Figure 1.5.c [68], electroporation-induced deformation (Figure 1.5.d [69]), optical stretcher (Figure 1.5.e [70]), and dielectrophoresis (DEP)-induced deformation (Figure 1.5.f [71]). In structure-induced deformation analyzer category where the microchip developed in this thesis falls, single cells move through a constriction channel that imposes mechanical stress on the cell body, and the transit time is measured using image data or electrical resistance changes which provides a rapid and fully automated acquisition technology for characterizing cell deformability biomarker [66-68, 72-74].

The results from these analyzers show that the average transit time of cancer cells is significantly shorter than that of normal cells. With considering this fact that the transit time is directly correlated with cell deformability, the results match the earlier reports generated by the traditional tools like AFM.

## *1.4 Overview and outline*

Chapter 2 reports determination of the differential effects of exogenous sphingolipid metabolites on the elastic modulus of mouse ovarian surface epithelial cells as they transition to cancer. The results indicate that tumor-supporting sphingolipid

metabolites act by making cells softer, while the anti-cancer metabolite sphingosine partially reverses the decreased elasticity associated with cancer progression. Thus, sphingosine may be an alternative to conventional chemotherapeutics in ovarian cancer prevention or treatment.

Chapter 3 reports the mechanical properties of ovarian cancer stem-like/tumor initiating cells (CSC/TICs). The represented model is a spontaneously transformed murine ovarian surface epithelial (MOSE) cell line that mimics the progression of ovarian cancer from early/non-tumorigenic to late/highly aggressive cancer stages. Altogether, our results demonstrate that the elastic modulus profile of CSC/TICs is unique and responsive to anti-cancer treatment strategies that impact the cytoskeleton architecture of cells. These findings increase the chance for obtaining distinctive cell biomechanical profiles with the intent of providing a means for effective cancer detection and treatment control.

Chapter 4 proposes the application of the Fractional Zener (FZ) model of viscoelasticity to extract mechanical parameters from the *entire* relaxation response, improving upon existing physical techniques e.g. the Standard Linear Solid (SLS) model to probe isolated cells. The results show an exceptional increase in conformance to the experimental data compared to that predicted by the SLS model. The cells' responses exhibit power-law behavior and complexity not associated with simple exponential relaxation predicted by the SLS that supports the application of a fractional model.

Chapter 5 reports investigation of the biomechanical properties of sub-cellular structural domains of breast cells using AFM. The cells are modeled as a triple-layered body where the Generalized Maxwell (GM) viscoelastic model is fit to the stress-relaxation curves to extract the viscoelastic properties of sub-cellular structures. The triple-layered modeling results allow for determination of the biomechanical properties of the three major sub-cellular structural domains for both normal MCF10A and cancerous MDA-MB-231 cells: the upper plasma membrane/actin cortex sub-domain, the middle cytoplasm/nucleus sub-domain, and the lower nuclear/integrin sub-domain.

Chapter 6 reports a microfluidic approach to single-cell biomechanical-bioelectrical profiling of heterogeneity within cell populations. Analysis of biomechanical-bioelectrical properties of a normal breast cell line and malignant breast cell lines with weak and high metastatic abilities indicated that malignant cells on average have greater

heterogeneity in shape before deformation, constriction entry time and specific membrane capacitance than normal cells. The shift of cells to an increasingly more metastatic phenotype was characterized by a significant decrease in constriction entry time, more rapid shape recovery after deformation, a decrease in channel interface resistance, and an increase in specific membrane capacitance. This chapter shows the potential application of this instrument for evaluation of metastatic risk of a cell population in human breast disease.

Chapter 7 presents a new paradigm to characterize the effects of a dynamic microenvironment on biomechanical properties of cells by subjecting them to a repetitive pulsed stress regimen using AFM. The force vs. time data obtained for non-metastatic and metastatic epithelial breast cells under this process revealed that the non-metastatic cells respond by an overall "stiffening" under repeated pulses of nano-mechanical stimulation whereas metastatic cells on average respond by "softening". This distinct behavior was recorded in four cell lines and provided a new promising biomarker to distinguish metastatic cells from non-metastatic cells at a single-cell level with a high confidence level of ~95%.

Chapter 8 aims at the development of a lab-on-a-chip microfluidic biosensor called the iterative mechanical characteristics (iMECH) analyzer enabling dynamic biomechanical profiling of individual living cells at a single-cell level, same as the experiments in chapter 6 via AFM. The results of the iMECH analysis on the breast cell lines revealed that the non-metastatic cells develop a more resistance and stiffening, while the metastatic cells exhibit a resistance loss and softening under the dynamic stresses. This distinct deformation modulatory response of the normal and cancer cells provide a new iMECH bio-signature. Through a series of drug-induced cell cytoskeleton stabilization and disruption tests, actin filaments were identified as an important element dominantly play a role on their iMECH signature. As a conclusion, the iMECH analyzer represents a significant advance in achieving a biomedical microdevice for diagnosing cancer at the single-cell level with a high ~95% confidence level.

Finally, chapter 9 presents a summary of the research performed and presented in this work. It also discusses about the contributions of this dissertation and the future directions and the priority for the future research in this subject.

## *References*


[1] S. Suresh, "Biomechanics and biophysics of cancer cells," *Acta Biomaterialia,* vol. 3, pp. 413-438, 2007.

[2] C. Zhu, G. Bao, and N. Wang, "Cell Mechanics: Mechanical response, cell adhesion, and molecular deformation," *Annu. Rev. Biomed. Eng,* vol. 2, pp. 189-226, 2000.

[3] C. S. Chen, M. Mrksich, S. Huang, G. M. Whitesides, and D. E. Ingber, "Geometric control of cell life and death," *Journal of Science,* vol. 276, pp. 1425-1428, 1997.

[4] D. E. Ingber, "Tensegrity I. Cell structure and hierarchical systems biology," *Journal of Cell Science,* vol. 116, pp. 1157-1173, 2003.

[5] J. Howard, *Mechanics of Motor Proteins and the Cytoskeleton*. Sunderland, MA: Sinauer Associates, 2001.

[6] B. Alberts, A. Johnson, J. Lewis, M. Raff, K. Roberts, and P. Walter, *Molecular Biology of the Cell,* Fifth ed. ed. New York: Garland Science, Taylor & Francis Group, 2008.

[7] R. D. Kamm and M. R. K. Mofrad, "Cytoskeletal mechanics: models and measurements," in *Introduction, with biological basis for cell mechanics*, ed Cambridge: Cambridge University Press, 2006, pp. 1-17.

[8] R. B. Fuller, "Tensegrity," *Portfolio and Art News Annual,* vol. 4, pp. 112-127,144,148, 1991.

[9] N. Wang, I. M. Tolic-Norrelykke, J. X. Chen, S. M. Mihailovich, J. P. Butler, J. J. Fredberg, *et al.*, "Cell Prestress. I. Stiffness and prestress are closely associated in adherent contractile cells.," *American Journal of Physiology,* vol. 282, pp. C606-616, 2002.

[10] D. E. Ingber, "Tensegrity II. How structural networks influence cellular information processing networks," *Journal of Cell Science,* vol. 116, pp. 1397-1408, 2003.

[11] D. E. Ingber, "Cellular tensegrity: defining new rules of biological design that govern the cytoskeleton," *Journal of Cell Science,* vol. 104, pp. 613-627, 1993.

[12] M. R. King, *Principles of cellular engineering: understanding the biomolecular interface*. Burlington: Elsevier Academic Press, 2006.

[13] D. A. Fletcher and R. D. Mullins, "Cell mechanics and the cytoskeleton," *Nature,* vol. 463, pp. 485-492, 2010.

[14] H. D. Huang, R. D. Kamm, and R. T. Lee, "Cell mechanics and mechanotransduction: pathways, probes, and physiology," *Am. J. Physiol. Cell Physiol.,* vol. 287, pp. C1-C11, 2004.

[15] P.A. Janmey and C.A. McCulloch, "Cell mechanics: integrating cell responses to mechanical stimuli," *Annu. Rev. Biomed. Eng.* , vol. 9, pp. 1-34, 2007.

[16] R. McBeath, D. M. Pirone, C. M. Nelson, and et al., "Cell shape, cytoskeletal tension, and RhoA regulate stem cell lineage commitment," *Dev. Cell.,* vol. 6, pp. 483-495, 2004.

[17] K. Kaibuchi, S. Kuroda, and M. Amano, "Regulation of the cytoskeleton and cell adhesion by the Rho family GTPases in mammalian cells," *Annu. Rev. Biochem.* , vol. 68, pp. 459-486, 1999.

[18] M. Nikkhah, J. Strobl, B. Peddi, and M. Agah, "Cytoskeletal Role in Differential Adhesion Patterns of Normal Fibroblasts and Breast Cancer Cells inside Silicon Microenvironments," *Biomedical Microdevices,* vol. 11, pp. 585-595, 2009.

[19] A. J. Ridley, M. A. Schwartz, K. Burridge, and et al., "Cell migration: integrating signals from front to back," *Science,* vol. 302, pp. 1704-1709, 2003.

[20] D. Yamazaki, K. S., and T. Takenawa, "Regulation of cancer cell motility through actin reorganization," *Cancer Sci.,* vol. 96, pp. 379-386, 2005.

[21] M. A. Wozniak and C. S. Chen, "Mechanotransduction in development: a growing role for contractility," *Nat. Rev. Mol. Cell Biol.* , vol. 10, pp. 34-43, 2009.

[22] R. A. Desai, L. Gao, S. Raghavan, and et al., "Cell polarity triggered by cell-cell adhesion via Ecadherin," *J. Cell Sci.,* vol. 122, pp. 905-911, 2009.

[23] D. E. Ingber, "Mechanobiology and diseases of mechanotransduction," *Ann. Med.*, vol. 35, pp. 564-577, 2003.

[24] P. C. Roberts, E. Motillo, A. C. Baxa, H. H. Q. Heng, N. Doyon-Reale, L. Gregoire, *et al.*, "Sequential Molecular and Cellular Events during Neoplastic progression: A Mouse Syngeneic Ovarian Cancer Model," *Neoplasia,* vol. 7, pp. 944-956, 2005.

[25] K. A. Ward, W. I. Li, S. Zimmer, and et al., "Viscoelastic properties of transformed cells: role in tumor cell progression and metastasis formation," *Biorheology,* vol. 28, pp. 301-313, 1991.

[26] S. Suresh, "Biomechanics and biophysics of cancer cells," *Acta Biomater.*, vol. 3, pp. 413-438, 2007.

[27] J. B. Wyckoff, J. G. Jones, J. S. Condeelis, and J. E. Segall, "A critical step in metastasis: in vivo analysis of intravasation at the primary tumor," *Cancer Res.*, vol. 60, pp. 2504-11, 2000.

[28] A. A. Shah-Yukich and A. C. Nelson, "Characterization of solid tumor microvasculature: a three-dimensional analysis using the polymer casting technique," *Lab. Invest.*, vol. 58, pp. 236-244, 1988.

[29] E. C. Faria, N. Ma, E. Gazi, P. Gardner, M. Brown, N. W. Clarke, *et al.*, "Measurement of elastic properties of prostate cancer cells using AFM," *Analyst*, vol. 133, pp. 1498-1500, 2008.

[30] Q. S. Li, G. Y. H. Lee, C. N. Ong, and C. T. Lim, "AFM indentation study of breast cancer cells," *J Biochemical and Biophysical research communications*, vol. 374, pp. 609-613, 2008.

[31] M. Nikkhah, J. S. Strobl, E. M. Schmelz, and M. Agah, "Evaluation of the influence of growth medium composition on cell elasticity," *Journal of Biomechanics*, vol. 44, pp. 762-766, 2011.

[32] M. Lekka, P. Laidler, D. Gil, J. Lekki, Z. Stachura, and A. Z. Hrynkiewicsm, "Elasticity of normal and cancerous human bladder cells studied by scanning force microscopy," *Biophysics Journal*, vol. 28, pp. 312-316, 1999.

[33] A. N. Ketene, E. M. Schmelz, P. C. Roberts, and M. Agah, "The effects of cancer progression on the viscoelasticity of ovarian cell cytoskeleton structures," *Nanomedicine: NBM*, vol. 8, pp. 93-102, 2012.

[34] S. E. Cross, Y. Jin, J. Rao, and J. K. Gimzewski, "Nanomechanical analysis of cells from cancer patients," *Nature Nanotechnology*, vol. 2, pp. 780-783, 2007.

[35] S. E. Cross, Y.-S. Jin, J. Tondre, R. Wong, J. Y. Rao, and J. K. Gimzewski, "AFM-based analysis of human metastatic cancer cells," *J Nanotechnology*, vol. 19, pp. 1-8, 2008.

[36] M. J. Rosenbluth, W. A. Lam, and D. A. Fletcher, "Force Microscopy of nonadherent cells: A comparison of Leukemia cell deformability," *Biophysics Journal*, vol. 90, pp. 2994-3003, 2006.

[37] E. M. Darling, M. Topel, S. Zauscher, T. P. Vail, and F. Guilak, "Viscoelastic properties of human mesenchymally-derived stem cells and primary osteoblasts, chondrocytes, and adipocytes," *Journal of Biomechanics*, vol. 41, pp. 454-464, 2008.

[38] G. T. Charras and M. A. Horton, "Single Cell Mechanotransduction and its modulation analyzed by atomic force microscope indentation," *Biophysics Journal*, vol. 82, pp. 2970-2981, 2002.

[39] M. Radmacher, M. Frtiz, C. M. Kacher, J. P. Cleveland, and H. G. Hansma, "Measuring the viscoelastic properties of human platelets with the atomic force microscope," *Biophysics Journal,* vol. 70, pp. 556-567, 1996.

[40] R. E. Mahaffy, S. Park, E. Gerde, J. Kas, and C. K. Shih, "Quantitative Analysis of the viscoelastic properties of thin regions of fibroblasts using atomic force microscopy," *Biophysics Journal,* vol. 86, pp. 1777-1793, 2004.

[41] M. Nikkhah, J. Strobl, R. De Vita, and M. Agah, "The cytoskeletal organization of breast carcinoma and fibroblast cells inside three dimensional (3-D) isotropic silicon microstructures," *Biomaterials,* vol. 31, pp. 1-10, 2010.

[42] A. N. Ketene, P. C. Roberts, A. A. Shea, E. M. Schmelz, and M. Agah, "Actin filaments play a primary role for structural integrity and viscoelastic response in cells," *Integrative Biology,* vol. 4, pp. 540-549, 2012.

[43] B. D. Hoffman and J. C. Crocker, "Cell mechanics: dissecting the physical responses of cells to force," *Annu. Rev. Biomed. Eng.,* vol. 11, pp. 259-288, 2009.

[44] C. T. Lim, E. H. Zhou, and S. T. Quek, "Mechanical models for living cells-a review," *J. Biomech.,* vol. 39, pp. 195-216, 2006.

[45] A. E. Pelling and M. A. Horton, "An historical perspective on cell mechanics," *Pflugers Arch.,* vol. 456, pp. 3-12, 2008.

[46] C. T. Lim, E. H. Zhou, A. Li, and et al., "Experimental techniques for single cell and single molecule biomechanics," *Mater. Sci. Eng. C Biomim. Supramol. Syst.,* vol. 26, pp. 1278-1288, 2006.

[47] M. A. Teitell, K. Sheraz, J. Schmit, and J. Reed, "Biomechanics of single cells and cell populations," *D. Ho. (ed.), Nanodiamonds: Applications in biology and Nanoscale Medicine,* pp. 235-246, 2010.

[48] S. Sen, S. Subramanian, and D. E. Discher, "Indentation and adhesive probing of a cell membrane with AFM: theoretical model and experiments," *Biophysics Journal.,* vol. 89, pp. 3203-13, 2005.

[49] E. M. Darling, S. Zauscher, J. A. Block, and F. Guilak, "A Thin-Layer Model for Viscoelastic, Stress-Relaxation Testing of Cells Using Atomic Force Microscopy: Do Cell Properties Reflect Metastatic Potential?," *Biophys. J.,* vol. 92, pp. 1784-91, 2007.

[50] R.M. Hochmuth, "Micropipette aspiration of living cells," *J. Biomech.,* vol. 33, pp. 15-22, 2000.

[51] O. Thoumine and A. Ott, "Time scale dependent viscoelastic and contractile regimes in fibroblasts probed by microplate manipulation," *Journal of Cell Science,* vol. 110, pp. 2109-16, 1997.

[52] N. Wang and D. E. Ingber, "Probing transmembrane mechanical coupling and cytomechanics using magnetic twisting cytometry," *Biochem. Cell Biol.*, vol. 73, pp. 327-335, 1995.

[53] D. R. Overby, B. D. Matthews, E. Alsberg, and D. E. Ingber, "Novel Dynamic rheological behavior of individual focal adhesions measured within single cells using electromagnetic pulling cytometry," *J Acta Biomaterialia*, vol. 1, pp. 295-303, 2005.

[54] M. Dao, C. T. Lim, and S. Suresh, "Mechanics of the human red blood cell deformed by optical tweezers," *Journal of the Mechanics and physics of solids.*, vol. 51, pp. 2259-80, 2003.

[55] J. Guck, S. Schinkinger, B. Lincoln, F. Wottawah, S. Ebert, M. Romeyke, *et al.*, "Optical deformability as an inherent cell marker for testing malignant transformation and metastatic competence," *Biophysics Journal*, vol. 88, pp. 3689-98, 2005.

[56] D. J. Muller and Y. F. Dufrene, "Atomic force microscopy as a multifunctional molecular toolbox in nanobiotechnology," *Nat. Nanotechnol.*, vol. 3, pp. 261-269, 2008.

[57] K.D. Costa, "Single-cell elastography: probing for disease with the atomic force microscope," *Dis Markers.*, vol. 19, pp. 139-154, 2003.

[58] D. Di Carlo, "A mechanical biomarker of cell state in medicine.," *J Lab Autom.*, vol. 17, pp. 32–42, 2012.

[59] M. J. Jaasma, W. M. Jackson, and T. M. Keaveny, "Measurement and characterization of whole cell mechanical behavior," *Annals of Biomedical Engineering*, vol. 34, pp. 748-758, 2006.

[60] P. Carl and H. Schillers, "Elasticity measurement of living cells with an atomic force microscope: data acquisition and processing," *Pflugers Arch-Eur J Physiol*, vol. 457, pp. 551-559, 2008.

[61] A. L. Weisenhorn, M. Khorsandi, S. Kasas, V. Gotzos, and H. Butt, "Deformation and height anomaly of soft surfaces studied with an AFM," *J Nanotechnology*, vol. 4, pp. 106-113, 1993.

[62] I. Sokolov, "Atomic Force Microscopy in Cancer Cell Research," *Cancer Nanotechnology*, pp. 1-17, 2007.

[63] H. J. Butt, B. Cappella, and M. Kappl, "Force measurements with the atomic force microscope: Technique, interpretation and applications," *Surface Science Reports*, vol. 59, pp. 1-152, 2005.

[64] I. Sokolov, *Atomic Force Microscopy in Cancer Cell Research*: Cancer Nanotechnology, 2007.

[65] Y. Zheng, J. Nguyen, Y. Wei, and Y. Sun, "Recent advances in microfluidic techniques for single-cell biophysical characterization," *Lab Chip,* vol. 13, pp. 2464-83, 2013.

[66] M. J. Rosenbluth, W. A. Lam, and D. A. Fletcher, "Analyzing cell mechanics in hematologic diseases with microfluidic biophysical flow cytometry," *Lab Chip,* vol. 8, pp. 1062-1070, 2008.

[67] Y. Zheng, E. Shojaei-Baghini, A. Azad, C. Wang, and Y. Sun, "High-throughput biophysical measurement of human red blood cells," *Lab Chip,* vol. 12, pp. 2560-2567, 2012.

[68] D. R. Gossett, H. T. K. Tse, S. A. Lee, Y. Ying, A. G. Lindgren, O. O. Yang, *et al.*, "Hydrodynamic stretching of single cells for large population mechanical phenotyping," *Proc. Natl. Acad. Sci. U.S.A.,* vol. 109, pp. 7630-7635, 2012.

[69] N. Bao, G. C. Kodippili, K. M. Giger, V. M. Fowler, P. S. Low, and C. Lu, "Single-cell electrical lysis of erythrocytes detects deficiencies in the cytoskeletal protein network," *Lab Chip,* vol. 11, pp. 3053-3056, 2011.

[70] E. Jonietz, "Mechanics: The forces of cancer," *Nature,* vol. 491, pp. S56-S57, 2012.

[71] I. Doh, W. C. Lee, Y. H. Cho, A. P. Pisano, and F. A. Kuypers, "Deformation measurement of individual cells in large populations using a single-cell microchamber array chip," *Appl. Phys. Lett.,* vol. 100, p. 173702, 2012.

[72] Q. Guo, S. Parka, and H. Ma, "Microfluidic micropipette aspiration for measuring the deformability of single cells," *Lab Chip,* vol. 12, pp. 2687-2695, 2012.

[73] A. Adamo, A. Sharei, L. Adamo, B. Lee, S. Mao, and K. F. Jensen, "Microfluidics-Based Assessment of Cell Deformability," *Anal. Chem.,* vol. 84, pp. 6438-6443, June 2012.

[74] J. Chen, Y. Zheng, Q. Tan, E. Shojaei-Baghini, Y. Liang Zhang, J. Li, *et al.*, "Classification of cell types using a microfluidic device for mechanical and electrical measurement on single cells," *Lab Chip,* vol. 11, pp. 3174-3181, 2011.

# 2 Bioactive sphingolipid metabolites modulate ovarian cancer cell structural mechanics

This chapter is produced from [1] with permission from Royal Society of Chemistry.

*H. Babahosseini, Paul C. Roberts, Eva M. Schmelz, and Masoud Agah, "Bioactive sphingolipid metabolites modulate ovarian cancer cell structural mechanics," Integrative Biology, vol. 5, no. 11, pp. 1385-1392, August 2013.*

## *2.1 Introduction*

During the progression of cancer, cells undergo numerous genetic and epigenetic changes that impact critical functions such as growth, motility, metabolism, communication, and others [2, 3]. In addition, alterations of the cells' mechanical phenotype, including changes in cell structure, morphology, and responses to mechanical stimuli, have been reported to accompany cancer progression [4, 5]. These result in an increased deformability of malignant cells and an enhanced migration capability–both effects are directly correlated with increased malignancy and metastasis [6]. Therefore, the structural and mechanical properties of cells could be exploited for effective characterization of cancer cells. Several experimental techniques including micropipette aspiration [7], optical tweezers [8], optical stretching rheometry [9, 10], microplate stretching [11], magnetic twisting [12], and most notably atomic force microscopy (AFM) [13-15] have already been utilized to quantify cell deformation characteristics and to correlate them with cancer progression. AFM is a well-established tool for mechanical characterization of biological cells under physiological conditions at a single-cell level. This microscopy technique has been used to confirm the differences in cellular stiffness of benign and malignant bladder [16], prostate [17], lung [18], blood [19], and breast [20, 21] epithelial cells. AFM has also been used to evaluate the effect of anti-cancer drugs providing insights into the sensitivity and efficiency of chemotherapies via biomechanical profiling of cells in response to treatment [22]. In this regard, it has been reported that upon short-term treatment with anti-cancer drug doxorubicin, both elastic modulus and adhesion force of human lung adenocarcinoma cells, measured quantitatively by AFM, were found to be increased while those of non-transformed human epithelial cells were decreased [23]. Moreover, results of two separate studies revealed that EGCG, a known potential anti-

cancer polyphenol in green tea [24] can cause a significant increase in stiffness of metastatic tumor mesothelial [25] and melanoma [26] cells. In another study via AFM, dexamethasone or daunorubicin chemotherapy increased leukemia cells' stiffness [27]. Recently, Sharma et al. have also found that the softening trend of ovarian cancer cells in the process of malignancy was reversed after cisplatin treatment [28]. The dose-dependent rate of stiffening was affected by the remodeling of the F-actin polymerization [28]. These studies suggest that cell stiffness measured by AFM can be used as a potential biomarker to predict the progression of cancer, its metastatic potential, and its response to drug treatment. In our previous studies [29, 30], we have employed AFM to determine changes in the mechanical responses during ovarian cancer progression. For these studies, we utilized our mouse ovarian surface epithelial (MOSE) cell system, a syngeneic model for progressive ovarian cancer that represents early/benign, intermediate/transitional, and late/malignant stages of ovarian cancer [31]. As MOSE cells progress, they exhibit alterations in their phenotype: they become smaller and their cytoskeleton becomes increasingly disorganized, with significant losses in filamentous actin [32]. This is associated with increasing softness and decreased viscosity [29], determined by the actin cytoskeleton organization [30]. Since the cytoskeleton determines not only the shape and structural integrity of cells but connects the extracellular physical, physiological and biochemical environment and the cell surface to intracellular signaling pathways and gene transcription [33-35], it plays a distinct role in the regulation of cell growth, motility, senescence, and apoptosis [33, 36].

The bioactive sphingolipid metabolites ceramide (Cer), sphingosine (So), and sphingosine-1-phosphate (S1P) play significant roles in the cells' response to intra- and extracellular stimuli; as lipid second messengers, they regulate cell growth, death, motility, and many more cellular functions and processes [37-39]. So and Cer are generally pro-apoptotic and anti-proliferative [37] and have been shown to inhibit growth and induce apoptosis in cancer cells [40]. However, Cer also increases inflammation and therefore exerts a pro-tumorigenic effect [41]. In contrast, S1P often induces cell growth, survival, motility, angiogenesis and thereby can support tumor development [42, 43]. These second messengers are rapidly inter-convertible and the sphingolipid profile generated in a cell will determine how the cells respond to the stimulus. Hence, the effect is typically context dependent and impacted by the cells origin, its function, and environment (among other

variables). We have previously shown that complex sphingolipids administered orally suppress colon [40, 44-46] and breast cancer progression [47]. The regulation of cell growth rather than overt toxicity towards transformed cells seems to be one of the underlying mechanisms of tumor suppression by sphingolipids [44, 45]. Sphingolipid metabolites also differentially modulate the cellular architecture and the cytoskeleton organization in various cell lines [48, 49]. However, the impact of sphingolipid treatment on the biomechanical properties of ovarian cancer cells representing different stages of aggressiveness is not known. Here we determined if these bioactive metabolites can reverse the aberrant biomechanical properties and responses of aggressive cancer cells, shifting them towards their benign precursor counterparts. Our results demonstrate that the biomechanics of aggressive cancer cells are modulated by sphingolipids and that exogenous So treatment may offer the means to deter tumor growth and metastasis by reversing aberrant biomechanical properties.

## *2.2 Materials and methods*

### 2.2.1 Sample preparation

The MOSE cell lines were generated from mouse ovarian surface epithelium as described [31]. The cells are categorized into early (passage no. 15-25) (MOSE-E), intermediate (passage no. 75-80) (MOSE-I), and late stage (passage no. 155-171) (MOSE-L) based on their phenotype. During progression, changes in the genotype include genes encoding cytoskeleton proteins and their regulators [32]. The cells were routinely grown in High Glucose Dulbecco's Modified Eagle's Medium (Sigma Aldrich), containing 4% fetal bovine serum (Atlanta Biological), 3.7 g/L of sodium bicarbonate, and 1% penicillin/streptomycin (Sigma Aldrich). To mimic the exposure to sphingolipid metabolites over time in a prevention regimen, the cells were grown in non-toxic concentrations of So (1.5 μM) (Avanti Polar Lipids) for at least three passages. To investigate the impact of potentially pro-tumorigenic metabolites, cells were also treated with Cer (2 μM), and S1P (500 nM).For AFM determinations, the cells were seeded at $1\times10^5$ cells per 12 $mm^2$glass coverslips coated with 0.1 mg/mL collagen type IV (Sigma) for 24-30 hrs prior to the AFM experiments to allow the cells to attach. The measurements were carried out on single cells in their respective culture medium at room temperature. A buffered HEPES solution was

added to the coverslip samples (final concentration of 13.5 mM) to maintain a physiological pH of 7.2 during about 2- 3 hrs test sessions.

### 2.2.2 AFM experiment

Measurements were performed via a Multimode V SPM atomic force microscope (Veeco Instruments, Santa Barbara, CA) in integration with an inverted optical microscope. Soft V-shaped SiNi cantilevers, TR400PSA (Olympus, Tokyo, Japan), with an approximate length of 200 μm and a nominal spring constant of 0.02 N/m were used for the indentation of adherent cells. The practical spring constant of the cantilevers was experimentally measured using thermal noise fluctuation. A glass microsphere bead (Duke Scientific, Palo Alto, CA) with an approximate diameter of 10 μm was attached to the sharp cantilever tip using a two-part epoxy (Miller Stephenson, Sylmar, CA)to increase the total surface contact area and as a consequence reduce the indentation stress on the soft biological samples and remove any nonlinearity in deformation. To minimize the changes in the measured practical spring constant of the cantilever, the glass bead is mounted and the laser spot is adjusted at the very possible endpoint of the cantilever beam. The exact size and the location of the attached glass bead on the cantilever were identified via a HIROX KH-7700 3D Digital Video Microscope. Since the elastic modulus of cells depends on the indentation location and speed [50], the indentations were performed at the cells' nuclei region and at an approach velocity of ~0.5 μm/s. Cantilever deflection vs. piezo displacement data were acquired at a sample rate of 5 kHz. To keep the validation of applying the Hertz model to the data, the indentation depth was kept up to 30% of total sample height by limiting the maximum indentation force to a trigger of 1.5±0.3 nN.

### 2.2.3 Data analysis

AFM is a powerful tool, capable of obtaining cantilever force vs. piezo displacement via indentations at the nanoscale. The cantilever deflection is sensed using an optical method in AFM. For a negligible cantilever deflection in comparison to the cantilever length, the cantilever force-$F$ is linearly proportional to the cantilever deflection-$d$ by the spring constant of the cantilever-$k$. The force curve should be converted to the force vs. tip-sample separation distance curve in order to estimate the sample's elastic modulus. The tip-sample separation distance-$D$ is described as the difference of the piezo position-$z$ and the

cantilever deflection-*d*. Elastic modulus of the sample can be calculated by fitting a proper contact model theory to the (*F*, *D*) curve. Several continuum contact mechanics models such as DMT, JKR, and Hertz models have been developed to describe the micro-scale deformations. The Sneddon's extended version of the Hertz model is a simple and applicable theory for soft materials like biological cells which is used here [51]. The model correlates the applied force-*F* and the induced indentation depth-$\delta$ in interaction between a spherical object and a sample as follow:

$$F = \frac{4}{3} E^* \sqrt{R} . \delta^{\frac{3}{2}} \tag{1}$$

where *R* is the radius of the spherical glass bead attached on the cantilever and *E** is relative elastic modulus of contact surfaces. For the infinitely hard tip $E_{tip} >> E_{cell}$, the relative elastic modulus is $E^* = E_{cell}/(1-\nu_{cell}^2)$, where $E_{cell}$ is elastic modulus and ν is Poisson's ratio of the cell. Cells' Poisson's ratio is assumed to be 0.5 for incompressible biological cells [52]. The indentation depth is described as the difference in the relative movement of the piezo scanner-z and the cantilever deflection-d as the following:

$$\delta = (z - z_0) - (d - d_0) \tag{2}$$

where $z_0$ and $d_0$ are the piezo scanner position and the cantilever deflection at the initial contact point of the probe with the cell. It is easier to find the elastic modulus and the initial contact point using a linear version of the Hertz's model Equation (2.1) in respect to the deformation-$\delta$ [53] as the following form:

$$F^{\frac{2}{3}} = \left[ \frac{4\sqrt{R}}{3(1-\nu_{cell}^2)} E_{cell} \right]^{\frac{2}{3}} (z - d) - \left[ \frac{4\sqrt{R}}{3(1-\nu_{cell}^2)} E_{cell} \right]^{\frac{2}{3}} (z_0 - d_0) \tag{3}$$

All the data analysis was implemented via MATLAB 2010a software.

## 2.3 Results

The AFM experiments were conducted on both control and sphingolipid-treated MOSE cells to obtain cantilever force vs. piezoelectric displacement via indentation as schematically shown in Figure 2.1.

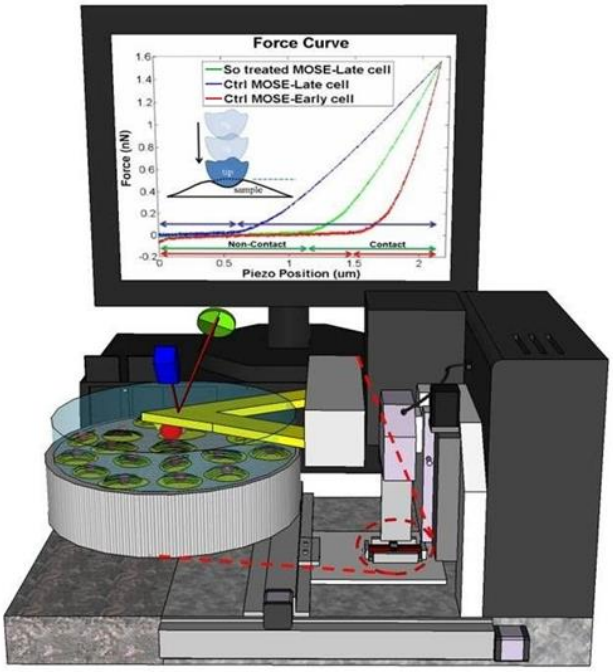


**Figure 2.1 Schematic illustration of experiment setup. The monitor is showing force curves obtained via AFM indentations. Although the aggressive MOSE-L cell has lower slope reading compared to the healthier MOSE-E cell, its slope and consequently stiffness increases significantly after treatment with So.**

The Hertz model fitted well to the acquired experimental data from 40-70 single cells randomly selected from each cell line/drug treated population with a high correlation coefficient ($0.85 \leq R^2 \leq 0.99$) to obtain their elastic modulus. It has already been studied that uncertainties in determination of the effective parameters values including the cantilever spring constant, the glass bead diameter, the contact point, and the cells' Poisson's ratio cause errors in extraction of the elastic properties of the sample by AFM.

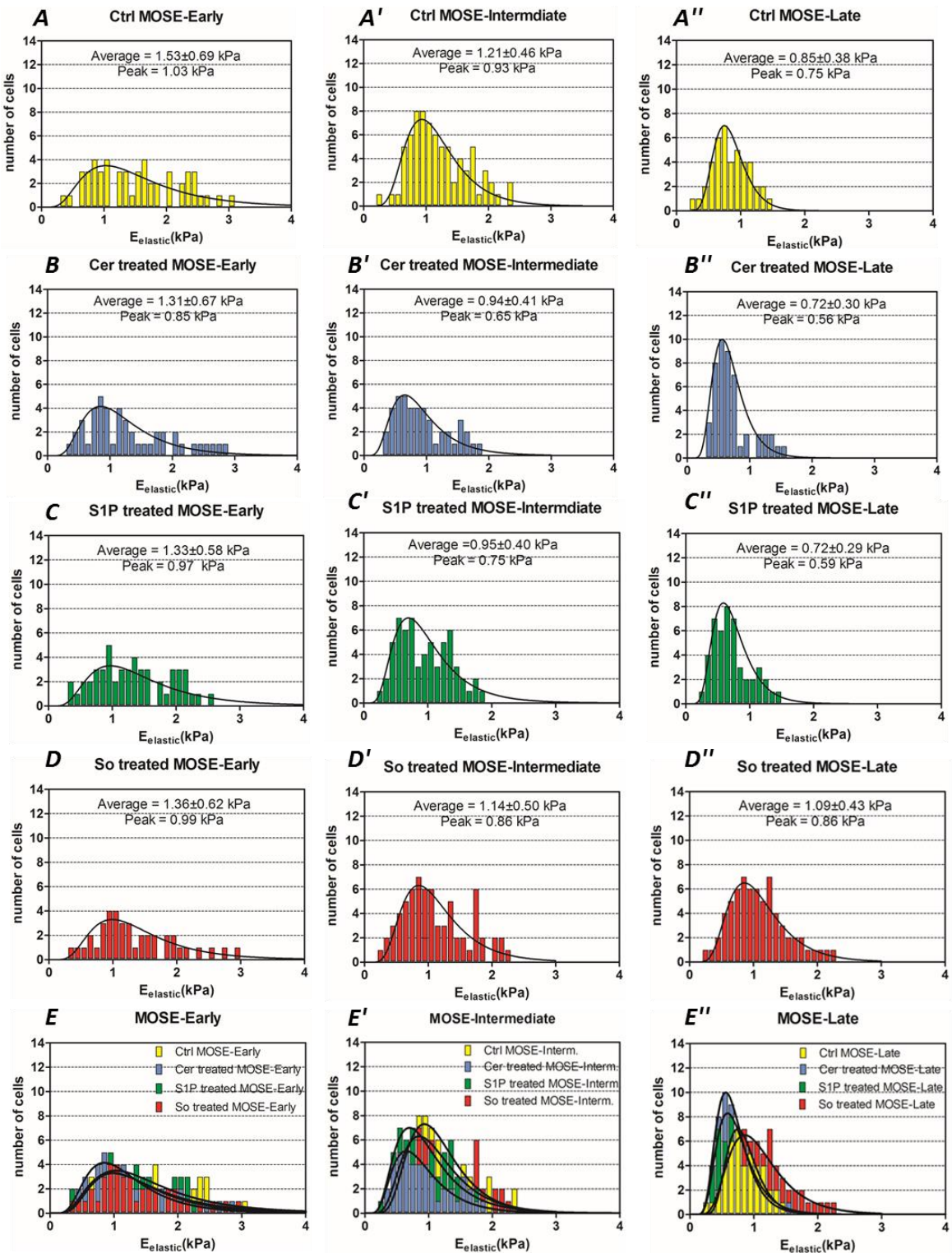


**Figure 2.2 Histograms of MOSE-Late, MOSE-Intermediate, and MOSE-Early cells in control and Cer, S1P, and So treated conditions depict the changes in distribution of measured elastic modulus after treatments.**

However, as long as sufficient replications of the experiments are conducted within

the same condition, the obtained results can be compared with a good estimation. Therefore, to minimize external and random variances in the experimental results as well as validate reproducibility of them, at least three separate AFM tests were conducted for each population. Within the same cell population, the experimental results were statistically consistent and there was no two experimental results contradicted each other. The population histograms generated by combining all measured elastic modulus responses from control and So, Cer, and S1P treated MOSE cells representing late, intermediate, and early stages of cancer progression are depicted in Figure 2.2.

The average ± standard deviation, and the peak (mode) values (correspond to peak points of Gaussian curves fitted to the elastic moduli distributions) of the measured elastic moduli are also summarized in Figure 2.2. Moreover, combination of the elastic moduli responses for each population are shown in column bar graph in Figure 2.3 and compared within each stage of cancer along with the statistical significance of changes ($p$-value) in comparison to the controls. Two sample independent t-tests were used to analyze the statistical significances of the changes in the elastic modulus.

The AFM measurements from early, intermediate, and late stage of untreated MOSE cells show that the average elastic modulus decreased as the cells progressed from a benign to a late, malignant stage, confirming our previous results [29]. Treatment of MOSE cells with non-toxic concentrations of Cer and S1P showed comparable decreases in the average and the mode elastic modulus values in all three stages compared to their respective control cells. The average elastic modulus decreased by 13% ($p \approx 0.1$) in MOSE-E, 21% ($p \approx 0.001$) in MOSE-I, and 15% ($p \approx 0.02$) in MOSE-L cells for both Cer and S1P treatment. On the other hand, So treatment resulted in a significant increase in the average and the mode elastic modulus values of the aggressive MOSE-L cells by 33% and 30% ($p \approx 0.0002$), respectively. MOSE-I cells did not appreciably respond to the So treatment ($p$

≈ *0.4*) while MOSE-E showed a slight decrease in the average elasticity after So treatment, indicating the cells became softer; however, this was not statistically significant ($p \approx 0.2$).

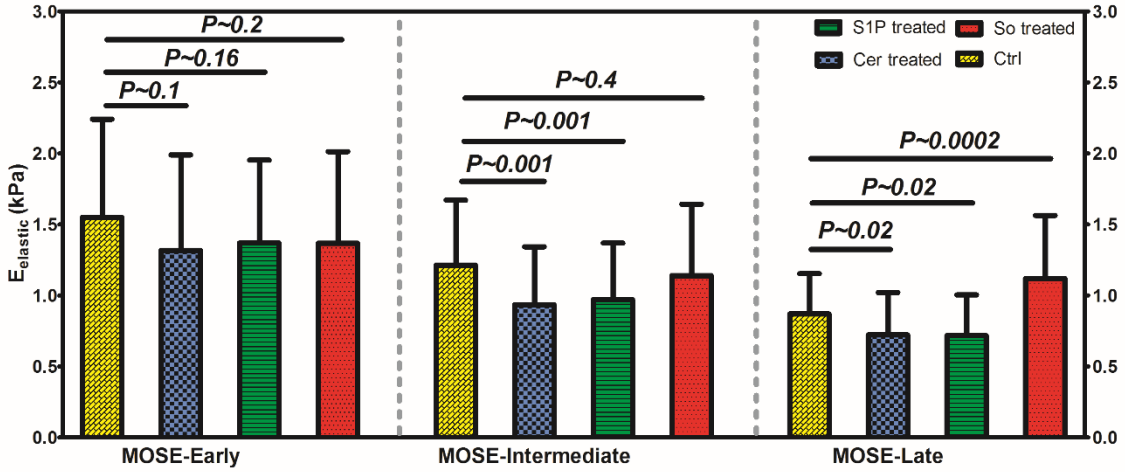


**Figure 2.3 Depiction of changes in elastic modulus of early, intermediate, and late stage of MOSE cell lines as effects of treatment with So, Cer, and S1P in comparison to control counterparts.**

Together, the results indicate that So treatment can at least partially reverse the decreasing elasticity of aggressive MOSE cells while both Cer and S1P treatment make the cells even softer. Neither treatment significantly impacted the non-malignant MOSE-E cells, suggesting that the treatment with exogenous sphingolipids may not increase the tumorigenic or metastatic properties of non-transformed cells.

Notably, the distributions of the untreated MOSE cells' elastic moduli reshape from a wide distribution for benign/early cells to a sharp concentration for malignant/late cells (Figure 2.2.A, 2.2.A', and 2.2.A"). This confirms our previous observations that benign MOSE-E cells are heterogeneous in their biomechanical phenotype but become more homogenous during progression [29]. Cer and S1P do not impact the histogram of MOSE-E cells (Figure 2.2.B and 2.2.C) while they have the same effect on the histograms of MOSE-I, slightly shifting them toward lower stiffness and making the curve slightly sharper (Figure 2.2.B' and 2.2.C'). So treatment of MOSE-E or MOSE-I cells also did not affect the distribution of the elastic modulus responses (Figure 2.2.D and 2.2.D'). This further delineates the lack of impact of the treatments on non-malignant MOSE-E cells. On the other hand, histograms of Cer and S1P treated MOSE-L cells (Figure 2.2.B" and 2.2.C") show a shift toward lower stiffness and a more homogeneous population as indicated by the

sharp curves in control MOSE-L. In contrast, So treatment effectively impacted the histogram of MOSE-L cells and notably shifted more cells towards the stiffer values, resulting in a broader distribution curve (Figure 2.2.D"). However, not all cells responded to the treatment with increased stiffness. The effects of the treatments on the histograms of MOSE-E, MOSE-I, and MOSE-L are depicted and compared in Figure 2.2.E, 2.2.E', and 2.2.E", respectively.

## 2.4 Discussion and conclusion

In this study, the AFM cell indentation was used as a technique for drug efficacy studies and development. Our findings indicate that non-toxic concentrations of So, a potential tumor suppressing sphingolipid metabolite, can induce aggressive ovarian cancer cells to mechanically behave more like benign cells by rendering them stiffer. Based on our previous studies, the changes in a cells' elastic modulus response is likely due to the remodeling of the actin cytoskeleton. MOSE-E cells exhibit a well-organized actin cytoskeleton and higher f-actin concentrations while MOSE-L cells exhibit thin and disorganized stress fibers [31, 32]. The disruption of the intact actin cytoskeleton in MOSE-E or stabilization in MOSE-L significantly reversed the cells' elastic modulus [30], highlighting the importance of the actin cytoskeleton for the biomechanical responses. However, treatment with So improved the actin organization and increased the f-actin levels [54], which correlates well with the increase in elastic modulus determined in this study. Conversely, the sphingolipid metabolites associated with supporting cancer growth (S1P) and tumor-promoting inflammation (Cer) decreased the elastic modulus of MOSE cells and made the cells softer; neither Cer nor S1P induced actin stress fiber formation in MOSE-L cells [54]. This is in contrast to the effect in endothelial cells where S1P increases barrier function and peripheral stress fiber organization [55]. The latter may be dependent upon the differentiation and activation status of cells; MOSE-L cells represent a poorly differentiated cell that has clearly undergone an epithelial-to-mesenchymal transition (EMT) phase [56]. Alternatively, responsiveness to S1P may be receptor specific; endothelial cells are known to express predominately S1PR1 and S1PR3. The S1P receptor profile of our MOSE cell lines has not been determined, but they may lack specific S1PR expression or other critical downstream effectors.

Overall, softening and increasing deformability are associated with enhanced capability for metastasis and tissue invasion [6]. Importantly, So treatment of benign MOSE cells did not alter the biomechanical properties of the cells. Future *in vivo* studies will shed light on whether treatments with Cer and S1P lead to an increased transformation and progression of benign and less aggressive ovarian cancer cells. This is especially important since the increased S1P levels in ascites fluid may promote not only the survival of the exfoliated cancer cells and increase adhesion and tumor outgrowth but also could impact the benign ovarian surface epithelial cells.

In summary, extended treatment with non-toxic concentrations of exogenous So partially reversed the aberrant biomechanical properties of aggressive ovarian cancer cells. This is comparable to treatment with conventional chemotherapeutics such as cisplatin but without their deleterious side effects. Thus, future studies will explore if the administration of So can suppress ovarian cancer progression and metastasis and if the biomechanical signature can be used as measure for treatment efficacy.

## *References*


[1] H. Babahosseini, P. C. Roberts, E. M. Schmelz, and M. Agah, "Bioactive sphingolipid metabolites modulate ovarian cancer cell structural mechanics," *Integr. Biol.*, vol. 5, pp. 1385-1392, 2013.

[2] B. Alberts, A. Johnson, J. Lewis, M. Raff, K. Roberts, and P. Walter, *Molecular biology of the cell*. New York: Garland Science, 2002.

[3] A. Ben-Zeev, "Cell-Cell Interaction and Cell Configuration Related Control of Cytokeratins and Vimentin Expression in Epithelial Cells and in Fibroblasts," *Annals of the New York Academy of Sciences*, vol. 455, pp. 597-613, 1985.

[4] S. Kumar and V. M. Weaver, "Mechanics, malignancy, and metastatis: The force journey of a tumor cell," *J Cancer Metastatis Rev.*, vol. 28, pp. 113-27, 2009.

[5] K. Rao and H. Cohen, "Actin Cytoskeletal network in aging and cancer," *Journal of Mutation Research*, vol. 256, pp. 139-148, 1991.

[6] S. Suresh, "Biomechanics and biophysics of cancer cells," *Acta Biomater.*, pp. 413-438, 2007.

[7] Q. Guo, S. Park, and H. Ma, "Microfluidic micropipette aspiration for measuring the deformability of single cells," *Lab Chip*, vol. 12, pp. 2687-95, 2012.

[8] M. Dao, C. T. Lim, and S. Suresh, "Mechanics of the human red blood cell deformed by optical tweezers," *Journal of the Mechanics and physics of solids,* vol. 51, pp. 2259-2280, 2003.

[9] J. Guck, S. Schinkinger, B. Lincoln, F. Wottawah, S. Ebert, M. Romeyke, *et al.*, "Optical deformability as an inherent cell marker for testing malignant transformation and metastatic competence," *Biophysics J.*, vol. 88, pp. 3689-98, 2005.

[10] T. W. Remmerbach, F. Wottawah, J. Dietrich, B. Lincoln, C. Wittekind, and J. Guck, "Oral cancer diagnosis by mechanical phenotyping," *Cancer Research,* vol. 69, pp. 1728-1732, 2009.

[11] O. Thoumine and A. Ott, "Time scale dependent viscoelastic and contractile regimes in fibroblasts probed by microplate manipulation," *Journal of Cell Science,* vol. 110, pp. 2109-16, 1997.

[12] V. Swaminathan, K. Mythreye, E. T. O'Brien, A. Berchuck, G. C. Blobe, and R. Superfine, "Mechanical stiffness grades metastatic potential in patient tumor cells and in cancer cell lines," *Cancer Research,* vol. 71, pp. 5075-80, 2011.

[13] M. Lekkaa, K. Pogodaa, J. Gosteka, O. Klymenkoa, S. Prauzner-Bechcickia, J. Wiltowska-Zubera, *et al.*, "Cancer cell recognition – Mechanical phenotype," vol. 43, pp. 1259-66, 2012.

[14] E. M. Darling, M. Topel, S. Zauscher, T. P. Vail, and F. Guilak, "Viscoelastic properties of human mesenchymally-derived stem cells and primary osteoblasts, chondrocytes, and adipocytes," *Journal of Biomechanics,* vol. 41, pp. 454-464, 2008.

[15] S. E. Cross, Y. Jin, J. Rao, and J. K. Gimzewski, "Applicability of AFM in cancer detection," *Nat. Nanotechnol.,* vol. 4 pp. 72-3, 2009.

[16] M. Lekka, P. Laidler, D. Gil, J. Lekki, Z. Stachura, and A. Z. Hrynkiewicz, "Elasticity of normal and cancerous human bladder cells studied by scanning force microscopy," *Biophysics J.,* vol. 28, pp. 312-316, 1999.

[17] E. C. Faria, N. Ma, E. Gazi, P. Gardner, M. Brown, N. W. Clarke, *et al.*, "Measurement of elastic properties of prostate cancer cells using AFM," *Analyst,* vol. 133, pp. 1498-1500, 2008.

[18] S. E. Cross, Y. S. Jin, J. Rao, and J. K. Gimzewski, "Nanomechanical analysis of cells from cancer patients," *Nature Nanotechnology,* vol. 2, pp. 780-783, 2007.

[19] M. J. Rosenbluth, W. A. Lam, and D. A. Fletcher, "Force Microscopy of nonadherent cells: A comparison of Leukemia cell deformability," *Biophysics J,* vol. 90, pp. 2994-3003, 2006.

[20] M. Nikkhaha, J. S. Strobl, E. M. Schmelzc, P. C. Robertsd, H. Zhouc, and M. Agah, "MCF10A and MDA-MB-231 human breast basal epithelial cell co-culture in silicon micro-arrays," *Biomaterials,* vol. 32, pp. 7625-7632, 2011.

[21] M. Nikkhah, J. S. Strobel, R. De Vita, and M. Agah, "The cytoskeletal organization of breast carcinoma and fibroblast cells inside three dimensional isotropic silicon microstructures," *Biomater.,* vol. 31, pp. 4552-61, 2010.

[22] J. Wanga, Z. Wan, W. Liu, L. Li, L. Ren, X. Wang, *et al.,* "Atomic force microscope study of tumor cell membranes following treatment with anti-cancer drugs," *Biosensors and Bioelectronics,* vol. 25, pp. 721-727, 2009.

[23] L. Xiao, M. Tang, Q. Li, and A. Zhou, "Non-invasive detection of biomechanical and biochemical responses of human lung cells to short time chemotherapy exposure using AFM and confocal Raman spectroscopy," *Analytical Methods,* vol. 5, pp. 874-879, 2012.

[24] C. S. Yang and X. Wang, "Green tea and cancer prevention," *Nutrition and Cancer,* vol. 62, pp. 931-7, 2010.

[25] S. E. Cross, Y. S. Jin, Q. Y. Lu, J. Rao, and J. K. Gimzewski, "Nanotechnology," *Green tea extract selectively targets nanomechanics of live metastatic cancer cells,* vol. 22, p. 215101 (9pp), 2011.

[26] M. Suganuma, T. Watanabe, A. Takahashi, and H. Fujiki, "Metastatic potential of B16 melanoma subclones indicated by cell stiffness measured by atomic force microscopy (AFM)," *Cancer Research,* vol. 71, p. Supplement 1, 2011.

[27] W. A. Lam, M. J. Rosenbluth, and D. A. Fletcher, "Chemotherapy exposure increases leukemia cell stiffness," *Blood,* vol. 109, pp. 3505-8, 2006.

[28] S. Sharma, C. Santiskulvong, L. A. Bentolila, J. Rao, O. Dorigo, and J. K. Gimzewski, "Correlative nanomechanical profiling with super-resolution F-actin imaging reveals novel insights into mechanisms of cisplatin resistance in ovarian cancer cells.," *Nanomedicine,* vol. 8, pp. 757-766, 2012.

[29] A. N. Ketene, E. M. Schmelz, P. C. Roberts, and M. Agah, "The effects of cancer progression on the viscoelasticity of ovarian cell cytoskeleton structures," *Nanomedicine : nanotechnology, biology, and medicine,* vol. 8, pp. 93-102, 2011.

[30] A. N. Ketene, P. C. Roberts, A. A. Shea, E. M. Schmelz, and M. Agah, "Actin filaments play a primary role for structural integrity and viscoelastic response in cells," *Integrative Biology,* vol. 4, pp. 540-549, 2012.

[31] P. C. Roberts, E. P. Mottillo, A. C. Baxa, H. H. Q. Heng, N. Doyon-Reale, L. Gregoire, *et al.,* "Sequential molecular and cellular events during neoplastic progression: A mouse syngeneic ovarian cancer model," *Neoplasia,* vol. 7, pp. 944-956, Oct 2005.

[32] A. L. Creekmore, W. T. Silkworth, D. Cimini, R. V. Jensen, P. C. Roberts, and E. M. Schmelz, "Changes in Gene Expression and Cellular Architecture in an Ovarian Cancer Progression Model," *PLOS ONE,* vol. 6, p. e17676, 2011.

[33] D. Kedrin, J. van Rheenen, L. Hernandez, J. Condeelis, and J. E. Segall, "Cell motility and cytoskeletal regulation in invasion and metastasis," *J Mammary Gland Biol. Neoplasia,* vol. 12, pp. 143-152, 2007.

[34] G. Pawlak and D. M. Helfman, "Cytoskeletal changes in cell transformation and tumorigenesis," *Curr. Opin. Genet. Dev.,* vol. 11, pp. 41-47, 2001.

[35] P. P. Provenzano and P. J. Keely, "Mechanical signaling through the cytoskeleton regulates cell proliferation by coordinated focal adhesion and Rho GTPase signaling," *J Cell Sci.,* vol. 124, pp. 1195-1205, 2011.

[36] D. Barkan, H. Kleinman, J. L. Simmons, H. Asmussen, A. K. Kamaraju, M. J. Hoenorhoff, *et al.,* " Inhibition of metastatic outgrowth from single dormant tumor cells by targeting the cytoskeleton," *Cancer Research,* vol. 68, pp. 6241-50, 2008.

[37] C. R. Gault, L. M. Obeid, and Y. A. Hannun, "An overview of sphingolipid metabolism: from synthesis to breakdown," *Adv. Exp. Med. Biol.,* vol. 688, pp. 1-23, 2010.

[38] P. Gangoiti, L. Camacho, L. Arana, A. Ouro, M. H. Granado, L. Brizuela, *et al.,* "Control of metabolism and signaling of simple bioactive sphingolipids: Implications in disease," *Prog. Lipid. Res.,* vol. 49, pp. 316-34, 2010.

[39] B. Ogretmen and Y. A. Hannun, "Biologically active sphingolipids in cancer pathogenesis and treatment," *Nat. Rev. Cancer,* vol. 4, pp. 604-616, 2004.

[40] E. M. Schmelz, P. C. Roberts, E. M. Kustin, L. A. Lemonnier, M. C. Sullards, D. L. Dillehay, *et al.,* "Modulation of intracellular beta-catenin localization and intestinal tumorigenesis in vivo and in vitro by sphingolipids," *Cancer Research,* vol. 61, pp. 6723-9, 2001.

[41] V. Teichgraber, M. Ulrich, N. Endlich, J. Riethmuller, B. Wilker, C. C. De Oliveira-Munding, *et al.,* "Ceramide accumulation mediates inflammation, cell death and infection susceptibility in cystic fibrosis.," *Nat. Med.,* vol. 14, pp. 382-391, 2008.

[42] L. K. Ryland, T. E. Fox, X. Liu, T. P. Loughran, and M. Kester, "Dysregulation of sphingolipid metabolism in cancer," *Cancer Biol. Ther.,* vol. 11, pp. 138-49, 2011.

[43] G. M. Strub, M. Maceyka, N. C. Hait, S. Milstien, and S. Spiegel, "Extracellular and intracellular actions of sphingosine-1-phosphate," *Adv. Exp. Med. Biol.,* vol. 688, pp. 141-55, 2010.

[44] E. M. Schmelz, M. C. Sullards, D. L. Dillehay, and A. H. Jr. Merrill, "Colonic cell proliferation and aberrant crypt foci formation are inhibited by dairy glycosphingolipids in 1, 2-dimethylhydrazine-treated CF1 mice," *J Nutr.*, vol. 130, pp. 522-7, 2000.

[45] L. A. Lemonnier, D. L. Dillehay, M. J. Vespremi, J. Abrams, E. Brody, and E. M. Schmelz, "Sphingomyelin in the suppression of colon tumors: prevention versus intervention," *Arch Biochem Biophys*, vol. 419, pp. 129-38, 2003.

[46] E. M. Schmelz, D. L. Dillehay, S. K. Webb, A. Reiter, J. Adams, and A. H. Jr. Merrill, "Sphingomyelin consumption suppresses aberrant colonic crypt foci and increases the proportion of adenomas versus adenocarcinomas in CF1 mice treated with 1,2-dimethylhydrazine: implications for dietary sphingolipids and colon carcinogenesis," *Cancer Research*, vol. 56, pp. 4936-41, 1996.

[47] K. W. Simon, L. Tait, F. Miller, C. Cao, K. P. Davy, T. Leroith, *et al.*, "Suppression of breast xenograft growth and progression in nude mice: implications for the use of orally administered sphingolipids as chemopreventive agents against breast cancer," *Food Funct.*, vol. 1, pp. 90-8, 2010.

[48] A. N. Hanna, L. G. Berthiaume, Y. Kikuchi, D. Begg, S. Bourgoin, and D. N. Brindley, "Tumor necrosis factor-alpha induces stress fiber formation through ceramide production: role of sphingosine kinase," *Mol. Biol. Cell*, vol. 12, pp. 3618-30, 2001.

[49] P. A. Singleton, S. M. Dudek, E. T. Chiang, and J. G. Garcia, "Regulation of sphingosine 1-phosphate-induced endothelial cytoskeletal rearrangement and barrier enhancement by S1P1 receptor, PI3 kinase, Tiam1/Rac1, and alpha-actinin," *FASEB J*, vol. 19, pp. 1646-56, 2005.

[50] Q. S. Li, G. Y. H. Lee, C. N. Ong, and C. T. Lim, "AFM indentation study of breast cancer cells," *J Biochemical and Biophysical research communications*, vol. 374, pp. 609-613, 2008.

[51] E. K. Dimitriadis, F. Horkay, J. Maresca, B. Kachar, and R. S. Chadwick, "Determination of Elastic Moduli of Thin Layers of Soft Material Using the Atomic Force Microscope," *Biophysical J*, vol. 82, pp. 2798-2810, 2002.

[52] A. Vinckier and G. Semenza, "Measuring Elasticity of biological materials by atomic force microscopy," *FEBS Letters*, vol. 430, pp. 12-16, 1998.

[53] P. Carl and H. Schillers, "Elasticity measurement of living cells with an atomic force microscope: data acquisition and processing," *Pflugers Arch*, vol. 457, pp. 551-559, 2008.

[54] A. L. Creekmore, C. L. Heffron, B. P. Brayfield, P. C. Roberts, and E. M. Schmelz, "Regulation of Cytoskeleton Organization by Sphingosine in a Mouse

Cell Model of Progressive Ovarian Cancer," *Biomolecules,* vol. 3, pp. 386-407, 2013.

[55] F. T. Arce, J. L. Whitlock, A. A. Birukova, K. G. Birukov, M. F. Arnsdorf, R. Lal, *et al.*, "Regulation of the Micromechanical Properties of Pulmonary Endothelium by S1P and Thrombin: Role of Cortactin," *Biophysical J,* vol. 95, pp. 886-894, 2008.

[56] P. C. Roberts, E. P. Mottillo, A. Baxa, N. Reale, L. Gregoire, R. Rabah, *et al.*, "Sequential molecular and cellular events during neoplastic progression: a mouse syngeneic ovarian cancer model," *Neoplasia,* vol. 7, pp. 944-956, 2005.

# 3 Biomechanical profile of cancer stem-like/tumor-initiating cells derived from a progressive ovarian cancer model

This chapter is produced from [1] with permission from Elsevier.

*H. Babahosseini, A. K. Ketene, E. M. Schmelz, P. C. Roberts, and M. Agah, "Biomechanical profile of cancer stem-like/tumor-initiating cells derived from a progressive ovarian cancer model," Nanomedicine: Nanotechnology, Biology and Medicine, vol. 10, no. 5, pp. 1013–1019, January 2014.*

## *3.1 Introduction*

The research on stem cells has achieved great momentum in the recent decades. According to the traditional cancer model, often referred to as the clonal evolution model [2], non-transformed cells can, in time, acquire an aggressive, dysregulated phenotype through the accumulation of multiple genetic or epigenetic alterations, ultimately leading to cancer. A key point in this assertion is that all cancer cells have the same potential for reinitiating a tumor. In other words, any cancer cell of a malignant tumor has the capability to form an identical tumor, if shed or re-implanted. Alternatively, a recently established cancer stem-like cell model suggests that only a unique and rare subset of cells within any given tumor are responsible for the growth, maintenance, and re-initiation of tumors [3]. It has been further suggested that the inability of today's therapeutics to target and eliminate those self-renewing "cancer stem-like cells" (CSCs) or "tumor initiating cells" (TICs) may be the cause for disease recurrence following chemotherapy; CSC/TICs are generally more resistant to chemotherapeutics compared to their fully differentiated tumor cell counterparts [4, 5]. The current challenge is to determine the self-renewal capacity of individual tumor cells in order to assess the validity of either model in a specific tumor type.

For some time now, it has been claimed that the deformation characteristics of cells, as determined by their cytoskeleton organization may be a potential biomarker or predictor of cells' disease status, overcoming the substantial individual differences in the expression of oncogenes in individual tumors that hinder cancer detection. Our recent studies in a progressive murine ovarian cancer model [6, 7] have demonstrated that cells exhibit an increasing deformability pattern and biomechanical homogeneity as they transition to more

aggressive phenotypes [8]; this is associated with changes in the actin cytoskeleton, with little to no effect by the microtubule network [9]. Our reports are in agreement with results from other studies on breast [10, 11], prostate [12], bladder [13], and ovarian [14] cancer cells, suggesting that cell stiffness is inversely related to tumorigenesis and metastatic potential.

Previously, studies on the stiffness of embryonic stem cells revealed that these cells are considerably softer before undergoing cellular differentiation process [15-17]. Also, a recent study using a mechanical separation microfluidic chip has shown that breast TICs exhibit a more uniform deformability compared to more differentiated cancer cells.[18] However, it has yet to be established whether CIC/TICs from other cancer types exhibit a similar deformability or whether anti-cancer compounds can modulate their deformability. Furthermore, the potential differences or similarities between the biomechanical properties of embryonic stem cells and CIC/TICs are yet to be identified.

In this study, we utilized the mouse ovarian surface epithelial (MOSE) cancer progression model, which has been shown to mimic many of the properties of benign and malignant human ovarian cancer cells [6, 7, 19]. Previously, we reported the increasing deformability of MOSE cells as they transition from early/benign to late/aggressive phenotypes [8]. Here, we have extended these observations and evaluated the biomechanical properties of the CSC/TICs population using AFM nano-indentation. The CSC/TICs were enriched from three distinct aggressive variant cell lines that display different degrees of tumorigenicity as defined by their *in vivo* tumor growth rates. By determining their mechanical phenotype and classification, we assessed the degree to which the CSC/TICs conformed to the biomechanical profiling of our established MOSE cancer model [8].

Additionally, we utilized our MOSE CSC/TIC population to assess the effect of serum-induced differentiation on the biomechanical signature of CSC/TICs. Cell differentiation is an important biological process, by which an unspecialized cell responds to environmental cues and develops into a more distinct cell type. A plethora of epigenetic and gene expression changes are associated with this process. Differentiation can dramatically change the cell size, shape, membrane potential, metabolic activity, and

responsiveness to exogenous signals [20-22]. Epithelial cancers are often associated with a de-differentiation phase, often referred to as epithelial-mesenchymal transition (EMT) [23].

Finally, we investigated whether the sphingolipid metabolite, sphingosine (*So*), an anti-cancer agent that inhibits or delays cancer cell proliferation, is able to modulate the deformability of MOSE CSC/TICs towards a less aggressive signature [24]. Our results thus far have indicated that CIC/TICs exhibit distinct biomechanical properties that can be modified by anti-cancer treatment with the sphingosine [19].

## *3.2 Materials and methods*

### 3.2.1 Sample preparation

MOSE cancer cells were generated and propagated as described previously [6]. The cells are categorized into early (passage no. 15-25) (MOSE-E), intermediate (passage no. 60-90) (MOSE-I), and late stage (passage no. 110-200) (MOSE-L) based on their phenotype and genotype. Normal growth medium consisted of high glucose Dulbecco's modified Eagle's medium (DMEM-HG) supplemented with 4% Fetal Bovine Serum, FBS, 3.7g/L of sodium bicarbonate, and1% Penn-strep solution.

The development of the Enhanced Green Fluorescent Protein-expressing (EGFP) and firefly luciferase-expressing (FFL) cell lines are reported elsewhere [25, 26]. They both represent *in vivo* passaged variants derived from the MOSE-L cells; the MOSE-$L^{EGFP}$ displays a moderate aggressiveness and results in slow-developing disease while the MOSE-$L^{FFL}$ is highly aggressive and results in rapidly establishing tumors following intraperitoneal implantation in mice. For this study, MOSE CSC/TICs were enriched from the parental MOSE-L, MOSE-$L^{EGFP}$ and MOSE-$L^{FFL}$ variant cell lines by culturing under non-adherent spheroid culture conditions for isolation of cancer stem-like cells for other tumor types [27, 28]. Briefly, cells were sequentially propagated under low attached conditions in serum-free DMEM:F12 (1:1) growth media supplemented with murine epidermal growth factor, (EGF; 20 ng/ml), basic fibroblast growth factor (bFGF; 5ng/ml), insulin (5ug/ml) and bovine serum albumin (BSA; 0.2%). Of note, the majority (60-99%) of the cells initially die off over the first several passages resulting in the enrichment of CSC/TIC population. The enriched population that was able to exhibit clonal expansion

from single cells is designated as a CSC/TICs population and has been stably maintained as spheroid cultures for at least 15 successive passages under these conditions.

To assess the impact of serum-induced differentiation on the biomechanics of CSC/TIC populations, single cells were seeded in the presence of complete DMEM-HG, supplemented with 4% FBS, for 24-48 hours prior to mechanical indentation experiments with the AFM.

For *So* modulatory therapy, CSC/TICs were cultured for at least three passages in the presence of exogenous *So*, added at a 1.5μM final concentration into complete DMEM-HG growth medium. This concentration was predetermined to be non-cytotoxic.

### 3.2.2 AFM experiment

Measurements were performed with the use of a Multimode V SPM integrated with a Nanoscope V controller (Veeco Instruments, Santa Barbara, CA). Uniform force loading was done at 1.5±0.3nN and a rate of 0.5μm/s among all cell samples. Cell elastic moduli were measured from ~300nm indentations in order to both maintain a constant convention and prevent deformations that exceeded 30% of total cell heights.[29, 30] According to our SEM images, the total thickness of adherent MOSE cells is 1-2μm for early stage cells while it is 3-4μm for late stage cells. Soft triangular-shaped cantilevers (K~0.02N/m, Olympus TR400PSA) were employed after modifying them with the addition of ~10μm diameter glass microspheres (Duke Scientific, Waltham MA); This promoted a better surface contact area between the probe and sample, enhanced the cell material homogeneity and isotropy approximation, and increased the likelihood that indentation was performed in the immediate nuclei region. Accurate measurements of glass microsphere diameters were made with a HIROX KH-7700 3D digital video microscope. All AFM tests were conducted within DMEM-HG cell culture medium at room temperature (~24°C) except designated *So*-treated cells which were tested within *So*-added DMEM-HG medium. For AFM experimentation, cells were grown and harvested within incubators at 37°C in humidified 5% $CO_2$ and later plated at $10^5$cells/slip on 0.15mm thick, 12mm$^2$ glass coverslips coated with 0.1mg/mL collagen type IV (Sigma-Aldrich) for 24hrs. 40μL/3mL of HEPES at 1M concentration was added to the cell samples to maintain a physiological pH of 7.2 during

the experimentation. Final pH concentration of HEPES in the testing medium was 13.5mM and stable for about 2 hrs, which was sufficient enough for each AFM test period.

### 3.2.3 Hertz model

Cell stiffness can be extracted by fitting the applied force-induced deformation data (force curves) with Sneddon's modified version of the Hertz contact model [31]. This model states that external forces are dominant over microscale surface and adhesive forces [31, 32]. By asserting the applicability of classical mechanics theory in nanoscale indentation caused by the AFM tip, the Hertz model expresses the relation between an applied normal force by a spherical body and a sample's indentation:

$$F = \frac{4}{3} E^* \sqrt{R} . \delta^{\frac{3}{2}} \tag{4}$$

where F is the applied force, $E^*$ is the relative stiffness term, $R$ is the radius of the indenting body, and $\delta$ is the sample's induced deformation. In accordance with prior literature [33, 34], the equation is transformed into the following form:

$$F = \frac{4}{3} \sqrt{R} \frac{E_{cell}}{1-\nu_{cell}^2} . \delta^{\frac{3}{2}} \tag{5}$$

where $E_{cell}$ and $\nu_{cell}$ are the elastic modulus and Poisson's ratio of the indented cell sample, respectively (cell assumed incompressible; $\nu_{cell}$=0.5). Furthermore, in the interest of identifying the most accurate point of tip-sample contact, the indentation, $\delta$, is both linearized [35, 36] and referred to as the difference between the relative change in piezo position ($z$) and cantilever deflection ($d$):

$$\delta = (z - z_0) - (d - d_0) \tag{6}$$

Hence, the final form of the Hertz contact expression is as follows:

$$F^{\frac{2}{3}} = \left[ \frac{4\sqrt{R}}{3(1-\nu_{cell}^2)} E_{cell} \right]^{\frac{2}{3}} (z - d) - \left[ \frac{4\sqrt{R}}{3(1-\nu_{cell}^2)} E_{cell} \right]^{\frac{2}{3}} (z_0 - d_0) \tag{7}$$

Since the fitting model assumes linearity in the tip-sample interaction data, Equation (3.4) can be analyzed such that the elastic modulus, $E_{cell}$, is determined from the slope, and

the contact point ($z_0$, $d_0$) is approximated by the intercept of the line fit, respectively. Force curve analysis which includes the Hertz model fitting to the cell indentation data and calculation of cell elastic modulus, was performed with MATLAB software.

### 3.2.4 Statistical analysis

Cells to be indented via AFM on the coverslips were arbitrarily selected, but had to macroscopically exhibit a well-adherent and healthy morphology/appearance prior to experimentation. The tested cells were only subjected to a single indentation, as repetitive indentations change cell morphology. For indenting the cell nucleus region, the AFM tip was positioned at the center of cells. The experiments were conducted so as to acquire sample sizes of 40–50 cells for the previously reported regular MOSE cells and 75-105 for MOSE CSC/TICs from at least three separate AFM tests performed on different days. The Hertz model fit well with the acquired experimental data, with a high correlation coefficient ($0.85 \leq R^2 \leq 0.99$) to quantify the cells' elastic moduli. Statistical Shapiro-Wilks tests were employed to analyze the measured elastic moduli for normality distributions. Levene's statistical tests were used to test for homogeneity of variances. Two independent samples t-tests were also applied to the normalized data to evaluate the statistical significance of differences between the means of selected populations. A 95% confidence interval ($p < 0.05$) was implemented to assess normality distribution of the data and the degrees of difference between two populations.

## *3.3 Results*

A series of AFM nanoindentation tests were conducted on selected populations to measure cell stiffness (Figure 3.1). The elastic modulus parameter was measured on MOSE populations undergoing cancer progression representing early, intermediate, late stage cells (MOSE-E, -I, and -L), in addition to CSC/TICs enriched from the late stage cancer cell line variants. Moreover, the impact of re-differentiation as well as the effects of *So* treatment on CSC/TICs were investigated by comparing elastic modulus measurements following serum differentiation and *So*-treatment to that of untreated "control" cells.

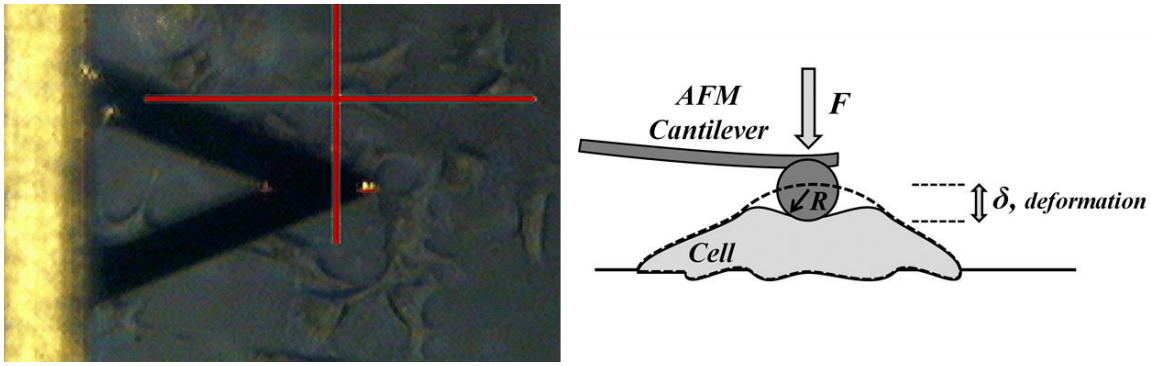


**Figure 3.1 AFM indentation top view screenshot during cell experimentation (Left) and indentation side view schematic illustration (right). AFM microcantilever is about 200µm in length and the indenting glass sphere is about 10µm in diameter. Cell indentations are usually in the sub-micrometer ranges as a result of applied nanoforce.**

The elastic modulus mean, standard deviation (SD), and mode values, (corresponding to the values most repeated in the sets of measurements) of the selected populations are represented in Table 3.1. Standard error of the means (SE) for the large selected sample sizes of the populations were very small, and were deemed negligible in terms of statistical significance. AFM measurements clearly show significant differences in stiffness of MOSE cells in three stages of cancer progression, confirming our previous results.[8] The Elastic modulus values showed that MOSE-L cells (0.601±0.212kPa) are on average 29% ($p<0.0001$) softer than MOSE-I cells (0.825±0.324kPa) which are 27% ($p<0.0001$) softer that MOSE-E cells (1.164±0.557kPa). Most notably however, the CSC/TICs population (0.321±0.119kPa) enriched from MOSE-L cells has shown to be 46% softer than MOSE-L cells ($p<0.0001$), which provides additional insight into the biomechanical profiling scheme for the MOSE cancer progression model.

The CSC/TIC re-differentiation by growth in the presence of complete media containing serum did not elicit any significant change in the CSC/TICs' mechanical response to external loading (0.333±0.125kPa). This suggests that short-term growth under differentiation conditions does not result in cell stiffness reversion. In contrast, *So* treatment caused a significant increase in the average elastic modulus value of the CSC/TICs (0.471±0.138kPa) by approximately 47% ($p<0.0001$), indicating that MOSE CSC/TICs are biomechanically influenced by the treatment of the *So* anti-cancer agent (Table 3.1).

**Table 3-1 Summary of elastic modulus responses for the early, intermediate, late MOSE cells and the control, differentiated, and So treated MOSE CSC/TICs.**

| MOSE Cells $E_{elastic}$ (kPa) | Early Stage | Intermediate Stage | Late Stage | Control CSC/TICs | Differentiated CSC/TICs | So treated CSC/TICs |
|---|---|---|---|---|---|---|
| *Mean±SD* | 1.164±0.557 | 0.825±0.324 | 0.601±0.212 | 0.321±0.119 | 0.333±0.125 | 0.471±0.138 |
| *Mode* | 0.95 | 0.7 | 0.5 | 0.25 | 0.28 | 0.42 |
| *n Cells* | 49 | 50 | 42 | 105 | 76 | 97 |

As depicted in Figure 3.2, Cell population histograms are generated by combining all recorded elastic modulus responses from each tested cell line. The data were best represented by log-normal distributions and log-Gaussian fits. The mode values may be extracted as the peak points of the histograms profile. The results from the Levene's tests rejected the equality of the histograms' variances. Thus, it was concluded that there is a difference in the homogeneity of variances between the populations. Furthermore, the decrease in mean elastic modulus in cancer progression was accompanied by a decrease in standard deviation, and therefore variance of the histogram. This finding supports our previously established biomechanics model [8] which indicates that cancer progression is associated with increasing deformability (Figure 3.2.A, 3.2.B, and 3.2.C), mechanical response homogeneity, and cytoskeleton disorganization. Most notably, the CSC/TIC population exhibited a more homogeneous stiffness profile and a very sharp concentrated histogram distributed in very low elastic modulus values in comparison to other MOSE-derived cancer cells. MOSE CSC/TICs mechanical response distributions before and after differentiation and *So* treatment are shown in Figure 3.2.D, 3.2.E, and 3.2.F, respectively. Serum-induced differentiation had no impact on the histogram curve due to the short-term differentiation process (Figure 3.2.E) while *So* treatment notably shifted the response curve towards the "stiffer" values for CSC/TICs MOSE (Figure 3.2.F).

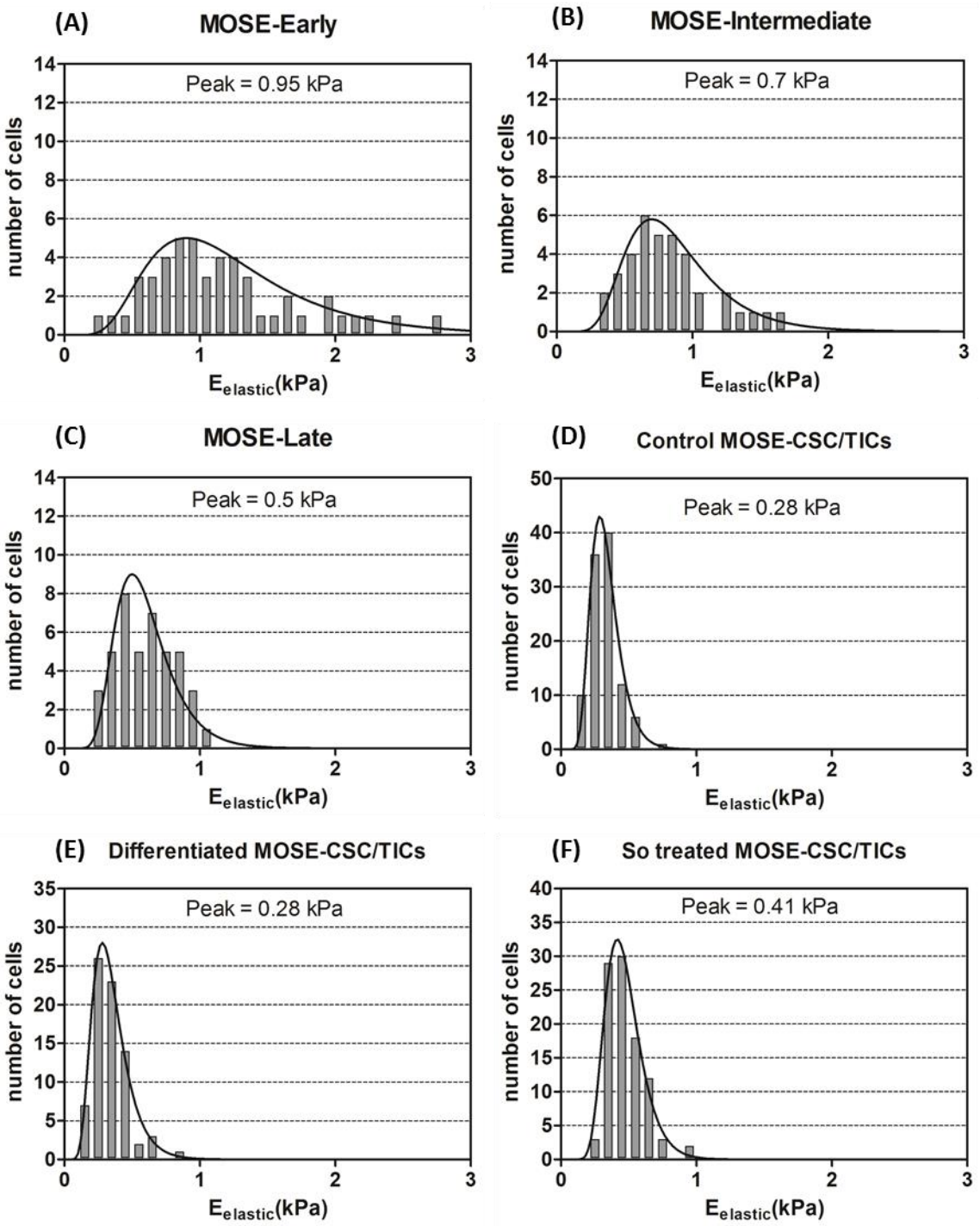


**Figure 3.2 Population distributions responses of (A) early, (B) intermediate, (C) late MOSE cells and the MOSE-CSC/TICs in (D) control (E) differentiated, and (F) So treated conditions.**

To confirm the unique, low stiffness response of CSC/TICs, the elastic modulus parameter for the CSC/TICs$^{FFL}$ and CSC/TICs$^{EGFP}$ populations were measured and compared to their parental counterparts. The AFM nano-indentation measurements are

summarized in Table 3.2. The results illustrate that both CSC/TICs$^{FFL}$ and CSC/TICs$^{EGFP}$ populations display significantly (about 47% and 40%, respectively) less average stiffness compared to that of the corresponding parental MOSE-L cells (Table 3.2), and thus, confirm the distinctive CSC/TICs response profile.

**Table 3-2 Summary of elastic modulus values for the MOSE-LFFL and MOSE-LEGFP and the corresponding enriched CSC/TICs.**

| MOSE cells $E_{elastic}$ (kPa) | MOSE-L$^{FFL}$ | MOSE-L$^{EGFP}$ | CSC/TICs$^{FFL}$ | CSC/TICs$^{EGFP}$ |
|---|---|---|---|---|
| *Mean±SD* | 0.657±0.194 | 0.682±0.229 | 0.347±0.148 | 0.407±0.179 |
| *Mode* | 0.59 | 0.6 | 0.25 | 0.25 |
| *n Cells* | 55 | 44 | 48 | 49 |

The distributions of the CSC/TICS populations are concentrated in lower stiffness values, and are more homogeneous than those of their respective parental MOSE-L variant cell lines. Column graphs representing mean values and error bars representing standard deviation of the measured elastic moduli for all selected populations are demonstrated in Figure 3.3. Therein, t-tests are applied to the logarithmic transformed and normalized data based on the Shapiro-Wilks test and the results from the t-tests (*p*-values) are illustrated and compared amongst each two populations.

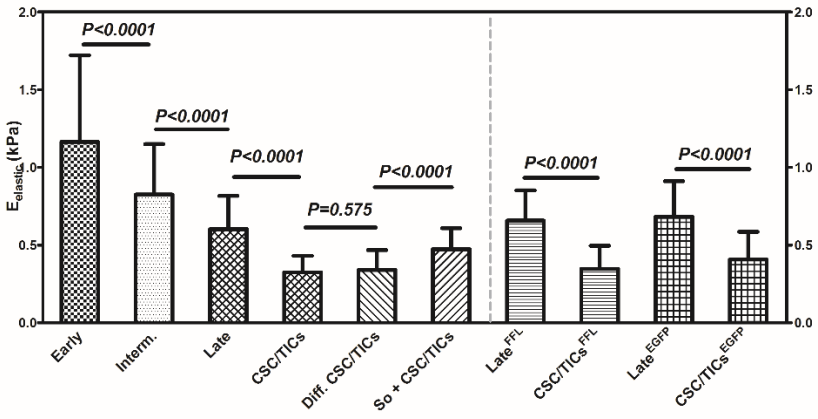


**Figure 3.3 Elastic modulus responses of three successive stages of MOSE cancer cells and three variants of MOSE CSC/TICs enriched from late stage cell lines. In comparison to the established MOSE cancer stage model, the tumor initiating phenotype matches well in the order of cancer malignancy-mechanics functionality profile.**

## 3.4 Discussion and conclusion

CSC/TIC populations enriched from three distinct, late stage variants of MOSE cancer cells exhibit a more homogeneous biomechanical signature in comparison to their parental counterparts. The CSC/TICs' stiffness distributions are in the very low elastic modulus values, which are a subset found in every transitional stage of this model including the early, intermediate, and late stages. Also, the short-term differentiation process did not cause any shift or change in the elastic modulus measurements. Finally, CSC/TICs, like their parental counterparts, are sensitive to *So* treatment, which targets cytoskeleton dysfunction in CSC/TIC phenotypes and reverts their deformability to a less aggressive phenotype.

The presented results have several implications. Most importantly, they may help explain some key questions about the nature of the CSC/TICs phenotypes. In particular, are CSC/TICs present throughout cancer progression or do they arise following accumulation of genetic alterations conferring the cancer-like phenotype? If the notion is followed that CSC/TICs do not develop with time, but are present at low levels, even at the earliest stages of cancer transformation, then softer cell types should be evident in all transition phases of our model, including the heterogeneous MOSE-E populations. These cells should be present with very high deformability profiles comparable to "cancer stem-like" or "tumor initiating" cells. However, it is unclear whether these early stage, relatively soft precursor cells would have acquired the necessary mutations or epigenetic changes to confer tumorigenicity but they may represent the earliest precursor tumor cell that is subject to further transformation. Hence, the deformability of cells may provide a signature to identify early premalignant cells. We are currently attempting to isolate the CSC/TIC populations derived from the MOSE-E (benign) and MOSE-I (intermediate stage) cell lines to assess whether biomechanical differences are inherent to culture conditions or are clear indices for pre-malignancy or aggressive phenotypes. Of note, the enrichment for CSC/TICs resulted in cells that were either more or as aggressive *in vivo*, leading to higher tumor burden scores than their adherent counterparts, supporting the fact that they do in fact represent true tumor-initiating cell populations.

In agreement with our previous studies using adherent cultures of MOSE cells, MOSE CSC/TICs are susceptible to biomechanical modulation via exposure to non-

cytotoxic doses of *So*. Based on our previous studies [9], the significant changes in cell stiffness most probably reflect changes in the cytoskeleton architecture of the CSC/TICs. *So* treatment over time improves cytoskeleton organization and increases f-actin levels in MOSE-L cells [19] and increases the average elastic modulus of aggressive MOSE cells [37], while not affecting their precursor benign cells.

The presented work suggests that MOSE CSC/TICs mechanical behavior conforms to the progression of our established MOSE cancer model [8] and carries a unique distribution profile. Our study also validates the mechanical properties of CSCs derived from breast cancer cell lines [18] and extends them to CSC/TICs derived from murine ovarian cancer cell lines. Future studies will clarify whether the softer biomechanical profile is a hallmark signature of all CSC/TICs irrespective of origin. The reported findings provide quantitatively supportive data that imply that the biomechanical properties of cells may be suitable for targeted isolation of malignant cells using biomedical microdevices. Indeed, the AFM technique may not prove to be amenable to high throughput cell identification or sorting based on the "deformability biomarker", but other recent techniques such as the use of microfluidics [38-40] could be employed for effective screening for stiffness and viscoelastic behavior of cells and as a means of biomechanical profiling of aggressive phenotypes.

## *References*


[1] H. Babahosseini, A. K. Ketene, E. M. Schmelz, P. C. Roberts, and M. Agah, "Biomechanical profile of cancer stem-like/tumor-initiating cells derived from a progressive ovarian cancer model," *Nanomedicine: NBM,* vol. 10, pp. 1013-9, 2014.

[2] P. C. Nowell, "The clonal evolution of tumor cell populations," *Science,* vol. **194**, pp. 23-28, 1976.

[3] M. A. Teitell, S. Kalim, J. Schmitt, and J. Reed, "Biomechanics of Single Cells and Cell Populations," in *Nanodiamonds: Applications in Biology and Nanoscale Medicine* Ho D, Ed., ed, 2010, pp. 235-247.

[4] C. H. Park, D. E. Bergsagel, and E. A. McCulloch, "Mouse myeloma tumor stem cells: a primary cell culture assay," *Journal of the National Cancer Institute,* vol. **46**, pp. 411-422, 1971.

[5] T. Lapidot, C. Sirard, J. Vormoor, Murdoch. B., T. Hoang, J. Caceres-Cortes, *et al.*, "A cell initiating human acute myeloid leukaemia after transplantation into SCID mice," *Nature,* vol. **367**, pp. 645-648, 1994.

[6] P. C. Roberts, E. Motillo, A. C. Baxa, H. H. Q. Heng, N. Doyon-Reale, L. Gregoire, *et al.*, "Sequential Molecular and Cellular Events during Neoplastic progression: A Mouse Syngeneic Ovarian Cancer Model," *Neoplasia,* vol. **7**, pp. 944-956, 2005.

[7] A. L. Creekmore, W. T. Silkworth, D. Cimini, R. V. Jensen, P. C. Roberts, and E. M. Schmelz, "Changes in Gene Expression and Cellular Architecture in an Ovarian Cancer Progression Model," *PLoS ONE,* vol. **6**, p. e17676, 2011.

[8] A. N. Ketene, E. M. Schmelz, P. C. Roberts, and M. Agah, "The effects of cancer progression on the viscoelasticity of ovarian cell cytoskeleton structures," *Nanomedicine : nanotechnology, biology, and medicine,* vol. **8**, pp. 93-102, 2011.

[9] A. N. Ketene, P. C. Roberts, A. A. Shea, E. M. Schmelz, and M. Agah, "Actin filaments play a primary role for structural integrity and viscoelastic response in cells," *Integrative Biology,* vol. **4**, pp. 540-549, 2012.

[10] M. Nikkhah, J. Strobl, R. De Vita, and M. Agah, "The cytoskeletal organization of breast carcinoma and fibroblast cells inside three dimensional (3-D) isotropic silicon microstructures," *Biomaterials,* vol. 31, pp. 1-10, 2010.

[11] M. Nikkhah, J. S. Strobel, E. M. Schmelz, and M. Agah, "Evaluation of the influence of growth medium composition on cell elasticity," *Journal of Biomechanics,* vol. **44**, pp. 762-766, 2011.

[12] E. C. Faria, N. Ma, E. Gazi, P. Gardner, M. Brown, N. W. Clarke, *et al.*, "Measurement of elastic properties of prostate cancer cells using AFM," *Analyst,* vol. **133**, pp. 1498-1500, 2008.

[13] M. Lekka, P. Laidler, D. Gil, J. Lekki, Z. Stachura, and A. Z. Hrynkiewicsm, "Elasticity of normal and cancerous human bladder cells studied by scanning force microscopy," *Biophysics Journal,* vol. **28**, pp. 312-316, 1999.

[14] W. Xu, R. Mezencev, B. Kim, L. Wang, J. McDonald, and T. Sulchek, "Cell stiffness is a biomarker of the metastatic potential of ovarian cancer cells.," *Plos One,* vol. **7**, p. e46609, 2012.

[15] J. D. Pajerowski, K. N. Dahl, F. L. Zhong, P. J. Sammak, and D. E. Discher, "Physical plasticity of the nucleus in stem cell differentiation," *PNAS,* vol. **104**, pp. 15619-15624, 2007.

[16] F. Chowdhury, S. Na, D. Li, Y. C. Poh, T. S. Tanaka, F. Wang, *et al.*, "Material properties of the cell dictate stress-induced spreading and differentiation in embryonic stem cells," *Nature Materials,* vol. **9**, pp. 82-88, 2010.

[17] I. Titushkin and M. Cho, "Modulation of cellular mechanics during osteogenic differentiation of human mesenchymal stem cells," *Biophys Journal,* vol. **93**, pp. 3693-3702, 2007.

[18] W. Zhang, Kai. K., Choi. D.S., T. Iwamoto, Y. H. Nguyen, H. Wong, *et al.*, "Microfluidics separation reveals the stem-cell–like deformability of tumor-initiating cells," *PNAS,* vol. **109**, pp. 18707-12, 2012.

[19] A. L. Creekmore and et al., *Biomolecules,* vol. (Special Issue Bioactive Lipids), 2013.

[20] P. V. N. Bodine, R. A. Henderson, J. Green, M. Aronow, T. Owen, G. S. Stein, *et al.*, "Estrogen Receptor-alfa Is Developmentally Regulated during Osteoblast Differentiation and Contributes to Selective Responsiveness of Gene Expression," *Endocrinology,* vol. **139**, pp. 2048-2057, 1998.

[21] A. Ben-Ze'ev, "The role of changes in cell shape and contacts in the regulation of cytoskeleton expression during differentiation.," *Journal of Cell Science. Supplement,* vol. **8**, pp. 298-312, 1987.

[22] J. L. Rodriguez Fernandez and A. Ben-Ze'ev, "Regulation of fibronectin, integrin and cytoskeleton expression in differentiating adipocytes: inhibition by extracellular matrix and polylysine," *Differentiation,* vol. **42**, pp. 65-74, 1989.

[23] S. Sell, "Cellular origin of cancer: dedifferentiation or stem cell maturation arrest?," *Environmental Health Perspectives,* vol. **101**, pp. 15-26, 1993.

[24] C. R. Gault, L. M. Obeid, and Y. A. Hannun, "An overview of sphingolipid metabolism: from synthesis to breakdown," *Advances in Experimental Medicine and Biology,* vol. **688**, pp. 1-23, 2010.

[25] C. A. Cohen, A. A. Shea, E. M. Schmelz, and P. C. Roberts, "Early immune modulatory events during ovarian cancer outgrowth in the omental fat band," *Cancer Research,* vol. 72, p. Suppl 1, 2012.

[26] C. A. Cohen, "The omental fat band as an immunomodulatory microenvironment for ovarian cancer," PhD thesis, Virginia Tech, 2013.

[27] G. Rappa, J. Mercapide, F. Anzanello, L. Prasmickaite, Y. Xi, J. Ju, *et al.*, "Growth of cancer cell lines under stem cell-like conditions has the potential to unveil therapeutic targets," *Exterimental Cell Research,* vol. **314**, pp. 2110 - 2122, 2008.

[28] D. Feng, C. Peng, C. Li, Y. I. Zhou, M. Li, B. Ling, *et al.*, "Identification and characterization of cancer stem-like cells from primary carcinoma of the cervix uteri," *Oncology Reports* vol. **22**, pp. 1129-1134, 2009.

[29] F. Rico, P. Roca-Cusachs, N. Gavara, R. Farre, M. Rotger, and D. Navajas, "Probing mechanical properties of living cells by atomic force microscopy with blunted pyramidal cantilever tips," *J Phys Rev E,* vol. **72**, pp. 1-10, 2005.

[30] S. Sen, S. Subramanian, and D. E. Discher, "Indentation and adhesive probing of a cell membrane with AFM: theoretical model and experiments.," *Biophysics Journal,* vol. **89**, pp. 3203-3213, 2005.

[31] H. Hertz, "On the contact of elastic solids," *Journal of Reine Angew Math.,* vol. **92**, pp. 156-171, 1881.

[32] I. N. Sneddon, "The relation between load and penetration in the axisymmetric Boussinesq problem for a punch of arbitrary profile," *International Journal of Engineering Science,* vol. **3**, pp. 47-57, 1965.

[33] E. M. Darling, S. Zauscher, J. M. Block, and F. Guilak, "A thin-layer model for viscoelastic, stress-relaxation testing of cells using Atomic Force Microscopy: Do Cell Properties Reflect Metastatic Potential," *Biophysical Journal,* vol. **92**, pp. 1784-1791, 2007.

[34] S. E. Cross, Y. Jin, J. Rao, and J. K. Gimzewski, "Nanomechanical analysis of cells from cancer patients," *Nature Nanotechnology,* vol. **2**, pp. 780-783, 2007.

[35] S. L. Guo and B. B. Akhremitchev, "Packing density and structural heterogeneity of insulin fibrils by AFM nanoindentation," *Journal of Biomacromolecules,* vol. **7**, pp. 1630-1636, 2006.

[36] P. Carl and H. Schillers, "Elasticity measurement of living cells with an atomic force microscope: data acquisition and processing," *Pflugers Arch-Eur J Physiol,* vol. **457**, pp. 551-559, 2008.

[37] H. Babahosseini, P. C. Roberts, E. M. Schmelz, and M. Agah, "Roles of bioactive Sphingolipid metabolites in ovarian cancer cell biomechanics," presented at the Engineering in Medicine and Biology Society (EMBC), San Diego, CA, 2012.

[38] A. Adamo, A. Sharei, L. Adamo, B. K. Lee, S. Mao, and K. F. Jensen, "Microfluidics-Based Assessment of Cell Deformability," *Analytical Chemistry,* vol. **84**, p. 6438−43, 2012.

[39] Y. Zheng, E. Shojaei-Baghini, A. Azad, C. Wang, and Y. Sun, "High-throughput biophysical measurement of human red blood cells," *Lab on a Chip,* vol. **12**, pp. 2560-67, 2012.

[40] H. W. Hou, Q. S. Li, G. Y. H. Lee, A. P. Kumar, C. N. Ong, and C. T. Lim, "Deformability study of breast cancer cells using microfluidics," *Biomedical Microdevices,* vol. **11**, pp. 557-564, 2009.

# 4 The fractional viscoelastic response of human breast tissue cells



*B Carmichael*, H Babahosseini*, S N Mahmoodi and M Agah (*Co-first authors), "The fractional viscoelastic response of human breast tissue cells," Physical Biology, vol. 12, no. 4, pp. 046001, May 2015.*

## *4.1 Introduction*

In recent years, the study of cellular mechanics has gained great significance for its contributions to the understanding of cell homeostasis and the behaviors of proliferation, motility, and differentiation, which influence many aspects of human health. Extensive research has developed techniques that allow for the extraction of mechanical properties of many cell groups, such as micropipette aspiration [2], optical tweezers [3], optical stretching rheometry [4], magnetic twisting [5], and atomic force microscopy (AFM) [6, 7]. Among these, the AFM is broadly used for the characterization of a variety of cell lines due to its nano-scale resolution, including prostate [8], bladder [7], lung [9], breast [10, 11], mesothelial [12], blood [13], and osteoblast cell samples [14, 15].

Many approaches are concerned solely with the elastic properties of the samples, drawing conclusions by comparing cell elastic moduli extracted by nano-indentation procedures via AFM under different environmental conditions. Among these, studies of malignant cancer cells and their benign counterparts have demonstrated extremely promising results for the mechanical differentiation and diagnosis of these conditions. For example, metastatic cancer cells harvested from body cavity fluid have already been shown to exhibit a stark difference in elasticity from their benign equivalents with the malignant cells being considerably softer [9-11]. Newer studies have also determined the differential effects of exogenous sphingolipid metabolites on the elastic modulus of mouse ovarian surface epithelial cells as they transition to cancer [16]. Recently, the same group has shown that the elastic properties of cancer stem-like/tumor initiating cells enriched from ovarian cancer cells exhibit considerably softer and more homogeneous characteristics in comparison to their less aggressive counterparts [17].

Despite recent progress, biological tissue remains one of the largest challenges to date for continuum mechanics. The heterogeneity of each sample and the near infinite catalog of cell types make any effort to generalize their responses to a certain forcing function impractical. Subcellular structure is highly complex and introduces nonlinear depth-dependent mechanical properties, which restrict the efficacy of differentiation studies. The effects become considerably more pronounced for deeper levels of indentation, where the cell's internal architecture engages and contributes to the response. Therefore, property measurement and differentiation studies generally limit the overall indentation to approximately 10% of the cell height. However, any information that may be locked away in the deeper parts of the cell are overlooked. These measurements may provide a wealth of information for mechanical diagnosis of disease and are worthy of consideration.

Additionally, newer research has indicated that time-dependent properties may also serve as indicators of disease and overall cell motility revealing similar trends in cell viscosity under shallow indentation [18, 19]. To make full use of this discovery and the cell's complete biomechanical fingerprint, an accurate model of stress-relaxation for nano-indentation tests is necessary. The data generated from testing may be fitted to any number of theoretical curves to produce a set of parameters that can describe the response. However, the composition of these theoretical curves must occur under certain assumptions that have biophysical and biological interpretations. Both the contact force between the tip and sample and the constituent viscoelastic equation must be incorporated. For AFM nano-indentation with a spherical indenter, the modified Hertz contact model is a common realization of the major interactions between the indenter and the sample. Several models have implemented this in combination with a mechanical analogy of viscoelasticity to effectively describe the sample response [20-24]. Mechanical analogies of viscoelasticity include elastic (Hookean springs) and viscous components (Newtonian dashpots) to emulate the mixed character of viscoelastic samples. The simplest one of these that captures both stress relaxation and creep is the Standard Linear Solid (SLS) model, also known as the Zener model [25]. Unfortunately, the shortcomings of a simple linear model are evident when testing materials with a short characteristic relaxation time or those with responses that cannot be characterized by a single exponential decay[20]. The benefits

of the SLS model, small parameter sets and easy curve-fitting procedures, do come at the price of information. Linear models ignore the early portion of the response in curve-fitting procedures. This study attempts to characterize the nonlinearities associated with an arbitrarily complex subcellular structure by exploiting the nature of fractional mechanics with degree between zero and one.

The field of fractional calculus has roots nearly as old as those of integer-differential calculus, but it has not seen significant growth and application until recent times. Its application to viscoelasticity has been thoroughly investigated with particular emphasis on materials that exhibit some degree of memory [26-29]. Specifically, several studies have taken advantage of its flexibility to describe the frequency-dependent viscous character of soft polymers [30-32]. Other variations of the FZ model have been used to describe the impact or relaxation response of brain, bone, and atrial tissue [33-36]. So, the application to individual cells is a novel step in this natural progression.

Following, this paper will address the concerns associated with the SLS model and soft-tissue sampling and will evaluate the utility of the Fractional Zener (FZ) model for the determination of time-dependent properties. The cell samples will undergo deep indentation to include the mechanical properties of deeper subcellular architecture. The equations governing the response of the SLS model are mentioned to provide the mathematical foundation for the FZ model. The FZ model differs from a linear model of viscoelasticity in that it allows for a non-integer time-derivative relationship between stress and strain. This added degree of freedom brings with it added degrees of complexity; however, the utility of such an extension is vast. A qualitative discussion concerning the physical interpretation of its parameters is included to ease its use in other comparative studies.

Data derived from the AFM stress-relaxation procedures on two sample populations of human breast tissue, non-invasive (MCF10A) (n = 44) and highly-invasive (MDA-MB-231) (n = 43), will be fit to theoretical curves generated by each model using a nonlinear least-squares method. Conclusions concerning the utility and scope of the fractional model will follow the analysis.

## *4.2 Materials and methods*

### 4.2.1 Sample preparation

The MDA-MB-231 and MCF10A cell lines, respectively representing a highly-invasive and non-invasive stage of breast cancer were used in this work. The cells were purchased from the American Type Culture Collections (ATCC). The MDA-MB-231 cells were maintained at 37°C in a humidified 5% CO2-95% air atmosphere in F12:DMEM (50:50) culture medium which contained 10% fetal bovine serum (FBS), 4 mM glutamine, and penicillin-streptomycin (100 Units/ml). The MCF10A cells were grown in F12:DMEM (50:50), 2.5 mM L-glutamine, 20 ng/ml epidermal growth factor (EGF), 0.1 μg/ml cholera toxin (CT), 10 μg/ml insulin, 500 ng/ml hydrocortisone and 5% horse serum. For AFM tests, cells were harvested, plated at a density of $1\times10^5$ cells per $12mm^2$ glass cover slip, and incubated for 24 hours. Cover slips were initially coated with 0.1 mg/mL collagen type IV (Sigma-Aldrich, St. Louis, MO) to help the cells attach to the glass cover slips. AFM tests were carried out on single cells in the standard culture medium at room temperature (24°C). A buffered HEPES solution was added to the samples at a final concentration of 13.5 mM before the AFM testing to maintain a constant physiological pH of 7.2 during experiment sessions.

### 4.2.2 AFM experiment

All experiments were conducted with a Dimension Icon AFM (Bruker Corporation, Billerica, MA). TR400PSA V-shaped silicon nitride cantilevers (Olympus, Tokyo, Japan) of ~200 μm lengths and ~0.02 N/m nominal spring constants were used. The practical spring constants of the cantilevers were experimentally measured using thermal noise tuning and were within 20% of the nominal values. The sharp probes were modified by attaching glass microspheres (Duke Scientific, Waltham, MA) of ~10 μm diameter onto the cantilever free end with two-part epoxy (Miller Stephenson, Sylmar, CA), which increased the total surface contact area and, consequently, reduced damage to the cells during contact. Their exact radius was identified using a HIROX KH-7700 3D Digital Video Microscope. The measurements were performed above each cell's nucleus under optical control with a constant approach velocity of ~5 μm/s at a 5 kHz sampling

frequency. The maximum indentation force was limited to a trigger of 9 ± 3 nN which induced a ~2-3 μm deep indentation into the cellular substructures.

### 4.2.3 Confocal microscopy

Both cell populations were seeded on collagen-coated glass coverslips and allowed to attach and grow for 24-30 hours. The cells were first rinsed with Hank's balanced salt solution (HBSS) and 3% paraformaldehyde (PF) solution in 250 mM HEPES, pH 7.2 for 10 minutes. To permeabilize the cell membrane, the cells were exposed to 6% PF solution with 0.25% Triton X-100 in Phosphate-Buffered Saline (PBS) for another 10 minutes. To remove any excess PF, 50 mM glycine in PBS was used for 10 minutes. A 2% chicken serum albumin (CSA) in a PBS solution was using for >30 minutes to block non-specific antibody binding. The actin cytoskeleton was stained with Alexa-488 conjugated phalloidin (Invitrogen, Carlsbad, CA) diluted 5 unit/ml in 140 mM NaCl-6% bovine serum albumin in 40 mM Tris, pH 7.2 for 20 minutes at room temperature, followed by three washes with PBS. Processed coverslips were mounted onto glass slides using Prolong Gold Antifade reagent containing DAPI (Invitrogen, Carlsbad, CA) to emphasize the nuclei. Images were captured with an inverted Zeiss LSM 510 confocal microscope (Carl Zeiss Microscopy LLC, Thornwood, NY) equipped with UV and argon lasers, filtered with DAPI (blue) and FITC (green) fluorescence filters using ZEN 2011 software, and processed with Adobe Photoshop.

### 4.2.4 Standard Linear Solid (SLS) model

The Hertz model is useful to predict elastic properties, but it does not predict time dependent behavior; therefore, it must be combined with an appropriate stress-relaxation model to fully describe the response of a sample that is not perfectly elastic. The method developed in Darling *et al* (2006) has been very successful in blending it with the SLS model using the correspondence principle in the Laplace domain. Fortunately, the same technique may be used for more extensive models assuming that the ratio of stress to strain in the Laplace domain may be expressed explicitly, such that:

$$\frac{\bar{\sigma}}{\bar{\varepsilon}} = E(s) \tag{8}$$

Unfortunately, this excludes certain quasi-linear models where stiffness is dependent on the strain ratio, which have been used to model breast tissue by other experimental methods [37]. The correspondence principle links viscoelastic systems with an equivalent elastic system and allows for the construction of a solution via analogy [20].

The procedure illustrated in previous works [20] allows for the transformation of Hertz model into the Laplace domain by replacing Young's modulus with a factor proportional to the transfer function illustrated in (4.1):

$$\overline{F}(s) = \frac{4}{3}\frac{\sqrt{R\delta_0^3}}{(1-\nu)}\frac{E(s)}{s} \tag{9}$$

where $\delta_0$ is the maximum indentation resulting from the application of the contact force. So, this conclusion allows any relaxation model with an explicit transfer function between stress and strain to be combined with the Hertz indentation model.

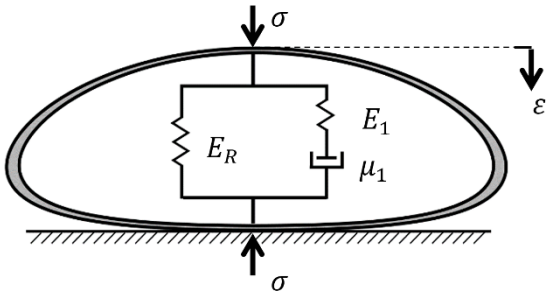


**Figure 4.1 The mechanical schematic of the SLS model is comprised of a single spring in parallel with a spring and damper in series.**

The simplest example that can handle the effects of both stress relaxation and creep is the Standard Linear Solid (SLS) model. Its mechanical schematic is comprised of a single spring in parallel with a spring and damper in series, as in Figure 4.1. The equation of motion for the system may be written as

$$\left(\frac{1}{E_1}\right)D\sigma(t) + \frac{1}{\mu}\sigma(t) = \left(1 + \frac{E_R}{E_1}\right)D\varepsilon(t) + \frac{E_R}{\mu}\varepsilon(t) \tag{10}$$

For brevity, the derivation for the extension to the Hertz model is not shown. Instead, the reader is directed to the work of Darling *et al* for an exhaustive investigation. The final equation of the SLS model may be written as

$$F(t) = \frac{4}{3}\frac{\sqrt{R\delta_0^3}}{(1-\nu)}\left[E_R + E_1 \exp\left(-\frac{\mathrm{E}_1}{\mu_1}t\right)\right] \tag{11}$$

This model has three flexible parameters and can effectively model samples that exhibit simple exponential relaxation (i.e. characterized by only one relaxation time). Due to its simplicity, it has a wide gamut of successful applications with some notable successes in AFM stress relaxation experiments [38, 39]. The coefficient of *t* in (4.4) may also be recast into a characteristic relaxation time that is often more useful in experimental procedures:

$$\tau = \frac{\mu_1}{E_1} \tag{12}$$

The relaxation time represents the point in time where the response has decayed to a certain fraction of the total response span according to:

$$F_\tau = F_\infty + \mathrm{e}^{-1}(F_0 - F_\infty) \tag{13}$$

The AFM stress relaxation experimental data can be sectioned into three regimes, as shown in Figure 4.2: approach, indentation, and relaxation. Before the relaxation response may be fit to an analytical curve, the maximum deflection, $\delta_0$, must be determined from the indentation region. This is extensively demonstrated in previous literature, but for the sake of continuity an overview is presented here as well. First, the indentation region of the response must be transformed from raw deflection data by multiplying the trial time by the approach velocity and the deflection error by the cantilever spring constant. Determination of the contact point for each cell was accomplished by fitting the resulting force-distance curve to a modified Hertz model, which describes contact between a spherical indenter and an infinite half-space.

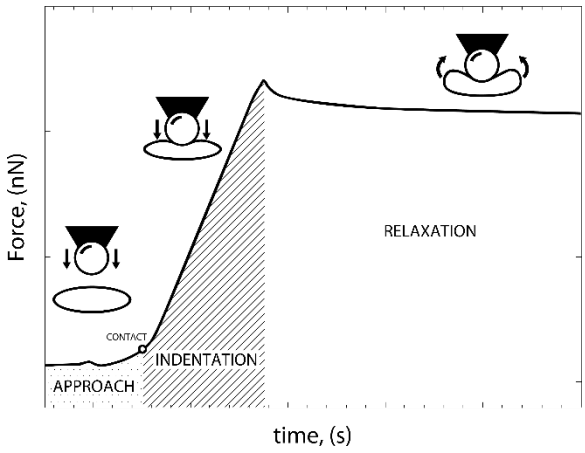


**Figure 4.2 The indentation-relaxation response of a cell can be divided into three regimes characterized by the relative movement of the indenter and sample.**

### 4.2.5 Fractional Zener (FZ) model

The FZ model operates on different physical principles than the SLS model. Shown in Figure 4.3, it replaces the damper with another more peculiar mechanical element known as the springpot. Its name, a portmanteau of "spring" and "dashpot," reflects its fuzzy character.

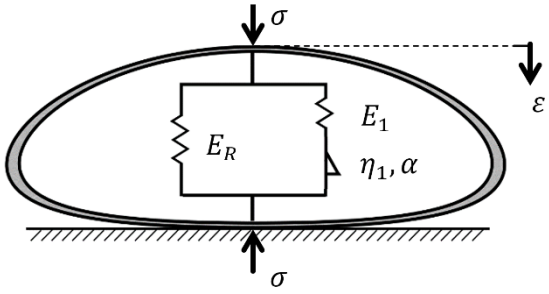


**Figure 4.3 The mechanical schematic of the FZ model is similar in structure to the SLS model but replaces the linear damper with a fractional element.**

Instead of depending on the zeroth or first derivative of strain, it depends on a derivative of fractional order such that:

$$\sigma(t) = \eta \frac{d^{\alpha}}{dt^{\alpha}}(\varepsilon) = \eta D^{\alpha}(\varepsilon) \tag{14}$$

where $\eta$ is a fractional viscous coefficient and $\alpha$ is the degree of the time derivative [28]. It is mathematically possible for $\alpha$ to be any number, complex, irrational, or otherwise; however, the utility of such constructions is debatable. Contrary to the case of integer-

order derivatives, it is often difficult to attribute a physical or geometric meaning to a non-integer-order time derivative. For a fractional $\alpha$ between zero and one, the springpot can be physically realized as a fractal arrangement of viscous branches whose pattern depends on the order of the derivative, such as the stacked sequence arrangement in Figure 4.4 [29]. Physically, this can serve as a representation of the interplay of a myriad of substructures connected by a complicated network of interfaces inside the sample.

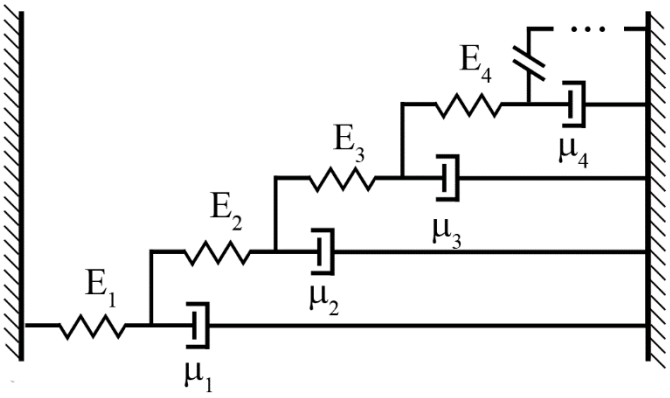


**Figure 4.4 For certain values of α, the fractional element may be visualized as an interconnected network (fractal) of mechanical elements that represent the complex contributions of substructures.**

The computation of these derivatives requires an extension to Cauchy's concept of repeated integration, but for this analysis, only an understanding of their transformative properties is necessary. For a more comprehensive take on the theory, the reader is directed to the work of Dalir *et al* [40]. For any function of time with zero initial conditions, the fractional derivative of the function may be expressed in the Laplace domain as:

$$L\left\{D^{\alpha} f(t)\right\} = s^{\alpha} F(s) \tag{15}$$

So, isolation of a transfer function is possible. The equation of motion with just one fractional branch may be written as

$$\left(\frac{1}{E_1}\right) D^{\alpha}\sigma(t) + \frac{1}{\eta}\sigma(t) = \left(1 + \frac{E_R}{E_1}\right) D^{\alpha}\varepsilon(t) + \frac{E_R}{\eta}\varepsilon(t) \tag{16}$$

The procedure illustrated in previous work [39] allows for the transformation of the Hertz model into the Laplace domain by replacing Young's modulus with $\frac{\bar{\sigma}}{\bar{\varepsilon}} = E(s)$:

$$\bar{F}(s) = \frac{4}{3}\frac{\sqrt{R\delta_0^3}}{(1-\nu)}\frac{E(s)}{s} \tag{17}$$

where $\delta_0$ is the maximum indentation resulting from the application of the contact force. So, this conclusion allows any relaxation model with an explicit transfer function between stress and strain to be combined with the Hertz indentation model. Substituting the resulting transfer function into Equation 4.10 and performing an inverse transformation produces an equation that includes a special function used almost exclusively in fractional calculus as a generalization of the exponential function:

$$\bar{F}(s) = \frac{4}{3}\frac{\sqrt{R\delta_0^3}}{(1-\nu)}\left[E_R + E_1\mathcal{E}_{\alpha,1}\left(-\frac{E_1}{\eta}t^{\alpha}\right)\right] \tag{18}$$

where $\varepsilon_{\alpha,1}$ is the Mittag-Leffler function defined as:

$$\mathcal{E}_{\alpha,1}(z) = \sum_{p=0}^{\infty}\frac{z^p}{\Gamma(\alpha p+1)} \tag{19}$$

where $\Gamma(.)$ is the Gamma function [41]. The Mittag-Leffler function does have a computational cost that depends on the truncation of the summation. For this analysis, the summation was allowed to continue until the difference between successive partial sums became on the order of $10^{-4}$. Again, the viscous and elastic coefficients may be combined into a characteristic relaxation time. Unlike the SLS model the process results in a power law relationship with the degree of derivative:

$$\tau = \left(\frac{\eta}{E_1}\right)^{1/\alpha} \tag{20}$$

A thorough discussion of this and the other parameters of the FZ model and their effects on the shape of the response is included in the Appendix.

### 4.2.6 Parameters of the Fractional Zener model

The application of a fractional model implies that the sample does not exhibit simple relaxation behavior, so any attempt to shoehorn the parameters of the model into the physical roles of the simple model's will fall short. Instead, a firm understanding of

how each fractional parameter affects the overall shape of a sample's response will provide an effective avenue for comparison between populations. The elastic parameters do roughly correspond to their linear counterparts. The relaxed modulus, $E_R$, represents the residual stress in the sample after relaxation has finished ($t \to \infty$). A change in the relaxed modulus does not correspond to a change in the shape of the response; although, the entire curve will shift proportionally in the direction of the change, illustrated in Figure 4.5.a. This behavior is identical to that exhibited by the SLS model.

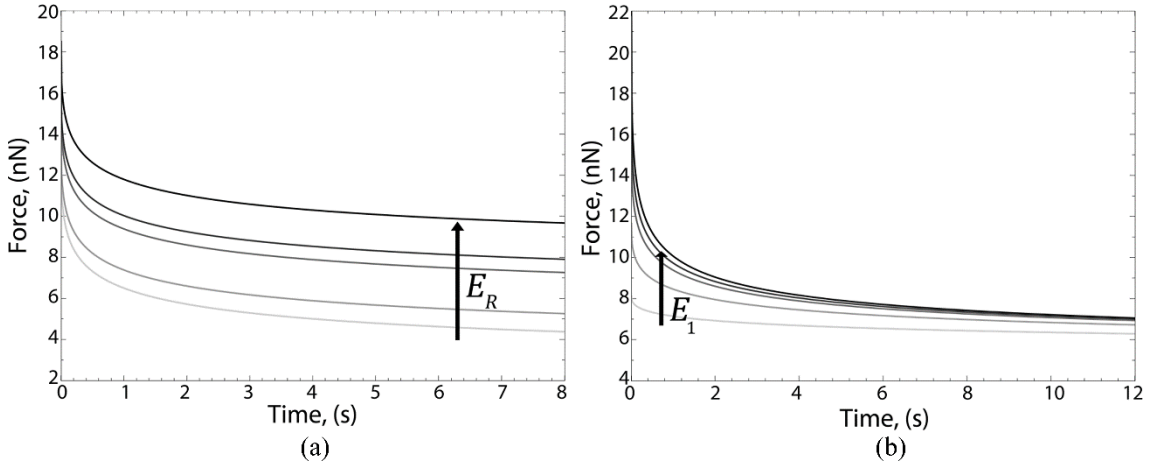


**Figure 4.5 The influence of the elastic parameters of the FZ model, (a) $E_R$ and (b) $E_1$, on the response shape is evident from the values of initial and residual force. The curves represent a change in the listed elastic parameter.**

The first elastic parameter in the FZ model, $E_1$, has a slightly more complicated influence than that of the SLS model. Biophysically, it may be interpreted as a measure of a sample's initial resistance to a load. Like the linear model, a change in $E_1$ will shift the initial force proportionally in the direction of the change, demonstrated in Figure 4.5.b. The effect of a change in $E_R$ or $E_1$ is quantified by the relationships:

$$\begin{aligned} F_0 &\propto E_R + E_1 \\ F_\infty &\propto E_R \end{aligned} \tag{4.14}$$

The degree of the arbitrary derivative is more abstract than the other parameters. It quantifies the complexity of the response. As $\alpha$ varies between zero and one, the character of the Mittag-Leffler function undergoes a transition between a power law to an exponential relationship [42], as in Figure 4.6. So, changes in $\alpha$ slide the response along this continuum from a constant, as in a fully elastic sample, to an exponential response, as

predicted by the SLS model. This is the intrinsic flexibility of the FZ model and the distinction between the spring-pot element and the dashpot.

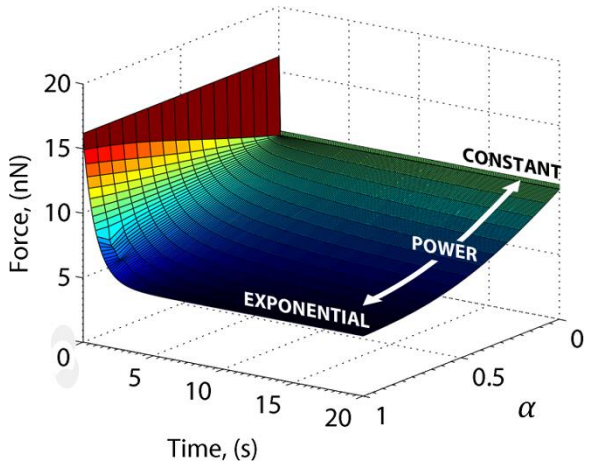


**Figure 4.6 Variations in the degree of derivative, a, incite a transition from power-law to simple exponential relaxation behavior.**

Individually, fractional viscosity, $\eta$, does not prove to be an effective tool for comparison. Noting that the argument of the Mittag-Leffler function must be non-dimensional, it can be shown that the units of $\eta$ depend on the degree of the derivative. Therefore, even within a population it is possible that each individual value for fractional viscosity can have a different unit. However, it may be rewritten as a characteristic relaxation time using a process similar to that used in the linear derivation. This allows for direct comparison of the viscosity of samples that do not have the same fractional-order time relationship. The relationship can be derived by resolving the units in the argument of the Mittag-Leffler function:

$$\tau = \left( \frac{\eta}{E_1} \right)^{1/\alpha} \tag{4.15}$$

According to (4.15), unlike the SLS model, the fractional elastic parameter does not have an inversely-proportional relationship to the characteristic relaxation time of the sample but instead a power-law dependence introduced by the inclusion of an arbitrary derivative. Figure 4.7 shows the effect of a change in relaxation time.

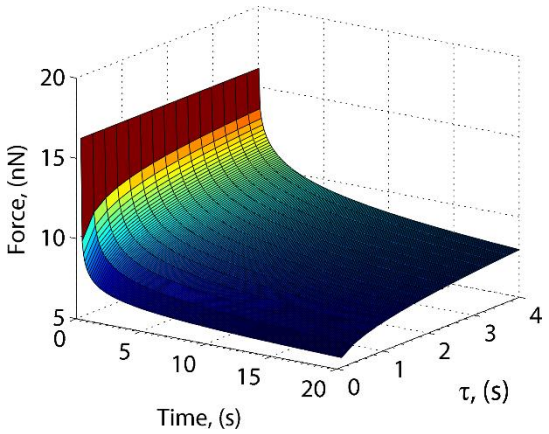


**Figure 4.7 Changes in fractional relaxation time are reflected in the magnitude and location of the drop-off in the initial force.**

In the SLS model, the relaxation time is much more accessible to an experimentalist using the initial, $F_0$, and ultimate, $F_\infty$, responses of the sample according to the relationship in (4.6). In the FZ model, the fractional relaxation time does not correspond to a fixed percentage of the response span for all samples; instead, the percentage is dependent on the degree of the arbitrary derivative:

$$F_\tau = F_\infty + \mathcal{E}_{\alpha,1}(-1)\cdot(F_0 - F_\infty) \tag{4.16}$$

### 4.2.7 Curve fitting and statistical analysis

The indentation and relaxation data were fit to their respective models using a nonlinear least-squares approach. For a good estimation of the contact point in the indentation region, each sample was fit iteratively until the difference in estimated contact points was below a very small threshold (~ 10 nm). The approximate point of contact was then used to calculate the maximum indentation depth for each sample, which is a factor in the relaxation models.

The curve-fitting procedure generates a set of values for each parameter that can provide statistical information about the cell population. Each parameter distribution was compared against its parallel in both models (FZ and SLS) for both sample populations (MDA-MB-231 and MCF10A). Paired sample t-tests were used to determine the statistical significance of the differences between the parameters of the two cell populations. The experimental factors do not allow for an assumption of normality in the distributions, so the statistics reflect changes in the median values of the parameters and do not omit outliers.

## 4.3 Results

A cursory visual assessment of the different model fits for any one cell is enough to see the drastic improvements in accuracy made by the implementation of the FZ model. From a qualitative standpoint, shown in Figure 4.8, it is evident that the FZ model effectively reproduced the fast relaxation characteristic of the sample populations with much higher accuracy than the SLS model. Figure 4.9.a and Figure 4.9.b show a comparison of the residuals from the nonlinear fitting procedure indicating a significant increase in fit quality even for those samples where the SLS model struggled.

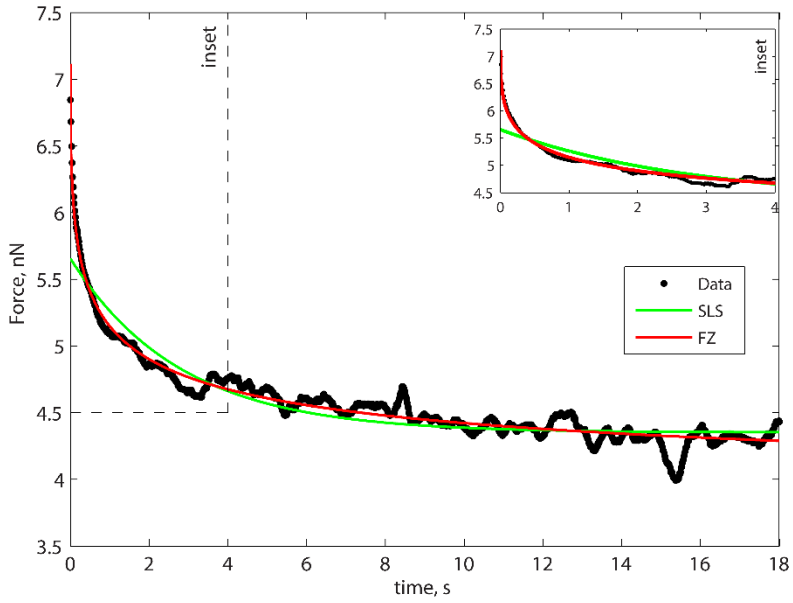


**Figure 4.8 The increase in fit accuracy is clearest at a small time scale where the FZ model captures the initial decline.**

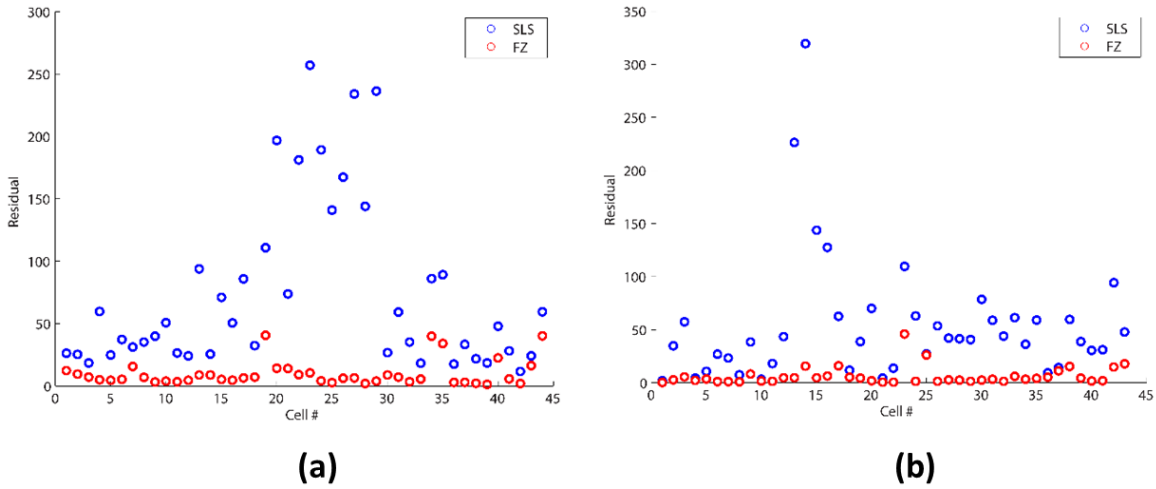


**Figure 4.9 Residuals of the nonlinear least-square process quantitatively show an increase in fit quality for the MCF10A (a) and MDA-MB-231 (b) populations.**

The parameter distributions extracted from the sample population are coherent and support the relevancy of both viscoelastic models. For each parameter, the distributions from both models for both cell populations are compared below. Note that the extended lines on each plot represent the reasonable span of each distribution, and outliers are marked with symbols. The position of the median line inside of the colored box is indicative of the skew in the distribution.

A comparison of the relaxed moduli generated by the linear model, $E_R$, conforms to the trends seen in previous comparative works, where the invasive line exhibits less capacity for residual stress. The MDA-MB-231 line shows a statistically significant ($p = 0.01$) 42% decrease in the median relaxed modulus relative to the MCF10A line in the SLS model. However, the distributions extracted by the FZ model do not exhibit a significant change in median value ($p = 0.09$). There is a notable rightward shift in the distributions with the lower quartile measurement much closer to zero than those of the linear model. Figure 4.10.a illustrates the distributions of the data generated by the FZ model and Figure 4.10.b shows the distribution from the SLS model.

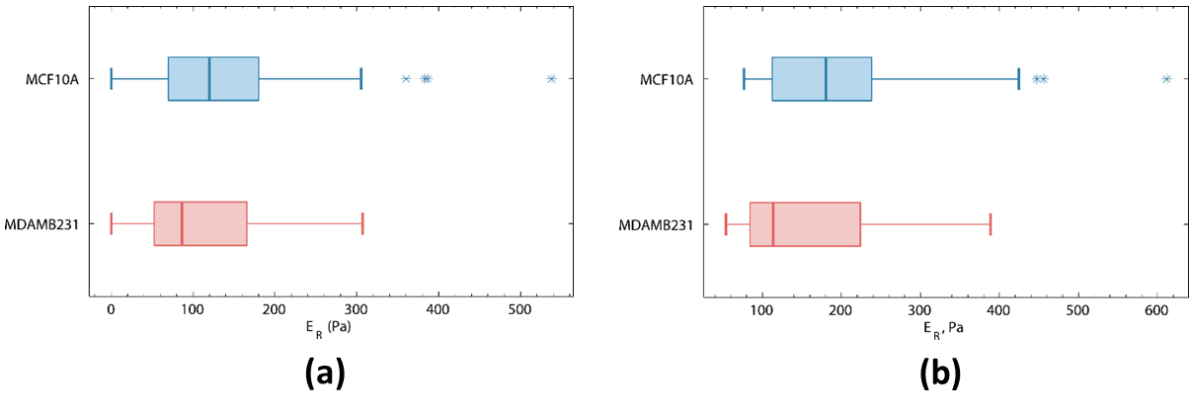


**Figure 4.10 The distributions of the relaxed modulus parameter are very similar for the FZ(a) model but significantly different for the SLS(b) model. The SLS model shows a decreasing trend in the median values from healthy to cancerous cells as in existing literature.**

A curious effect to the increase in overall fit quality is a significant increase in the first elastic parameter, $E_1$. Because the FZ model successfully captures relaxation at the fast time scale (within the first few seconds of the application of force), it correctly models the initial force between the tip and sample. Otherwise, the trend captured in the SLS model is paralleled in the results of the FZ model. The MDA-MB-231 population exhibits softer elastic qualities than the MCFCF10A by 54% ($P=1\times10^{-5}$) in the FZ model and 53% ($P=1\times10^{-5}$) in the SLS model, shown Figure 4.11.a and Figure 4.11.b.

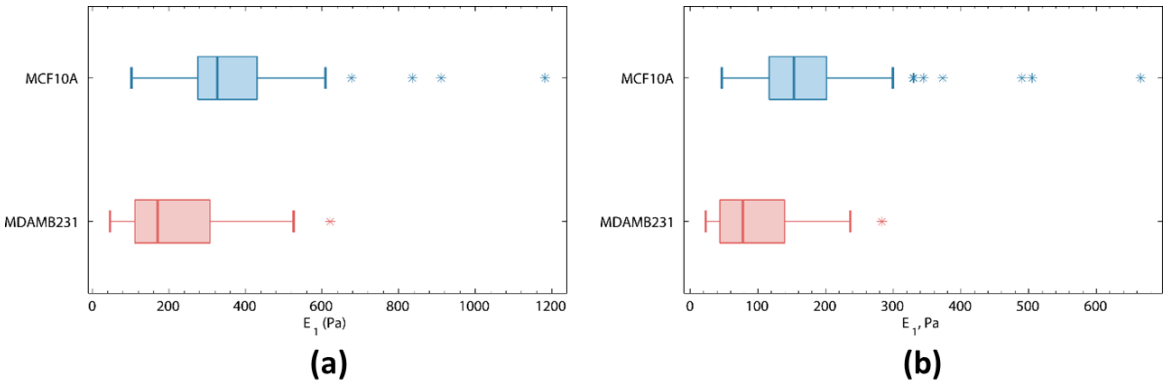


**Figure 4.11 The distributions of E1 for both the FZ (a) and SLS (b) models exhibit the same decreasing trend as seen in previously reported studies. The raw values for the FZ model are considerably higher due to the increase it fit quality.**

The comparable measure of viscosity between the two models is the characteristic relaxation times for both populations, which describes the shape of the response in conjunction with the degree of derivative. Like the first elastic modulus, the two model

produce very different raw values. Figure 4.12.a and 4.12.b show the disparity in the raw values of the time scales. For the MCF10A line, the median for the SLS model is 2.36 seconds while that of the FZ model is approximately half that value at 1.01 seconds. Recall that the relaxation time is a measure of the rate of initial decay of the response. So, the lower value from the FZ model reflects the contribution of the fast-relaxation behavior within the first few seconds of the trial. Across the populations, the median values do not change with any statistical significance for both the SLS ($p = 0.92$) and the FZ ($p = 0.31$) models. The dispersion of the distributions exhibits the same trend across populations for both models where the MDA-MB-231 line is considerably more heterogeneous; however, the distributions generated by the FZ model show considerably less dispersion overall.

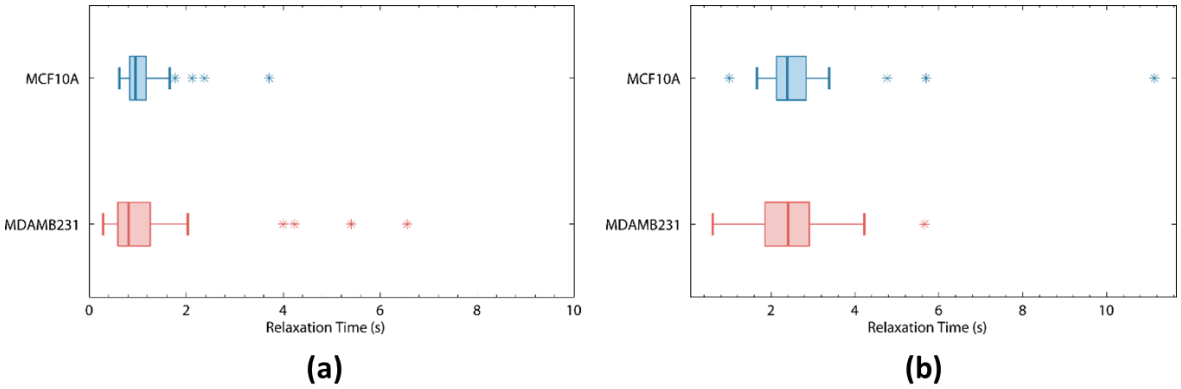


**Figure 4.12 The distributions of the characteristic relaxation times show an overall decrease in dispersion for the FZ model (a) as compared to the SLS model (b) but no statistically significant differences between median values across populations.**

The distributions of the degree of the derivative, $\alpha$, representing the mechanical complexity of the samples are show in Figure 4.13. The difference between the median values of both cells lines is statistically insignificant ($p = 0.45$). The shapes of the distributions are also extremely similar with the MCF10A line exhibiting a slight leftward skew.

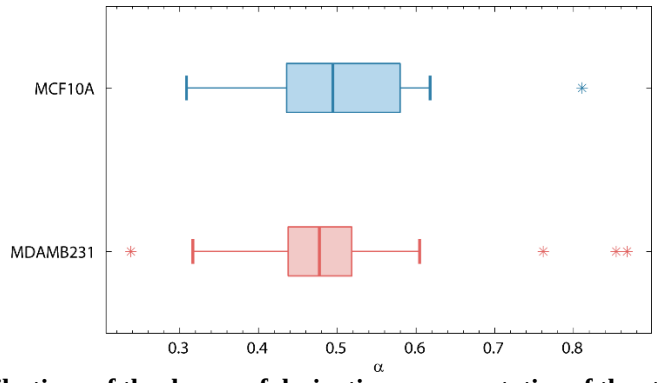


**Figure 4.13 The distributions of the degree of derivative, representative of the structural complexity of the sample, are nearly indistinguishable.**

The results are also reported in Table 4.1. Note that the reported values are the median and standard deviation of each distribution to ease in the comparison of non-normal data.

**Table 4-1 A numerical comparison of the distributions of parameters for both the FZ and SLS models for both the MCF10A and MDA-MB-231 populations. Note that all values are reported as median ± standard deviation to reasonably account for non-normality, and significant outliers (marked in previous figures with stars) were excluded.**

| | Parameter | | | |
|---|---|---|---|---|
| **FZ Model** | $E_R$ , (kPa) | $E_1$, (kPa) | $\tau$, (s) | $\alpha$ |
| MCF10A | 111.5 ± 63.75 | 316.6 ± 115.8 | 1.01 ± 0.05 | 0.51 ± 0.07 |
| MDA-MB-231 | 84.42 ± 56.81 | 143.4 ± 100.0 | 1.04 ± 0.11 | 0.48 ± 0.06 |
| **SLS Model** | | | | |
| MCF10A | 170.2 ± 67.15 | 149.1 ± 68.46 | 2.36 ± 0.45 | -- |
| MDA-MB-231 | 98.54 ± 63.63 | 69.12 ± 48.03 | 2.40 ± 0.84 | -- |

A set of experiments were conducted to image the cytoskeleton of the MCF10A and MDA-MB-231 cells. The cytoskeletal organization is a primary determinant of cell mechanical properties, and specifically the contribution of actin stress fibers has been found to be the most dominant factor. As shown in Figure 4.14, the confocal images illustrate a distinguishable difference in both the organization and concentration of the actin fibers between the two cell types. The MCF10A cell shows a denser and more organized F-actin fiber network compared to that of the MDA-MB-231 cell. This change in the actin cytoskeleton is associated with the decreasing trend in median values of the elastic parameters from the MCF10A line to the MDA-MB-231 line measured using both models.

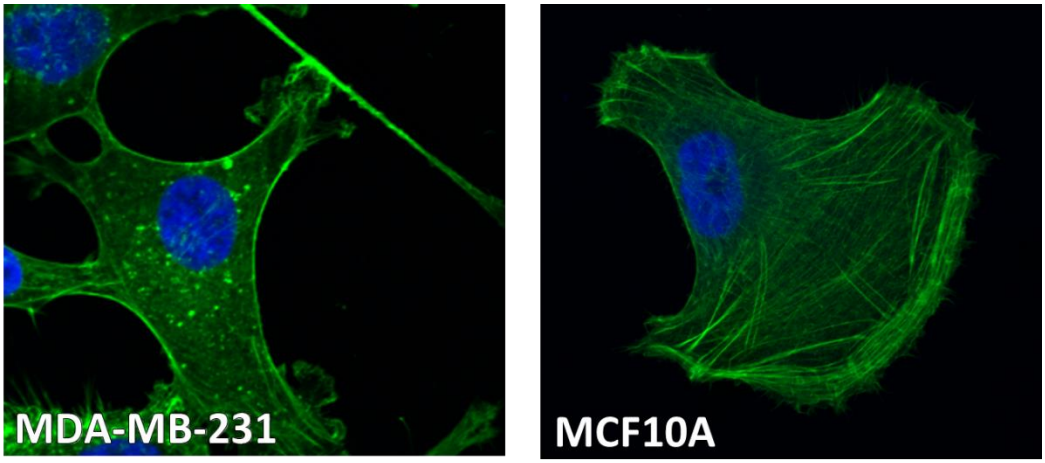


**Figure 4.14 Immunofluorescence images of the two cell lines illustrates that the MCF10A cell has a much denser concentration of actin stress fibers compared to the MDA-MB-231 cell.**

## 4.4 Discussion

The stress relaxation responses of a population of highly invasive MDA-MB-231 human breast cancer cells (n=43) and a population of MCF10A non-invasive human breast epithelial cells were fitted to two constitutive models of viscoelasticity: the Standard Linear Solid (SLS) model and the Fractional Zener (FZ) model. The former was used as a control in order to compare the fractional model to previous trend results. The heterogeneous and complex nature of the cell substructure introduces the possibility of a non-exponential relaxation function. The FZ model was tremendously successful in capturing the entirety of this response by including only one additional parameter, and the results corresponding to the fractional time derivative are noteworthy. While it is true that the introduction of additional parameters generally increases the quality of any fit, this study makes no ad hoc additions to the model. Instead, it grounds the model in physical principles that differ from the framework used in common practice. The fact that the median degree of derivative, a potential measure of the structural complexity of the sample and description of the shape of the response, does not significantly change between the non- and highly invasive cell populations solidifies the idea that the fractional behavior of the sample is a property of the cell type or geometry and is not susceptible to reduction as are the elastic properties of the cells.

The trends observed in the elastic parameters extracted with the SLS model are consistent with previous cell studies. The highly invasive line tends to be considerably

softer in both the relaxed and first elastic moduli [16, 43]. The FZ model preserves this trend in the first modulus; however, there was not a statistically distinct difference between the median values of the relaxed moduli. This is due to the FZ model's correct representation of the overall shape of the curve. The precise relationship between the elastic parameters and the shape of the response is discussed in the Appendix, but, in short, the FZ model fit more accurately captures the initial force on the sample; therefore, the first elastic parameter is more independent of the relaxed modulus. It may be concluded that the observed trends in the relaxed modulus may then be an artifact of the forced coupling of the elastic parameters that occurs in the SLS model fit. Instead, the actual softening occurs in the first elastic parameter. The physical mechanism of softening is illustrated by the immunofluorescence imaging of the two cell lines, where the MDA-MB-231 cell shows an actin fiber network that is much less dense and considerably less organized than the MCF10A cell.

The increased flexibility, and resulting fit quality, of the FZ model incorporates more of the sample's response into its measure of the characteristic relaxation time. As opposed to the SLS model, which cannot react to the fast-relaxation behavior seen in biological samples and therefore produces a time constant representative of the later part of the response, the relaxation time generated by the FZ model is a composite measure of the viscosity of the entire response. This is evident in the distribution of this parameter. This conclusion is hidden from the SLS analysis due to the lack of a similar effect later on in relaxation. A point of importance, this does *not* reflect an inadequacy of the linear model. Contrarily, the SLS model gives different insight on a cell's relaxation behavior which is still valuable and is relevant as an approximation of cell viscoelasticity. Instead, it further illustrates the necessity for the inclusion of early-time behavior in a differentiation study. A fit of a cell from the MDA-MB-231 line that is segmented at a point that separates the contribution of the early-time nonlinearities, as in Figure 4.15, indicates that the SLS model is an excellent representation of the dynamics of the cell on a longer time scale.

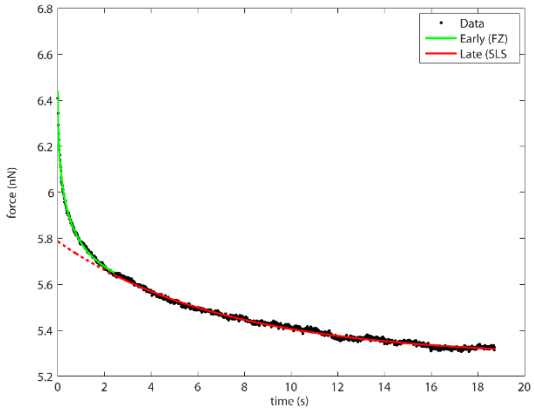


**Figure 4.15 The SLS model (red curve) captures the relaxation response of the cell on a long time scale. A segmented fit that removes the nonlinearities of the beginning of the response shows the relevance of the linear model in this time scale.**

The nonlinearities associated with the subcellular architecture are manifest in the green portion of the curve in Figure 4.15. This region is the cause of the severe difference between the composite relaxation time of the FZ model and the relaxation time of the SLS model. It is evident from the distributions that the long-term relaxation behavior is consistent with previous results.

These results have important implications for biomedical research hoping to use mechanical characteristics as markers for disease progression. Applying a linear model, such as the SLS model, may cloud the distributions of certain parameters due to its restrictive mathematical framework. This can be seen in the distributions of the relaxation times of the cell lines. Heterogeneity, manifest as dispersion in the parameter distributions, is an innate feature of biological populations. Previous literature has shown that the spread of elastic parameter distributions decreases with the onset of cancer. However, the relaxation times extracted by the FZ model are significantly more homogeneous for both lines; therefore, the fraction of the dispersion associated with an inaccurate reproduction of response shape is eliminated. The reduction of this modeling uncertainty while preserving certain distinctions shown in the linear model gives merit to the application of the FZ model for cell studies.

## *4.5 Conclusion*

This work provides a method to verify previous trends revealed by linear models between cell populations within a disease progression by imposing fractional mechanics

to better quantify the response of the samples. This clears the way for more extensive identification schemes for the broader classes of biological samples. The importance of mechanical characterization cannot be overemphasized. The number of studies linking changes in mechanical parameters to disease progression and other cell biomarkers continues to grow, and more credible parameter sets will sharpen the focus on more subtle changes in cell properties.

The results of this study corroborate the general trends seen in existing literature but suggest that the trends in specific elastic parameters may be an artifact of the residual error in fitting. Furthermore, the description of viscous properties given by the FZ model lacks the dispersion caused by modeling uncertainty present in the SLS model results while maintaining the heterogeneity inherent in the biological sample population.

## *References*


[1] B. Carmichael, H. Babahosseini, S. N. Mahmoodi, and M. Agah, "The fractional viscoelastic response of human breast tissue cells," *Phys. Biol.*, vol. 12, p. 046001, 2015.

[2] K. Ward, W. Li, and S. Zimmer, "Viscoelastic Properties of Transformed Cells: Role in Tumor Cell Progression and Metastasis Formation," *Biorheology*, vol. 28, pp. 301-313, 1991.

[3] M. Dao, C. T. Lim, and S. Suresh, "Mechanics of the Human Red Blood Cell Deformed by Optical Tweezers," *Journal of the Mechanics and physics of solids.*, vol. 51, pp. 2259-2280, 2003.

[4] J. Guck, S. Schinkinger, and B. Lincoln, "Optical Deformability as an Inherent Cell Marker for Testing Malignant Transformation and Metastatic Competence," *Biophysical Journal*, vol. 88, pp. 3689-3698, 2005.

[5] S. M. Mijailovich, M. Kojic, and M. Zivkovic, "A Finite Element Model of Cell Deformation during Magnetic Bead Twisting," *Journal of Applied Physiology (Bethesda, Md.: 1985)*, vol. 93, pp. 1429-1436, 2002.

[6] G. Binnig, C. F. Quate, and C. Gerber, "Atomic Force Microscope," *J Physical Letters*, vol. 56, pp. 930-3, 1986.

[7] M. Lekka, P. Laidler, and D. Gil, "Elasticity of Normal and Cancerous Human Bladder Cells Studied by Scanning Force Microscopy," *European Biophysics Journal*, vol. 28, pp. 312-316, 1999.

[8] E. C. Faria, N. Ma, and E. Gazi, "Measurement of Elastic Properties of Prostate Cancer Cells using AFM," *Analyst,* vol. 133, pp. 1498-1500, 2008.

[9] S. E. Cross, Y. Jin, and J. Rao, "Nanomechanical Analysis of Cells from Cancer Patients," *Nature Nanotechnology,* vol. 2, pp. 780-783, 2007.

[10] M. Nikkhah, J. S. Strobl, R. De Vita, and M. Agah, "The Cytoskeletal Organization of Breast Carcinoma and Fibroblast Cells Inside Three Dimensional (3-D) Isotropic Silicon Microstructures," *Biomaterials,* vol. 31, pp. 4552-4561, 2010.

[11] M. Nikkhah, J. S. Strobl, E. M. Schmelz, and M. Agah, "Evaluation of the Influence of Growth Medium Composition on Cell Elasticity," *Journal of Biomechanics,* vol. 44, pp. 762-766, 2011.

[12] S. E. Cross, Y. S. Jin, J. Tondre, R. Wong, J. Rao, and J. K. Gimzewski, "AFM-Based Analysis of Human Metastatic Cancer Cells," *Nanotechnology,* vol. 19, p. 384003, 2008.

[13] M. J. Rosenbluth, W. A. Lam, and D. A. Fletcher, "Force Microscopy of Nonadherent Cells: A Comparison of Leukemia Cell Deformability," *Biophysical Journal,* vol. 90, pp. 2994-3003, 2006.

[14] G. T. Charras and M. A. Horton, "Single Cell Mechanotransduction and its Modulation Analyzed by Atomic Force Microscope Indentation," *Biophysical Journal,* vol. 82, pp. 2970-2981, 2002.

[15] E. M. Darling, M. Topel, and S. Zauscher, "Viscoelastic Properties of Human Mesenchymally-Derived Stem Cells and Primary Osteoblasts, Chondrocytes, and Adipocytes," *Journal of Biomechanics,* vol. 41, pp. 454-464, 2008.

[16] H. Babahosseini, P. C. Roberts, E. M. Schmelz, and M. Agah, "Bioactive Sphingolipid Metabolites Modulate Ovarian Cancer Cell Structural Mechanics," *Integrative Biology,* vol. 5, pp. 1385-92, 2013.

[17] H. Babahosseini, A. N. Ketene, E. M. Schmelz, P. C. Roberts, and M. Agah, "Biomechanical Profile of Cancer Stem-Like/Tumor-Initiating Cells Derived from a Progressive Ovarian Cancer Model," *Nanomedicine: Nanotechnology, Biology and Medicine,* vol. 10, pp. 1013-9, 2014.

[18] A. N. Ketene, P. C. Roberts, A. A. Shea, E. M. Schmelz, and M. Agah, "Actin Filaments Play a Primary Role for Structural Integrity and Viscoelastic Response in Cells," *Integrative Biology,* vol. 4, pp. 540-549, 2012.

[19] S. Shim, M. G. Kim, K. Jo, Y. S. Kang, B. Lee, S. Yang, *et al.*, "Dynamic Characterization of Human Breast Cancer Cells using a Piezoresistive Microcantilever," *Journal of Biomechanical Engineering,* vol. 132, p. 104501, 2010.

[20] E. M. Darling, S. Zauscher, and F. Guilak, "Viscoelastic Properties of Zonal Atricular Chondrocytes Measured by Atomic Force Microscopy," *Osteoarthritis and Cartilage,* vol. 14, pp. 571-579, 2006.

[21] E. M. Darling, S. Zauscher, J. A. Block, and F. Guilak, "A Thin-Layer Model for Viscoelastic, Stress-Relaxation Testing of Cells using Atomic Force Microscopy: Do Cell Properties Reflect Metastatic Potential?," *Biophysical Journal,* vol. 92, pp. 1784-1791, 2007.

[22] E. Dimitriadis, F. Horkay, J. Maresca, B. Kachar, and R. S. Chadwick, "Determination of Elastic Moduli of Thin Layers of Soft Material using the Atomic Force Microscope," *Biophysical Journal,* vol. 82, pp. 2798-2810, 2002.

[23] R. Long, M. Hall, M. Wu, and C. Y. Hui, "Effects of Gel Thickness on Microscopic Indentation Measurements of Gel Modulus," *Biophysical Journal,* vol. 101, pp. 643-650, 2011.

[24] B. Wang, P. Lançon, C. Bienvenu, P. Vierling, C. Di Giorgio, and G. Bossis, "A General Approach for the Microrheology of Cancer Cells by Atomic Force Microscopy," *Micron,* vol. 44, pp. 287-297, 2013.

[25] D. Roylance. Engineering viscoelasticity [Online].

[26] R. L. Bagley and P. J. Torvik, "A Theoretical Basis for the Application of Fractional Calculus to Viscoelasticity," *Journal of Rheology,* vol. 27, pp. 201-210, 1983.

[27] R. L. Bagley and P. J. Torvik, "On the Fractional Calculus Model of Viscoelastic Behavior," *Journal of Rheology,* vol. 30, pp. 133-155, 1986.

[28] N. Heymans, "Dynamic Measurements in Long-Memory Materials: Fractional Calculus Evaluation of Approach to Steady State," *Journal of Vibration and Control,* vol. 14, pp. 1587-1596, 2008.

[29] H. Schiesel, R. Metzlert, A. Blument, and T. F. Nonnenmacher, "Generalized Viscoelastic Models: Their Fractional Equations with Solution," *Journal of Physics A: Mathematical and General,* vol. 28, pp. 6567-6584, 1995.

[30] M. Alcoutlabi and J. J. Martinez-Vega, "Application of Fractional Calculus to Viscoelastic Behaviour Modelling and to the Physical Ageing Phenomenon in Glassy Amorphous Polymers," *Polymer,* vol. 39, pp. 6269-6277, 1998.

[31] A. Hernandez-Jimenez, J. Hernandez-Santiago, A. Macias-Garcia, and J. Sanchez-Gonzaleza, "Relaxation Modulus in PMMA and PTFE Fitting by Fractional Maxwell Model," *Polymer Testing,* vol. 21, pp. 325-331, 2002.

[32] T. Pritz, "Five-Parameter Fractional Derivative Model for Polymeric Damping Materials," *Journal of Sound and Vibration,* vol. 265, pp. 935-952, 2003.

[33] T. K. Chang, Y. A. Rossikhin, M. V. Shitikova, and C. K. Chaoa, "Application of Fractional-Derivative Standard Linear Solid Model to Impact Response of Human Frontal Bone," *Theoretical and Applied Fracture Mechanics,* vol. 56, pp. 148-153, 2011.

[34] M. Kohandel, S. Sivaloganathan, G. Tenti, and K. Darvish, "Frequency Dependence of Complex Moduli of Brain Tissue using a Fractional Zener Model," *Physics in Medicine and Biology,* vol. 50, p. 2799, 2005.

[35] J. Shen, C. Li, H. Wu, and M. Kalantari, "Fractional Order Viscoelasticity in Characterization for Atrial Tissue," *Korea-Australia Rheology Journal,* vol. 25, pp. 87-93, 2013.

[36] B. Suki, A. L. Barabasi, and K. R. Lutchen, "Lung Tissue Viscoelasticity: A Mathematical Framework and its Molecular Basis," *Journal of Applied Physiology,* vol. 76, pp. 2749-2759, 1994.

[37] Y. Fung, *Biomechanics: Mechanical Properties of Living Tissues*. New York: Springer-Verlag, 1993.

[38] A. N. Ketene, P. C. Roberts, A. A. Shea, E. M. Schmelz, and M. Agah, "Actin filaments play a primary role for structural integrity and viscoelastic response in cells," *Integrative Biology,* vol. 4, pp. 540-549, 2012.

[39] E. M. Darling, S. Zauscher, and F. Guilak, "Viscoelastic properties of zonal articular chondrocytes measured by atomic force microscopy," *J Osteoarthritis and Cartilage,* vol. 14, pp. 571-579, 2006.

[40] D. M. and B. M., "Applications of Fractional Calculus," *Applied Mathematical Sciences,* vol. 4, pp. 1021-1032, 2010.

[41] C. Monje, Y. Chen, B. Vinagre, D. Xue, and V. Feliu-Batlle, *Fraction-Order Systems and Controls: Fundamentals and Applications*: Springer, 2010.

[42] M. Berberan-Santos, "Properties of the Mittag-Leffler Relaxation Function," *Journal of Mathematical Chemistry,* vol. 38, pp. 629-635, 2005.

[43] S. E. Cross, Y. Jin, J. Rao, and J. K. Gimzewski, "Nanomechanical analysis of cells from cancer patients," *Nature Nanotechnology,* vol. 2, pp. 780-783, 2007.

# 5 Sub-cellular force microscopy in single normal and cancer cells

This chapter is produced from [1] with permission from Elsevier.

*H. Babahosseini*, B. Carmichael*, J.S. Strobl, S.N. Mahmoodi, M. Agah (*Co-first authors), "Sub-cellular force microscopy in single normal and cancer cells," Biochemical and Biophysical Research Communications, vol. 463, no. 4, pp. 587–592, June 2015.*

## *5.1 Introduction*

Atomic force microscopy (AFM) is an established method for tissue-level and single-cell biomechanical characterization. Several studies have shown that transformed cells are generally softer and more deformable than their healthier counterparts which can facilitate their motility and metastasis [2]. Particularly for breast epithelial cells, AFM results have shown that the highly metastatic MDA-MB-231 cell line is significantly more deformable than the non-tumorigenic MCF10A cells [3, 4]. Experimentally, agents that increase cell stiffness decrease breast cancer invasiveness, providing evidence for a direct relationship between the metastatic potential of cancer cells and their mechanical properties [5]. Several articles have also revealed that time-dependent viscoelastic properties can also serve as indicators of cell disease [6]. The determination of viscoelastic properties has been done by implementing stress-relaxation test using different techniques, particularly AFM [6, 7]. Meanwhile, the network of cytoskeletal proteins and the nucleus have been found to play the most significant role in determining the biomechanical properties of cells [8].

To determine single cell representative biomechanical properties, the generated experimental data are typically analyzed through the Hertz model and its extension into the time domain, the Standard Linear Solid (SLS) model [9-11]. Different research groups have used this approach to introduce cell biomechanical properties as “label-free” biophysical markers to predict cancer risk, cancer progression from benign to aggressive stages, and treatment efficacy. Despite promising results, the current trend in single-cell force microscopy does not provide the most comprehensive and information-rich picture of cell biomechanics. The use of the SLS model for quantification of cell biomechanical properties assumes that the cell is an entirely homogenous material, ignores the cell’s

complex multi-layered architecture, and neglects the cell's nonlinear depth-dependent elastic and viscoelastic properties [12-14]. Moreover, the indentation depth for cell measurements is typically kept below 10% of a cell thickness to keep the validity of the assumptions and to avoid possible error introduced by deformation nonlinearity and substrate contributions [15]. However, there is growing evidence in the literature that this limitation is too conservative and contributions from the substrate are negligible up to 50% of the cell thickness [16, 17], overlooking detailed information about the cell mechanics in deeper layers of the cells [18].

The Generalized Maxwell (GM), a more advanced viscoelastic model has been successfully applied to relaxation measurements of biological samples [19-21]. This model incorporates the idea of multiple relaxation times, and therefore, it can provide insight about the transient response of sub-cellular structures to external mechanical stimuli by distributing the response across several time scales. Consequently, the model leads to more extensive parameter sets to characterize and analyze the biomechanical properties of cell components. There have been only a few studies based on the GM model for characterizing cell viscoelastic properties by AFM nano-indentation [22, 23], however the comparison of the biomechanical characterization of the sub-cellular structures among normal and cancerous cells has been left untouched.

This paper reports the biomechanical properties of sub-cellular structurs of breast carcinoma MDA-MB-231 and benign MCF10A cells. For this purpose, stress-relaxation AFM tests are conducted on single cells after applying a deep probe indentation (up to 50% of cell height), and the resulting experimental data are analyzed with the GM viscoelastic model.

## *5.2 Materials and methods*

### 5.2.1 Sample preparation

MCF10A and MDA-MB-231 breast cell lines representative of non-invasive and highly invasive breast cancer models, respectively, were purchased from the American Type Culture Collection (ATCC). The cells were maintained in plastic T-25 $cm^2$ culture flasks in standard cell culture medium presented in [3, 4]. For the AFM tests, the cells were harvested and then seeded at a density of $1\times10^5$ cells per 12 $mm^2$ glass coverslips coated

with 0.1 mg/mL collagen type IV (Sigma-Aldrich, St. Louis, MO) for 24-30 hours at 37ºC in humidified 7% CO2-93% air atmosphere prior to the AFM experiments to allow the cells to adhere. A buffered HEPES solution was then added to the coverslip samples (final concentration of 13.5 mM) to maintain a physiological pH of 7.2 during testing.

### 5.2.2 AFM experiment

The AFM experiments were performed with a Dimension Icon AFM with a closed loop controller (Bruker Corporation, Billerica, MA) integrated with an optical microscope. Olympus TR400PSA V-shaped SiNi cantilevers (Olympus, Tokyo, Japan) of ~200 μm length with approximate spring constant values of ~0.02 N/m were employed in all AFM experiments; exact spring constant values were measured via the thermal tuning method. The sharp probes were modified by attaching glass spheres (Duke Scientific, Waltham, MA) of ~10μm diameter onto the cantilever free end with two-part epoxy (Miller Stephenson, Sylmar CA), which helped reduce damage to the cells due to contact. The exact diameter of the glass sphere and its attachment location were identified using a HIROX KH-7700 3D Digital Video Microscope. The measurements were carried out on single cells in their respective culture medium at room temperature (24°C) using AFM contact mode. The indentations were done above each cell's nucleus under optical control. Stress-relaxation test corresponding to each cell response to a unit step displacement was implemented [11] to acquire stress-relaxation curves for a total period of 60 seconds at a 5 kHz sample rate and a constant high approach velocity of 5 μm/s to approximate a pure step displacement. A maximum force trigger of 30 nN was implemented for all curve acquisition, leading to a deep indentation of about 3 μm on the cells, which are sufficient to probe the membrane and the underlying cytoplasm and nucleus [24].

### 5.2.3 Confocal microscopy

Both MCF10A and MDA-MB-231 cell lines were grown on collagen-coated coverslips for 24-30 hours. The cells were washed in Hank's balanced salt solution (HBSS), then fixed with 3% paraformaldehyde (PF) in 250mM Tris, pH 7.2 for 10 minutes followed by 6% PF- 0.25% Triton X-100 in PBS for 10 minutes. The fixed cells were incubated with AlexaFluor488-phalloidin (Invitrogen, Carlsbad, CA) at room temperature (10U/ml in 140

mM NaCl-6% bovine serum albumin in 40 mM Tris, pH 7.2, Invitrogen) for staining actin structure. Then, the samples were rinsed three times in PBS and mounted on ProLong Gold antifade reagent with DAPI (Invitrogen, Carlsbad, CA) to stain the cell nuclei. The confocal imaging was performed on the samples at different depths of focus to construct Z-stack images using a confocal laser scanning microscope (LSM510, Zeiss, Thornwood, NY) equipped with DAPI and FITC filters.

### 5.2.4 Scanning Electron Microscopy (SEM)

SEM was performed to investigate morphology and the height for both cell lines on the surface. The cells were fixed in 3.7% formaldehyde in PBS for 10 minutes, 24-30 hours after plating on collagen-coated coverslips. The samples were critical-point-dried to eliminate changes in the cell morphology, sputter-coated with a thin layer of gold palladium, and mounted on a SEM sample holder using conductive tape prior to the SEM imaging. To approximate the cells height, the SEM images were acquired with 85° tilt of the sample stage to allow a side-view visualization. The images were obtained using a Leo ZEISS 1550 field-emission SEM instrument.

### 5.2.5 Generalized Maxwell (GM) viscoelastic model

One model that has been successfully applied to AFM stress-relaxation experiments on biological samples is the Generalized Maxwell (GM) model [19-21]. The GM model is similar in form to the Standard Linear Solid (SLS) model which was previously widely employed [9-11], but incorporates the concept of multiple relaxation times corresponding to a larger number of viscous elements. A helpful visualization is an arrangement of stacked viscous balls of increasing viscosity. As shown in Figure 5.1.A, an applied force would quickly deform the less viscous element, which would slowly relax. The more viscous elements, however, would quickly snap back to their initial shape due to the larger restoring force. The same is true for sub-structures of heterogeneous composition. A parallel representation of the elements effectively represents the same effect but distributes the response across the time domain. Figure 5.1.B shows the representative mechanical system of the GM model, where the subscript on the parameters denotes the branch in the parallel structure. The equations of motion for the system may be written compactly:

$$\sigma = \left(E_R + \frac{E_1\mu_1\mathcal{D}}{E_1 + \mu_1\mathcal{D}} + \cdots + \frac{E_n\mu_n\mathcal{D}}{E_n + \mu_n\mathcal{D}}\right)\varepsilon\,, \tag{5.1}$$

where $E_R$ is the relaxed modulus, $E_n$ is the *n*-th elastic coefficient, $\mu_n$ is the *n*-th viscous coefficient, and $\mathcal{D}$ is the differential operator such that $\mathcal{D}^n(\,\cdot\,) = d^n/dt^n(\,\cdot\,)$. A transformation into the Laplace domain results in the ratio of stress to strain equation:

$$\frac{\bar{\sigma}}{\bar{\varepsilon}} = K(s) = \left(E_R + \frac{E_1\mu_1 s}{E_1 + \mu_1 s} + \cdots + \frac{E_n\mu_n s}{E_n + \mu_n s}\right). \tag{5.2}$$

Through the analogous modulus of rigidity, a time-dependent elastic modulus may be expressed in the Laplace domain as:

$$\bar{E}(s) = (1 + \nu)\,K(s). \tag{5.3}$$

The relation between an applied normal force, F, by a spherical body with radius, R, and a sample deformation, δ, with Poisson's ratio, ν and elastic modulus, E, can be expressed by the Hertz model [25] as follows:

$$F = \frac{4E\sqrt{R}}{3(1-\nu^2)}\delta^{\frac{3}{2}} \tag{5.4}$$

Assuming that the initial contact force is applied constantly throughout the relaxation, it may be modeled as a Heaviside function. Equation 5.4 may then be extended into the Laplace domain by replacing elastic modulus with the result of Equation 5.3:

$$\bar{F}(s) = \frac{4}{3}\frac{\sqrt{R\delta_0^3}}{(1-\nu)}\frac{K(s)}{s}, \tag{5.5}$$

where $\delta_0$ is the maximum indentation resulting from the application of the contact force. Substitution of Equation 5.2 into Equation 5.5 and transformation back into the time domain show the contribution of the multiple branches:

$$F(t) = \frac{4}{3}\frac{\sqrt{R\delta_0^3}}{(1-\nu)}\left[E_R + E_1 e^{-\frac{E_1}{\mu_1}t} + \cdots + E_n e^{-\frac{E_n}{\mu_n}t}\right]. \tag{5.6}$$

$E_n$ and $\mu_n$, associated with the elastic modulus and apparent viscosity of the *n*th layer can be extracted in Equation 5.6. The fitted parameters may also be recast into a set of relaxation times as:

$$\tau_n = \frac{\mu_n}{E_n}, \tag{5.7}$$

where $\tau_n$ is the *n*th relaxation time associated with the response. For this paper, only three viscous branches were required to effectively model the cell body as a triple-layered structure. The SLS model is a particular case of the GM model with only one viscous branch and, thus, only one exponential term such that:

$$F(t) = \frac{4}{3}\frac{\sqrt{R\delta_0^3}}{(1-\nu)}\left[E_R + E_1 e^{-\frac{E_1}{\mu_1}t}\right]. \tag{5.8}$$

As shown in Figure 5.1.C, the improvements in the GM model over the SLS model to provide a better fit for stress-relaxation curve are considerable, particularly the conformance to the early-time fast relaxation behavior demonstrated by the cells in their initial responses.

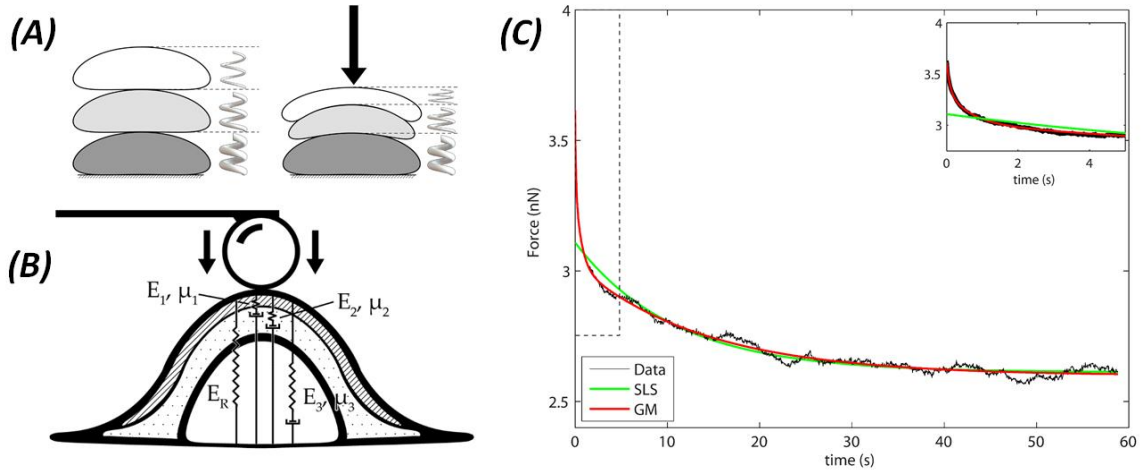


**Figure 5.1 (A) An illustration of a triple-layered structure before and after load application. The higher restoring force of the more viscous element would quickly correct the deflection, while the less viscous element would require much more time. (B) Mechanical Schematic of the Generalized Maxwell model of a cell. (C) Comparison of experimental data and the SLS and the GM fits with a highlighted difference in the initial cell response fitting.**

### 5.2.6 Statistical analysis and curve fitting procedure

Data analysis including the GM model fitting to the experimental data and calculation of elastic modulus, apparent viscosity, and relaxation time of the sub-domains was performed with MATLAB software. The fittings were performed using a nonlinear

least squares method to minimize the squared residual error of each fit. The GM model was given initial conditions that promoted the effective selection of consecutive relaxation times to ensure that higher modes were not considered. Shapiro-Wilks tests were conducted to analyze the data for normality. Two sample-independent t-tests with a 95% confidence interval ($P < 0.05$) were used to assess the degree of statistical difference between the two sets of results.

## 5.3 Results

For both the MCF10A and MDA-MB-231 cell types, AFM tests were performed on a set of about 30 single cells for acquiring stress-relaxation curves. Care was taken with the large indentation depth to avoid puncturing or damaging the cell membrane. If puncturing occurs, the curve exhibits local saw tooth behavior. No such behavior was observed in the data. The profiles of the distribution of the elastic moduli, the apparent viscosities, and the relaxation times among the two cell types calculated for the whole cell and each of the three sub-domains are compared using a series of histograms in Figure 5.2 and the mean (± SD) values are also summarized in Table 5.1.

The biomechanical properties corresponding to the whole cell body are approximated for both cell types by fitting the SLS model. The results in Table 1 show that the average elastic modulus and apparent viscosity values of MCF10A cells are 33% ($p<0.001$) and 61% ($p<0.0001$) larger than those of MDA-MB-231 cells, respectively, indicating that MCF10A cells are stiffer and more viscous than MDA-MB-231 cells. The histograms of measured elastic modulus and apparent viscosity compared between two cell types (Figure 5.2.A and 5.2.B) reveal that MDA-MB-231 cells are mechanically more homogeneous with a more concentrated distribution in comparison to MCF10A cells with a broad distribution. These results are in agreement with previously reported measurements on the elasticity [3, 4] and viscosity [26] of the malignant cell lines at a shallow indentation. However, here, an upward shift toward larger $E_{elastic}$ and $\mu_{viscoelastic}$ values are observed for both cell types which is because of the application of a deep indentation in the measurements [16].

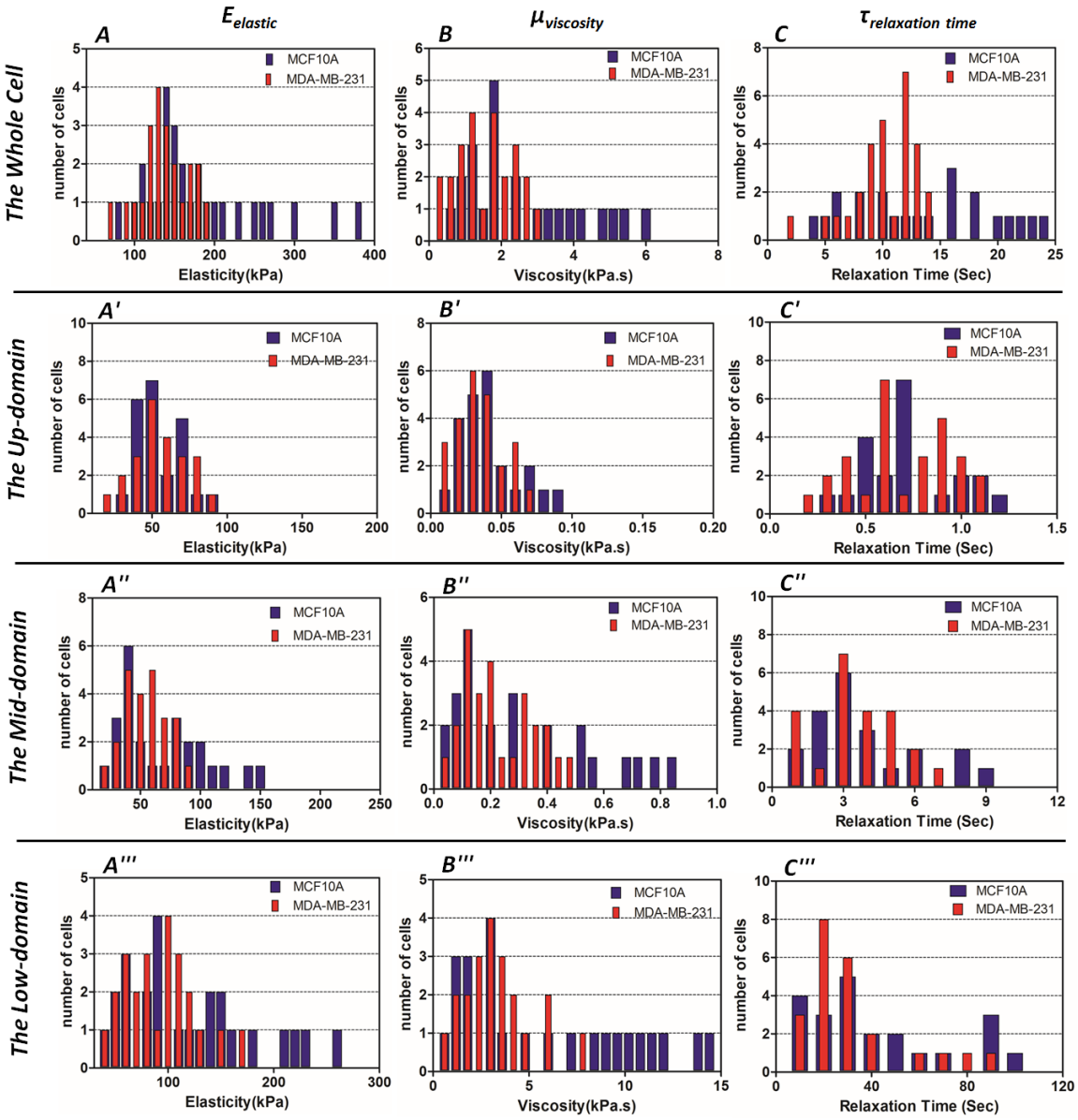


**Figure 5.2 Histograms of MCF10A and MDA-MB-231 cells depict the changes in distribution of measured elastic modulus (A, A', A'', A'''), apparent viscosity (B, B', B'', B'''), and relaxation time (C, C', C'', C''') for the whole cells and three sub-domains of the cells.**

The biomechanical properties of the sub-cellular domains i.e. elastic moduli, apparent viscosities, and relaxation times are estimated using the GM models which significantly improved the fitting quality to the experimental data compared to the SLS models as shown in Figure 5.1.C. The data in Table 5.1 show there is a statistically significant ($p<0.0001$) decreases in these values from up to low sub-domains, regardless of

cell type. The up sub-domain corresponding to the cell membrane/cortex, is softer and extremely less viscous relative to the mid and low sub-domains.

Table 1 also shows how the biomechanical properties of sub-domains compare between normal and cancerous breast cells. In the up sub-domain, the biomechanical properties are fairly similar in the normal MCF10A and malignant MDA-MB-231 cells. Here, the average values of the elastic modulus and the apparent viscosity were only slightly 10% ($p \approx 0.8$) and 12% ($p \approx 0.2$) less in the cancer cells, respectively, and this differences are statistically insignificant. In contrast, for the mid and low sub-domains corresponding to the cell cytoskeleton/nucleus and nuclear/integrin sub-domains, respectively, the difference in the biomechanical properties is more significant between the normal and cancer cells. For the mid and low sub-domains, the average elastic moduli of the cancer cells are, respectively, 15% ($p<0.1$) and 41% ($p<0.01$) less than that of normal cells. Similarly, the average apparent viscosities of the mid and low sub-domains are 25% ($p<0.01$) and 80% ($p<0.001$) less in the cancer cells compared to the normal cells, respectively. Conclusively, the deeper indentation which probes the internal structural sub-domains is more sensitive to mechanically differentiating normal and cancer cells than a typical shallow indentation.

We also analyzed the relaxation times which is a measure of stress-relief under a constant deformation. The average relaxation time measurements for the whole cell and the three sub-domains in Table 1, show an overall decrease in this parameter from the normal to the cancer cells, which, however, are statistically insignificant ($p<1$).

The distributions of the elastic moduli (Figure 5.2.A') and the apparent viscosities (Figure 5.2.B') calculated for the up sub-domain reveal they are similar for the normal and cancer cells consistent with population data summarized in Table 1. However, for the mid and low sub-domains, the distributions of the two cell types are distinct for $E_{elastic}$ (Figure 5.2.A" and 5.2.A'") and $\mu_{viscoelastic}$ (Figure 5.2.B" and 5.2.B'"). The normal MCF10A cells exhibited a broader distribution through the larger $E_{elastic}$ and $\mu_{viscoelastic}$ values, than that of the cancerous MDA-MB-231. The histograms of the relaxation time shown in Figure 5.2.C, 5.2.C', 5.2.C", and 5.2.C'" also showed a slight shift toward larger time for normal cells compared to cancer cells.

**Table 5-1 Summary of elastic modulus, apparent viscosity, and relaxation time responses for the whole and three sub-domains of normal and cancerous cells.**

| *Mean ± SD* | Cell Type | Whole cell | Up-domain of cell | Mid-domain of cell | Low-domain of cell |
|---|---|---|---|---|---|
| $E_{elastic}$ (kPa) | ***MCF10A*** | 181.7 ± 73.4 | 58.97 ± 16.57 | 71.2 ± 39.74 | 127.8 ± 69.6 |
| | ***MDA-231*** | 136.4 ± 31.8 | 53.74 ± 18.04 | 61.9 ± 20.44 | 90.4 ± 36.8 |
| $\mu_{viscoelastic}$ (kPa.s) | ***MCF10A*** | 2.57 ± 1.52 | 0.046 ± 0.015 | 0.309 ± 0.255 | 5.85 ± 4.54 |
| | ***MDA-231*** | 1.59 ± 0.72 | 0.041 ± 0.015 | 0.247 ± 0.137 | 3.25 ± 1.86 |
| $T_{relaxation\ time}$ (Sec.) | ***MCF10A*** | 14.14 ± 6.12 | 0.78 ± 0.26 | 4.34 ± 2.51 | 45.78 ± 31.48 |
| | ***MDA-231*** | 11.65 ± 2.43 | 0.76 ± 0.24 | 3.98 ± 1.89 | 35.90 ± 22.37 |

Morphological analyses were performed to confirm the dimensions of the cells used in the calculations. Scanning electron microscopy (SEM) images were used to directly measure the height of the cells, (Figure 5.3.A, MDA-MB-231; Figure 5.3.B, MCF10A). The average values taken from 12 samples measurements in each cell type indicate that the MDA-MB-231 cells have a thickness of about 5.71 μm while MCF10A cells are about 6.66 μm thick.

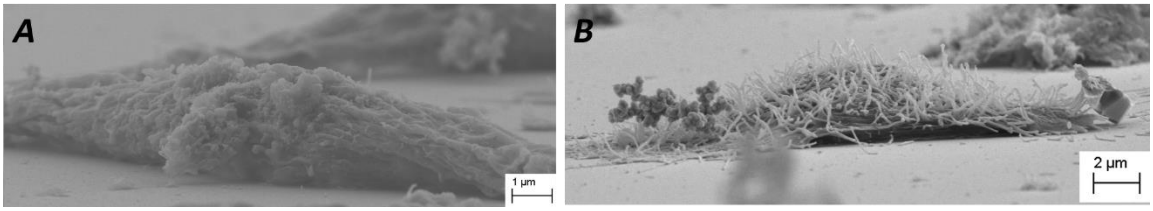


**Figure 5.3 SEM side-view image of (A) MDA-MB-231 cell and (B) MCF10A cell.**

## *5.4 Discussion*

The simple models that assume the cell body as a homogeneous solid can be extended to a multi-layered model for biomechanical characterization of the cells. The multi-modal response of both MCF10A and MDA-MB-231 cells and the biomechanical parameters reflect the cell heterogeneity across the body. By recognizing that living cells behave mechanically as a multi-layered structure, the presented force microscopy analysis provides valuable information about the biomechanics of the different sub-cellular structures that are located in different depths.

As the AFM tip indents deeper into the cell, it perturbs various cellular structures that respond differently to a mechanical stimulus. Our results show, for a deep indentation, the elastic modulus and the apparent viscosity are higher when compared to a shallow

indentation scenario, and this can possibly be attributed to the effects of a stiff and viscous inner cytoplasmic layer and nucleus [16]. However, when using models that assume a homogeneous cell body, the mechanical changes occurring at different depths of the cell are averaged. An important finding in our work is that a shallow indentation that exerted biomechanical actions in the cell relatively localized to the up sub-domain revealed relatively modest differences between the normal and malignant cells. However, the responses of normal and malignant cells differed quite significantly when a deep indentation was applied. As a note, using a modified AFM needle penetration technique, it was demonstrated in another recent study that nuclei and also membrane/cytoplasm of the highly metastatic bladder cancer cell line have significantly lower Young's moduli when compared to its less metastatic counterpart [27]. This result is in agreement with known oncogenic events that exert pleiotropic alterations in cytoskeleton and nuclear components, and the implication of this result is that use of deep, rather than shallow indentation might provide a more robust probe of the progression of normal cells to malignancy.

The assignment of the three sub-domains to an outer membrane/cortex, a central cytoplasm/nucleus, and an inner nuclear/integrin can be verified by correlating the corresponding measurements to the literature values. The results of previous studies show there is a continuum of biological elements which establish a mechano-transduction cascade linking membrane displacements to cytoskeletal filaments, the nucleus and sub-nuclear structures, and cell integrin-substrate forces [28, 29]. Thus, the biomechanical measurements cannot be assigned to a particular sub-structure, but dominated by the response of a sub-cellular structural domain. The term ‘cortex’ refers to a cortical actin layer, located right underneath the membrane [30, 31]. The term ‘cytoplasm’ is attributed to the intracellular cytoskeletal proteins composed mainly of actin filaments, intermediate filaments, and microtubules. Importantly, the previously reported time constants for the cell membrane/cortex (milli-second), the cell cytoskeleton (second), and the cell nucleus (ten-seconds) [30, 32] in the literature are of the same order as the relaxation times extracted by the GM model measurements in Table 1 for the three sub-domains. Notably, a recent AFM-based work has measured the viscosity of the membrane/cortex (0.081 ± 0.018 kPa.s) and cytoplasm (0.720 ± 0.161 kPa.s) for breast MCF-7 cells using the GM model [23]. The viscosity measurement of the chondrocyte cell nucleus (~4-5 kPa.s) was

also measured by applying the GM model to the micropipette aspiration data [32]. The results presented in Table 1 for three different sub-cellular domains are in good agreement with the previously reported data.

Together, the approach outlined here can be used as a powerful tool to investigate the biomechanical properties of sub-cellular structures as biomechanical signature of malignancy, metastatic potential, and anti-cancer drug sensitivity and drug resistance.

## 5.5 Conclusion

In this work, a proposed AFM-based experimental framework allows for the investigation of the biomechanical properties of sub-cellular structural domains. For this purpose, the AFM is used for stress-relaxation measurements on living cells. The collected data have been analyzed by applying a viscoelastic Generalized Maxwell model to extract the biomechanical properties of structures lying underneath the cell surface. According to the results, there are significant increases in the elasticity and viscosity magnitudes from the up to the low sub-domains, indicating depth-dependent elastic and viscoelastic properties of a cell. Moreover, we showed that compared with normal MCF10A cells, malignant breast MDA-MB-231 cells exhibited decreases in both elasticity and viscosity corresponding to the up, mid, and low sub-domains which are most remarkable when measured in the deeper cellular sub-domains. Comparing the biomechanical responses of normal and cancer cells with the literature permitted the assignment of the three sub-domains to the plasma membrane/actin cortex interface, the cytoplasm/nucleus interface, and the nuclear/integrin interface. The approach outlined here can be used as a powerful tool to investigate the biomechanical properties of sub-cellular domains as biomechanical signature of malignancy, metastatic potential, and anti-cancer drug sensitivity and drug resistance.

## References


[1] H. Babahosseini, B. Carmichael, J. S. Strobl, S. N. Mahmoodi, and M. Agah, "Sub-cellular force microscopy in single normal and cancer cells," *Biochem. Biophys. Res. Commun.*, vol. 463, pp. 587–592, 2015.

[2] S. Suresh, "Biomechanics and biophysics of cancer cells," *Acta Biomaterialia,* vol. 3, pp. 413-438, 2007.

[3] M. Nikkhah, J. S. Strobel, R. De Vita, and M. Agah, "The cytoskeletal organization of breast carcinoma and fibroblast cells inside three dimensional isotropic silicon microstructures," *Biomaterials,* vol. 31, pp. 4552-61, 2010.

[4] M. Nikkhah, J. S. Strobl, E. M. Schmelz, and M. Agah, "Evaluation of the influence of growth medium composition on cell elasticity," *Journal of Biomechanics,* vol. 44, pp. 762-766, 2011.

[5] B. Lincoln, H. M. Erickson, S. Schinkinger, F. Wottawah, D. Mitchell, S. Ulvick, *et al.*, "Deformability-based flow cytometry," *Cytometry Part A,* vol. 59, pp. 203-209, 2004.

[6] R. Zhao, K. Wyss, and C. Simmons, "Comparison of Analytical and Inverse Finite Element Approaches to Estimate Cell Viscoelastic Properties by Micropipette Aspiration," *Journal of Biomechanics,* vol. 42, pp. 2768-2773, 2009.

[7] M. Sato, D. P. Theret, and L. T. Wheeler, "Application of the Micropipette Technique to the Measurement of Cultured Porcine Aortic Endothelial Cell Viscoelastic Properties," *Journal of Biomechanical Engineering,* vol. 112, pp. 263-268, 1990.

[8] E. L. Elson, "Cellular mechanics as an indicator of cytoskeletal structure and function," *Annual Review of Biophysics and Biophysical Chemistry,* vol. 17, pp. 397-430, 1988.

[9] E. M. Darling, S. Zauscher, and F. Guilak, "Viscoelastic Properties of Zonal Atricular Chondrocytes Measured by Atomic Force Microscopy," *Osteoarthritis and Cartilage,* vol. 14, pp. 571-579, 2006.

[10] E. M. Darling, S. Zauscher, J. A. Block, and F. Guilak, "A Thin-Layer Model for Viscoelastic, Stress-Relaxation Testing of Cells Using Atomic Force Microscopy: Do Cell Properties Reflect Metastatic Potential?," *Biophysical Journal,* vol. 92, pp. 1784-91, 2007.

[11] E. M. Darling, M. Topel, S. Zauscher, T. P. Vail, and F. Guilak, "Viscoelastic properties of human mesenchymally-derived stem cells and primary osteoblasts, chondrocytes, and adipocytes," *Journal of Biomechanics,* vol. 41, pp. 454-464, 2008.

[12] Q. S. Li, G. Y. H. Lee, C. N. Ong, and C. T. Lim, "AFM indentation study of breast cancer cells," *J Biochemical and Biophysical research communications,* vol. 374, pp. 609-613, 2008.

[13] G. McPhee, M. J. Dalby, M. Riehle, and H. Yin, "Can common adhesion molecules and microtopography affect cellular elasticity? A combined atomic force microscopy and optical study," *Medical & Biological Engineering & Computing,* vol. 48, pp. 1043-1053, 2010.

[14] I. D. Medalsy and D. J. Muller, "Nanomechanical Properties of Proteins and Membranes Depend on Loading Rate and Electrostatic Interactions," *ACS Nano,* vol. 7, pp. 2642-2650, 2013.

[15] T. Tsui and G. Pharr, "Substrate effects on nanoindentation mechanical property measurement of soft films on hard substrate," *Journal of Materials Research,* vol. 14, pp. 292-301, 1999.

[16] M. Zhao, C. Srinivasan, D. J. Burgess, and B. D. Huey, "Rate- and depth-dependent nanomechanical behavior of individual living Chinese hamster ovary cells probed by atomic force microscopy," *Journal of Materials Research,* vol. 21, pp. 1906-1912, 2006.

[17] A. B. Mathur, A. M. Collinsworth, W. M. Reichert, W. E. Kraus, and G. A. Truskey, "Endothelial, cardiac muscle and skeletal muscle exhibit different viscous and elastic properties as determined by atomic force microscopy," *Journal of Biomechanics*, vol. 34, pp. 1545-1553, 2001.

[18] S. Kasas, X. Wang, H. Hirling, R. Marsault, B. Huni, A. Yersin, *et al.*, "Superficial and deep changes of cellular mechanical properties following cytoskeleton disassembly," *Cell Motility and the Cytoskeleton,* vol. 62, pp. 124-132, 2005.

[19] T. K. Chang, Y. A. Rossikhin, and M. V. Shitikova, "Application of Fractional-Derivative Standard Linear Solid Model to Impact Response of Human Frontal Bone," *Theoretical and Applied Fracture Mechanics,* vol. 56, pp. 148-153, 2011.

[20] H. Liu, D. P. Noonan, and Y. H. Zweiri, "The development of nonlinear viscoelastic model for the application of soft tissue identification," presented at the IEEE/RSJ International Conference on Intelligent Robots and Systems, 2007.

[21] J. Shen, C. Li, and H. Wu, "Fractional Order Viscoelasticity in Characterization for Atrial Tissue," *Korea-Australia Rheology Journal,* vol. 25, pp. 87-93, 2013.

[22] B. Wang, P. Lançon, and C. Bienvenu, "A General Approach for the Microrheology of Cancer Cells by Atomic Force Microscopy," *Micron,* vol. 44, pp. 287-297, 2013.

[23] S. Moreno-Flores, R. Benitez, M. dM Vivanco, and J. L. Toca-Herrera, "Stress relaxation and creep on living cells with the atomic force microscope: a means to calculate elastic moduli and viscosities of cell components," *Nanotechnology,* vol. 21, p. 445101, 2010.

[24] M. O. Krisenko, A. Cartagena, A. Raman, and R. L. Geahlen, "Nanomechanical Property Maps of Breast Cancer Cells As Determined by Multiharmonic Atomic Force Microscopy Reveal Syk- Dependent Changes in Microtubule Stability Mediated by MAP1B," *Biochemistry,* 2014.

[25] H. Hertz, "On the contact of elastic solids," *Journal of Reine Angew Math,* vol. 92, pp. 156-171, 1881.

[26] A. N. Ketene, E. M. Schmelz, P. C. Roberts, and M. Agah, "The effects of cancer progression on the viscoelasticity of ovarian cell cytoskeleton structures," *Nanomedicine : nanotechnology, biology, and medicine,* vol. 8, pp. 93-102, 2011.

[27] H. Liu, J. Wen, Y. Xiao, J. Liu, S. Hopyan, M. Radisic, *et al.*, "In Situ Mechanical Characterization of the Cell Nucleus by Atomic Force Microscopy," *ACS NANO,* vol. 8, pp. 3821-3828, 2014.

[28] N. Wang, J. D. Tytell, and D. E. Ingber, "Mechanotransduction at a distance: mechanically coupling the extracellular matrix with the nucleus," *Nature Reviews Molecular Cell Biology,* vol. 10, pp. 75-82, 2009.

[29] K. M. Imbalzano, N. Cohet, Q. Wu, Underwood, J. M. A. N. Imbalzano, and J. A. Nickerson, "Nuclear shape changes are induced by knockdown of the SWI/SNF ATPase BRG1 and are independent of cytoskeletal connections," *PLoS One,* vol. 8, p. e55628, 2013.

[30] H. Karcher, J. Lammerding, H. Huang, R. T. Lee, R. D. Kamm, and M. R. Kaazempur-Mofrad, "A three-dimensional viscoelastic model for cell deformation with experimental verification " *Biophysical Journal,* vol. 85, pp. 3336-49, 2003.

[31] T. Kazutaka, T. Takehito, M. Ryusuke, N. Ichiro, M. Takuro, and O. Aiji, "Human erythrocytes possess a cytoplasmic endoskeleton containing β-actin and neurofilament protein," *Archives of Histology and Cytology,* vol. 69, pp. 329-340, 2006.

[32] F. Guilak, J. R. Tedrow, and R. Burgkart, "Viscoelastic Properties of the Cell Nucleus," *Biochemical and Biophysical Research Communications,* vol. 269, pp. 781-786, 2000.

# 6 Microfluidic approach to high-content single-cell analysis of biophysical heterogeneity

*V. Srinivasaraghavan, H. Babahosseini, J. Strobl and M. Agah, "Microfluidic approach to high-content single-cell analysis of biophysical heterogeneity," Under review.*

*This paper has also been presented in V. Srinivasaraghavan's PhD dissertation.*

## *6.1 Introduction*

The need for technologies for single cell analysis is driven by a clear appreciation that a single clonogenic tumor stem cell is sufficient to produce a fatal tumor [1]. Such technologies also enable assessments of population level heterogeneity present in cancer cells within a single tumor which has implications in predicting disease progression and therapy resistance [2, 3]. Quantifying cellular properties and their responses to treatments at the single-cell level, in order to detect, cure or manage this disease is a great challenge. Recent technological advancements in micro- and nano-engineering have enabled researchers to identify, sort, and probe the properties of individual cancer cells [4, 5]. Han et al. recently reported a microfluidic chip for controlled separation and sequencing of nuclear genomic DNA and cytoplasmic messenger RNA from the same single leukemia cells which provides further opportunities to investigate the link between genetic and transcriptional signatures in cancer [6]. Another example is a high throughput microfluidic platform that employs hydrodynamic forces to measure the deformability of single cells which can be used for large population analyses such as identifying malignant cells in pleural fluids and pluripotency in stem cells [7]. These research directions promise to improve patient care by making more precise, individualized diagnostic and prognostic decisions for cancer patients possible.

The genetic heterogeneity of tumor populations is well-documented [8, 9]. More recently, the impact of non-genetic heterogeneity arising through epigenetic, metabolic and morphological/biophysical mechanisms on creation of distinct phenotypes has gained interest, and it will become important to decipher how these non-genetic sources of heterogeneity interact in tumor cells of diverse genetic backgrounds [10, 11]. Cells undergo biophysical changes as they go through cancer progression [12, 13]. Many research reports

have shown that cancer cells are softer and less viscous than corresponding benign cells [14, 15]. The dysregulation of the cell cytoskeleton in cancer cells increases their invasion potential, enables them to escape from the primary tumor and migrate to distant sites during metastasis to form secondary tumors [16]. Our laboratory has used atomic force microscopy (AFM) to demonstrate this relationship between cancer progression and visco-elastic properties of cells in human breast and mouse ovarian cancer cell models [15, 17]. In addition, metabolic reprogramming modulates intracellular signaling in cancer cells engages mitochondrial pathways [18], promotes alternative membrane glycosylation patterns [19] and effects desmoplasia, a process whereby cells increase stromal stiffness, both of which impact cellular biomechanics [20].

The electrical properties of biological cells and tissues become altered because of morphological and physiological changes [21]. For instance, the membrane capacitance can be impacted due to changes in surface charge, lipid composition and ion channel regulation which occur during cancer progression [22]. The use of bioimpedance in cancer has afforded investigators a simple means to monitor cell suspensions, tissues, cell-substrate adhesion, spreading, micromotility, and differentiate between normal and cancer cell types [23-25]. These differences have been attributed to the dielectric properties of cells which are governed by cell membrane composition, internal conductivities, and size [26-28]. All these studies support the development of devices to analyze the biophysical heterogeneity of individual cells within cell populations and the use of biophysical parameters as possible label-free biomarkers of tumor grade, metastatic potential, and response to drug treatments.

Microfluidics-based assays offer a variety of high throughput, rapid analysis platforms to measure the biophysical properties of single cells [4, 5]. The transit time of single cells through a narrow constriction channel has been used as a biophysical measure of deformability to differentiate between cell types [29, 30]. The remarkable cellular deformation that occurs during passage through a constriction channel suggests that cellular bioimpedance responses to this mechanical stress might provide new biophysical markers. We pursued development of technology to monitor bioimpedance properties in real-time as a function of mechanical stress. Here, we report a microfluidic assay in which the passage

of single cells through a narrow deformation region is monitored using an electrode pair integrated into the microchannel. These electrodes serve the dual purpose of automating transit time measurements and measuring the impedance at multiple frequencies enabling content-rich measurements from single cells pre-, post- and during mechanical deformation. In addition, the narrow constriction channel confers high sensitivity to the impedance measurements due to the fact that the cells, being larger than the deformation region, occupy the channel completely when travelling through it, thereby minimizing alternate current paths around the cell. We used this assay to obtain measurements from two tumorigenic (MDA-MB-468, MDA-MB-231) breast cancer and one non-tumorigenic (184A1) breast cell line and assessed the heterogeneity in their single-cell biophysical properties.

## *6.2 Materials and methods*

### 6.2.1 Design

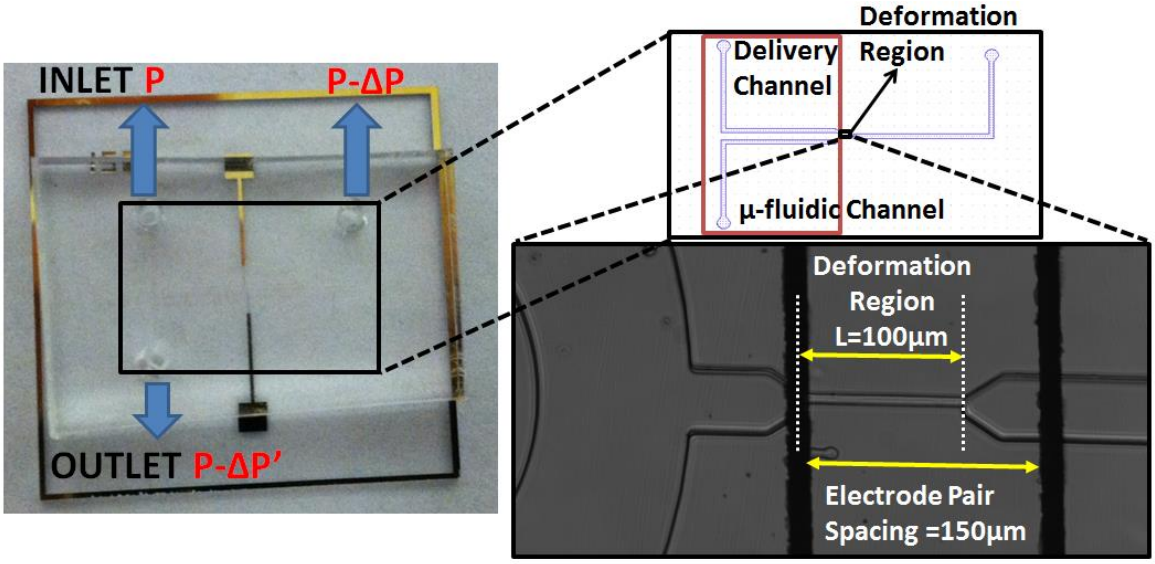


**Figure 6.1 Photograph of the microfluidic device with a magnified view of the deformation region.**

The device is shown in Figure 6.1 with a magnified view of the microfluidic channel design. The delivery channel is U-shaped with an inlet and an outlet and the deformation region which is 8 μm-wide, 8 μm-deep, 100 μm-long branches off from the middle of the U. The dimensions of the cross section are about half the typical cell diameter and ensure that the cell is completely deformed when it passes through this region. A pressure gradient is applied through a difference in the liquid level in the inlet and outlet reservoirs which

establishes a continuous free flow of single cells suspended in the culture medium through the delivery channel. Cells are then pulled through the deformation region by applying a negative pressure on the third port and two electrodes 150 μm apart are integrated into the channel to measure the impedance of single cells as they pass. One electrode is aligned with the entrance of the channel in order to enable automated measurement of entry time of cells into the channel. It should be noted that when a cell is in the deformation region, it completely blocks the channel and shields the cells in the delivery channel from the influence of the negative pressure on the other side. Therefore, for the duration of its travel through the channel, it prevents a second cell from being attracted into the deformation region. Also, the pressure gradient in the delivery channel ensures that cells are deflected towards the outlet reservoir and do not line up near the entrance, when a cell is already in the deformation region. This mechanism greatly reduces the clogging in the device.

### 6.2.2 Fabrication

The device was fabricated in polydimethylsiloxane (PDMS) using a master mold with the negative photoresist SU-8. The master mold was obtained using a two-step fabrication process with SU-8 2007 and SU-8 2025 to obtain different thicknesses for the channel (~60 μm) and the deformation region (8 μm). The electrodes were patterned on a pyrex/glass wafer by evaporation of Cr/Au after photolithography followed by a lift off process in acetone. The diced glass/pyrex and the PDMS layers were exposed to oxygen plasma for 50 seconds; the electrodes on the pyrex chip were aligned with the deformation region in the PDMS channel under a microscope using a few drops of methanol and transferred onto a hot plate. After 10 minutes, the device was removed from the hot plate and left to cure overnight for a strong bond before experiments.

### 6.2.3 Microfluidic experimental setup

The microfluidic device was mounted on a general purpose board (GPB), which has a cut-out for optical access to the device for microscopy and SMA adaptors for connectivity to make impedance measurements. The IDT Redlake NX-3 high speed camera was used to obtain images at the rate of 250 fps for 32 s. We used the Zurich instruments impedance spectroscope (HF2IS) to make measurements continuously at four frequencies (10 kHz, 20 kHz, 100 kHz and 800 kHz) in parallel using an excitation voltage of 1.25V at each

frequency. The frame rate of the high speed camera was matched with the data acquisition rate of the impedance spectroscope and a measurement was made from the cell every 4 ms which was sufficient to get good resolution of the transit time measurements. A syringe pump (Harvard Apparatus) was used to apply the negative pressure on the third port. Since, the same device was used for measurements from different cell types, the device was cleaned by flushing the delivery and the deformation channels thoroughly with deionized water for 5 minutes prior to the introduction of a new cell type.

### 6.2.4 Sample preparation

Three breast cancer cell lines with low passage numbers, 184A1 (passage 12), MDA-MB-468 (passage 25) and MDA-MB-231 (passage 22), were used in this study that were generously provided to us by Dr. Ayesha Shajahan-Haq from Georgetown University. 184A1 cells are a non-tumorigenic breast epithelial cell line while the MDA-MB-468 and MDA-MB-231 cells are tumorigenic triple-negative breast cancer cell lines with low and high metastatic potentials, respectively. The growth medium for the 184A1 cells was prepared from the MEGM kit obtained from Lonza by adding 0.005 mg/ml transferrin (Sigma Aldrich), 1 ng/ml cholera toxin (Sigma Aldrich) all the additives in the kit except the gentamycin-amphotericin B mix to the MEBM medium. The MDA-MB-468 cell growth medium was L-15 supplemented with 10% FBS. The MDA-MB-231 cell growth medium was DMEM-HG (ATCC) with 10% FBS. The 184A1 and MDA-MB-231 cells were maintained in a humidified incubator (37 $^{o}$C, 5% $CO_2$) while the MDA-MB-468 cells were maintained in a chamber at 37 $^{\circ}$C, 100% air. For experiments, cells were harvested from confluent cell cultures and suspended ($5x10^5$ cells/ml) in corresponding growth media.

### 6.2.5 Data analysis

The high-speed movie for each run was analyzed in conjunction with the impedance profile to match the cells in the movies to events in the impedance profiles. Multicellular aggregates and cell fragments were eliminated from analysis at this stage. A MATLAB program was used to calculate cell entry and travel time through channel, peak and baseline impedance magnitude and phase at each frequency for single cells. Image J was used to measure the diameter of the cell in X and Y directions, before and after deformation. The size of the cell was calculated by taking the average of the diameter of the cell measured in

the X and Y directions before deformation. The axial ratio (AR) before and after deformation was calculated by dividing the higher of the two values obtained from the diameter measurement in X and Y directions, by the lower value and is an indication of the shape of the cell. An AR of 1 indicated a uniformly round cell whereas ARs greater than one indicated the degree of elongation of the cell in one direction compared to another. The change between the peak and baseline of the real and imaginary parts of the complex impedance was calculated for 50 cells of each cell type.

### 6.2.6 Statistical tests

The D'Agostino & Pearson omnibus statistical test in Prism GraphPad was performed on all biophysical parameters analyzed in this study to test for normality of the distribution. Since the majority of the biophysical parameters did not pass the statistical test for normality, the following statistical methods were used to compare and contrast the data obtained from different cell lines. Box and whiskers plots of the median interquartile with range were used to enable visualization of the level of heterogeneity in the data for each cell line where larger boxes indicate a more heterogeneous population. The asymmetry of the box indicates the skewness in the population heterogeneity. Quadratic entropy (QE) was used as a metric for comparing heterogeneity levels among the three cell lines. It is sensitive to the spread of the distribution and has been used by researchers in quantifying the diversity of cellular phenotypes in cancer tissues [31]. It is calculated as $QE = \sum_{i>j=1}^{N} d_{ij} \times p_i \times p_j$ where $d_{ij}$ is the difference in the value of the ith and jth cells, $p_i$ and $p_j$ are the frequency of ith and jth values respectively. Bootstrapping was used to calculate 95% confidence intervals using 10000 bootstrap samples of the median in MATLAB. These confidence intervals are depicted using bars marked on the scatter plots along with the median. The non-parametric Kruskal-Wallis analysis of variance was used to test for statistical differences between the three cell lines and the Dunn-Sidak post hoc test was used to compare each pair.

## 6.3 Results

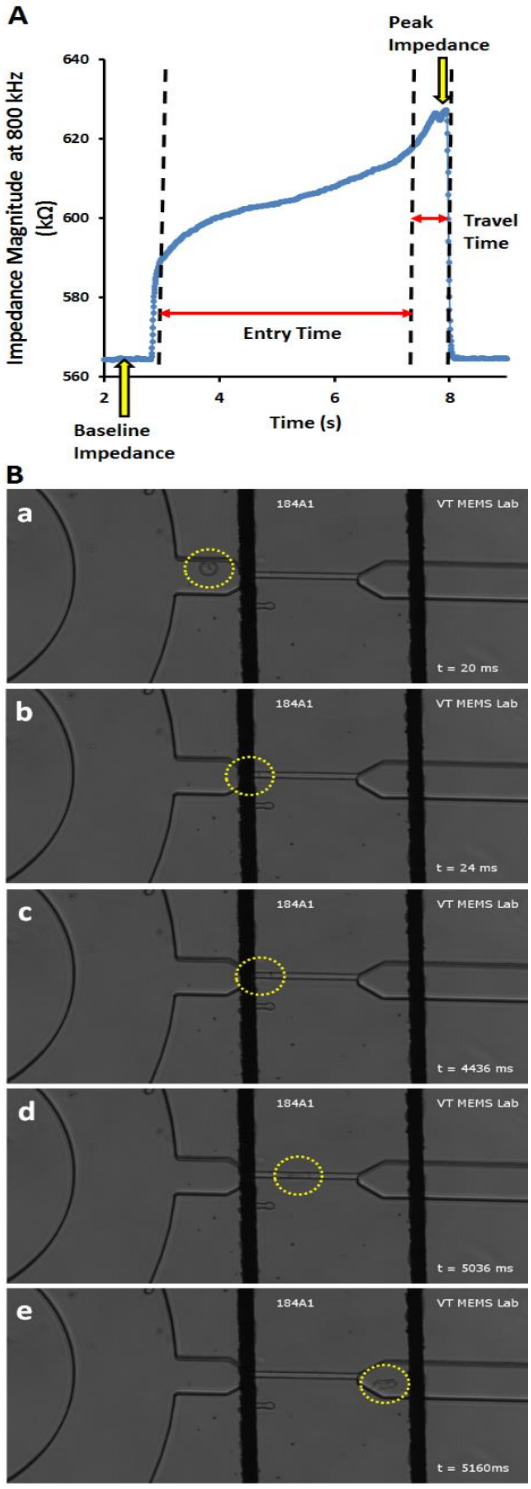


**Figure 6.2 (A) The impedance change due to a single 184A1 cell as it passes through the deformation region (B) Images tracking the 184A1 cell through the deformation region.**

Figure 6.2.A shows the characteristic impedance profile at 800 kHz as a single 184A1 cell moves through the deformation region in the microfluidic channel and Figure 6.2.B tracks the cell in images obtained using the high-speed camera. The impedance value measured due to the cell culture medium only in the absence of a cell is referred to as the baseline impedance. When a cell approaches the entrance of the channel (Figure 6.2.B-a), there is a sudden change in the impedance as can be seen from the steep slope. When the cell gets trapped at the entrance and is squeezing into the deformation region (Figure 6.2.B-b), the impedance rises more gradually. This process of cell entry is slow and contributes to the majority of the transit time of the cell through the deformation region as observed from the timestamp in Figure 6.2.B-c. When the cell has completely entered the channel and is traveling through the deformation region, the impedance reaches a maximum or peak value (Figure 6.2.B-d). The cell exits the deformation region rapidly as can be seen from the steep slope back to the baseline and Figure 6.2.B-e. Therefore, the entry and travel times of the cell through the channel can be calculated from the impedance profile. Supplementary video 3 shows the captured high-speed images of a single MDA-

MB-231 cell transiting through the deformation region in the device and the corresponding impedance changes recorded.

### 6.3.1 Cell deformability

The time the cell takes to squeeze into the narrow channel is the entry time and the time the cell spends traveling through the channel is the travel time. As the cell has to completely deform in order to squeeze into the channel, the transit time, defined as entry time plus travel time through the deformation region, can be used as a measure of its deformability and hence, its mechanical properties. The entry time of cells into a narrow channel is a sensitive indicator of their visco-elastic properties [32]. Here, for populations of 50 cells of each cell line, we analyzed the entry time (Figure 6.3.A) and travel time (Figure 6.3.B) of cells moving through the deformation channel.

The entry times for the non-tumorigenic 184A1 cell population were more homogeneous (QE=0.3) and displayed a tight distribution near the central median in contrast with the tumorigenic MDA-MB-468 (QE=0.6) and MDA-MB-231 (QE=0.5) cell populations that displayed a larger spread (Figure 6.3.A-inset). The highly metastatic MDA-MB-231 cells showed the shortest entry time which was significantly lower than the non-tumorigenic 184A1 and the MDA-MB-468 cells with low metastatic potential. These measurements indicate that the highly invasive MDA-MB-231 cells are more deformable than non-tumorigenic 184A1 cells, which is in agreement with previously published stiffness measurements from AFM [33]. The MDA-MB-468 cells with low metastatic potential are also significantly less deformable than the MDA-MB-231 but slightly more deformable than the non-tumorigenic 184A1 cells. Interestingly, the normal 184A1 cell line have the largest median entry time despite their smaller size indicating they were very stiff in comparison to the malignant cell lines. Hence, the entry time of a cell population can be correlated with its tumorigenic potential.

The travel time (Figure 6.3.B) through the deformation channel followed a pattern similar to the entry time for three cell lines. Travel times through the channel occurred more rapidly than entry, and there was little heterogeneity in travel time. These observations agree with a previous study of non-tumorigenic and tumorigenic breast cells [32].

The variation in cell size within each of the cell lines studied was normally distributed (Figure 6.3.C). The average diameter (±SD) of the metastatic cell lines, MDA-MB-468 (16.8±2.1 µm) and MDA-MB-231 (16.5±1.7 µm), was similar; because the highly metastatic MDA-MB-231 cells showed a significantly shorter entry time despite their similarity in size to the MDA-MB-468 cells, this suggests that the more highly metastatic cell line is more deformable. In contrast, the non-tumorigenic 184A1 (15.4±1.6 µm) cells were significantly smaller than both metastatic cell lines, yet 184A1 had an entry time comparable to that of the MDA-MB-468 cells and slower than that of the MDA-MB-231 cells. Thus, taking into consideration both the cell size and the entry time parameters, the non-tumorigenic 184A1 line typifies a stiffer biophysical phenotype than observed for the metastatic lines which show greater ease of deformability.

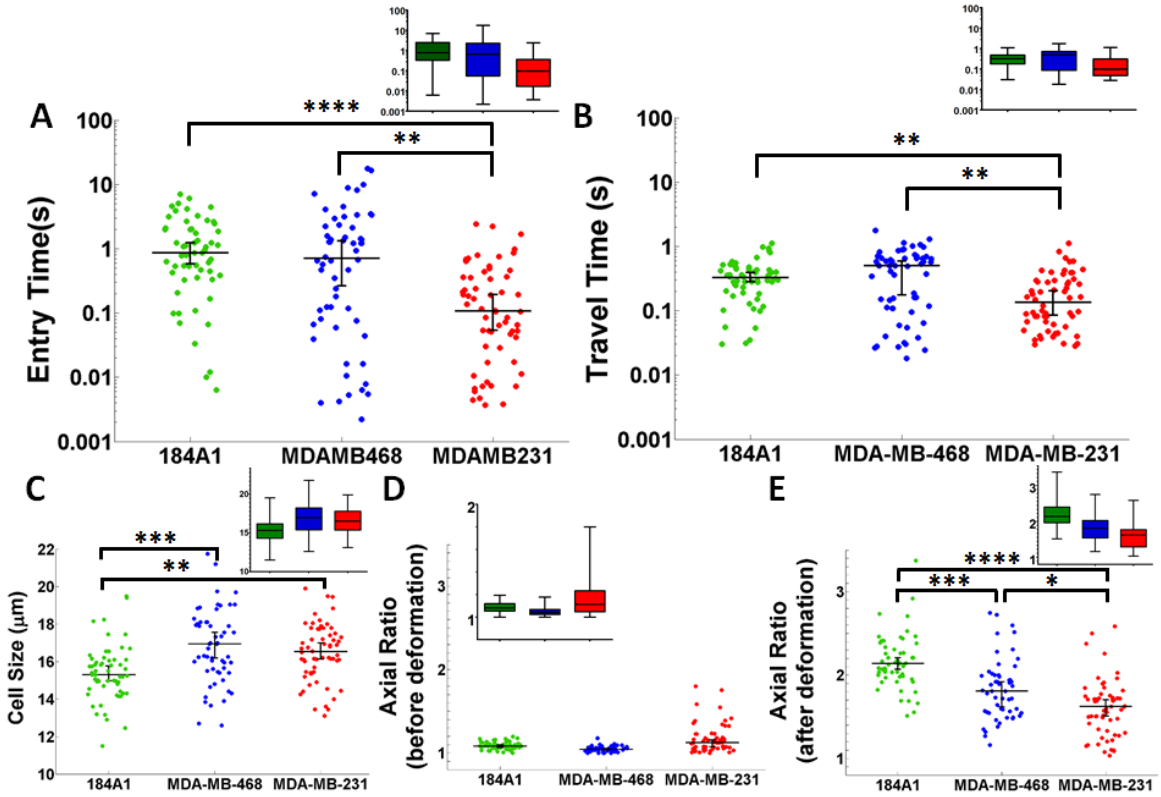


**Figure 6.3 Scatter plots of entry time (A) and travel time (B) through the deformation region extracted from the impedance data and cell size (C), axial ratio before (D) and after (E) deformation extracted from the high-speed videos for (n=50) cells of each cell type. Bars indicate 95% confidence intervals for the median. Inset images are box and whiskers plots for same data. Bars indicate range. * P<0.05 ** P<0.01 *** P<0.001 **** P<0.0001**

### 6.3.2 Shape recovery after deformation

The median ARs of each cell culture line before deformation (Figure 6.3.D) indicate that all 3 lines were comprised of highly rounded cells: 184A1 (1.08), MDA-MB-468 (1.04) and MDA-MB-231 (1.11). There was however, a greater range in the ARs within the MDA-MB-231 cell population (1.0-1.8; QE=0.09) than the MDA-MB-468 (QE=0.02) and 184A1 (QE=0.03) cells (Figure 6.3.D-inset) and these highly metastatic cells were more elongated with an AR skewed towards a value of 2. During transit through the constriction channel where cells were forced to deform to the channel size (8 μm) and hence, AR of all cell lines was similar (median AR≈3.75).

As a measure of recovery from mechanical deformation, the ARs of the cells as they emerged from the deformation channel were compared. After exiting the deformation channel, the non-tumorigenic 184A1 (AR 2.14) breast epithelial cells were significantly more elongated than both the breast cancer cell lines MDA-MB-468 (AR 1.81) and MDA-MB-231 (AR 1.62) (Figure 6.3.E). The non-tumorigenic 184A1 cells recovered more slowly than either metastatic cell line and, the most highly metastatic MDA-MB-231 cells recovered fastest. AR at exit thus correlated with tumorigenicity and metastatic potential.

### 6.3.3 Electrical model

Impedance is a complex number that is a measure of the opposition to the flow of electric current. In this device, electrodes are located on either side of the deformation region and the path of current flow is through the narrow channel. A cell positioned in the deformation region blocks the flow of electric current more effectively than culture medium. Thus, impedance increases when the cell is in the channel. Also, the electric field lines are concentrated in the narrow deformation region as seen from a two dimensional simulation done in COMSOL Multiphysics. Figure 6.4.A shows the surface plot of the electric field strength in the microfluidic device and it shows that the electric field due to the applied voltage (1.25 V, 800 kHz) on the electrodes with 150 μm spacing is maximal in the deformation region. This is true for all excitation frequencies tested and implies that the impedance measurements are most sensitive to events occurring close to or in this deformation region.

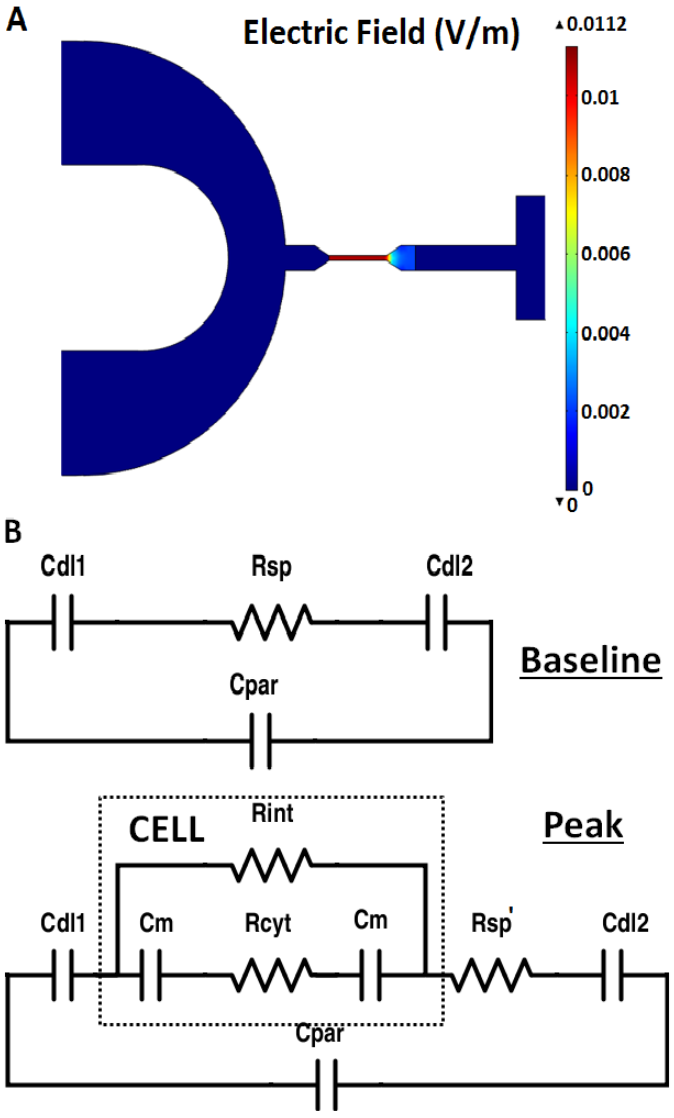


**Figure 6.4 (A) 2D surface plot of electric field strength in the microfluidic channel. (B) Schematic of the electric circuit model used to extract cell parameters from impedance measurements. Circuit element legend Cdl1,2- double layer capacitance; Rsp- spreading resistance; Cpar- parasitic capacitance; Cm- membrane capacitance; Rcyt- cytoplasm resistance; Rint- cell-channel wall interface resistance.**

The cell electrical response during deformation was continuously and simultaneously monitored at four frequencies, 10 kHz, 20 kHz, 100 kHz and 800 kHz, (Figure 6.4) to capture the cell impedance profile to mechanical stress at both high and low frequency imposed voltages.

The electric circuit model used to extract cell parameters from the multi-frequency impedance measurements is shown in Figure 6.4.B. When no cells are present near the electrode, the primary contribution to complex impedance is the capacitance of the double layer formed at the interface of the electrode and the surrounding medium that effectively acts as an electrolyte. Hence, the circuit used to model the baseline impedance consists of a double layer capacitance (Cdl1, Cdl2) at each electrode present in series with the spreading resistance (Rsp) of the culture medium in the deformation region. Capacitance (Cpar) is used to capture any parasitic effects in the measurement circuit.

Biological cell membranes can be modeled as a capacitance (Cm) and the cell cytoplasm as a resistance (Rcyt). The maximum change in impedance magnitude or peak impedance, occurs when the cell is in the center of the deformation region and completely blocks the channel. Hence, the path of current flow at the peak impedance is either through the cell, which is represented by cell membrane capacitance in series with cytoplasm resistance, or between the cell and the channel wall which is represented by the interface resistance (Rint). The deformed cell is approximately 30 μm long when it is in the narrow channel. Hence, the spreading resistance (Rsp') in this circuit was estimated as 0.7*Rsp. It should be noted that all capacitors in the circuit were modeled as constant phase elements which is a standard practice in electrochemical circuits.

To obtain unique values from curve fitting, Cdl1 and Cdl2 were modeled together to obtain a single capacitance Cdl. First, the baseline impedance was used to obtain Cdl, Cpar and Rsp. These values were inserted into the circuit for peak impedance to obtain Cm, Rcyt and Rint. All parameter values were obtained from curve fitting in MATLAB using the non-linear least squares method where the $R^2$ values for goodness of fit were greater than 0.95. The membrane capacitance (Cm) obtained from the model was converted to specific membrane capacitance by dividing by area of cell membrane at the two ends which is estimated as the hemispherical surface area ($4\pi r^2$ where r=4 μm). The cytoplasm conductivity was obtained by multiplying the inverse of Rcyt with the cell length in the channel (~30 μm) and dividing it by the channel cross section area ($8\times8$ $\mu m^2$).

### 6.3.4 Cell bioelectrical properties

The interface resistance (Rint) represents the resistance between the cell and the walls of the narrow microfluidic channel as the cell is traveling through it. As shown in Figure 6.5.A-inset. Rint was significantly larger in non-tumorigenic 184A1 cells in comparison to the tumorigenic cells. Thus, 184A1 cells, despite their smaller size appear to contact the channel wall more tightly during deformation, which might reflect increased surface friction. The median Rint values of the highly metastatic MDA-MB-231 cells were significantly lower than that of 184A1 cells.

The tumorigenic breast cell lines (MDA-MB-468 and MDA-MB-231) had significantly higher specific membrane capacitance than the non-tumorigenic 184A1 cells. Biological determinants of membrane capacitance include changes in cell dielectric

properties due to alterations in lipid composition, surface charges and ion channel profile, and there is some published evidence that these alterations do associate with increasing invasion potential [22, 34]. The specific membrane capacitance values for the tumorigenic MDA-MB-468 (QE=0.5) and MDA-MB-231 (QE=0.2) cell populations were prominently more heterogeneous than the non-tumorigenic 184A1 (QE=0.1) cell line (Figure 6.5.B-inset).

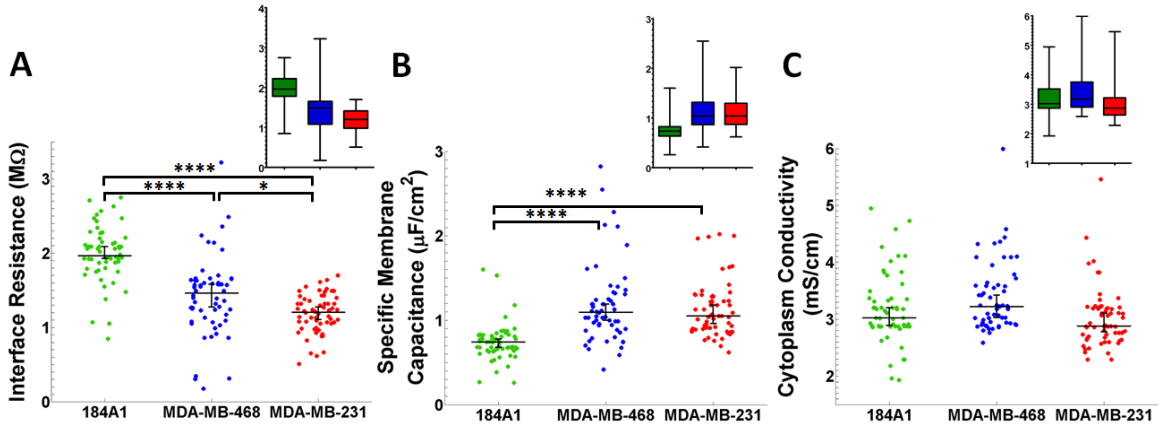


**Figure 6.5 Interface resistance (A), specific membrane capacitance (B), and cytoplasm conductivity (C) obtained for the three breast cell lines. Bars indicate 95% confidence intervals for the median. Inset images are box and whiskers plots for same data. Bars indicate range. * P<0.05 **** P<0.0001**

The cytoplasm conductivity is one measure of the biophysical properties of the cell interior. Interestingly, the cytoplasmic conductivity of all three cell lines studied was similar (Figure 6.5.C-inset). This suggests that the known tumor-associated reorganization of internal cytoskeleton, particularly acto-myosin complexes [35], microtubules [36], and the marker of epithelial-mesenchymal transition, the intermediate filament vimentin [37], do not effect significant changes in the cells' electrical conductivity.

Resistance at the interface (Rint) between the cell and the channel wall is dependent on the closeness of contact and the friction between these two surfaces. A parametric analysis (Figure 6.6) shows that of all the cell parameters, Rint has the largest effect on peak impedance changes. When, the average Rint value from MDA-MB-231 cells was combined with parameters obtained from 184A1 baseline impedance, the impedance changes of these 'hypothetical' cells moved into MDA-MB-231 cell regime on the graph. Whereas, when the cell parameters Ccell and Rcyt were used, they resulted in smaller shifts in impedance. Lower surface friction also enables faster transit through the deformation region suggesting aggressive cells maybe aided by this factor during metastasis [30].

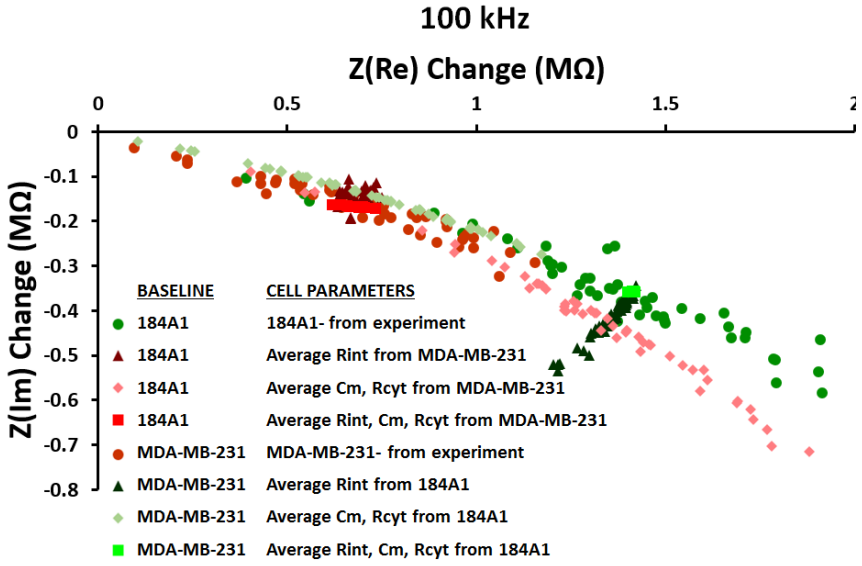


**Figure 6.6 Parametric analysis of impedance changes with respect to baseline.**

### 6.3.5 Classification of normal and tumor cells using single-cell biophysics

The highly sensitive measurement of bioimpedance in cells during deformation within a narrow channel provided us with a detailed single-cell impedance profile. The complex impedance value measured at each frequency can be expressed as a magnitude (Z) and a phase angle (θ) or as the real part (Z(Re)=Zcosθ) and imaginary part (Z(Im)=Zsinθ). In Figure 6.7.A, single-cell changes in real ((Z(Re)) versus imaginary (Z(Im)) components of impedance at 800 kHz are plotted. Individual normal 184A1 cells (green) are distinguishable from the tumorigenic MDA-MB-468 (blue) and MDA-MB-231 (red) cells. The high frequency (800 kHz) stimulation probes the internal cytoskeletal and membrane properties, and the assortment of cells into the green, red, and blue sub-groups is an

indication that internal/membrane structures differ sufficiently among these cells to enable their identification using bioelectric profiling.

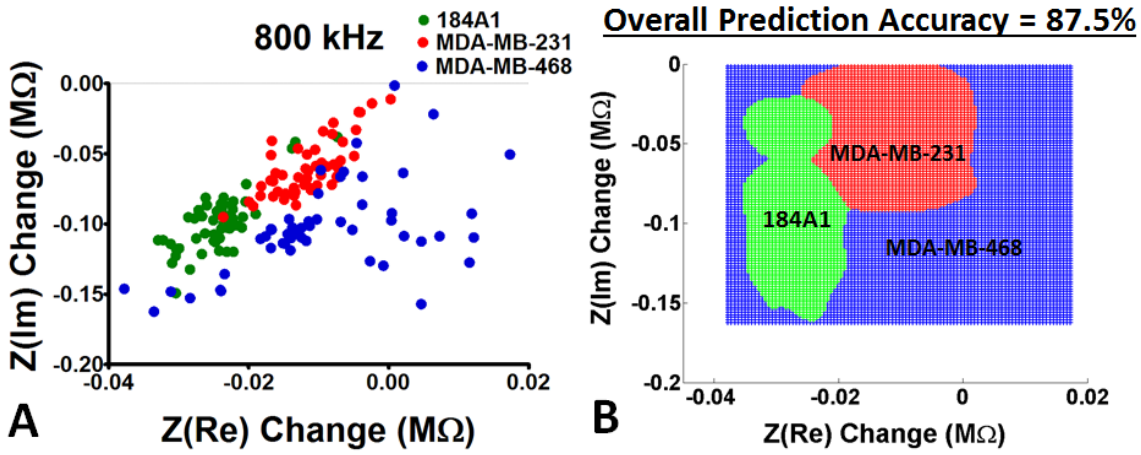


**Figure 6.7 (A) Impedance changes in real versus imaginary parts due to single cells at 800 kHz and (B) zones defined for each cell line by the non-parametric Naive Bayes classification.**

To analyze the accuracy of bioelectric profiling, cell zones were defined using the Naive Bayes classifiers (Figure 6.7.B). This model was then applied to the raw bioimpedance data that was used to assign a cell to a particular cell line. The percentage of non-tumorigenic 184A1 cells that were correctly assigned was 92%. Highly metastatic MDA-MB-231 were correctly identified in 94% of cells. Thus the electrical distinctions between non-tumorigenic and highly metastatic breast cell lines were quite prominent. Somewhat less robust identification (76%) of the low metastatic breast cells of the MDA-MB-468 line was achieved by electrical profiling. Overall, Naive Bayes analysis of the complex components of single-cell impedance using our technology accurately identified three pathologically distinct subtypes of breast cancer with 87.5% accuracy.

## *6.4 Discussion and conclusion*

During cancer progression, cells and their microenvironment undergo coevolution that ultimately results in tumor metastasis [38]. During this process, tumors frequently undergo what is referred to as the epithelial-mesenchymal transition [39], and tumor cell-stromal cell cross-talk results in pro-metastatic alterations in gene expression and cytoskeleton [40]. Among tumors there is also variation in the relative composition of tumor stem cells/cancer-initiating cells that will impact progression to metastatic disease [41].

These represent sources of cell heterogeneity in tumor populations which we and others suggest are important in ascertaining disease progression and patient prognosis. Biophysical profiling of tumor cell populations is an emerging approach to ascertain malignancy and risk for cell invasion and migration considered to be one of the hallmarks of cancer [42].

The tendency for cell softening in the viscoelastic properties during cancer progression is a well-documented biophysical alteration that might play a role in tumor cell penetration of the tissue-matrix, access to circulatory systems and metastasis [43]. Mechanical changes have been attributed to the reorganization of the cell cytoskeletal proteins actin and tubulin and cytoskeleton-targeted therapeutics is one strategy to contain cancer and impede metastasis [44, 45]. Also important are alterations in cell electrical properties during cancer progression. Tumor cell membranes are relatively enriched in many classes of lipids [22, 34, 46], with the result that tumor cells can exhibit an increased electronic polarizability of the cell membrane and increased specific membrane capacitance. In fact, we observed that 84% of breast cancer cells exhibited increased membrane capacitance compared to non-tumorigenic 184A1 cells (Figure 6.5.B). Within the cell membrane, levels of subtypes of calcium, chloride, and potassium ion channels are extensively modified, and these effect not only intracellular signaling pathways, but also cell membrane potential [47, 48].

Our interests lie in the design and development of microfluidic based devices to profile single-cell biomechanical and bioelectrical attributes simultaneously as a means for identifying individual cells within a sample population that display "high-risk" profiles. To achieve this, we fabricated a microfluidic chip with embedded electrodes and profiled a small panel of breast cells using cell lines of known tumorigenic and metastatic potential. Using the combined capabilities of microfluidics and bioimpedance, we observed that model breast cell lines representing tumorigenic and non-tumorigenic breast epithelium display significant differences in the parameters of channel entry time, cell shape recovery after deformation, cell-channel interface resistance, and specific membrane capacitance. The Naïve Bayes classification method applied to bioelectric profiling accurately assigned individual cells from three different breast cell culture models to their appropriate

pathobiologic subtypes. Furthermore, the unique ability of our technology to obtain deformability and multi-frequency impedance information simultaneously for the same single cell permits us to begin to understand the biophysical attributes resulting in the outlier cells in the Naïve Bayes classification system. For instance, tumorigenic cells with very high ARs after deformation also had lower specific membrane capacitance values. We showed that these cells exhibit properties similar to the non-tumorigenic cells. A further application of this work is the use of label-free profiling of single-cell biophysical properties to quantify the effectiveness of targeted therapeutic drugs in cell populations.

## *References*


[1] M. S. Wicha, S. L. Liu, and G. Dontu, "Cancer stem cells: An old idea - A paradigm shift," *Cancer Research,* vol. 66, pp. 1883-1890, Feb 2006.

[2] A. H. Gough, N. Chen, T. Y. Shun, T. R. Lezon, R. C. Boltz, C. E. Reese, *et al.*, "Identifying and Quantifying Heterogeneity in High Content Analysis: Application of Heterogeneity Indices to Drug Discovery," *PloS one,* vol. 9, p. e102678, 2014.

[3] C. E. Meacham and S. J. Morrison, "Tumour heterogeneity and cancer cell plasticity," *Nature,* vol. 501, pp. 328-337, 2013.

[4] W. M. Weaver, P. Tseng, A. Kunze, M. Masaeli, A. J. Chung, J. S. Dudani, *et al.*, "Advances in high-throughput single-cell microtechnologies," *Current opinion in biotechnology,* vol. 25, pp. 114-123, 2014.

[5] J. Chen, C. Xue, Y. Zhao, D. Chen, M.-H. Wu, and J. Wang, "Microfluidic Impedance Flow Cytometry Enabling High-Throughput Single-Cell Electrical Property Characterization," *International Journal of Molecular Sciences,* vol. 16, pp. 9804-9830, 2015.

[6] L. Han, X. Zi, L. X. Garmire, Y. Wu, S. M. Weissman, X. Pan, *et al.*, "Co-detection and sequencing of genes and transcripts from the same single cells facilitated by a microfluidics platform," *Scientific reports,* vol. 4, 2014.

[7] D. R. Gossett, T. Henry, S. A. Lee, Y. Ying, A. G. Lindgren, O. O. Yang, *et al.*, "Hydrodynamic stretching of single cells for large population mechanical phenotyping," *Proceedings of the National Academy of Sciences,* vol. 109, pp. 7630-7635, 2012.

[8] T. Yang, K. Rycaj, Z.-M. Liu, and D. G. Tang, "Cancer stem cells: constantly evolving and functionally heterogeneous therapeutic targets," *Cancer research,* vol. 74, pp. 2922-2927, 2014.

[9] L. G. Martelotto, C. Ng, S. Piscuoglio, B. Weigelt, and J. S. Reis-Filho, "Breast cancer intra-tumor heterogeneity," *Breast Cancer Res,* vol. 16, p. 210, 2014.

[10] B. Gottlieb, L. K. Beitel, and M. Trifiro, "Changing genetic paradigms: creating next-generation genetic databases as tools to understand the emerging complexities of genotype/phenotype relationships," *Hum. Genomics,* vol. 8, 2014.

[11] S. Huang, "Non-genetic heterogeneity of cells in development: more than just noise," *Development,* vol. 136, pp. 3853-3862, 2009.

[12] S. Suresh, "Biomechanics and biophysics of cancer cells," *Acta Biomater.,* vol. 3, pp. 413-438, 2007.

[13] C. T. Mierke, "The fundamental role of mechanical properties in the progression of cancer disease and inflammation," *Reports on Progress in Physics,* vol. 77, p. 076602, 2014.

[14] G. Weder, M. C. Hendriks-Balk, R. Smajda, D. Rimoldi, M. Liley, H. Heinzelmann, *et al.*, "Increased plasticity of the stiffness of melanoma cells correlates with their acquisition of metastatic properties," *Nanomedicine: Nanotechnology, Biology and Medicine,* vol. 10, pp. 141-148, 2014.

[15] A. N. Ketene, E. M. Schmelz, P. C. Roberts, and M. Agah, "The effects of cancer progression on the viscoelasticity of ovarian cell cytoskeleton structures," *Nanomed: Nanotechnology, Biol and Med.,* vol. 8, pp. 93-102, 2012.

[16] D. Wirtz, K. Konstantopoulos, and P. C. Searson, "The physics of cancer: the role of physical interactions and mechanical forces in metastasis," *Nature Reviews Cancer,* vol. 11, pp. 512-522, Jul 2011.

[17] H. Babahosseini, A. N. Ketene, E. M. Schmelz, P. C. Roberts, and M. Agah, "Biomechanical profile of cancer stem-like/tumor-initiating cells derived from a progressive ovarian cancer model," *Nanomedicine: Nanotechnology, Biology and Medicine,* 2014.

[18] A. S. Tan, J. W. Baty, and M. V. Berridge, "The role of mitochondrial electron transport in tumorigenesis and metastasis," *Biochimica et Biophysica Acta (BBA)-General Subjects,* vol. 1840, pp. 1454-1463, 2014.

[19] I. Häuselmann and L. Borsig, "Altered tumor-cell glycosylation promotes metastasis," *Frontiers in oncology,* vol. 4, 2014.

[20] J. C. Tung, J. M. Barnes, S. R. Desai, C. Sistrunk, M. Conklin, P. Schedin, *et al.*, "Tumor mechanics and metabolic dysfunction," *Free Radical Biology and Medicine,* 2014.

[21] P. R. Gascoyne, S. Shim, J. Noshari, F. F. Becker, and K. Stemke-Hale, "Correlations between the dielectric properties and exterior morphology of cells revealed by dielectrophoretic field-flow fractionation," *Electrophoresis,* vol. 34, pp. 1042-1050, 2013.

[22] B. Szachowicz-Petelska, I. Dobrzynska, S. Sulkowski, and Z. Figaszewski, "Characterization of the cell membrane during cancer transformation," *Journal of Environmental Biology,* vol. 31, pp. 845-850, Sep 2010.

[23] L. J. Yang, L. R. Arias, T. S. Lane, M. D. Yancey, and J. Mamouni, "Real-time electrical impedance-based measurement to distinguish oral cancer cells and non-cancer oral epithelial cells," *Analytical and Bioanalytical Chemistry,* vol. 399, pp. 1823-1833, Feb 2011.

[24] C. Murdoch, B. H. Brown, V. Hearnden, P. M. Speight, K. D'Apice, A. M. Hegarty, *et al.*, "Use of electrical impedance spectroscopy to detect malignant and potentially malignant oral lesions," *International journal of nanomedicine,* vol. 9, p. 4521, 2014.

[25] V. Srinivasaraghavan, J. Strobl, D. Wang, J. R. Heflin, and M. Agah, "A comparative study of nano-scale coatings on gold electrodes for bioimpedance studies of breast cancer cells," *Biomedical microdevices,* pp. 1-8, 2014.

[26] K. Heileman, J. Daoud, and M. Tabrizian, "Dielectric spectroscopy as a viable biosensing tool for cell and tissue characterization and analysis," *Biosensors and Bioelectronics,* vol. 49, pp. 348-359, 2013.

[27] V. Srinivasaraghavan, J. Strobl, and M. Agah, "Bioimpedance rise in response to histone deacetylase inhibitor is a marker of mammary cancer cells within a mixed culture of normal breast cells," *Lab on a Chip,* vol. 12, pp. 5168-5179, 2012.

[28] Y. Zhao, X. T. Zhao, D. Y. Chen, Y. N. Luo, M. Jiang, C. Wei, *et al.*, "Tumor cell characterization and classification based on cellular specific membrane capacitance and cytoplasm conductivity," *Biosensors and Bioelectronics,* vol. 57, pp. 245-253, 2014.

[29] A. Adamo, A. Sharei, L. Adamo, B. Lee, S. Mao, and K. F. Jensen, "Microfluidics-Based Assessment of Cell Deformability," *Analytical Chemistry,* vol. 84, pp. 6438-6443, Aug 2012.

[30] S. Byun, S. Son, D. Amodei, N. Cermak, J. Shaw, J. H. Kang, *et al.*, "Characterizing deformability and surface friction of cancer cells," *Proceedings of the National Academy of Sciences of the United States of America,* vol. 110, pp. 7580-7585, May 2013.

[31] S. J. Potts, J. S. Krueger, N. D. Landis, D. A. Eberhard, G. D. Young, S. C. Schmechel, *et al.*, "Evaluating tumor heterogeneity in immunohistochemistry-stained breast cancer tissue," *Laboratory Investigation,* vol. 92, pp. 1342-1357, 2012.

[32] H. W. Hou, Q. S. Li, G. Y. H. Lee, A. P. Kumar, C. N. Ong, and C. T. Lim, "Deformability study of breast cancer cells using microfluidics," *Biomed Microdevices,* vol. 11, pp. 557-564, 2009.

[33] M. Lekka, D. Gil, K. Pogoda, J. Dulinska-Litewka, R. Jach, J. Gostek, *et al.*, "Cancer cell detection in tissue sections using AFM," *Archives of Biochemistry and Biophysics,* vol. 518, pp. 151-156, Feb 2012.

[34] M. L. Doria, Z. Cotrim, B. Macedo, C. Simoes, P. Domingues, L. Helguero, *et al.*, "Lipidomic approach to identify patterns in phospholipid profiles and define class differences in mammary epithelial and breast cancer cells," *Breast Cancer Research and Treatment,* vol. 133, pp. 635-648, Jun 2012.

[35] V. Betapudi, L. S. Licate, and T. T. Egelhoff, "Distinct roles of nonmuscle myosin II isoforms in the regulation of MDA-MB-231 breast cancer cell spreading and migration," *Cancer research,* vol. 66, pp. 4725-4733, 2006.

[36] L. Dvir, R. Nissim, M. B. Alvarez-Elizondo, and D. Weihs, "Quantitative measures to reveal coordinated cytoskeleton-nucleus reorganization during in vitro invasion of cancer cells," *New Journal of Physics,* vol. 17, p. 043010, 2015.

[37] K. Vuoriluoto, H. Haugen, S. Kiviluoto, J. Mpindi, J. Nevo, C. Gjerdrum, *et al.*, "Vimentin regulates EMT induction by Slug and oncogenic H-Ras and migration by governing Axl expression in breast cancer," *Oncogene,* vol. 30, pp. 1436-1448, 2011.

[38] K. Polyak, I. Haviv, and I. G. Campbell, "Co-evolution of tumor cells and their microenvironment," *Trends in Genetics,* vol. 25, pp. 30-38, Jan 2009.

[39] A. Vincent-Salomon and J. P. Thiery, "Epithelial-mesenchymal transition in breast cancer development," *Breast Cancer Research,* vol. 5, pp. 101-106, 2003.

[40] C.-W. Peng, X.-L. Liu, X. Liu, and Y. Li, "Co-evolution of cancer microenvironment reveals distinctive patterns of gastric cancer invasion: laboratory evidence and clinical significance," *J Transl Med,* vol. 8, pp. 1479-5876, 2010.

[41] I. Baccelli, A. Schneeweiss, S. Riethdorf, A. Stenzinger, A. Schillert, V. Vogel, *et al.*, "Identification of a population of blood circulating tumor cells from breast cancer patients that initiates metastasis in a xenograft assay," *Nature Biotechnology,* vol. 31, pp. 539-544, 2013.

[42] D. Hanahan and R. A. Weinberg, "Hallmarks of Cancer: The Next Generation," *Cell*, vol. 144, pp. 646-674, Mar 2011.

[43] K. Ward, W. Li, S. Zimmer, and T. Davis, "Viscoelastic properties of transformed cells: role in tumor cell progression and metastasis formation," *Biorheology*, vol. 28, pp. 301-313, 1990.

[44] A. N. Ketene, P. C. Roberts, A. A. Shea, E. M. Schmelz, and M. Agah, "Actin filaments play a primary role for structural integrity and viscoelastic response in cells," *Integrative Biology*, vol. 4, pp. 540-549, 2012.

[45] J. R. Stehn, N. K. Haass, T. Bonello, M. Desouza, G. Kottyan, H. Treutlein, *et al.*, "A Novel Class of Anticancer Compounds Targets the Actin Cytoskeleton in Tumor Cells," *Cancer Research*, vol. 73, pp. 5169-5182, Aug 2013.

[46] E. Cifkova, M. Holcapek, M. Lisa, D. Vrqna, J. Gatek, and B. Melichar, "Determination of lipidomic differences between human breast cancer and surrounding normal tissues using HILIC-HPLC/ESI-MS and multivariate data analysis," *Analytical and bioanalytical chemistry*, pp. 1-12, 2014.

[47] M. Yang and W. J. Brackenbury, "Membrane potential and cancer progression," *Frontiers in Physiology*, vol. 4, p. 10, 2013.

[48] J. S. Strobl, W. F. Wonderlin, and D. C. Flynn, "Mitogenic signal transduction in human breast cancer cells," *General Pharmacology: The Vascular System*, vol. 26, pp. 1643-1649, 1995.

# 7 Single Cell Metastatic Phenotyping using Pulsed Nanomechanical Indentations



*H. Babahosseini, J. Strobl, and M. Agah, "Single Cell Metastatic Phenotyping using Pulsed Nanomechanical Indentations," Nanotechnology, vol. 26, no. 35, pp. 354004, August 2015.*

## *7.1 Introduction*

The study of cell biomechanics has made great strides in the past decades as a result of advances in nanotechnologies enabling the manipulation and mechanical loading of single cells, and has brought significant new insight to how induced cell deformation and cyto-architecture remodeling impacts many aspects of human health and disease. The cytoskeleton provides mechanical support and integrity to the cell [2] but also plays a pivotal role in transducing mechanical stimuli from the microenvironment to intracellular signaling events that affect changes in gene expression, differentiation, adhesion [3], contractility, morphology and migration [4]. These are mechanically-oriented processes that are of critical importance in developmental biology, tissue homeostasis, tissue regeneration and wound healing [5], as well as cancer dissemination and metastasis [6]. With progression to a metastatic phenotype, cells become softer to facilitate motility [7]. In fact, highly metastatic, aggressive cells acquire the ability to deform and squeeze through tumor stroma matrix and endothelial barriers to gain access to the circulatory system, and subsequently, adhere to and extravagate blood or lymph vessels to establish secondary tumors [8]. The suggestion that the metastatic potential of transformed cells is related to their mechanical properties is now widely accepted. Furthermore, critical signaling intermediates and intracellular signaling pathways are altered due to the deregulation of cytoskeleton organization [9]. Because the evidence that the cytoskeletal changes which typify malignancy play active roles in pathobiology continues to increase, there is huge interest in identifying biophysical markers of metastatic cells.

A sufficiently accurate means for cancer detection at its earliest, potentially treatable stage is a great challenge. Researchers from engineering disciplines have sought to apply nanotechnology to interrogate physical properties of cells and to provide reliable

biophysical markers for early cancer detection. Methods to interrogate cellular mechanical properties chiefly measure elasticity and viscosity at the single-cell level. The application of Atomic Force Microscopy (AFM) as a key tool in nanotechnology has led to great achievements in the characterization of biological cells structure because of its precise nanoscale resolution and ability to probe live samples under their culture media *in vitro*. A wide variety of established transformed and non-transformed cell lines have been studied [7]. The overall findings by our group [10-13] and others [14, 15] agree that as cells transform and progress toward more aggressive stages, they become, on average, more deformable and less viscous. Along these lines, aggressive cancer cells often exhibit a less organized cytoskeleton with a less dense actin fiber network [16]. The importance of the principal cytoskeletal elements to cell elasticity and viscosity has been investigated in adherent cells where the actin filaments network was identified as a primary determinant with a minor influence of microtubules [17].

The application of biomechanical markers for single cell discrimination of non-metastatic and metastatic cells has met with notable lack of success. Despite progress, the current methods typically define a mean or median descriptor for a population of metastatic cells which differs from that of a population of non-metastatic cells, but the distribution of non-metastatic and metastatic cells across this descriptor overlaps considerably [18-20]. Current methods, therefore, do not discriminate each individual metastatic cell from every individual non-metastatic at the single-cell level with sufficient confidence. The purpose of the work we present here is to define a protocol which does achieve the necessary single-cell biomechanical signature for such an early cancer detection assay.

The existing methods of cell biomechanical characterization typically utilize "switch-like models of mechano-transduction" [21] in which cell responses are analyzed under transient force loading conditions, i.e. creep or stress relaxation. The basis for our approach is the concept that the micromechanical environment of a cell constantly changes and that each cell is subjected to dynamic forces in its physiological environment. Therefore, the dynamic behavior of cells is of particular interest. In response to dynamic force, a cell constantly modifies its cytoskeleton architecture, and it is dynamic regulation that allows the cell to adapt its biomechanical properties to compensate for environmental forces [22]. Hence, the switch-like models cannot fully explain and predict the cellular

responses *in vivo* [21]. Oscillatory AFM [23] as well as magnetic twisting cytometry (MTC) [24] are popular techniques used for conducting dynamic force tests on adherent cells. Cell cytoskeleton reorganization and subsequent cell biomechanical alterations under periodic stretch or compression depend on the frequency and the magnitude of the loading forces [25-27]. The structural subcellular components, such as actin and intermediate filament networks, have dynamic behaviors when perturbed. With regard to the role of cyclic strain/stress in regulating cellular cytoskeleton organization, researchers have shown that actin stress fiber alignment changes in a frequency-dependent manner [28, 29]. It has also been shown that mechanical stiffening of cells in response to external stress highly depends on actin network [30].

Here, we have used models of human breast cancer to develop a single cell biomechanical signature protocol for metastatic phenotyping. Breast cancer is the most common cancer and the leading cause of cancer death among women world-wide [31]. Four cell lines representative of non-metastatic (184A1 and MCF10A) and metastatic (MDA-MB-468 and MDA-MB-231) breast subtypes are used for this study. Observations in this study depict the dynamic characteristics of the cell responses under pulsed nano-indentations. We have utilized AFM to create pulsed stresses on both non-metastatic and metastatic breast cells. The elastic and viscoelastic parameters for each pulse were measured by fitting the Standard Linearized Solid (SLS) model. The opposing trend of biomechanical parameters of non-metastatic and metastatic breast cells in responses to the pulsed stresses is proposed as a new biomarker for cell differentiation at the single-cell level.

## *7.2 Materials and methods*

### 7.2.1 Sample preparation

Four human cell lines were used here. Immortalized, yet non-tumorigenic and non-metastatic 184A1 (derived from normal breast epithelial cells after exposure to benzo(a)pyrene) and MCF10A (derived from fibrocystic tissue localized to the breast in a patient) cell lines are representative of the non-metastatic breast cell type. Low-metastatic MDA-MB-468 and high-metastatic MDA-MB-231, derived from two different patients' pleural effusions, a site of metastasis, are representative of metastatic cell type. Cell

cultures were maintained in plastic T-25 culture flasks using growth conditions recommended by the ATCC. The standard culture medium used for 184A1 cells was the MEGM kit (Lonza, Basel, Switzerland) in which we used all the kit additives except the gentamycin-amphotericin B, with supplementation of 5 μg/ml transferrin (Sigma Aldrich, St. Louis, MO) and 1 ng/ml cholera toxin. The culture medium for MCF10A cells composed of F12:DMEM (Lonza, Basel, Switzerland) with penicillin-streptomycin (100 Units/ml), 2.5 mM L-glutamine, 20 ng/ml epidermal growth factor (EGF), 0.1 μg/ml cholera toxin (CT), 10 μg/ml insulin, 0.5 μg/ml hydrocortisone, and 5% horse serum. The culture medium for MDA-MB-468 cells was L-15 supplemented with 10% FBS, 4 mM glutamine and penicillin-streptomycin (100 Units/ml). Finally, the culture medium for MDA-MB-231 cells consisted of F12:DMEM with 10% FBS, 4 mM glutamine and penicillin-streptomycin (100 Units/ml). For AFM experiments, cells were grown in incubators at 37°C in humidified 5% $CO_2$ and later harvested, counted using the hemocytometer, and plated with the density of $1x10^5$ cells/slip on 0.15 mm thick, 12 $mm^2$ glass cover slips coated with 0.1 mg/mL collagen type IV (Sigma Aldrich, St. Louis, MO) to promote cell adhesion and incubated for 24 hours prior to AFM experiments. All measurements were performed in their standard culture medium at room temperature (~24°C). A buffered HEPES at final concentration of 13.5 mM was added to the samples to help maintain a physiological pH of 7.2 during the experiment. The final pH in the culture medium will be stable for more than 2 hours at room temperature, which is considered adequate time for the total duration of individual experiment sessions.

### 7.2.2 AFM experiment

An Icon dimension AFM (Bruker, Santa Barbara, CA) with Pico-Force functionality was used to perform the pulsed ramping experiments on the cells. Olympus TR400PSA V-shaped SiNi cantilevers (Asylum Research, Santa Barbara, CA) with approximate spring constant values of ~0.02 N/m were used in all AFM experimentations; exact spring constant values were measured via thermal tuning method in the AFM system. The probes were modified by attaching glass spheres (Duke Scientific, Waltham, MA) of ~10 μm diameter onto the cantilever free end with two-part epoxy (Miller Stephenson, Sylmar, CA), which helped the cells remain minimally damaged during contact. In

addition, cell deformation nonlinearity was reduced due to a more homogenous contact between the cells and the probe. Indentations were performed at the cell nucleus proximities at a constant approach and retract velocity of ~5 μm/s and at the 5 kHz sampling frequency. The maximum indentation force is limited to a trigger of 10 nN which causes a deep indentation (2-3 μm) into the cellular structure which engages sub-cellular components in the measurements. The AFM cantilever was programmed to come into the engagement with the cell surface and indent it for a certain deformation amount and subsequently held in the place for a period of τ to cause a stress on the cell structure during which the corresponding z-scanner's position was held constant to record the change in deflection of the cantilever as a function of time on the sample. The cantilever was then retracted from the cell and left stationary for a period of T before allowing re-indentation at the same location. Essentially, each cell was indented and remained in contact with the AFM cantilever for 'n' times with τ stress duration and *T* recovery interval times as shown in Figure 7.1. The algorithm used to perform these tests was done within the force scripting mode in the AFM software.

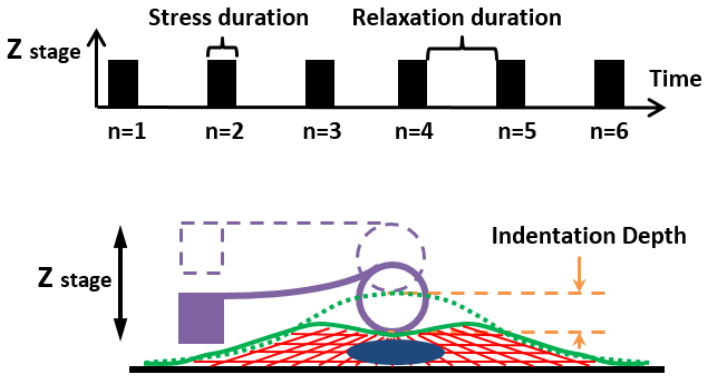


**Figure 7.1 The AFM probe is programmed to repeat a pulse of indenting a cell and subsequently is held in place and then is retracted from the cell for 'n' times at the same location.**

### 7.2.3 Immunofluorescence preparation and imaging

The actin cytoskeleton in the breast cells attached to the collagen-coated cover slip were assessed using confocal microscopy (ZEISS-LSM-510 META, Thornwood, NY) after tagging them. For actin staining, the cells were fixed with 3% paraformaldehyde in 250 mM HEPES, pH 7.2, permeabilized with 0.25% Triton-X100 in 6% paraformaldehyde in 250 mM HEPES, quenched with 50 mM glycine, and blocked with 2% chicken serum albumin

(CSA) in Phosphate-Buffered Saline (PBS) solution. The actin cytoskeleton was stained using AlexaFluor-488 phalloidin (Invitrogen, Carlsbad, CA) diluted 10 Units/ml in 140 mM NaCl-6% bovine serum albumin in 40 mM Tris, pH 7.2. Following the actin staining, the samples were rinsed three times in PBS and mounted on ProLong Gold antifade reagent with DAPI (Invitrogen, Carlsbad, CA) for final imaging.

### 7.2.4 Cell dynamic biomechanics

The elastic modulus ($E$) and apparent viscosity ($\mu$) measurements are performed by acquiring sample's stress-relaxation response. The parameters are calculated by using the Standard Linear Solid (SLS) model theory [32]. This model provides an analytical equation of the viscoelastic force as a function of time. Material properties are extracted by fitting the model to the stress-relaxation data and accounting for several variables, including force $F(t)$, deformation $\delta_0$, relaxed modulus $E_R$, Poisson's ratio $v_{cell}$, contact surface radius $R$ as follows [33]:

$$F(t) = \frac{4}{3}\frac{\sqrt{R}}{(1-v_{cell})}\,\delta_0^{\frac{3}{2}}\left[E_R + Ee^{-\frac{E}{\mu}t}\right] \tag{7.1}$$

For sequential indentations along with stress-relaxation periods, the cell elastic modulus ($E_n$) and apparent viscosity ($\mu_n$) parameters are calculated for each pulse ($n=1, 2\ldots 6$) by fitting the SLS model to the stress-relaxation portion of the acquired data. The relative percentage change (RPC) of elastic modulus ($PCR_{\mu n\text{-}n+1}=\frac{\mu_{n+1}-\mu_n}{\mu_n}\times 100$) and relative percentage change of apparent viscosity ($PCR_{En\text{-}n+1}=\frac{E_{n+1}-E_n}{E_n}\times 100$) of individual cell between $n$ and $n+1$ successive pulses are determined. The rate of change (α) for elastic modulus, $\alpha_E = \frac{\partial E}{\partial n}$, and the rate of change for apparent viscosity, $\alpha_\mu = \frac{\partial \mu}{\partial n}$, are derived from the best fit (regression) straight line through a set of the measured parameters values of a cell in all pulses. The elastic modulus, $E_{cell}(n)$, and the apparent viscosity, $\mu_{cell}(n)$, for a cell under pulsed stress events can be estimated and expressed as follows:

$$E_{cell}(n) \approx \alpha_E(n-1) + E_1 \tag{7.2}$$

$$\mu_{cell}(n) \approx \alpha_\mu(n-1) + \mu_1 \tag{7.3}$$

where $E_1$ and $\mu_1$ are the initial elastic modulus and apparent viscosity of the cell under the initial stress pulse.

### 7.2.5 Statistical analysis

Pulsed stress were performed via AFM on a 40-45 samples size of cells from 184A1 (number=45), MCF10A (number = 44), MDA-MB-231 (number=43), and MDA-MB-231 (number = 40) populations in at least 5 separate test sessions on different days. No signs of puncturing the cells as a consequence of repeated indentations were seen in the experimental data. Cell elasticity and viscoelasticity measurements for each pulse, their RPC between each successive pulses, and their α values are expressed as mean ± standard deviation (SD). The statistical significance of differences in mean values between two sets was assessed using a two-sample independent t-test with a 95% confidence interval ($P < 0.05$).

## *7.3 Results*

### 7.3.1 E and μ under pulsed stress

To test the hypothesis about distinct biomechanical properties of non-metastatic and metastatic cells under pulsed stress, we indented well-spread individual cells from the four selected breast cell type populations 6 times using a stress duration of 20 sec and relaxation time of 80 sec (n=6, τ=20, T=80) (Figure 7.1). The elastic modulus ($E_{elastic}$) and apparent viscosity ($\mu_{viscosity}$) measurements in each pulse for the selected breast populations under pulsed stress are shown in Figure 7.2.a and Figure 7.2.b, respectively. The summary of these biomechanical properties measurements are also presented in Table 7.1.

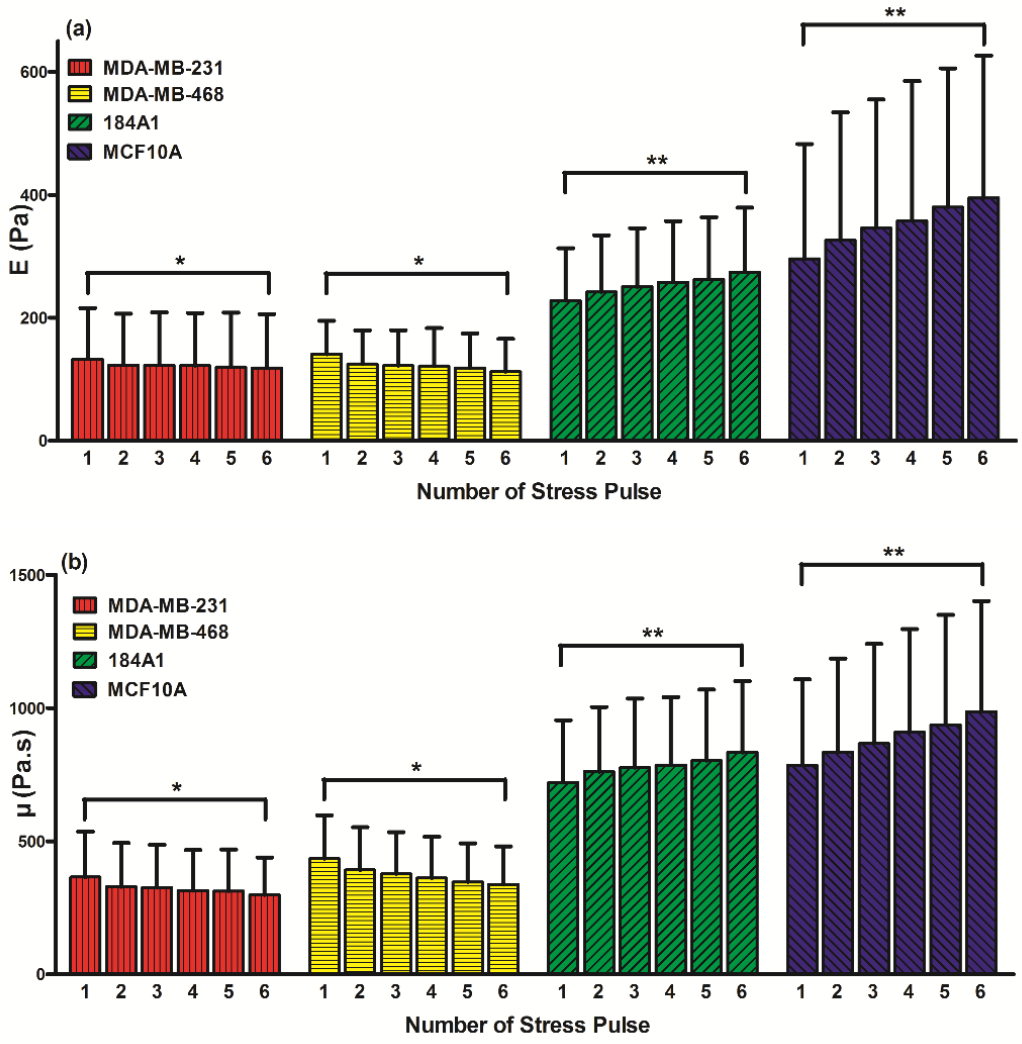


**Figure 7.2 Depiction of changes in (a) the elastic modulus and (b) the apparent viscosity of breast cell lines under pulsed stresses.**

Evidence that MCF10A and 184A1 non-metastatic cells develop "stiffening" under the pulsed stimuli in their average elastic modulus (Figure 7.2.a) and their average apparent viscosity measurements (Figure 7.2.b) is statistically significant. MCF10A and 184A1 had an increase of ~34% and ~21% ($p < 0.05$) in their average elastic moduli between the initial (n=1) and final (n=6) pulse, respectively. Similarly, the average apparent viscosities of MCF10A and 184A1 between the initial and final pulse increased by ~26% and ~16% ($p < 0.05$), respectively. Therefore, the non-metastatic cells responded by a significant increase in their mechanical resistance against the pulsed stress and a stiffening behavior. The variation of biomechanical responses upon applying the pulsed stimuli shows that the

SDs in the $E_{elastic}$ and $\mu_{viscosity}$ responses of MCF10A cells expand by 25% and 28%, respectively. Likewise, for 184A1 cells, the diversity of the $E_{elastic}$ and $\mu_{viscosity}$ responses develop by 23% and 15%, respectively. It implies that the non-metastatic cells mechanically become more heterogeneous while they develop stiffening under pulsed stresses.

In contrast, MDA-MB-468 and MDA-MB-231 metastatic cells exhibited on average a "softening" trend in their measured biomechanical properties under pulsed stress. The measurements from MDA-MB-468 and MDA-MB-231 cells showed 20% and 11% ($p < 0.1$) decreases in their average elastic moduli (Figure 7.2.a) and 22% and 19% ($p < 0.05$) decreases in their average apparent viscosities (Figure 7.2.b) between the initial and final pulse, respectively, These data indicate that the metastatic cells lose their resistance and become softer after being subjected to multiple stress pulses. The variation of biomechanical responses of MDA-MB-468 and MDA-MB-231 cells remain almost unchanged in $E_{elastic}$ responses and suppress in $\mu_{viscosity}$ values by 11% and 17% decreases in the SDs, respectively. These results indicated the metastatic cells behave slightly more homogeneously as they become softer in response to the pulsed stresses.

**Table 7-1 Summary of the measured biomechanical properties of breast cell lines under pulsed stresses.**

| Mean ± SD | **Cell Type** | **$E_1$** | **$E_2$** | **$E_3$** | **$E_4$** | **$E_5$** | **$E_6$** |
|---|---|---|---|---|---|---|---|
| **Elasticity (Pa)** | ***MCF10A*** | 296.7 ± 186.4 | 325.9 ± 208.1 | 345.8 ± 209.2 | 357.8 ± 227.2 | 387.0 ± 224.0 | 397.1 ± 234.1 |
| | ***184A1*** | 226.5 ± 87.2 | 240.3 ± 94.6 | 250.2 ± 97.7 | 257.2 ± 102.4 | 263.4 ± 103.4 | 274.1 ± 107.5 |
| | ***MDA-MB-468*** | 140.6 ± 54.3 | 124.6 ± 54.6 | 122.0 ± 57.5 | 121. ± 61.9 | 118.4 ± 56.0 | 112.3 ± 53.2 |
| | ***MDA-MB-231*** | 132.1 ± 80.8 | 123.0 ± 84.5 | 121.8 ± 85.9 | 121.8 ± 85.9 | 119.8 ± 88.4 | 117.4 ± 86.6 |
| Mean ± SD | **Cell Type** | **$\mu_1$** | **$\mu_2$** | **$\mu_3$** | **$\mu_4$** | **$\mu_5$** | **$\mu_6$** |
| **Viscosity (Pa.s)** | ***MCF10A*** | 784.7 ± 322.1 | 833.3 ± 352.1 | 866.4 ± 374.0 | 911.2 ± 386.3 | 932.4 ± 419.5 | 986.6 ± 414.8 |
| | ***184A1*** | 713.6 ± 240.6 | 753.1 ± 250.3 | 772.1 ± 266.7 | 782.0 ± 262.4 | 800.9 ± 274.1 | 830.9 ± 275.8 |
| | ***MDA-MB-468*** | 434.5 ± 161.9 | 391.8 ± 160.6 | 376.9 ± 157.2 | 361.6 ± 154.3 | 346.6 ± 144.7 | 337.0 ± 142.9 |
| | ***MDA-MB-231*** | 365.2 ± 170.3 | 329.6 ± 167.3 | 315.9 ± 157.9 | 315.9 ± 157.9 | 312.4 ± 156.3 | 298.2 ± 140.5 |

### 7.3.2 $RPC_E$ and $RPC_\mu$ under pulsed stress

The relative percentage change of elastic modulus ($RPC_E$) and apparent viscosity ($RPC_\mu$) of individual cells between each two successive pulses for the four cell types are calculated and the average values are depicted in Figure 7.3.a and 7.3.b, respectively. The average values of $RPC_E$ and $RPC_\mu$ for both non-metastatic cell lines were positive at each successive stress pulses, confirming that non-metastatic cells exhibit a continuous stiffening response. However, comparing the average values of $RPC_E$ and $RPC_\mu$ for the both non-metastatic cells reveals appreciably decreasing trends from $RPC_{E1\text{-}2}$ to $RPC_{E5\text{-}6}$ and from $RPC_{\mu 1\text{-}2}$ to $RPC_{\mu 5\text{-}6}$. Most importantly, it implies that the stiffening seen in the non-metastatic cells might not have a constant rate and eventually slow down under pulsed stress.

We next examined the $RPC_E$ and $RPC_\mu$ values of the individual non-metastatic cells; no non-metastatic cell was found to show negative numbers in all of their $RPC_E$ or $RPC_\mu$, and therefore all non-metastatic cells exhibited some degree of stiffening in response to the pulsed stress-relaxation paradigm. 59% and 28% of MCF10A and 184A1 cells showed positive values for both $RPC_E$ and $RPC_\mu$ parameters, respectively. These cells can be labeled with some confidence as a sub-population of non-metastatic cells with persistent elastic and viscoelastic stiffening responses. There also exist subpopulations, 68% and 37% of MCF10A and 184A1 cells, respectively, that have positive values for all of their $RPC_E$ and 77% and 53% which have positive values for all of their $RPC_\mu$, respectively.

The average $RPC_E$ and $RPC_\mu$ values for the metastatic cell lines (Figure 7.3) are all negative. It is remarkable that the magnitude of the average $RPC_E$ and $RPC_\mu$ in metastatic cells largely decline immediately after the initial decrease from $RPC_{E1\text{-}2}$ to $RPC_{E2\text{-}3}$ and from $RPC_{\mu 1\text{-}2}$ to $RPC_{\mu 2\text{-}3}$, suggesting that the metastatic cell softening occurs quickly in one primary transition which is less sensitive to subsequent stress pulses.

At the individual cell level, no MDA-MB-468 or MDA-MB-231 cell shows persistent positive values in all of their $RPC_E$ or $RPC_\mu$ illustrating that populations of metastatic cells can begin to be defined by a softening trend in their biomechanical state in response to pulsed stress. 47% and 39% of MDA-MB-468 and MDA-MB-231 cells, respectively, have negative values for all of their $RPC_E$. 50% and 46% of them have

negative values for all of their $RPC_{\mu}$, respectively. There is also a subpopulation of 25% of MDA-MB-468 and 34% of MDA-MB-231 cells that exhibit a persistent elastic and viscoelastic softening as measured by negative values for all $RPC_E$ and all $RPC_{\mu}$.

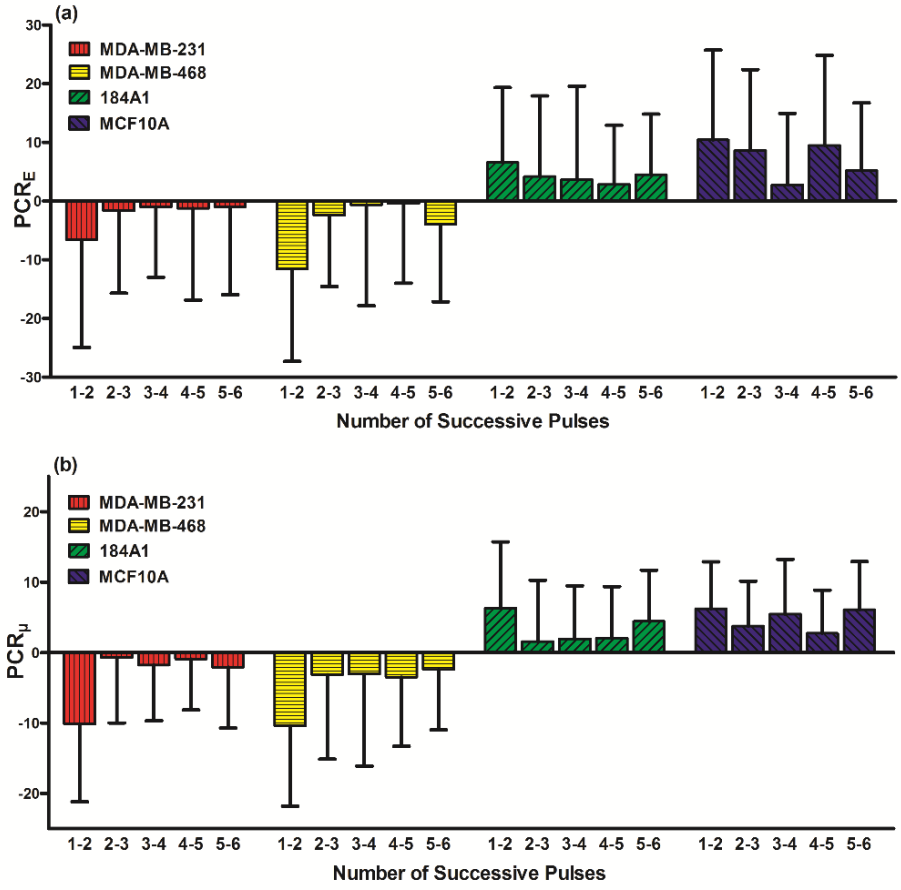


**Figure 7.3 Depiction of changes in calculated (a) the PCR of elastic modulus and (b) the PCR of apparent viscosity of breast cell lines under pulsed stresses.**

### 7.3.3 Population level metastatic phenotyping using standard single stress-relaxation method

#### $E_1$ and $\mu_1$ corresponding to initial stress pulse

The biomechanical properties of individual cells obtained under a single stress-relaxation tests typically used as a biomarker, even though capable of showing difference at population level, does not predict malignancy or normalcy at single-cell levels. Figure 7.4 shows a scatter plot of every individual cell's elastic moduli versus apparent viscosities

corresponding to the initial pulse ($E_1$, $\mu_1$), equivalent to the cell biomechanical measurements under a single stress-relaxation test. The distributions of the cells of the two non-metastatic cell lines with those of the two metastatic cell lines in this figure show that the metastatic cells tend to be concentrated towards smaller $E_1$ and $\mu_1$ values compared to the non-metastatic cells. It implies that the metastatic cells are, on average, more deformable and softer and mechanically more homogeneous in comparison to the non-metastatic cells. The biomechanical measurements for the initial stress pulse in Table 7.1 show that the average elastic moduli and apparent viscosities of the non-metastatic populations are significantly larger ($p < 0.0001$) than those of the metastatic populations. The results are similar to that of a previous AFM study which reported the same reductions in the calculated stiffness of MCF10A > MDA-MB-468 > MDA-MB-231 [34].

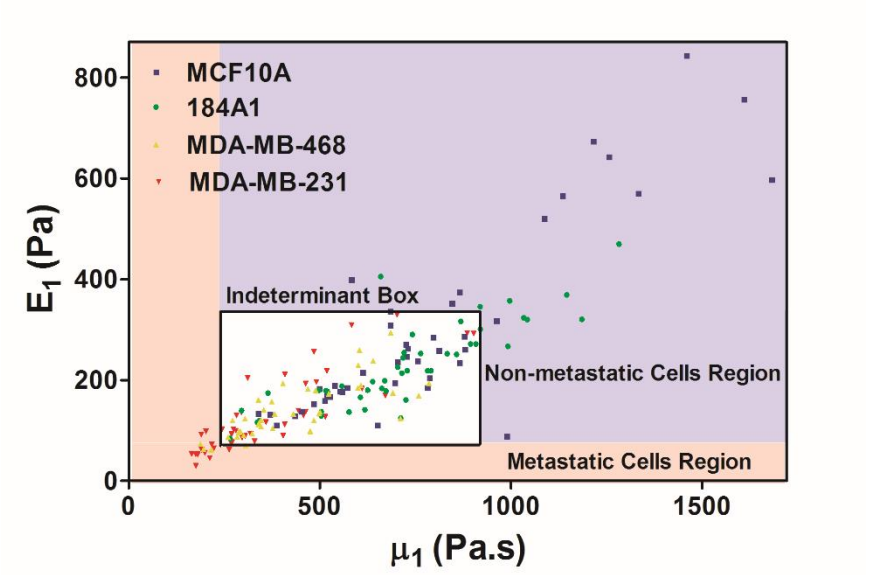


**Figure 7.4 Scatter plots of initial elastic moduli ($E_1$) vs. initial apparent viscosities ($\mu_1$) corresponding to the initial stress pulse.**

The decreases in the cell elasticity and viscosity accompanying cancer progression is correlated to the changes in the cell cytoskeletal organization, and F-actin disruption, shown to be a dominant cytoskeleton component regulating cell elasticity and viscosity, causes cells to become softer and less viscous [17]. As shown in Figure 7.5, the confocal images of the cells suggest that there is a difference in both the density and the organization of actin stress fibers. The non-metastatic cells have more stretched and denser actin

architecture while the metastatic cells demonstrate a more progressive dysregulation of the actin cytoskeleton.

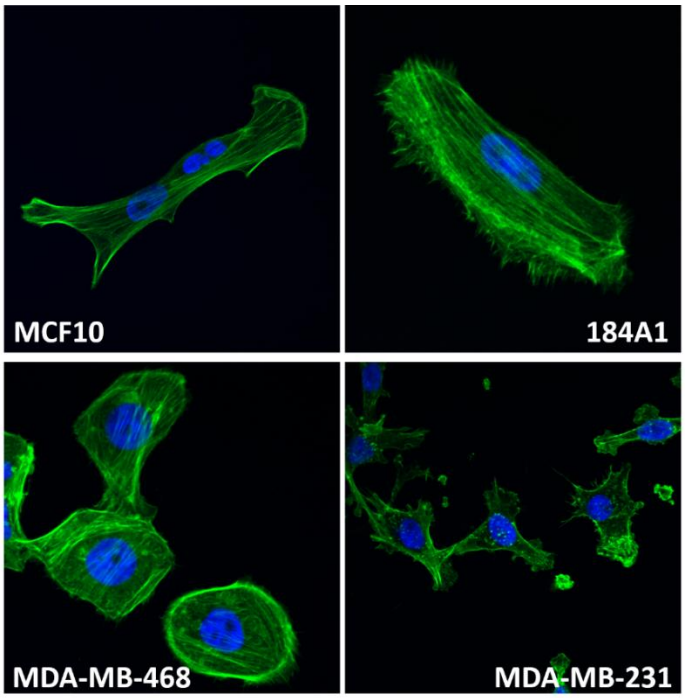


**Figure 7.5 Immunofluorescence images of F-actin in non-metastatic 184A1 and MCF10A and metastatic MDA-MB-468 and MDA-MB-231 cells grown on collagen-coated substrates.**

Figure 7.4 clearly illustrates the limitation of elastic modulus and apparent viscosity measurements from a single stress for single-cell level identification because there is a significant overlapped area in the measured elastic modulus and apparent viscosity between the non-metastatic and metastatic cells. 93% of the non-metastatic cells (86% of MCF10A and 100% of 184A1) and 86% of the metastatic cells (93% of MDA-468, and 77% of MDA-231) present within an overlapped range of $E_1$, 80-380 Pa. Furthermore, 89% of the non-metastatic cells (81% of MCF10A and 95% of 184A1) and 78% of the metastatic cells (80% of MD-468 and 77% of MDA-231) fall within an overlapped range of $\mu_1$, 260-800 Pa.s. If a combination of both elastic and viscoelastic parameters is considered, still 75% of the non-metastatic cells (70% of MCF10A and 80% of 184A1) and 80% of the metastatic cells (90% of MDA-468 and 72% of MDA-231) are within an overlapped elasticity and viscosity range. In other words, 78% of all tested cells are located in a region of "indeterminant" status designated by the box drawn in Figure 7.4. We conclude that cell biomechanics ($E_1$, $\mu_1$) measured under a single stress pulse provides a

low confidence level of 22% for differentiating between non-metastatic and metastatic cells at the single-cell level.

### 7.3.4 Single-cell-level metastatic phenotyping using pulsed stress-relaxation paradigm

#### $E_n$ and $\mu_n$ corresponding to final stress pulse

We showed (Figure 7.2), under pulsed stress, the difference in the measured elastic moduli and apparent viscosities between non-metastatic and metastatic cells becomes more significant after 6 stress relaxation pulses because non-metastatic and metastatic cells have stiffening and softening responses, respectively. Figure 7.6 shows a scatter plot of every individual cell's elastic moduli versus apparent viscosities corresponding to the final ($6^{th}$) pulse ($E_6$, $\mu_6$). As illustrated in Figure 7.6, at the single-cell level, 27% of the non-metastatic cells (29% of MCF10A and 26% of 184A1) and 37% of the metastatic cells (40% of MDA-468 and 35% of MDA-231) are present within an overlapped box. Therefore, the percentages of all non-metastatic and metastatic cells falling inside this "indeterminant" box has reduced to 32%, compared to 78% in the $E_1$ vs. $\mu_1$ plot (Figure 7.4). Consequently, the confidence level to label each cell as non-metastatic and metastatic has been increased to 68% based on ($E_6$, $\mu_6$) plot. Thus, after applying our AFM pulsed stress-relaxation protocol, the confidence level for single-cell level metastatic phenotyping and identification is significantly improved.

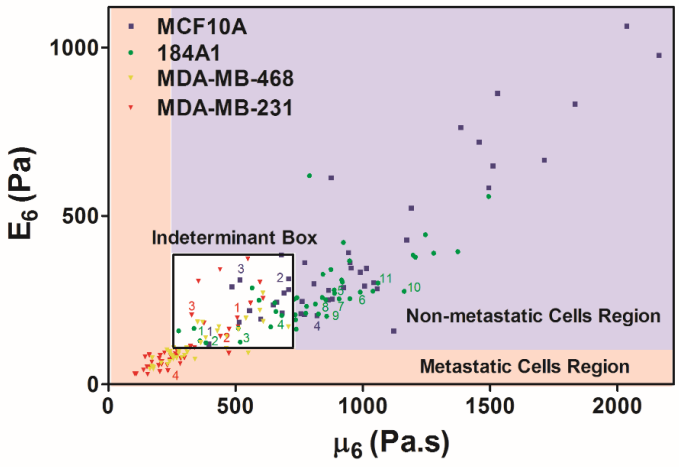


**Figure 7.6 Scatter plots of final elastic moduli ($E_6$) vs. final apparent viscosities ($\mu_6$) corresponding to the last stress-relaxation pulse.**

## $\alpha_E$ and $\alpha_\mu$ under pulsed stress

Our earlier observation that non-metastatic and metastatic cells showed overall opposite trends in adjusting their biomechanical properties under pulsed stress-relaxation paradigm (Figure 7.2) suggested that the incorporation of a rate of change of the cell biomechanical parameters rather than their absolute values might even be a more effective marker to label single cells and reduce the number of cells falling within the "indeterminant" region. The rate of change of the elastic modulus ($\alpha_E$) and apparent viscosity ($\alpha_\mu$) are defined and derived for individual cells and the average values for the four cell lines are shown in Figure 7.7. The averages of both $\alpha_E$ and $\alpha_\mu$ are positive for the non-metastatic cells which substantiate the stiffening trend in both $E_{elastic}$ and $\mu_{viscosity}$ for the non-metastatic cells, and the average of both $\alpha_E$ and $\alpha_\mu$ are negative for the metastatic cells, again showing the biomechanical softening for the metastatic cells.

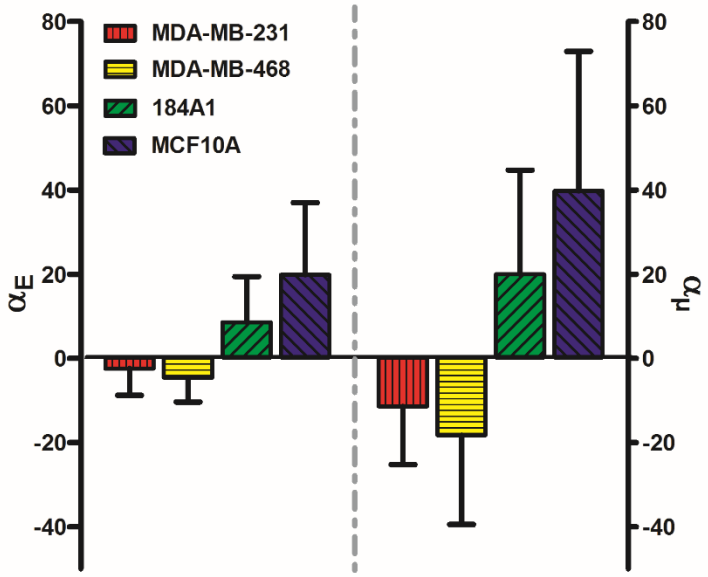


**Figure 7.7 Column graphs of the calculated $\alpha_E$ and $\alpha_\mu$ for the breast cell lines under pulsed stresses.**

The scatter plots of the two parameters ($\alpha_E$, $\alpha_\mu$) calculated for the individual tested cells are depicted separately for each cell line population in Figure 7.8. Now, 90% of MCF10A cells and 75% of 184A1 cells (Figure 7.8.a) show positive values for both $\alpha_E$ and $\alpha_\mu$. Furthermore, 100% of MDA-MB-468 cells and 90% of MDA-MB-231 cells (Figure 7.8.b) have negative values for either $\alpha_E$ or $\alpha_\mu$. These data show that a more powerful

biomechanical descriptor of a non-metastatic breast cell is one having positive values for both $\alpha_E$ and $\alpha_\mu$, and for a metastatic cell is one having at least one negative value for either $\alpha_E$ or $\alpha_\mu$.

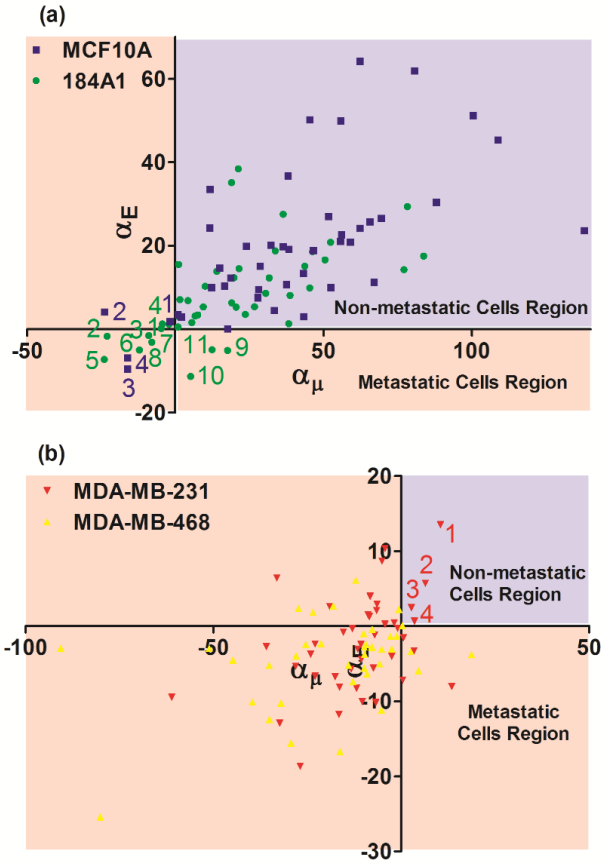


**Figure 7.8 Scatter plots of elastic modulus rate of change ($\alpha_E$) vs. apparent viscosity rate of change ($\alpha_\mu$) under pulsed stresses for (a) the non-metastatic and (b) the metastatic cells propose a new biomarker for single-cell level metastatic phenotyping.**

Using these definitions, 83.2% of the non-metastatic cells and 95.2% of the metastatic cells, and overall, 89% of all cells tested are accurately classified as non-metastatic or metastatic. In fact, most cells that fell within the indeterminant region (in Figure 7.4 and Figure 7.6) can now be correctly identified based on these criteria. The few outlier cells from each population which have not met the defined criteria are numbered in Figure 7.8.a and Figure 7.8.b and correspondingly in Figure 7.6. Clearly, in Figure 7.6 with the exception of 3 MCF10A, 4 184A1, and 3 MDA-MB-231 cells, none of those numbered cells are within the indeterminant box and therefore, can be identified as a non-metastatic or metastatic cell using their elastic modulus and apparent viscosity measurements

corresponding to the last pulse ($E_6$, $\mu_6$). The key to this method is the collective use of single-cell biomechanical data obtained in 6 successive stress pulses. By using 1) the sign of $\alpha_E$ and $\alpha_\mu$ and 2) the absolute values of $E_6$ vs. $\mu_6$, we define a new "dynamic stress" bio-signature with a very high confidence level of 94.2% for distinguishing between non-metastatic and metastatic single cells.

### 7.3.5 Confidence level for single-cell level metastatic phenotyping

The results in Table 7.2 summarize how the confidence level to differentiate single cells as non-metastatic or metastatic rises from 22% achieved using the standard single stress-relaxation method ($E_1$, $\mu_1$) to 94.2% achieved using the proposed pulsed stress-relaxation paradigm ($\alpha_E$, $\alpha_\mu$ & $E_n$,$\mu_n$). In pulsed stress-relaxation paradigm, the confidence level of single cell phenotyping for the non-metastatic cells is based on the definition as those located in quadrant I of $\alpha_E$ vs. $\alpha_\mu$ plot (i.e. showing positive values for their both $\alpha_E$ and $\alpha_\mu$) or those located in the non-metastatic cells region in $E_n$ vs. $\mu_n$ plot. Metastatic cells are defined as those located in quadrants II, III, and IV of $\alpha_E$ vs. $\alpha_\mu$ plot (i.e. showing at least one negative value for either $\alpha_E$ or $\alpha_\mu$) or those located in the metastatic cells region in $E_n$ vs. $\mu_n$ plot. The confidence level of single cell phenotyping increased as the number of stress pulses increased. It is probable that the biomechanical properties better diverge between two cell types and/or the cells get more opportunities to express their inherent biomechanical properties with increasing numbers of stress pulse events.

**Table 7-2 Confidence level for phenotyping single non-metastatic and metastatic cells increases with the number of stress pulses.**

| Number of Stress Pulses | | 1 | 2 | 3 | 4 | 5 | 6 |
|---|---|---|---|---|---|---|---|
| **Criteria** | **Confidence level of single cells phenotyping** | | | | | | |
| | Metastatic cells | 20% | | | | | |
| $(E_1 , \mu_1)$ | Non-metastatic cells | 25% | - | - | - | - | - |
| | Total cells | 22% | | | | | |
| $(\alpha_E , \alpha_\mu)$ | Metastatic cells | | 95.2% | 95.2% | 95.2% | 95.2% | 96.4% |
| & | Non-metastatic cells | - | 79.8% | 85.4% | 86.6% | 88.8% | 92.2% |
| $(E_n , \mu_n)$ | Total cells | | 87.2% | 90.1% | 91.3% | 91.9% | 94.2% |

## 7.4 Discussion

Most of the recent literature uniformly emphasizes stiffening of non-metastatic/normal cells in response to dynamic stress/strain. For example, normal monkey kidney cells were demonstrated to become less susceptible to deformation when they are exposed to oscillatory force [35]. In addition, by imposing oscillations on mechanically pre-stressed 3T3 fibroblasts, the cells developed a stress stiffening [36]. In this study, cytoskeleton perturbation with the actin depolymerization inducer (latrunculin A; 1 mg/ml) or the myosin heavy chain ATPase inhibitor (2,3-butanedione monoxime (BDM); 2 mg/ml) abolished the stiffening regime, while no appreciable effect was seen with the microtubule disruptor (nocodazol; 10 mg/ml). Another study showed rapid stretch of adherent endothelial cells resulted in a quick increase in actin lattice stiffness and thus, cell stiffening [37]. In a recent study by Cartagena and Raman [38], the viscoelastic properties of live fibroblast cells *in vitro* were measured using both dynamic and quasi-static AFM, and these investigators found that the dynamically measured viscosity is larger than that of the statically measured one, showing a frequency-dependence of viscoelastic properties. Importantly, the difference between the dynamic to static measured viscosities increased when the AFM tip indents the cell deeply into the nuclear region, justifying our chosen deep indentation depth in this study. Using a reconstructed cytoskeletal network of biopolymers *in-vitro*, cross-linked actin filaments are found as the main cytoskeletal component responsible for the stress/strain stiffening [39-41].

Multiple cell types are constantly exposed to a time-dependent interstitial fluid flow in their specific physiological environment, resulting in shear stress on the individual cell structure [42]. Shear flow model experiments have revealed that mouse fibroblasts show increased rigidity in response to periodic environmental shear stress through increased actin cytoskeletal reorganization and Rho kinase activation [43]. Bio-microrheology studies conducted by Kole et al. [44] have also shown that mouse fibroblasts exhibit increased viscosity along with rigidity upon activation of Rho-associated protein kinase which are known to regulator and induce stress fibers in the cell structural body [45-47]. Moreover, Sander et al. exposed mouse fibroblasts to LPA, a Rho-kinase activator, and found that cell elasticity doubled as a result of this treatment [48]. As a note, in our current study, implementing the stationary stress phase in the AFM pulsed stress-relaxation

paradigm possibly generate shearing forces on the entire adherent cytoskeleton of cells. By following the above findings, it can be inferred that the normal cells exhibited increased viscosity and rigidity in response to the applied force stimulation.

Application of a pulsed force regimen composed of consecutive force pulses with relaxation intervals same as the paradigm used in this study, on normal endothelial cells using magnetic bead rheology conducted by Matthews et al. [49]. The results revealed a significant pulse-to-pulse attenuation in bead displacement, indicating cell strengthening response. For short force pulses (3 sec), this stress-induced stiffening response was suppressed by dissipating cytoskeletal pre-stress with either inhibitors of myosin-dependent contractility (BDM; 10 mM) or Rho-associated kinase (Y27632; 20 μM). In addition, the stiffening response was abolished when the cells were chilled to 4°C which slows down the cell biochemical remodeling. However, a robust stiffening response that occurred after the application of a prolonged force (>15 sec) was unaffected by pharmacological inhibition of cytoskeletal tension generation by Rho (Y27632; 20 μM), Src tyrosine kinase known to interface focal adhesion formation (4-amino-5-(4-chloro-phenyl)-7-(t-butyl)pyrazolo[3,4-d]pyrimidine (PP2); 25 μM), or by blocking mechano-sensitive ion channel activity (Gadolinium chloride; 25 μM). This cell stiffening to a prolonged stress remained sensitive to a reduction in temperature. Conclusively, cells use multiple mechanisms to sense and respond to static and dynamic mechanical microenvironment changes [49].

Microfluidic assay is a high-throughput technique recently utilized to characterize the cell deformability [50-53]. Most importantly, a recent study on metastatic cells using microfluidic technique has shown that subsequent deformations of metastatic breast cells through sequential narrow constrictions with short recovery intervals which resembles the pulsed nano-mechanical stress experienced by the cells in the metastasis process has been associated with a decrease in the measured transit times [54, 55]. By considering this fact that the transit times are directly correlated to the cell deformability and stiffness, the observations suggest metastatic cell softening under the pulsed deformations. Conclusively, during the metastasis process, metastatic cells lose their resistant against deformation which makes the subsequent invasion events even easier.

There is reason to suspect that application of mechanical force to metastatic breast cancer cells same as non-metastatic cells might promote some actin organization and increase cell stiffness, but our observations indicate that in fact, the metastatic cells soften. We suggest that the metastatic phenotype, we observed with the pulsed stresses paradigm might be related to the altered expression of intermediate filaments (IF) typical of breast cancer cells that have undergone the epithelial-mesenchymal transition (EMT). Here, as an example we focus on vimentin, the principal IF of mesenchymal cells [56, 57], because many investigations identify vimentin as a marker of poor prognosis and metastatic disease [56, 58]. IF are bundled into fibers by IF-associated proteins within the cytoplasm to form networks that interact with both the actin cytoskeleton and microtubules [56]. IF bundling form stiff structures that according to the tensegrity model, play a major role in establishing cellular pre-stress that in turn, can modulate how rapidly a cell responds to an applied force [59]. Furthermore, as reported in the Jamney laboratory *in vitro*, vimentin polymerization has the ability to weaken the actin cytoskeleton by causing breakage of F-actin fibers [60]. Perhaps in metastatic breast cells, the presence of cytoplasmic networks of the IF vimentin, influences the biomechanical properties in ways that cannot occur in non-metastatic breast epithelial cells or in cells that have not undergone the EMT. For these reasons, the IF structure rather than the actin cytoskeleton might underlie the differential response to the pulsed stresses that enables the biomechanical discrimination between non-metastatic and metastatic cells.

## *7.5 Conclusion*

The current study describes the biomechanical response of breast epithelial cells in a pulsed nanomechanical indentations. In a pulsed stress-relaxation paradigm where AFM is used to deliver repetitive deformations to the cell structure, non-metastatic cells showed an enhancement in resistance against pulsed stress. In contrast, the malignant cells did not resist the stresses, and responded specifically to an initial deformation to become slightly softer and more fluidic. Analysis of this differential biomechanical response, led to the development of a new algorithm based upon the biomechanical descriptors for biosensing single cells as non-metastatic or metastatic with a high confidence level of ~95%. This algorithm represents a breakthrough in single-cell level phenotype identification using

biomechanical stimulation. The biomechanical principles identified here have a potential clinical significance and are applicable to refinements in high-throughput circulating tumor cell detection and in discovery of novel therapeutic strategies to reduce metastatic potential by not only reversing the decreased viscosity and stiffness of metastatic cells, but also restoring the ability of metastatic cells to stiffen upon sequential stress.

## *References*


[1] H. Babahosseini, S.S. Strobl, and M. Agah, "Single cell metastatic phenotyping using pulsed nanomechanical indentations," *Nanotechnology*, vol. 26, p. 354004, 2015.

[2] H. D. Huang, R. D. Kamm, and R. T. Lee, "Cell mechanics and mechanotransduction: pathways, probes, and physiology," *Am. J. Physiol. Cell Physiol.*, vol. 287, pp. C1-11, 2004.

[3] M. Nikkhah, J. Strobl, B. Peddi, and M. Agah, "Cytoskeletal Role in Differential Adhesion Patterns of Normal Fibroblasts and Breast Cancer Cells inside Silicon Microenvironments," *Biomedical Microdevices*, vol. 11, pp. 585-595, 2009.

[4] D. Yamazaki, S. Kurisu, and T. Takenawa, "Regulation of cancer cell motility through actin reorganization," *Cancer Sci.*, vol. 96, pp. 379-386, 2005.

[5] R. A. Desai, L. Gao, S. Raghavan, Liu W.F., and Chen C.S., "Cell polarity triggered by cell-cell adhesion via Ecadherin," *J. Cell Sci.*, vol. 122, pp. 905-911, 2009.

[6] D. E. Ingber, "Tensegrity II. How structural networks influence cellular information processing networks," *Journal of Cell Science*, vol. 116, pp. 1397-1408, 2003.

[7] S. Suresh, "Biomechanics and biophysics of cancer cells," *Acta Biomaterialia*, vol. 3, pp. 413-438, 2007.

[8] J. B. Wyckoff, J. G. Jones, J. S. Condeelis, and J. E. Segall, "A critical step in metastasis: in vivo analysis of intravasation at the primary tumor," *Cancer Res.*, vol. 60, pp. 2504-11, 2000.

[9] A. L. Creekmore, W. T. Silkworth, D. Cimini, R. V. Jensen, P. C. Roberts, and E. M. Schmelz, "Changes in gene expression and cellular architecture in an ovarian cancer progression model. ," *PLoS ONE*, vol. 6, p. e17676, 2011.

[10] H. Babahosseini, P. C. Roberts, E. M. Schmelz, and M. Agah, "Bioactive sphingolipid metabolites modulate ovarian cancer cell structural mechanics," *Integrative Biology*, vol. 5, pp. 1385-1392, 2013.

[11] H. Babahosseini, A. N. Ketene, E. M. Schmelz, P. C. Roberts, and M. Agah, "Biomechanical Profile of Cancer Stem-Like/Tumor-Initiating Cells Derived from a Progressive Ovarian Cancer Model," *Nanomedicine: Nanotechnology, Biology and Medicine,* vol. 10, pp. 1013-9, 2014.

[12] B. Carmichael, H. Babahosseini, N. Mahmoodi, and M. Agah, "The fractional viscoelastic response of human breast tissue cells," *Physical Biology,* vol. 12, p. 046001, 2015.

[13] H. Babahosseini, B. Carmichael, J. Strobl, N. Mahmoodi, and M. Agah, "Sub-cellular force microscopy in single normal and cancer cells," *Biochem Biophys Res Commun.,* vol. 15, pp. 30022-X, 2015.

[14] E. C. Faria, N. Ma, E. Gazi, P. Gardner, M. Brown, N. W. Clarke, *et al.*, "Measurement of elastic properties of prostate cancer cells using AFM," *Analyst,* vol. **133**, pp. 1498-1500, 2008.

[15] Q. S. Li, G. Y. H. Lee, C. N. Ong, and C. T. Lim, "AFM indentation study of breast cancer cells," *Biochem Biophys Res Commun.,* vol. 374, pp. 609-13, 2008.

[16] A. N. Ketene, E. M. Schmelz, P. C. Roberts, and M. Agah, "The effects of cancer progression on the viscoelasticity of ovarian cell cytoskeleton structures," *Nanomedicine : nanotechnology, biology, and medicine,* vol. **8**, pp. 93-102, 2011.

[17] A. N. Ketene, P. C. Roberts, A. A. Shea, E. M. Schmelz, and M. Agah, "Actin filaments play a primary role for structural integrity and viscoelastic response in cells," *Integrative Biology,* vol. 4, pp. 540-549, 2012.

[18] M. Lekka, "Atomic force microscopy: A tip for diagnosing cancer," *Nature Nanotechnology,* vol. 7, pp. 691-692, 2012.

[19] M. Plodinec, M. Loparic, C. A. Monnier, E. C. Obermann, R. Zanetti-Dallenbach, P. Oertle, *et al.*, "The nanomechanical signature of breast cancer," *Nature Nanotechnology,* vol. 7, pp. 757–765, 2012.

[20] S. E. Cross, Y. S. Jin, J. Rao, and J. K. Gimzewski, "Nanomechanical analysis of cells from cancer patients," *Nature Nanotechnology,* vol. 2, pp. 780-783, 2007.

[21] B. D. Hoffman, C. Grashoff, and M. A. Schwartz, "Dynamic molecular processes mediate cellular mechanotransduction," *Nature,* vol. 475, pp. 316-323, 2011.

[22] G. Bao and S. Suresh, "Cell and molecular mechanics of biological materials," *Journal of Nature Materials,* vol. 2, pp. 715-725, 2003.

[23] J. Alcaraz, L. Buscemi, M. Grabulosa, X. Trepat, B. Fabry, R. Farre, *et al.*, "Microrheology of human lung epithelial cells measured by atomic force microscopy," *Biophysical Journal,* vol. 84, pp. 2071-2079, 2003.

[24] B. Fabry, G. N. Maksym, J. P. Butler, M. Glogauer, D. Navajas, and J. J. Fredberg, "Scaling the microrheology of living cells," *Physical Review Letters*, vol. 87, p. 148102, 2001.

[25] B. Fabry, G. N. Maksym, J. P. Butler, M. Glogauer, D. Navajas, and J. J. Fredberg, "Scaling the microrheology of living cells," *Phys. Rev. Lett.*, vol. 87, p. 148102, 2001.

[26] P. J. Mack, M. R. Kaazempur-Mofrad, H. Karcher, R. T. Lee, and R. D. Kamm, "Force-induced focal adhesion translocation: effects of force amplitude and frequency," *Am. J. Physiol. Cell Physiol.*, vol. 287, pp. C954-C962, 2004.

[27] D. R. Overby, B. D. Matthews, E. Alsberg, and D. E. Ingber, "Novel dynamic rheological behavior of individual focal adhesions measured within single cells using electromagnetic pulling cytometry," *Acta Biomaterialia*, vol. 1, pp. 295-303, 2005.

[28] H. J. Hsu, C. F. Lee, and R. Kaunas, "A dynamic stochastic model of frequency-dependent stress fiber alignment induced by cyclic stretch," *PLoS ONE*, vol. 4, p. e4853, 2009.

[29] B. Liu, M. J. Qu, K. R. Qin, H. Li, Z. K. Li, B. R. Shen, *et al.*, "Role of cyclic strain frequency in regulating the alignment of vascular smooth muscle cells in vitro," *Biophys J.* , vol. 94, pp. 1497-1507, 2008.

[30] D. Icard-Arcizet, O. Cardoso, A. Richert, and S. He´non, "Cell Stiffening in Response to External Stress is Correlated to Actin Recruitment," *Biophysical Journal*, vol. 94, pp. 2906-2913, 2008.

[31] A. C. Society, "Global Cancer Facts & Figures 2nd edition," ed, 2008.

[32] E. M. Darling, S. Zauscher, J. A. Block, and F. Guilak, "A Thin-Layer Model for Viscoelastic, Stress-Relaxation Testing of Cells Using Atomic Force Microscopy: Do Cell Properties Reflect Metastatic Potential?," *Biophys. J.*, vol. 92, pp. 1784-91, 2007.

[33] E. M. Darling, S. Zauscher, and F. Guilak, "Viscoelastic properties of zonal articular chondrocytes measured by atomic force microscopy," *J Osteoarthritis and Cartilage*, vol. 14, pp. 571-579, 2006.

[34] A. Qureshi, "THE NOVEL FUNCTION OF sJAM-C IN PROMOTING CYTOSKELETON REARRANGEMENT AND MIGRATION IN MAMMARY EPITHELIAL CELLS," Master of Science The Charles E. Schmidt College of Medicine Florida Atlantic University Boca Raton, Florida, August 2012.

[35] C. A. J. Putman, K. O. Van der Werf, B. G. De Grooth, N. F. Van Hulst, and J. Greve, "Viscoelasticity of living cells allows high resolution imaging by tapping mode atomic force microscopy," *Biophysics Journal*, vol. 67, pp. 1749-53, 1994.

[36] P. Fernandez, P. A. Pullarkat, and A. Ott, "A Master Relation Defines the Nonlinear Viscoelasticity of Single Fibroblasts," *Biophysical Journal,* vol. 90, pp. 3796–3805, 2006.

[37] J. Pourati, A. Maniotis, D. Spiegel, J. L. Schaffer, J. P. Butler, J. J. Fredberg, *et al.*, "Is cytoskeletal tension a major determinant of cell deformability in adherent endothelial cells?," *Am J Physiol.* , vol. 274, pp. C1283-9, 1998.

[38] A. Cartagena and A. Raman, "Local Viscoelastic Properties of Live Cells Investigated Using Dynamic and Quasi-Static Atomic Force Microscopy Methods," *Biophysical Journal,* vol. 106, pp. 1033-1043, March 2014.

[39] M. L. Gardel, J. H. Shin, F. C. MacKintosh, L. Mahadevan, P. Matsudaira, and D. A. Weitz, "Elastic behavior of cross-linked and bundled actin networks. Science," *Science,* vol. 304, pp. 1301-5, 2004.

[40] C. Storm, J. J. Pastore, F. C. MacKintosh, T. C. Lubensky, and P. A. Janmey, "Nonlinear elasticity in biological gels," *Nature,* vol. 435, pp. 191-4, 2005.

[41] M. Gardel, F. Nakamura, J. Hartwig, J. Crocker, T. Stossel, and D. A. Weitz, "Stress-Dependent Elasticity of Composite Actin Networks as a Model for Cell Behavior," *Physical Review Letters,* vol. 96, pp. 12-15, 2006.

[42] W. J. Polacheck, R. Li, S. G. M. Uzela, and R. D. Kamm, "Microfluidic platforms for mechanobiology," *Lab Chip,* vol. 13, pp. 2252-2267, 2013.

[43] J. S. H. Lee, P. Panorchan, C. M. Hale, S. B. Khatau, T. P. Kole, Y. Tseng, *et al.*, "Ballistic intracellular nanorheology reveals ROCK-hard cytoplasmic stiffening response to fluid flow," *Journal of Cell Science,* vol. 119, pp. 1760-1768, 2006.

[44] T. P. Kole, Y. Tseng, L. Huang, J. L. Katz, and D. Wirtz, "Rho kinase regulates the intracellular micromechanical response of adherent cells to rho activation," *Journal of Molecular Biology of the Cell,* vol. 15, pp. 3475-3484, 2004.

[45] K. Riento and A. J. Ridley, "Rocks: multifunctional kinases in cell behaviours," *Nat Rev Mol Cell Biol,* vol. 4, pp. 446-456, 2003.

[46] T. Leung, X. Q. Chen, E. Manser, and L. Lim, "The p160 RhoA-binding kinase ROK alpha is a member of a kinase family and is involved in the reorganization of the cytoskeleton," *Journal of Molecular and Cellular Biology,* vol. 16, pp. 5313-5327, 1996.

[47] M. Maekawa, T. Ishizaki, S. Boku, N. Watanabe, A. Fujita, A. Iwamatsu, *et al.*, "Signaling from Rho to the actin cytoskeleton through protein kinases ROCK and LIM-kinase," *Journal of Science,* vol. 285, pp. 895-898, 1999.

[48] E. E. Sander, J. P. Ten Klooster, S. Van Delft, R. A. Van der krammen, and J. G. Collar, "Rac downregulates Rho activity: reciprocal balance between both

GTPases determines cellular morphology and migratory behavior," *Journal of Cell Biology,* vol. 147, pp. 1009-1022, 1999.

[49] B. D. Matthews, D. R. Overby, R. Mannix, and D. E. Ingber, "Cellular adaptation to mechanical stress: role of integrins, Rho, cytoskeletal tension and mechanosensitive ion channels," *J Cell Sci.,* vol. 119, pp. 508-518, 2006.

[50] H. T. K. Tse, D. R. Gossett, Y. S. Moon, M. Masaeli, M. Sohsman, Y. Ying, *et al.*, "Quantitative Diagnosis of Malignant Pleural Effusions by Single-Cell Mechanophenotyping," *Sci. Transl. Med.,* vol. 5, p. 212ra163 2013.

[51] W. Zhang, K. Kaid, D. S. Choi, T. Iwamoto, Y. H. Nguyen, H. Wong, *et al.*, "Microfluidics separation reveals the stem-cell–like deformability of tumor-initiating cells," *PNAS,* vol. 109, pp. 18707-12, 2012.

[52] D. R. Gossett, H. T. K. Tse, S. A. Lee, Y. Ying, A. G. Lindgren, O. O. Yang, *et al.*, "Hydrodynamic stretching of single cells for large population mechanical phenotyping," *PNAS,* vol. 109, pp. 7630–7635, 2012.

[53] Y. Zheng, J. Nguyen, Y. Wei, and Y. Sun, "Recent advances in microfluidic techniques for single-cell biophysical characterization," *Lab Chip.,* vol. 13, pp. 2464-83, 2013.

[54] M. Maka and D. Erickson, "A serial micropipette microfluidic device with applications to cancer cell repeated deformation studies," *Integr. Biol.,* vol. 5, pp. 1374-1384, 2013.

[55] M. Mak, C. A. Reinhart-King, and D. Erickson, "Elucidating mechanical transition effects of invading cancer cells with a subnucleus-scaled microfluidic serial dimensional modulation device," *Lab Chip,* vol. 13, pp. 340-348, 2013.

[56] A. Satelli and S. Li, "Vimentin in cancer and its potential as a molecular target for cancer therapy," *Cell Mol Life Sci.,* vol. 68, pp. 3033-46, 2011.

[57] C. D. May, N. Sphyris, K. W. Evans, S. J. Werden, W. Guo, and S. A. Mani, "Epithelial-mesenchymal transition and cancer stem cells. A dangerously dynamic duo in breast cancer progression," *Breast Cancer Research,* vol. 13, p. 202, 2011.

[58] P. Karihtala, P. Auvinen, S. Kauppila, K. M. Haapasaari, A. Jukkola-Vuorinen, and Y. Soini, "Vimentin, zeb1 and Sip1 are up-regulated in triple-negative and basal-like breast cancers: association with an aggressive tumour phenotype," *Breast Cancer Res Treat.,* vol. 138, pp. 81-90, 2013.

[59] N. Wang, J. D. Tytell, and D. E. Ingber, "Mechanotransduction at a distance: mechanically coupling the extracellular matrix with the nucleus," *Nature Reviews Molecular Cell Biology,* vol. 10, pp. 75-82, 2009.

[60] J. V. Shah, L. Z. Wang, P. Traub, and P. A. Janmey, "Interaction of vimentin with actin and phospholipids," *Biol Bull.*, vol. 194, pp. 402-5, 1998.

# 8 Single-Cell Cancer Identification using a Microfluidic Iterative Mechanical Characteristics (iMECH) Analyzer

*H. Babahosseini, V. Srinivasaraghavan, J. Strobl and M. Agah, " Single-Cell Cancer Identification using a Microfluidic Iterative Mechanical Characteristics (iMECH) Analyzer," Under review.*

## *8.1 Introduction*

Chemical and physical factors in concert direct cell growth, function and homeostasis, but also can cause or contribute to diseases such as cancer. The biophysical properties of cells are modulated in response to these cues and thereby linked to physiological and pathophysiological functions. To date, biophysical sensing has gained broad acceptance in cell biology as a highly sensitive, label-free, non-destructive method for determining the health state of cell without the use of fluorescent, magnetic, or other cell markers. The biomechanical properties of cancer cells are constantly changing during progression and metastases [1] as a consequence of altered expression of cytoskeleton genes and regulators of cytoskeletal organization, which impacts migration, adherence and invasion of cancer cells at distant sites. Thus, the ability to characterize the mechanical nature of a cell could provide novel insights into how cells receive and integrate regulatory signals from the surrounding environment which can impact disease progression diagnosis and cancer treatment.

There are currently different instruments and methods available for assessing cell biomechanical properties [2]. There have been a handful of reports highlighting the differences in biomechanical properties of normal and cancer cells [3]. The progression of cancer is associated with an alteration of the cell cytoskeleton [4] which in turn causes transformed cells to be softer and hence more deformable than their healthier counterparts to facilitate motility [5, 6]. Nevertheless, most endeavors in cell biomechanics have utilized "switch-like models of mechanotransduction" [7] in which cellular responses are analyzed under transient mechanical stimulus. These measurements even though are capable of showing differences in the biomechanical properties of normal and cancer at population-level, cannot predict malignancy or normalcy at single-cell level.

Accurate cell characterization involves their investigation in the most realistic environments, and researchers have made attempts to mimic the physiological microenvironments of cells where they undergo dynamic mechanical stimuli. Living cells are dynamic structure that respond to external environmental loads by converting them into biological process and adapting their cytoskeletal structure [8]. Different studies have reported different responses of normal and cancer cells to such dynamic stressors even under artificial dynamically changing microenvironment. Some recent studies in literature have reported stiffening of non-metastatic/normal cells in response to dynamic stress/strain. It has also been shown that normal cells "stiffen" during tapping motions by probing AFM cantilever and become less susceptible to deformation [9]. Another study also showed rapid stretch of adherent endothelial cells resulted in a quick increase in actin lattice stiffness and thus, cell stiffening [10]. Furthermore, a recent microfluidic study has shown a decrease in the measured transit times of invasive MDA-MB-231 breast cells under a repeated deformability through serial constriction channels which is associated with cell softening [11, 12]. Dynamic behaviors and reorganization of subcellular structural cytoskeleton components are the main cause of cell biomechanical alterations and the stiffening/softening behaviors under periodic stretch or compression [13-15].

Our group has recently produced solid evidence indicating that metastatic and non-metastatic single cells can respond differently to indentation forces applied to them via atomic force microscopy (AFM) in a periodic mode [16]. The non-metastatic MCF10A and 184A1 cells increased their resistance against deformation and came more stiffened while metastatic MDA-MB-231 and MDA-MB-468 cells became slightly softened when they went to the mechanical microenvironment changes. Unprecedentedly, for the first time, this distinct behavior of the non-metastatic and metastatic cells to the pulsed stresses paradigm was used in this work as a new signature for single-cell level metastatic diagnosis with a high confidence level of ~95%.

The development of single-cell level analyses in cancer diagnosis and treatment is a critical need in light of the knowledge that tumor masses are comprised of a heterogeneous mixture of cells [17]. Single-cell level analysis will contribute significantly to the evolution in precision medicine to bring individualized diagnostic and prognostic decisions to cancer patients [18, 19].

The development of microfluidic devices has been on the rise since its emerging in the beginning of the 1980s. Among its potential uses, prototypes for the biotechnology and biomedical applications have gained tremendous importance. Microfluidic-based analyzers for cell biophysical screening have emerged as a higher throughput and clinically more relevant approach to single-cell analysis [20-25] and promise potential speeds of 1-5 cells per sec compared to AFM [26, 27] which is characterized by an extremely low throughput (1 cell per 5-10min), high operation costs, and the need to skilled operators. Microfluidic constriction channels are typically utilized for quantifying mechanical properties of various types of cells including red blood cells, white blood cells, and tumor cells [28].

Our aim here is to transition principles gained by the AFM technique [16] into a suitable single-cell analysis platform on a high-throughput microfluidic chip. To this end, the microfluidic iterative mechanical characteristics (iMECH) analyzer has been developed and its ability to reveal unique information about the health status of single cells and their response to cytoskeletal modulating agents is demonstrated.

## *8.2 Materials and methods*

### 8.2.1 Sample preparation

The microfluidic biosensor iMECH analyzer's performance is evaluated by using four breast cancer cell lines including non-malignant 184A1 and non-metastatic MCF10A, representative of non-metastatic breast cell type, and moderately-metastatic MDA-MB-468 and highly-metastatic MDA-MB-231, representative of metastatic cell type. The standard culture medium for 184A1 cell growth was MEGM kit supplemented with 5 μg/ml transferrin (Sigma Aldrich, St. Louis, MO) and 1 ng/ml cholera toxin (Lonza, Basel, Switzerland); the gentamycin-amphotericin B was omitted. MCF10A cells were grown in F12:DMEM (Lonza, Basel, Switzerland) with penicillin-streptomycin (100 Units/ml), 2.5 mM L-glutamine, 20 ng/ml epidermal growth factor (EGF), 0.1 μg/ml cholera toxin (CT), 10 μg/ml insulin, 0.5 μg/ml hydrocortisone, and 5% horse serum. MDA-MB-468 cells were grown in L-15 supplemented with 10% fetal bovine serum (FBS), 4 mM glutamine and penicillin-streptomycin (100 Units/ml). Finally, MDA-MB-231 cells were grown in F12:DMEM with 10% FBS, 4 mM glutamine and penicillin-streptomycin (100 Units/ml).

The sensitivity of the iMECH signature to drug-induced changes in the cell cytoskeletal components (i.e. actin filaments and microtubules) which directly impacts the cell biomechanics is also assessed. To determine the contribution of actin filaments in iMECH signature, metastatic cells were treated with jasplankinolide (Jasp, 50 pM, 2 hr). Non-metastatic cells were treated with latrunculin A (LatA, 0.5 µM, 2 hr). To study the impact of tubulins on the iMECH signature, metastatic cells were treated with suberoylanilide hydroxamic acid (SAHA, 2.75 µM, 4 hr), and non-metastatic cells were treated with nocodazole (Noc, 0.5 µM, 4 hr). These compounds were used at non-cytotoxic times and concentrations known to provide the well-defined changes to the cell cytoskeleton determined from previous dose-dependent cytoskeleton studies [29]. The cells were suspended in culture medium at a concentration of $5x10^5$ cells/mL for delivery into the iMECH analyzer.

### 8.2.2 Microchip design and fabrication

A schematic of the iMECH setup and operation principles is shown in Figure 1. The iMECH analyzer consists of a multi-segmented test channel which mimics a dynamic stress paradigm and a U-shaped delivery channel (200µm-wide and 60 µm-deep). The test channel contains three deformation channels (6µm-wide, 12 µm-deep, 500 µm-long) separated by two relaxation regions (30 µm-wide, 30 µm-deep, 100 µm-long). The design of iMECH analyzer depicted schematically in Figure 2A. To deliver single cells to the test channel, a free flow of suspended cells in culture medium is established in the delivery channel by the height difference of medium in the reservoirs at the inlet/outlet ports. Single cells are trapped and pulled into the test channel by applying negative pressure ($\Delta P$=-150 Pa) via a syringe pump (Harvard apparatus, Holliston, MA) at another end of the test channel. A trapping mechanism adapted from literature [30] based on hydrodynamic resistance at the entrance of the test channel helps the single cell trapping. As cells pass through the test channel, they undergo a series of deformation and relaxation regions that alters the cell cytoskeletal architecture. The microchip collects information about the iterative biomechanical properties of single cells under a dynamically changing microenvironment resulting in the establishment of a more comprehensive mechanical biomarker translated in cell deformation modulatory iMECH signature. The velocity of the

cells in the deformation channels is measured as an indicator of cell biomechanical properties which provides information about cell cytoskeletal structure. The iMECH analyzer enables the analysis of 1 cells/sec without sacrificing the sensitivity of the system to discriminate between the behavior of metastatic and non-metastatic cells.

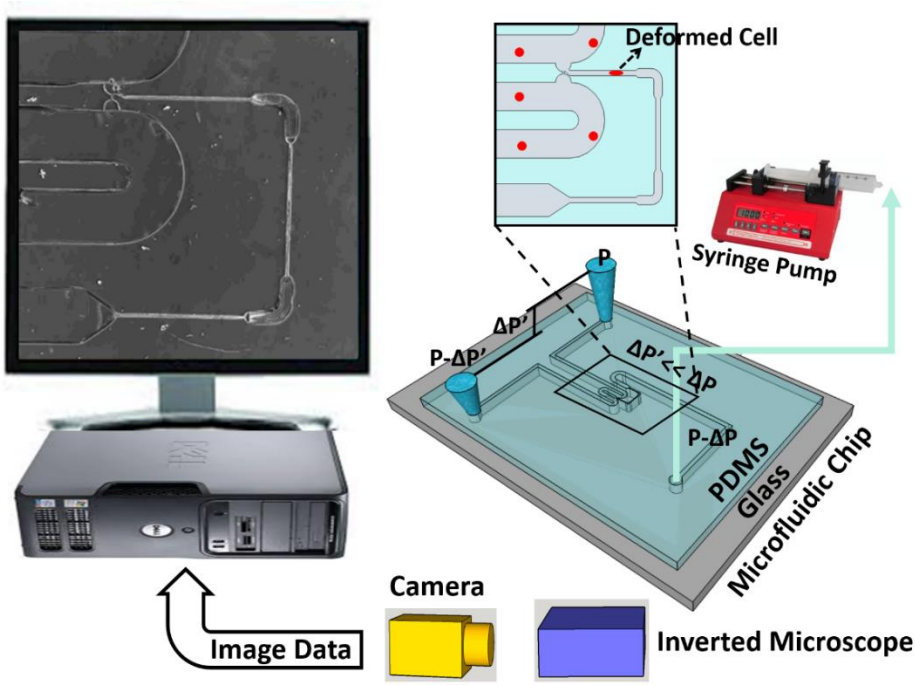


**Figure 8.1 Schematic image of setup and operation principle of the iMECH analyzer on a microfluidic chip. The device provides information about the iterative mechanical characteristics of single cells.**

The iMECH analyzer was fabricated in the clean room facility. A master wafer was initially fabricated using a two-step etching process to obtain the shallow constriction channel and the deep delivery channel. Briefly, a thin photoresist (Shipley 1827) was spun coated on a silicon wafer and patterned using photolithography. A shallow etch was done using deep reactive ion etching (DRIE, Bosch, Germany) for a depth of 12 μm. The photoresist was stripped before a second round of photolithography using a thicker photoresist (AZ9260) to fabricate the delivery channel. The wafer was etched for 20 min in the DRIE to obtain an overall depth of 30 μm. Finally, the photoresist was stripped and the wafer was cleaned before a layer of saline was evaporated on the wafer to enable easy peel-off of PDMS. PDMS prepolymer and curing agent were mixed at a ratio of 10:1, poured over the silicon master placed in an aluminum foil plate, degassed in a vacuum desiccators to remove air bubbles, and baked in a convection oven (15 min @ 125°C). The

device was allowed to cool, then peeled off from the master, diced and reservoir holes were punched through. At the end, the PDMS layer and a glass slide were concurrently treated with oxygen plasma in a plasma cleaner (Harrick Plasma, Plasma Cleaner) for 1 min and bonded together. The fabrication process of the iMECH analyzer is shown step by step in Figure 2B.

### 8.2.3 Data acquisition and analysis

For data acquisition, the device was mounted onto the Zeiss Axio Observer inverted microscope (Carl Zeiss, Jena, Germany). The video images of the cells passing through the test channel were recorded via Motion Xtra NX4-S3 high speed camera (IDT, Tallahassee, FL) with 5 GB of on chip memory and Motion Studio software at 500 frames per sec. To examine and validate the reproducibility and consistency of the results, at least three separate tests were conducted for each cell population with about 50 cells from each sample. Within the same cell population, there was no more than 5% variation between the average measured parameters of any two tests. *P*-values between the different populations were calculated using two independent samples t-tests ($\alpha = 0.05$). Results are presented as arithmetic mean ± standard error of the mean (SEM) using GraphPad Prism software.

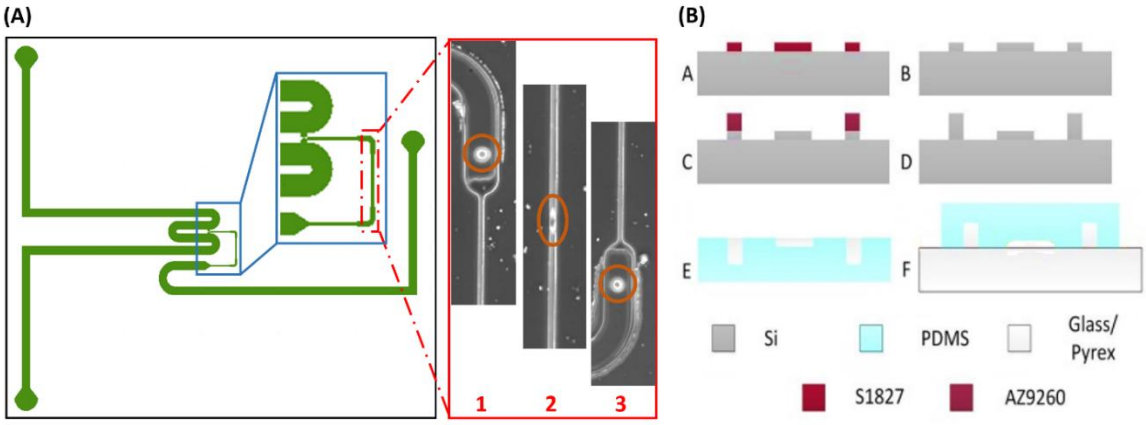


**Figure 8.2 A) Illustration design of the iMECH analyzer. B) Process flow of the iMECH analyzer fabrication.**

## *8.3 Results*

### 8.3.1 Cell mechanical characteristics in micro-channels

A cell movement in the deformation channel can be separated into two phases; phase I in which the cell moves with a non-constant velocity after undergoing a heavy deformation during entering into the narrow channel and phase II in which the cell velocity remains constant after reaching a steady state [31]. Figure 3A shows a schematic profile of location versus time for a cell in the deformation channel. The cell movement in the deformation channel is driven by a pressure gradient applied across two sides of the channel. The two-dimensional plot of the pressure gradient in the microfluidic channels is simulated in COMSOL Multiphysics and is shown in Figure 3B. Here it can be seen that the pressure gradient across the narrow deformation regions are equal. It implies that the cells are experiencing the same applied pulling pressure across each deformation channel. In addition, 4 µm beads passed through the test channel showed equal traveling times in all three deformation channels. It indicates that the deformation channels were fabricated with an identical size and cross section and the beads experience an equal pressure gradient across them.

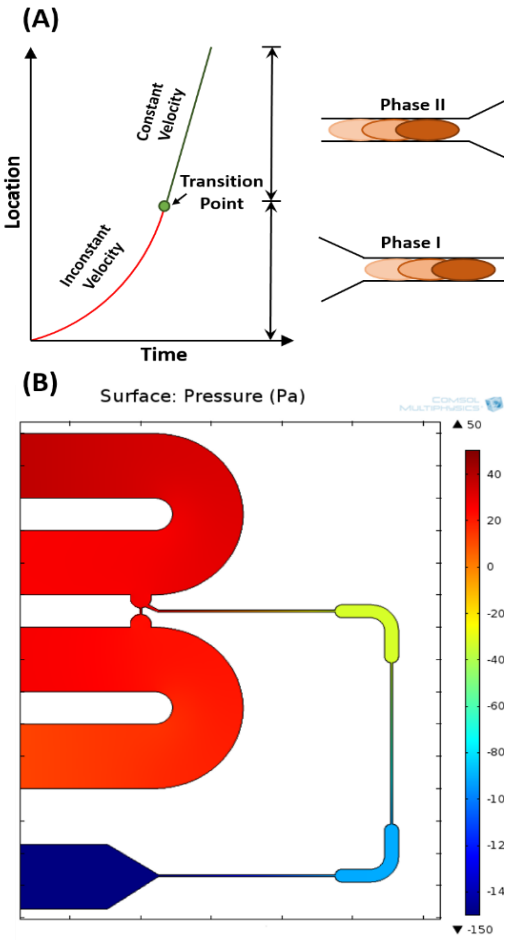


**Figure 8.3 A) The plot of the location versus time for a single cell traveling through a deformation channel. B) The plot of pressure gradient in the iterative microfluidic deformation channels.**

### 8.3.2 Cell iMECH signature:

Analysis of the images of cells as they traversed a deformation channel revealed that the transition point between phase I (non-constant velocity) and phase II (constant

velocity) always occurred in the first-half of the 500 µm deformation channels. For our analyses, we divided the deformation channels into two halves: the transient (phase I) and equilibrium (phase II) sections. The average transient and equilibrium velocity values of the iterative deformation channels for a typical non-metastatic and metastatic cell are depicted in Figure 4A and 4B, respectively. The average velocity of the cells subjected to iterative mechanical stresses by passing through the deformation channels revealed that the non-metastatic cells exhibit a velocity drop after each relaxation region once they enter to the next deformation channel (Figure 4A). The drop in the average velocity of the non-metastatic cells after recovery period might be due to the effect of stiffening in their biomechanical characteristics under iterative deformations. However, this trend is reversed in the metastatic cells after each relaxation region. The average velocity of the metastatic cells raises or stays constant right after entering to the next deformation channel (Figure 4B). It indicates that the metastatic cells exhibit on average a "softening" trend in their structure under iterative deformations.

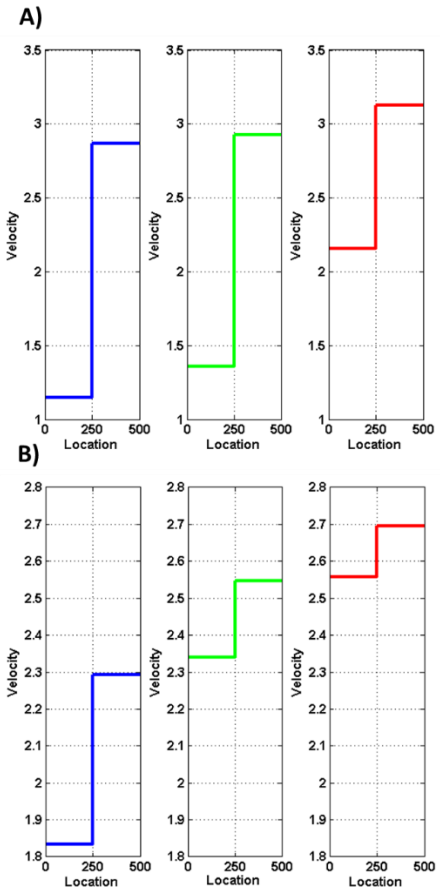


**Figure 8.4 The average transient and equilibrium velocity values in the iterative deformation channels for A) a typical non-metastatic (normal-like) (MCF10A) cell and B) metastatic cancer (MDA-MB-231) cell.**

The average transient and equilibrium velocity measurements ($u_{i,1}$ and $u_{i,2}$, respectively) of the deformation channels (i=1, 2, 3) for the selected breast cell type populations are presented in Figures 5. MDA-MB-231 and MDA-MB-468 metastatic cells showed 10% and 5% increases in their average velocity from $u_{12}$ to $u_{21}$ and 2% and 4% increases from $u_{22}$ to $u_{31}$, respectively. These data indicate that the metastatic cells lose their resistance and exhibited on average a "softening" trend in their biomechanical characteristics under iterative deformation stresses. In contrast, the average velocity of 184A1 and MCF10A cells decreased by ~12% and ~22% from $u_{12}$ to $u_{21}$ and ~6% and ~5%

from $u_{22}$ to $u_{31}$, respectively. Therefore, these non-metastatic cells responded by decrease in their equilibrium velocity in the next deformation channel after each given relaxation period. It indicates an increase in their mechanical resistance and a stiffening behavior.

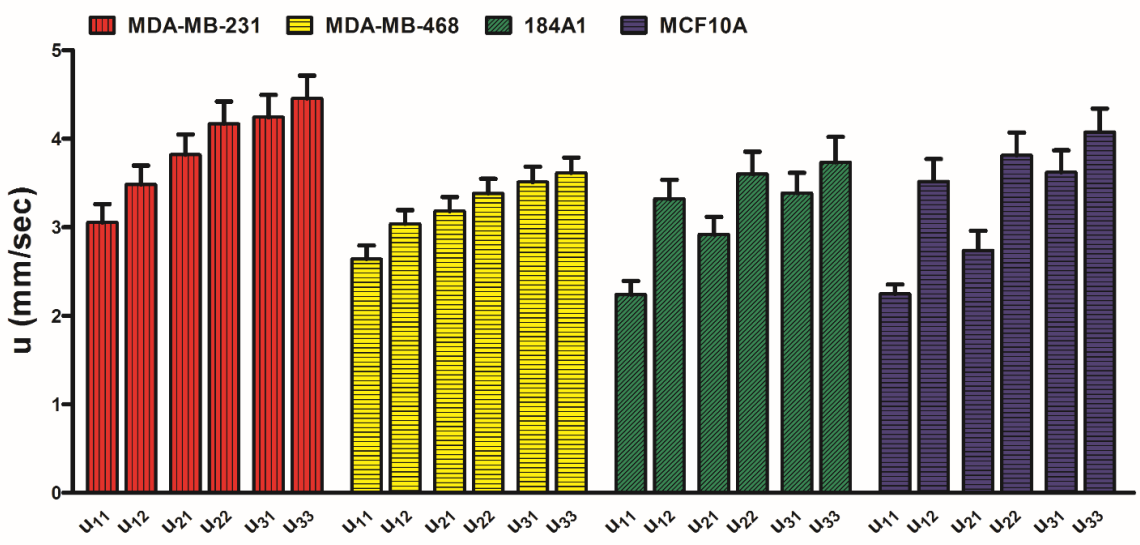


**Figure 8.5 Depiction of changes in the average transient and equilibrium velocity of breast cell lines in the iterative deformation channels.**

### 8.3.3 Relative Percentage Changes of Cell Velocity ($\alpha_u$):

The relative percentage changes of velocity for individual cells can be defined as the average equilibrium velocity in one deformation channel comparing to the average transient velocity in the next deformation channel ($\alpha_{u,i\text{-}i+1} = (u_{i,2}\text{-}u_{i+1,1})/u_{i,2}$) for i=1, 2). The relative percentage change of cell velocity is used as an index for examining the modulation in the mechanical resistance of cells and development of softening or stiffening. $\alpha_u$ for the four cell types are calculated and their column bars are depicted in Figures 6.

The average values of $\alpha_u$ for both non-metastatic cell lines are positive at each two successive deformation channels, confirming that this cell type exhibits a continuous stiffening response. However, comparing the average values of $\alpha_u$ for the two non-metastatic cell lines reveals appreciably decreasing trends from $\alpha_{u1\text{-}2}$ to $\alpha_{u2\text{-}3}$. Most importantly, it implies that the stiffening trend seen in the non-metastatic cells might not have a constant rate and quickly reach a steady-state under iterative deformation. Moreover, the average $\alpha_u$ values for both metastatic cell lines (Figure 6) are all negative.

It is remarkable that the magnitude of the average $\alpha_u$ in metastatic cancer cells largely decline from $\alpha_{u1\text{-}2}$ to $\alpha_{u2\text{-}3}$, suggesting that in the metastatic cells, the cell softening trend eventually stops.

We also examined the $\alpha_u$ values of the individual cells; each of all the MCF10A cells tested was found to show a positive number in $\alpha_{u1\text{-}2}$. Only 2% of 184A1 cells, whose $u_{11}$ velocity were under the average velocity of the non-metastatic cells, showed a negative number in $\alpha_{u1\text{-}2}$. Also, 76% and 72% of MCF10A and 184A1 cells, respectively, showed positive values for $\alpha_{u2\text{-}3}$. Thus, there are 76% and 70% sub-populations of MCF10A and 184A1 cells which have positive values for both $\alpha_{u1\text{-}2}$ and $\alpha_{u2\text{-}3}$ parameters, respectively. These cells can be labeled with some confidence as a sub-population of non-metastatic cells with a persistent stiffening response. Therefore, the majority of non-metastatic cells exhibited some degree of stiffening in response to the iterative deformations paradigm. At the single-cell level of the metastatic cells, 96% and 87% of MDA-MB-231 and MDA-MB-468 cells, have negative/zero values for their $\alpha_{u1\text{-}2}$, respectively. 81% and 89% of MDA-MB-231 and MDA-MB-468 cells have negative/zero values for their $\alpha_{u2\text{-}3}$, respectively. There is also a sub-population of 80% of MDA-MB-231 and 81% of MDA-MB-468 cells that exhibit a persistent softening as measured by negative values for both $\alpha_{u1\text{-}2}$ and $\alpha_{u2\text{-}3}$. More importantly, only 2% and 5% of MDA-MB-231 and MDA-MB-468 cells were observed to exhibit a persistent positive value in all of their $\alpha_u$, respectively. Therefore, the populations of metastatic cells can begin to be defined by a softening trend in their biomechanical state in response to iterative deformations.

According to the results in Figure 6, the relative percentage change of velocity between two initial successive channels ($\alpha_{u1\text{-}2}$) provides the most distinct and sensitive index for differentiation between non-metastatic and metastatic cells. Thus, only two successive deformation channels in this design might be enough to discriminate between metastatic and non-metastatic cells with single-cell resolution. Together, these distinct responses of metastatic and non-metastatic cells to dynamic mechanical stimuli provided a solid proof-of-principle for the significance of our proposed modulatory iMECH signature.

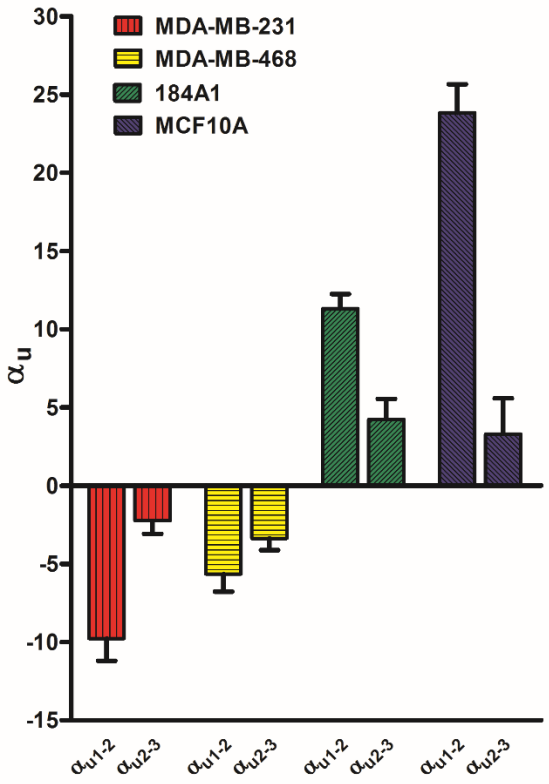


**Figure 8.6 Column bars of the calculated αu for breast cell lines between each two successive deformation channels.**

### 8.3.4 Single-Cell Level Identification using iMECH Bio-Signature:

Figure 7A shows a scatter plot of every individual cell's average transient velocity versus equilibrium velocity corresponding to the first deformation channel ($u_{11}$, $u_{12}$), equivalent to the results extracted from a single transient stress. Figure 7A clearly illustrates inadequacy of using a single microfluidic deformation channel to differentiate non-metastatic and metastatic cells at single-cell level due to a significant overlap in their measured $u_{11}$ and $u_{12}$. Therefore, a single microfluidic deformation channel measurements typically used for showing difference in the deformability of cells at population-level [32], cannot predict malignancy or normalcy and differentiate between metastatic and non-metastatic cells at single-cell level.

Our hypothesis that non-metastatic and metastatic cells show overall opposite trends in adjusting their biomechanical resistance under iterative deformations paradigm suggested that incorporation of the relative percentage change of velocity for the individual

cells rather than their absolute velocity provides a more effective marker to label single cells.

The scatter plot of the relative percentage change of velocity ($\alpha_{u1\text{-}2}$) vs. absolute transient velocity of the cells in the first deformation channel ($u_{11}$) for the individual tested cells are depicted in Figure 7B. These data show that a more powerful biomechanical descriptor of a non-metastatic cell is one having positive values for $\alpha_{u1\text{-}2}$, and for a metastatic cell is one having one negative/zero value for $\alpha_{u1\text{-}2}$. Using these definitions, 99% of the non-metastatic (normal-like) cells (100% of MCF10A cells and 98% of 184A1 cells) and 91% of the metastatic cancer cells (96% of MDA-MB-231 cells and 87% of MDA-MB-468 cells) and overall, 91% of all cells tested are accurately classified as non-metastatic or metastatic. Therefore, we define a new bio-signature by evaluating the dynamic changes in cell iterative biomechanical characteristics with a very high confidence level of >90% for distinguishing between non-metastatic (normal-like) and metastatic cancer single cells.

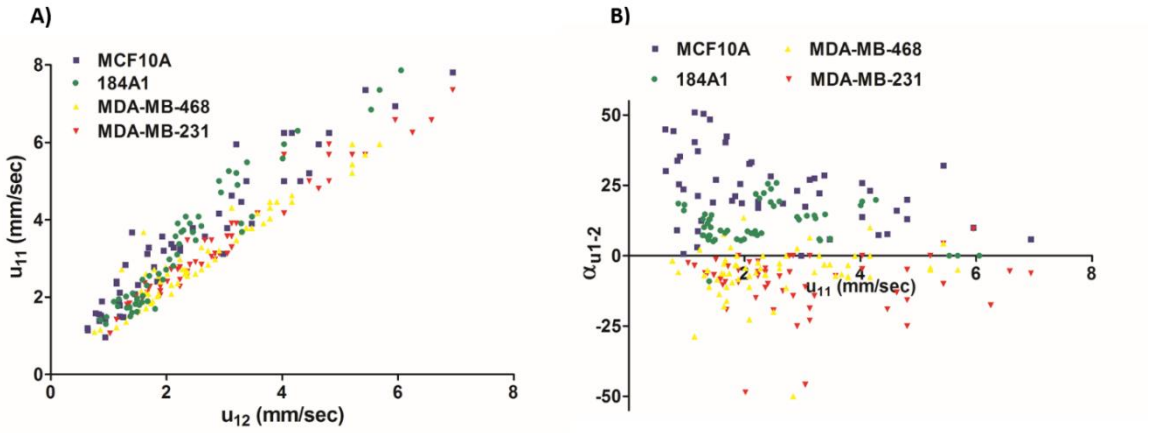


**Figure 8.7 A) Scatter plot of the absolute transient and equilibrium velocities of breast cell lines in of the first deformation region. B) Scatter plot of the relative percentage change of velocity ($\alpha_{u1\text{-}2}$) vs. absolute transient velocity ($u_{11}$) proposes a new biomarker for single-cell level identification.**

### 8.3.5 Cell cytoskeleton contribution in iMECH signature:

It was previously shown that cancer progression is associated with the disorganization and decrease in concentration of actin and microtubule filaments as the fundamental components of the cell cytoskeleton [33]. Furthermore, in an AFM study, it was demonstrated that actin filaments but not microtubules play a pivotal role in the structural mechanical response of adherent cells using specific drugs that target and modify

these two structural components in cell cytoskeleton [29]. Here, the impact of actin filaments and tubulin on the structural biomechanics of suspended cells and also their contribution in the proposed iMECH bio-signature are evaluated. In this section, MCF10A and MDA-MB-468 were used as the representatives of non-metastatic and metastatic cells, respectively. Specifically, we assayed the iMECH bio-signature in response to LatA treatment in the non-metastatic cells which causes depolymerization of the actin cytoskeleton, and to Jasp in the metastatic cells to induce actin polymerization. Also, to study the impact of tubulins on the iMECH bio-signature, we used SAHA, which causes an increase in tubulin acetylation in the metastatic cells and Noc which depolymerizes the tubulin network while keeping the actin network in the non-metastatic cells.

The transient and equilibrium velocities through the first deformation channel under control and drug treatments are measured and demonstrated in Figure 8A to study the impacts of treatments on cell biomechanics. Under control condition, the average transient velocity ($u_{11}$) of MCF10A cells is 3.05±0.21 mm/s which is significantly larger ($p<0.001$) than that of 2.26±0.11 mm/s for MDA-MB-231 cancer cells ($P<0.0001$). However, the average equilibrium velocity ($u_{12}$) of the cells are statistically insignificant between two cell types. These results imply that the metastatic cells are, on average, more deformable and softer in comparison to the non-metastatic cells. The results are similar to that of a previous microfluidic study which reported no significant difference in the average velocity of two MCF10A and MDA-MB-231 cell populations in steady state and the same reductions in the calculated transient velocity of MCF10A > MDA-MB-231 [34].

After treatments, the differences between the equilibrium velocities of all four treated cell populations are still insignificant. The average transient velocity of the cancer cells when treated with Jasp decreased significantly ($P\approx0.001$) to 2.34±0.19 mm/s due to the induced polymerization of actin filaments, while the average transient velocity slightly change when tubulins of the metastatic cells were induced with SAHA; 3.24±0.26 mm/s. When treated with LatA, the average transient velocity of the non-metastatic cells increased dramatically ($P<0.0001$) to 3.24±0.26 mm/s due to disruption of the actin network, although disruption in tubulins of the non-metastatic cells by Noc did not have significant effect on the average transient velocity; 2.06±0.22 mm/s. The changes in the average transient velocity for the control and treated cells through the deformation channel

closely correlated to their corresponding viscoelastic measurements using AFM [29]. These results indicate that the actin fiber network is a dominant structural component that regulates the biomechanical resistance of suspended cells same as that for the adherent cells as shown before [29].

To determine the impact of the actin filaments and tubules on the modulatory iMECH signature, we examined the effects of the treatments on $\alpha_u$ of the tested breast cell lines. Figure 8B shows the average values of $\alpha_{u1\text{-}2}$ for the control and treated non-metastatic and metastatic cells. As discussed earlier, the metastatic cells have a stress-softening trend with a negative average $\alpha_{u1\text{-}2}$; -9.77±1.43 while the non-metastatic cells show a stress-stiffening response with a positive average $\alpha_{u1\text{-}2}$; 23.84±1.81. According to the results, after treatment of the metastatic cells with Jasp, the average $\alpha_{u1\text{-}2}$ becomes positive; 18.03±1.63, confirming that actin filaments network stabilization leads to a stiffening response of the treated metastatic cells. However, when tubulins of the metastatic cells were induced by SAHA, the average $\alpha_{u1\text{-}2}$ value did not change noticeably; -8.33±2.19. On the other hand, when the non-metastatic cells were treated with LatA, the average $\alpha_{u1\text{-}2}$ significantly changed and showed a negative value; -1.67±2.00. It indicates that actin filaments network disruption causes a softening behavior of the non-metastatic cells. Although the average $\alpha_{u1\text{-}2}$ of the non-metastatic cells remains a positive value with an inappreciable change after the disruption of their tubulins by Noc treatment; 23.31±2.64. It was previously reported that by imposing oscillations on mechanically pre-stressed 3T3 fibroblasts, the cells developed stress stiffening [35]. In this study, cytoskeleton perturbation with the actin depolymerization inducer (Lat A) abolished the stiffening regime, however, no appreciable effect was seen with the microtubule disruptor (Noc).

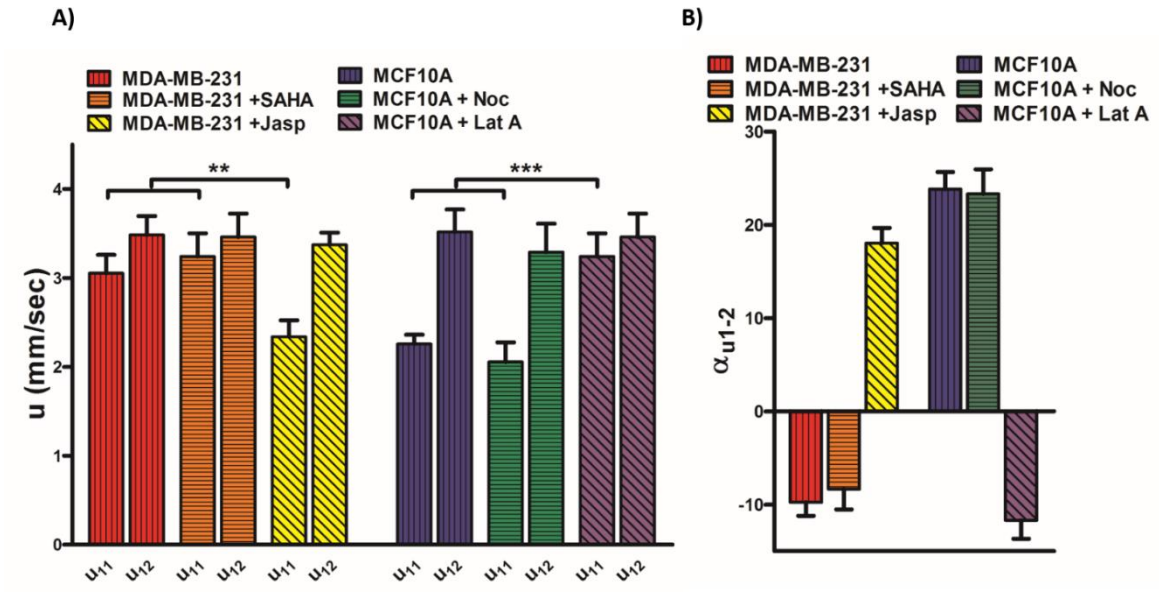


**Figure 8.8 A) Depiction of changes in the average transient and equilibrium velocities of the cancer and normal cells in the first deformation channels before and after drug-induced cytoskeleton stabilizations/disruptions. B) Column bars of the calculated $\alpha_{u1\text{-}2}$ for cancer and normal cells in control and after drug treatments.**

We also examined the $\alpha_u$ values of the individual cells after treatments in Figure 9. As discussed earlier, 100% of MCF10A cells showed a positive value for $\alpha_{u1\text{-}2}$ while 91% of MDA-MB-231 cells have negative/zero values for their $\alpha_{u1\text{-}2}$. After treatment of the metastatic cells with SAHA and thus tubulin stabilization, still 85% of the treated metastatic cells show a negative/zero value for $\alpha_{u1\text{-}2}$ while treatment of the metastatic cells with Jasp and thus actin polymerization causes 95% of the metastatic cells show a positive $\alpha_{u1\text{-}2}$. Furthermore, after treatment of the non-metastatic cells with Noc and thus tubulin disruption, still 97% of the non-metastatic cells have a positive $\alpha_{u1\text{-}2}$, while actin depolymerization with LatA causes 96% of the non-metastatic cells to show a negative/zero value for $\alpha_{u1\text{-}2}$. Together, these results indicate that actin but not tubulin play a dominant role and the most contribution in the modulatory iMECH bio-signature of the individual cells and their stiffening/softening response.

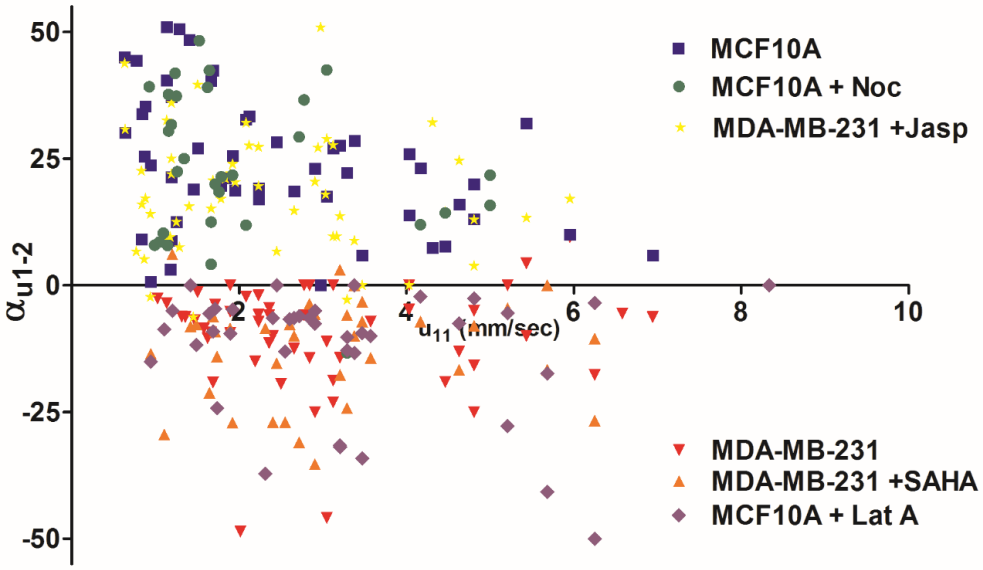


**Figure 8.9 Scatter plot of the relative percentage change of velocity ($\alpha_{u1-2}$) vs. absolute transient velocity ($u_{11}$) for the individual normal and cancer cells under control and drug treatment conditions.**

## *8.4 Conclusion*

A biosensing microchip was developed in this work to provide iterative mechanical characteristics (iMECH) of living cells and their responses to chemotherapeutic cytoskeleton modulators. The described iMECH microfluidic device, the first of its kind, provides a low-cost yet high-throughput and alternative to the established AFM method [16]. In summary, as cells pass through successive deformation/relaxation regions, the resistance of metastatic cells decreased while the non-metastatic cells demonstrated a more resistance after each relaxation period. Hence, two populations can be differentiated from their dynamic behavior even if the two populations produce the same velocity in the first deformation channel. Therefore, the proposed microchip makes the deformation modulatory iMECH signature of cells a readily available label-free biomechanical marker and was able to identify metastatic cells from non-metastatic cells by a >90% confidence level using their iterative biomechanical characteristics (iMECH). In addition, the effect of drug treatments known to target actin and tubulin cytoskeletal elements was examined in order to assess their role in iMECH bio-signature. As a result, actin filaments were identified as the most dominant cytoskeletal component in both cell biomechanical transient and modulatory (iMECH) signatures. Several chemotherapeutic agents are designed to target the cell cytoskeleton. In the future work, we will examine if the iMECH

analyzer may provide instrumentation to enable novel ways for screening drugs based on their biomechanical modulatory iMECH signature.

## *References*


[1] A. Lambrechts, M. Van Troys, and C. Ampe, "The actin cytoskeleton in normal and pathological cell motility," *International Journal of Biochemistry & Cell Biology,* vol. 36, pp. 1890-1909, Oct 2004.

[2] S. Suresh, "Biomechanics and biophysics of cancer cells," *Acta Biomater.,* vol. 3, pp. 413-438, 2007.

[3] H. Babahosseini, J. S. Strobl, and M. Agah, "Using nanotechnology and microfluidics in search of cell biomechanical cues for cancer progression," *Nanomedicine,* vol. 10, pp. 2635-2638, 2015.

[4] P. C. Roberts, E. Motillo, A. C. Baxa, H. H. Q. Heng, N. Doyon-Reale, L. Gregoire, *et al.*, "Sequential Molecular and Cellular Events during Neoplastic progression: A Mouse Syngeneic Ovarian Cancer Model," *Neoplasia,* vol. 7, pp. 944-956, 2005.

[5] K. A. Ward, W. I. Li, S. Zimmer, and et al., "Viscoelastic properties of transformed cells: role in tumor cell progression and metastasis formation," *Biorheology,* vol. 28, pp. 301-313, 1991.

[6] M. Nikkhah, J. S. Strobel, R. De Vita, and M. Agah, "The cytoskeletal organization of breast carcinoma and fibroblast cells inside three dimensional isotropic silicon microstructures," *Biomater.,* vol. 31, pp. 4552-61, 2010.

[7] B. D. Hoffman, C. Grashoff, and M. A. Schwartz, "Dynamic molecular processes mediate cellular mechanotransduction," *Nature,* vol. 475, pp. 316-323, 2011.

[8] G. Bao and S. Suresh, "Cell and molecular mechanics of biological materials," *Journal of Nature Materials,* vol. 2, pp. 715-725, 2003.

[9] C. A. J. Putman, K. O. Van der Werf, B. G. De Grooth, N. F. Van Hulst, and J. Greve, "Viscoelasticity of living cells allows high resolution imaging by tapping mode atomic force microscopy," *Biophysics Journal,* vol. 67, pp. 1749-53, 1994.

[10] J. Pourati, A. Maniotis, D. Spiegel, J. L. Schaffer, J. P. Butler, J. J. Fredberg, *et al.*, "Is cytoskeletal tension a major determinant of cell deformability in adherent endothelial cells?," *Am J Physiol. ,* vol. 274, pp. C1283-9, 1998.

[11] M. Maka and D. Erickson, "A serial micropipette microfluidic device with applications to cancer cell repeated deformation studies," *Integr. Biol.,* vol. 5, pp. 1374-1384, 2013.

[12] M. Mak, C. A. Reinhart-King, and D. Erickson, "Elucidating mechanical transition effects of invading cancer cells with a subnucleus-scaled microfluidic serial dimensional modulation device," *Lab Chip,* vol. 13, pp. 340-348, 2013.

[13] H. J. Hsu, C. F. Lee, and R. Kaunas, "A dynamic stochastic model of frequency-dependent stress fiber alignment induced by cyclic stretch," *PLoS ONE,* vol. 4, p. e4853, 2009.

[14] B. Liu, M. J. Qu, K. R. Qin, H. Li, Z. K. Li, B. R. Shen, *et al.,* "Role of cyclic strain frequency in regulating the alignment of vascular smooth muscle cells in vitro," *Biophys J. ,* vol. 94, pp. 1497-1507, 2008.

[15] D. Icard-Arcizet, O. Cardoso, A. Richert, and S. He´non, "Cell Stiffening in Response to External Stress is Correlated to Actin Recruitment," *Biophysical Journal,* vol. 94, pp. 2906-2913, 2008.

[16] H. Babahosseini, S.S. Strobl, and M. Agah, "Single cell metastatic phenotyping using pulsed nanomechanical indentations," *Nanotechnology,* vol. 26, p. 354004, 2015.

[17] C. E. Meacham and S. J. Morrison, "Tumour heterogeneity and cancer cell plasticity," *Nature,* vol. 501, pp. 328-337, 2013.

[18] B. Alberter, C. A. Klein, and B. Polzer, "Single-cell analysis of CTCs with diagnostic precision: opportunities and challenges for personalized medicine," *Expert Review of Molecular Diagnostics,* 2015.

[19] S. J. Lo and D. J. Yao, "Get to Understand More from Single-Cells: Current Studies of Microfluidic-Based Techniques for Single-Cell Analysis " *Int. J. Mol. Sci.,* vol. 16, pp. 16763-77, 2015.

[20] D. Di Carlo, "A mechanical biomarker of cell state in medicine.," *J Lab Autom.,* vol. 17, pp. 32–42, 2012.

[21] D. Kim, E. Choi, S. S. Choi, S. Lee, J. Park, and K. S. Yun, "Measurement of Single-Cell Deformability Using Impedance Analysis on Microfluidic Chip," *Japanese Journal of Applied Physics,* vol. 49, p. 4, 2010.

[22] B. K. Lee, J. Y. Ko, H. J. Lim, J. H. Nam, and S. Shin, "Investigation of critical shear stress with simultaneous measurement of electrical impedance, capacitance and light backscattering," *Clinical Hemorheology and Microcirculation,* vol. 51, pp. 203-212, 2012.

[23] J. Chen, Y. Zheng, Q. Y. Tan, E. Shojaei-Baghini, Y. L. Zhang, J. Li, *et al.,* "Classification of cell types using a microfluidic device for mechanical and electrical measurement on single cells," *Lab on a Chip,* vol. 11, pp. 3174-3181, 2011.

[24] A. Adamo, A. Sharei, L. Adamo, B. Lee, S. Mao, and K. F. Jensen, "Microfluidics-Based Assessment of Cell Deformability," *Analytical Chemistry,* vol. 84, pp. 6438-6443, Aug 2012.

[25] C. Xue, J. Wang, Y. Zhao, D. Chen, W. Yue, and J. Chen, "Constriction Channel Based Single-Cell Mechanical Property Characterization," *Micromachines,* vol. 11, pp. 1794-1804, 2015.

[26] H. Babahosseini, A. K. Ketene, E. M. Schmelz, P. C. Roberts, and M. Agah, "Biomechanical profile of cancer stem-like/tumor-initiating cells derived from a progressive ovarian cancer model," *Nanomedicine: NBM,* vol. 10, pp. 1013-1019, 2014.

[27] H. Babahosseini, P. C. Roberts, E. M. Schmelz, and M. Agah, "Bioactive sphingolipid metabolites modulate ovarian cancer cell structural mechanics," *Integr. Biol.,* vol. 5, pp. 1385-1392, 2013.

[28] C. Xue, J. Wang, Y. Zhao, D. Chen, W. Yue, and J. Chen, "Constriction Channel Based Single-Cell Mechanical Property Characterization," *Micromachines,* vol. 6, pp. 1794-1804, 2015.

[29] A. N. Ketene, P. C. Roberts, A. A. Shea, E. M. Schmelz, and M. Agah, "Actin filaments play a primary role for structural integrity and viscoelastic response in cells," *Integr. Biol.,* vol. 4, pp. 540-549, 2012.

[30] W. Kim, "A Micro-aspirator Chip Using Vacuum Expanded Microchannels for High-throughput Mechanical Characterization of Biological Cells," Master of Science, Biomedical Engineering Texas A&M University, 2010.

[31] C. H. D. Tsai, S. Sakuma, F. Arai, and M. Kaneko, "A New Dimensionless Index for Evaluating Cell Stiffness-Based Deformability in Microchannel," *IEEE Trans. Biomed. Eng.,* vol. 61, 2014.

[32] H. Babahosseini, V. Srinivasaraghavan, Z. Zhao, G. F, E. Childress, J. S. Strobl, *et al.*, "The Impact of Sphingosine Kinase Inhibitor-Loaded Nanoparticles on Bioelectrical and Biomechanical Properties of Cancer Cells," *Lab Chip,* 2015.

[33] A. N. Ketene, E. M. Schmelz, P. C. Roberts, and M. Agah, "The effects of cancer progression on the viscoelasticity of ovarian cell cytoskeleton structures," *Nanomedicine: NBM,* vol. 8, pp. 93-102, 2012.

[34] H. W. Hou, Q. S. Li, G. Y. H. Lee, A. P. Kumar, C. N. Ong, and C. T. Lim, "Deformability study of breast cancer cells using microfluidics," *Biomed Microdevices,* vol. 11, pp. 557-564, 2009.

[35] P. Fernandez, P. A. Pullarkat, and A. Ott, "A Master Relation Defines the Nonlinear Viscoelasticity of Single Fibroblasts," *Biophysical Journal,* vol. 90, pp. 3796–3805, 2006.

# 9 Summary and outlook

This chapter partly is produced from [1] with permission from Future Medicine.

*H. Babahosseini, J. Strobl, and M. Agah, "Using Nanotechnology and Microfluidics in Search of Cell Biomechanical Cues for Cancer Progression," Nanomedicine, vol. 10, no. 17, pp. 2635-2638, September 2015.*

## *9.1 Summary*

### 9.1.1 Cell biomechanical changes in cancer progression

During cancer progression, cells undergo numerous genetic and epigenetic changes that impact various cellular functions such as motility, adhesion, proliferation, and signaling. These fundamental changes are accompanied by alterations in the cellular structural cytoskeleton which modulates cell biomechanical properties [2]. The biomechanical changes in cells during cancer progression can potentially enable invasion of metastatic cells into the surrounding tissues to access the circulatory system and establish secondary tumors [3]. This suggests that malignancy and the metastatic potential of cancer cells are correlated with their biomechanical phenotype. Advances in nanotechnology and microfluidics facilitate interrogation of the biomechanical properties of single cells and can be directed towards identification of label-free cues to predict the risk of cancer invasiveness and metastatic potential in its early stages.

### 9.1.2 Cell biomechanical cues for cancer detection

The overall findings on the cell biomechanical properties from a wide variety of cell lines using Atomic Force Microscopy (AFM) and other nanotechnology tools are in general agreement that as cells transform and progress towards more aggressive stages, they become on average softer, more deformable, and less viscous [4]. These changes in biomechanical properties of cancer cells are directly associated with a decrease in the organization and density of structural cytoskeleton components [5]. Subsequent study by AFM identified the actin fiber network as the primary determinant of cell structural integrity and biomechanical responses [6].

### 9.1.3 Effects of anti-cancer drugs on cell biomechanics (chapter 2)

Alterations to cell biomechanics induced by anti-cancer drugs and subsequent changes in cancer cell state can be utilized for efficacy screening of therapeutic agents that target cytoskeleton dysfunction. One application of this approach is the determination whether the actions of therapeutic agents reverse aberrant biomechanical characteristics of aggressive cancer cells, possibly shifting their biomechanical phenotype to a more benign, less invasive state [7]. For instance, exogenous sphingosine treatment selectively induces aggressive ovarian cancer cells to mechanically behave more like benign cells by rendering them stiffer [8]. This study suggests that the cell biomechanical profiling has potential utility in drug discovery, evaluating new types of anti-cancer agents that impact cell biomechanics relevant to invasiveness.

### 9.1.4 Cell biomechanical cues for cancer stem-like/tumor initialing cells isolation (chapter 3)

The role of cancer stem-like/tumor initialing cells (CSC/TICs) has received much attention in the search for effective cancer treatments. In contrast to the traditional clonal evolution cancer model that purports all malignant cells have the same potential for reinitiating a tumor, the CSC/TIC model suggests that self-renewal CSC/TICs are solely capable of tumor propagation [9]. CSC/TICs are generally more drug resistant compared to their tumor cell counterparts and this is thought to contribute to chemotherapeutic failures and disease recurrence. The biomechanical properties of CSC/TIC have the capability to address isolation and eradication of CSC/TICs but to date, the knowledge is limited. It has been reported that the biomechanical properties of CSC/TIC populations are more homogeneous [10] and extremely softer compared to the bulk cancer cell population. Moreover, the biomechanical properties of CSC/TICs are responsive to treatments which convert their deformability to that of a less aggressive phenotype [11]. Conclusively, the distinct biomechanical properties of CSC/TICs provides promising clues for their targeted isolation using clinical microdevices.

### 9.1.5 Accurate modeling of cell biomechanical responses (chapter 4 and 5)

While simple linear models are typically used for modeling of the cell biomechanical responses, the highly complex, heterogeneous, and nonlinear characteristics of cell structure preclude them from a precise characterization. To make full use of cell biomechanical cues, accurate modeling of cell biomechanical responses is necessary. For instance, the power-law, fast early-relaxation behavior of the cells is not associated with a simple exponentially decaying function predicted by a linear viscoelastic model and rather, suggests the application of a fractional model might be more useful. The fractional model differs from the linear viscoelastic model by allowing a non-integer (between zero and one) time-derivative relationship between stress and strain. This added degree of freedom brings with it an excellent increase in conformance to the cell biomechanical responses. The order of the fractional derivative is found remarkably homogeneous with a median value of ~0.5 for both normal and cancer populations, supporting the application of the fractional model [12]. The resulting viscosity measured by a fractional model exhibits considerably less dispersion due to a better-fitting than the distribution generated by the linear model and therefore serves as a more powerful biomarker for cancer cell identification [12].

The current trend for cell biomechanical characterization also generally assumes that the cell is an entirely homogenous material neglecting the complex multi-layered architecture of the living cells. To maintain the validity of this assumption, the biomechanical response are probed at a limited depth of the cell structure (typically 10%) and this overlooks valuable information about the biomechanical properties of the entire cell structure. The Generalized Maxwell viscoelastic model incorporates the idea of multiple relaxation times, and it can provide insight about the biomechanical responses of sub-cellular structures [13]. Applying this model to the cell biomechanical responses reveals that the well-established decreasing trend in the elastic modulus and viscosity from normal to cancer cells presents in the all corresponding sub-cellular structures of two cell types, which becomes most significant in the deeper sub-cellular structures. These examples indicate that accurate modeling of cell biomechanical responses can provide the most comprehensive information-rich picture of the cell biomechanical properties.

### 9.1.6 A high throughput microfluidic alterative to AFM (chapter 6)

The emerging need for a high-throughput clinically relevant alternative technique for evaluating deformability of individual cell has led to the development of microfluidic-based analyzers [14]. In a typical microfluidic-based transit analyzer, single cells move through a deformation region that imposes mechanical stress on the cell structure, and the transit time, as measured using electrical resistance changes, provides rapid and fully automated acquisition of the cell deformability biomarker [15]. The observations show that the average transit time of cancer cells is significantly shorter than that of normal cells [16], supporting earlier reports by considering that the transit time is directly correlated with cell deformability.

### 9.1.7 Single-cell level versus population level (chapter 7 and 8)

Tumor masses are comprised of a heterogeneous mixture of cancer cells. This highlights the importance of analyzing the biomechanical cues at single-cell-resolution as an aid to improving cancer diagnosis and treatment. However, typical approaches to characterize cell biomechanical properties utilize switch-like mechano-transduction models [17] in which the biomechanical descriptors extracted under a transient loading averagely differs between normal and cancer cell populations. Although these approaches demonstrate biomechanical discrimination between normal and cancer on the population level, at a single-cell level, there exists considerable overlap in the distribution of the biomechanical descriptors of individual normal and cancer cells and this precludes single-cell-resolution analysis. An alternative approach is to explore the biomechanical response of cells upon a dynamic loading, because richer data can be acquired considering that the micromechanical environment of the cells evokes constant change in their physiological condition. In response to dynamic loading, a cell continually modifies its cytoskeleton architecture in such a way that allows the cell to adapt its biomechanical properties to compensate for environmental forces [18]. Normal and cancer cells subjected to such a pulsed stress regimen exerted by AFM or generated by a microfluidic multi-segmented channel are found to exhibit distinct biomechanical responses. While the majority of normal cells responded by an increase in their resistance against the pulsed stress and stiffening behavior, cancer cells generally responded by losing their resistance and

becoming slightly softened [19]. Therefore, the use of dynamic loading paradigms to evaluate cell biomechanical responses may provide powerful biomarkers for single cancer cell detection and personalized medicine applications.

## 9.2 Significance and contribution

The aim of this dissertation was to integrate microfluidics and nanotechnology in search of cell biomechanical cues for cancer diagnosis and treatment. While AFM as an effective nanoscale resolution tool is suitable for fundamental studies on the cell biomechanical cues, the microfluidic technology provides an alternative for the development of a high-throughput and label-free biosensing platform for rapid cell biomechanical profiling. AFM was utilized in this dissertation to establish a framework for better understanding about the biology and progression of cancer disease. The cell biomechanical markers were used to screen the efficacy and evaluate the effects of sphingolipid metabolites as the potential chemotherapeutic agents in Chapter 2 and also to characterize cancer stem-like/tumor initialing populations in Chapter 3. The heterogeneous and complex nature of the cell structure with nonlinear depth-dependent mechanical characteristics led us to consider the application of nonlinear viscoelastic models to extract more accurate cell biomechanical responses for better differentiation between the normal and cancer cells in Chapter 4 and also to provide insight about the biomechanical responses of sub-cellular structures in Chapter 5.

In parallel with the AFM fundamental studies and by taking the advantages of the outcomes of these studies, we attempted to develop a rapid label-free assay for assessing cell biophysical markers. Thus, microfluidic technology was utilized for the development of a novel biomedical microdevice in this dissertation. In Chapter 6, the first generation microfluidic chip provided an automated assay to identify biophysical (biomechanical and bioelectrical) signatures of normal and malignant cell populations and monitor the therapeutic efficacy of drugs.

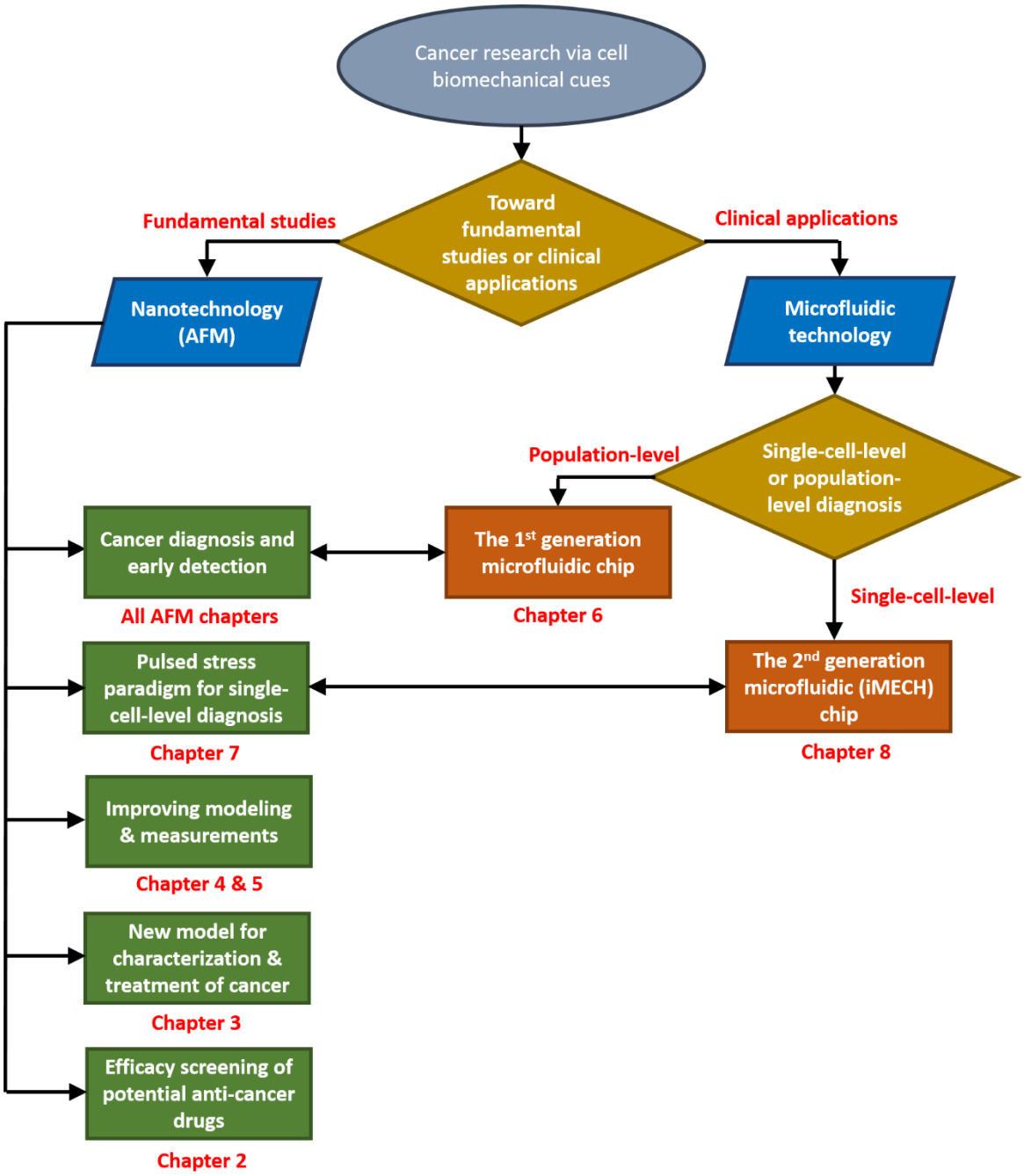


**Figure 9.1 A breakdown of key contributions of this dissertation to the cancer research via cell biomechanical cues.**

Since the existing approaches for cell biomechanical phenotyping which typically utilize a single transient stress are inadequate at a single-cell level, we explored application of a pulsed stress regimen via AFM for cell biomechanical phenotyping in Chapter 7.

Interestingly, it could provide a richer bio-signature for single-cell level metastatic phenotyping. To extend the proposed idea into the microfluidic technology, the second generation microfluidic biosensor called the iterative mechanical characteristics (iMECH) analyzer was developed in Chapter 8 which represents a significant advance in achieving a biomedical microdevice for use at single-cell level analysis. Figure 9.1 demonstrates a breakdown of key contributions of this dissertation.

## 9.3 Future prospects

To date, most studies have focused on proof-of-concept of the application of biomechanical cues to predict cancer progression, metastatic potential, and response to treatment. Although remarkable progress has been made, there is work ahead to fulfill the promise for translation of cell biomechanical markers to the clinic. Commercial development of microdevices with improved capabilities as high-throughput, low-cost, automated, and label-free assays with single-cell-resolution of cell biomechanical cues in heterogeneous cell populations is essential. In addition, these devices must be assembled with simple, low-cost fabrication techniques that are scalable for mass-production. Finally, accurate mathematical modeling must be developed to improve the reliability and predictive value of measured indicators of cell biomechanical properties before the assay can practically be accepted as a clinical marker. The potential application of these products also lies in the research laboratory where they can be used to facilitate database generation and evaluate the merits of the cell biomechanical cues to the broader biology of healthy and diseased cells.

## References


[1] H. Babahosseini, J. S. Strobl, and M. Agah, "Using nanotechnology and microfluidics in search of cell biomechanical cues for cancer progression," *Nanomedicine,* vol. 10, pp. 2635-2638, 2015.

[2] S. Kumar and V. M. Weaver, "Mechanics, malignancy, and metastatis: The force journey of a tumor cell," *J Cancer Metastatis Rev.,* vol. 28, pp. 113-27, 2009.

[3] J. B. Wyckoff, J. G. Jones, J. S. Condeelis, and J. E. Segall, "A critical step in metastasis: in vivo analysis of intravasation at the primary tumor," *Cancer Research,* vol. 60, pp. 2504-2511, 2000.

[4] A. N. Ketene, E. M. Schmelz, P. C. Roberts, and M. Agah, "The effects of cancer progression on the viscoelasticity of ovarian cell cytoskeleton structures," *Nanomedicine : nanotechnology, biology, and medicine,* vol. 8, pp. 93-102, 2011.

[5] J. Strobl, M. Nikkhah, and M. Agah, "Action of Anticancer Drug Suberoylanilide hydroxamic Acid (SAHA) on Human Breast Cancer Cell Cytoarchitecture in Silicon Microstructures," *Biomaterials,* vol. 31, pp. 7043-7050, 2010.

[6] A. N. Ketene, P. C. Roberts, A. A. Shea, E. M. Schmelz, and M. Agah, "Actin filaments play a primary role for structural integrity and viscoelastic response in cells," *Integrative Biology,* vol. 4, pp. 540-549, 2012.

[7] S. Sharma, C. Santiskulvong, L. A. Bentolila, J. Rao, O. Dorigo, and J. K. Gimzewski, "Correlative nanomechanical profiling with super-resolution F-actin imaging reveals novel insights into mechanisms of cisplatin resistance in ovarian cancer cells.," *Nanomedicine: Nanotechnology, Biology and Medicine,* vol. 8, pp. 757-766, 2012.

[8] H. Babahosseini, P. C. Roberts, E. M. Schmelz, and M. Agah, "Bioactive sphingolipid metabolites modulate ovarian cancer cell structural mechanics," *Integrative Biology,* vol. 5, pp. 1385-1392, 2013.

[9] S. Dawood, L. Austin, and M. Cristofanilli, "Cancer stem cells: implications for cancer therapy," *Oncology,* vol. 28, pp. 1101-7, 2014.

[10] W. Zhang, K. Kai, D. S. Choi, T. Iwamoto, Y. H. Nguyen, H. Wong, *et al.*, "Microfluidics separation reveals the stem-cell–like deformability of tumor-initiating cells," *PNAS,* vol. 109, pp. 18707-12, 2012.

[11] H. Babahosseini, A. N. Ketene, E. M. Schmelz, P. C. Roberts, and M. Agah, "Biomechanical profile of cancer stem-like/tumor-initiating cells derived from a progressive ovarian cancer model," *Nanomedicine: Nanotechnology, Biology and Medicine,* vol. 10, pp. 1013–1019, 2014.

[12] B. Carmichael, H. Babahosseini, N. Mahmoodi, and M. Agah, "The fractional viscoelastic response of human breast tissue cells," *Physical Biology,* vol. 12, p. 046001, 2015.

[13] H. Babahosseini, B. Carmichael, J. Strobl, N. Mahmoodi, and M. Agah, "Sub-Cellular Force Microscopy in Single Normal and Cancer Cells," *Biochemical and Biophysical Research Communications,* 2015.

[14] Y. Zheng, J. Nguyen, Y. Wei, and Y. Sun, "Recent advances in microfluidic techniques for single cell biophysical characterization," *Lab Chip,* vol. 13, pp. 2464-2483, 2013.

[15] V. Srinivasaraghavan, D. Aggarwal, H. Babahosseini, D. Nakidde, J. S. Strobl, and M. Agah, "Analyses of single-cell mechanoelectrical properties via microfluidics," presented at the IEEE Sensors Valencia, Spain, 2014.

[16] H. Babahosseini, V. Srinivasaraghavan, and M. Agah, "Microfluidic chip bio-sensor for detection of cancer cells," presented at the IEEE Sensors, Taipei, Taiwan, 2012.

[17] B. D. Hoffman, C. Grashoff, and M. A. Schwartz, "Dynamic molecular processes mediate cellular mechanotransduction," *Nature,* vol. 475, pp. 316-323, 2011.

[18] G. Bao and S. Suresh, "Cell and molecular mechanics of biological materials," *Nature Materials,* vol. 2, pp. 715-725, 2003.

[19] H. Babahosseini, J. S. Strobl, and M. Agah, "Single Cell Metastatic Phenotyping using Pulsed Nanomechanical Indentations," *Nanotechnology,* 2015.

# Appendix
## *A: List of publications*

**Journal Articles:**

1. **H. Babahosseini**, P.C. Roberts, E.M. Schmelz, and M. Agah, "Bioactive sphingolipid metabolites modulate ovarian cancer cell structural mechanics," **Integrative Biology**, 5, 1385-1392, Aug 2013.
2. **H. babahosseini**, A.N. Ketene, E.M. Schmelz, P.C. Roberts, and M. Agah, "Biomechanical profile of cancer stem-like/tumor initiating cells derived from a progressive ovarian cancer model," **Nanomedicine: Nanotechnology, Biology and Medicine**, 10(5):1013–1019, Jan 2014.
3. B. Carmichael*, **H babahosseini***, S.N. Mahmoodi, and M. Agah, (*Co-first authors), "The fractional viscoelastic response of human breast tissue cells," **Physical Biology**, 12(4):046001, May 2015.
4. **H. babahosseini***, B. Carmichael*, J.S. Strobl, S.N. Mahmoodi, and M. Agah, (*Co-first authors), "Sub-cellular force microscopy in single normal and cancer cells," **Biochemical and Biophysical Research Communications**, 463(4):587–592, June 2015.
5. **H. babahosseini**, J.S. Strobl, and M. Agah, "Single cell metastatic phenotyping using pulsed nanomechanical indentations," **Nanotechnology**, (special issue, focus on biosensing), 26(35):354004, Aug 2015.
6. **H. Babahosseini**, J.S. Strobl, and M. Agah, "Using Nanotechnology and Microfluidics in Search of Cell Biomechanical Cues for Cancer Progression," **Nanomedicine**, (editorial article), 10(17):2635-2638, Sep 2015.
7. **H. Babahosseini**, V. Srinivasaraghavan, Z. Zhao, F. Gillam, E. Childress, J. S. Strobl, W. Santos, C. Zhang, and M. Agah, "The impact of sphingosine kinase inhibitor-loaded nanoparticles on bioelectrical and biomechanical properties of cancer cells", **Lab on a Chip**, 16:188-198, Nov 2015.

8. **H. babahosseini**, V. Srinivasaraghavan, J.S. Strobl, and M. Agah, "Single cancer cell identification using a microfluidic iterative mechanical characteristics (iMECH) analyzer," **Under review**.
9. V. Srinivasaraghavan, **H. babahosseini**, J.S. Strobl, and M. Agah, "Content-rich measurements of mechano-electrical properties from breast cancer cells via microfluidics," **Under review**.
10. V. Srinivasaraghavan, **H. babahosseini**, J.S. Strobl, A. Shajahan-Haq, R. Clarke, and M. Agah, "Biophysical characterization of a hormone therapy resistant breast cancer cell model, " **Under preparation**.

**Conference Proceedings/Abstracts:**

1. **H. Babahosseini**, P.C. Roberts, E.M. Schmelz, and M. Agah, "Roles of Bioactive Sphingolipid Metabolites in Ovarian Cancer Cell Biomechanics," 34th Annual International Conference of the IEEE EMBS (EMBC 2012), August 2012, San Diego, CA, pp. 2436- 2439.
2. **H. Babahosseini**, V. Srinivasaraghavan, and M. Agah, "Microfluidic Chip Bio-Sensor for Detection of Cancer Cells," IEEE Sensors 2012, October 2012, Taipei, Taiwan, pp. 2030-2033.
3. V. Srinivasaraghavan, **H. Babahosseini**, E.M. Schmelz, P.C. Roberts and M. Agah, "Actin filaments regulate migration time of cells through a microfluidic constriction channel," Biomedical Engineering Society (BMES) Annual Meeting 2013, September 2013, Seattle, WA.
4. **H. Babahosseini**, A. Ly, and M. Agah, "Probing the Mechanics of Adherent and Suspended Breast Cancer Cells with AFM and Microfluidics," ASME 2014 3rd Global Congress on NanoEngineering for Medicine and Biology (NEMB2014), February 2014, San Francisco, CA.
5. **H. Babahosseini**, J.S. Strobl, and M. Agah, "Repetitive Stress-Relaxations Cause Cell Stiffening," Biomedical Engineering Society (BMES) Annual Meeting 2014, October 2014, San Antonio, Texas.

6. V. Srinivasaraghavan, D. Aggarwal, **H. Babahosseini**, D. Nakidde, J.S. Strobl and M. Agah, "Analyses of single-cell mechanoelectrical properties via microfluidics," IEEE Sensors 2014, November 2014, Valencia, Spain, pp. 1772 - 1775.
7. **H. Babahosseini**, J.S. Strobl, and M. Agah, "Opposing Biomechanical Trends of Normal and Cancer Cells in Response to Pulsed Stresses Provide a Biomarker for Single-Cell-Level Identification," The ASME 2015 4th Global Congress on NanoEngineering for Medicine and Biology (NEMB2015), April 2015, Minneapolis, MN.
8. V. Srinivasaraghavan, **H. Babahosseini**, J.S. Strobl and M. Agah, "Content-rich biophysical measurements from single cells," 2015 Single Cell Analysis Program (SCAP) Investigators Meeting, April 2015, NIH, Bethesda, MD.
9. **H. Babahosseini**, V. Srinivasaraghavan, C. Zhang, and M. Agah, "Nanoparticles Modulate Bio-Electromechanical Properties of Cells," 19th International Conference on Miniaturized Systems for Chemistry and Life Sciences (MicroTAS 2015), October 2015, Gyeongju-South Korea.
10. V. Srinivasaraghavan, **H. babahosseini**, P. Ghassemi, A. Shajahan-Haq, R. Clarke, and M. Agah, "Characterization of hormone therapy resistance in breast cancer using single-cell mechanoelectrical properties," 26th Anniversary World Congress on Biosensors( Biosensors 2016), May 2016, Gothenburg, Sweden.

## *B: MATLAB Codes*

### Elastic modulus (AFM)

Force-indentation curves fitting to extract cell elastic modulus.

```
clc
clear all

data=dlmread('C:\Users\Desktop\Run1\cell1.txt','\t',1,0);

%-------------------------------------------------------
%                       Original(raw) data plot
piezo_pos=data(:,1)*1e-6; %in m %*1e-6
def_m=data(:,2)*1e-9; % in m
subplot(2,3,1)
plot(piezo_pos,def_m)
xlabel('piezo position (m)')
ylabel('deflection (m)')
grid on
title('Cantilever deflection vs. Piezo position')

%-------------------------------------------------------------
%                       True deflection calculation
voltage_offset=mode(def_m);
def_m=def_m - voltage_offset;
subplot(2,3,2)
plot(piezo_pos,def_m)
xlabel('piezo position (m)')
ylabel('true deflection (m)')
grid on
title('True Cantilever deflection vs. Piezo position')

%-------------------------------------------------------------
%                     Important analysis parameters
k=0.025; %N/m
Force=k*def_m;
force=max(Force);
D=(piezo_pos)-(def_m);
indentation=max(D)
subplot(2,3,3)
plot(D,Force)
xlabel('separation distance (m)')
ylabel('Force (N)')
title('Force vs.Separation distance')
grid on

%-------------------------------------------------------------
%                    DATA FITTING INTO HERTZ MODEL
Force_powered=abs(Force).^(2/3);
subplot(2,3,4)
plot(D,Force_powered)
xlabel('separation distance (m)')
ylabel('Force^2^/^3 (N)')
grid on
```

```
%-------------------------------------------------------
%              Determining the hertz model fitting region
tol_fit=2.2e-6; %put the separation distance at initial indentation
point
tol_h_fit=6e-6;

j=1;
for j=1:10

q=1;
for w=1:length(D)

    if D(w) >= tol_fit && D(w) <= tol_h_fit
        hertz_y(q)=Force_powered(w);
        hertz_x(q)=D(w);
        q=q+1;
    end

end

P_hertz=polyfit(hertz_x,hertz_y,1);
d_o=abs(voltage_offset);
z_o=-(P_hertz(2)/P_hertz(1))+d_o;
tol_fit=z_o;

j=j+1;
end

%-------------------------------------------------------------
%         Calculate and plot the contact point onto force curve
subplot(2,3,5)
plot(hertz_x,hertz_y)
title('hertz model fitting region')
xlabel('separation distance (m)')
ylabel('Force^2^/^3 (N)')
grid on
mu_sample=0.5;
R=(11e-6)/2;
E_sample=(P_hertz(1)^(3/2))*(3/4)*(1-(mu_sample)^2)/sqrt(R);
text(1e-6,1e-6,strcat('E=',num2str(E_sample)))
E=E_sample*1e-3

%-------------------------------------------------------------
%         Calculate and plot the contact point onto force curve
subplot(2,3,6)
plot(D,Force_powered)
xlabel('separation distance (m)')
ylabel('Force^2^/^3 (N)')
grid on
hold on
new_tol=P_hertz(1)*z_o+P_hertz(2);
plot(z_o,new_tol,'o','Color','green')

%-------------------------------------------------------
```

```
%                    Correlation coefficient(R^2)
r=corrcoef(hertz_y,hertz_x);
r_squared=r(2,1)^2
```

## Apparent viscosity (AFM)

Stress-relaxation curves fitting to extract cell apparent viscosity.

```
clc
clear all

data=dlmread('C:\Users\Desktop\cell1.txt','\t',1,0);

%-------------------------------------------------------------
%                        Original(raw) data plot
time=data(:,1);
def_m=data(:,2)*1e-6;
subplot(2,3,1)
plot(time,def_m)
xlabel('time (s)')
ylabel('deflection (m)')
grid on
title('Cantilever deflection vs. time')

%-------------------------------------------------------------
%Determining the deflection offset while during the first 1 seconds of
scripting

tol_fit=1;
q=1;
for w=1:length(time) %scan through all data points
    if time(w) < tol_fit
        approach_def(q)=def_m(w); %pulling out the deflection data
        approach_time(q)=time(w); %pulling out time data
        q=q+1;
    end
end

def_m=def_m-mode(approach_def);
subplot(2,3,2)
plot(time,def_m)
xlabel('time (s)')
ylabel('true deflection (m)')
grid on
title('True Cantilever deflection vs. time')

%-------------------------------------------------------------
%                      Important analysis parameters
k=0.0201; %N/m
Force=k*def_m; % Newton
subplot(2,3,3)
plot(time,Force.*1e9)
xlabel('time (s)')
ylabel('Force (nN)')
title('Force vs.time')
```

```
grid on

%-----------------------------------------------------------
%                Determining the extraction points for fit
aa=max(Force)
zz=min(Force);
for bb=1:length(Force)
    if Force(bb)==aa
        start_visco_time_fit=time(bb); %left bound
    elseif Force(bb)==zz
        end_visco_time_fit=time(bb); %right bound
     end
end

%-------------------------------------------------------------
%        Extracting the viscoelastic parameter model fitting region
%all data points after this tolerance value will be considered in the
viscoelastic model fitting
tol_fit=start_visco_time_fit;
tol_h_fit=end_visco_time_fit-2;
q=1; %counter
for w=1:length(time) %scan through all data points
    if time(w) > tol_fit && time(w) < tol_h_fit
        def_fit(q)=def_m(w); %pulling out the deflection data
        time_fit(q)=time(w); %pulling out piezo position data
        q=q+1;
    end
end

Force_fit=k*def_fit;
subplot(2,3,4)
figure(1)
plot(time_fit,Force_fit,'Color','r')
title('Viscoelastic model fitting region')
xlabel('time (s)')
ylabel('Force (N)')
grid on
hold on

%-------------------------------------------------------------
%         Using curve fitting tool within matlab software
% cftool(time_fit,Force_fit)
% parameter fit interpretations and variable definitions

C1_C2=input('please enter fitted parameter A value:');
tau_eps_inv=input('please enter fitted parameter B value:');
C1=input('please enter fitted parameter C value:');
indentation_time= input('please enter indentation time in seconds: ');
C2=C1_C2/C1;
app_vel=5e-6;
d_0= indentation_time*app_vel;
R=11e-6; %Diameter of glass sphere contact area
nu=0.5;%assumed poisson's ratio value for sample
E_R=C1*(3/4)*(1-nu)/(sqrt(R/2)*d_0^(3/2))
Tau_eps=1/(tau_eps_inv);
Tau_sigma=Tau_eps*(1+C2);
```

```
%-------------------------------------------------------------
%        Viscoelastic response of sample as a standard linear solid
k1=E_R; %kelvin spring element 1
k2=E_R*C2; %kelvin spring element 2
visc=E_R*(Tau_sigma-Tau_eps; %viscous behavior as the damper element
E_inst=E_R*(1+C2);
E_Y=(3/2)*E_R;
```

## Biomechanical & bioimpedance parameters (Microfluidics)

Using the impedance measurements to extract entry and travel times in addition to the impedance magnitude and phase angels of individual cells in four frequencies.

```
clear;
clc;

%-------------------------------------------------------------
%                 Enter cell number in Line 4
j=1;
in_path='C:\Users\Desktop\Run1 Demod0.xls';
in_path1='C:\Users\Desktop\Run1 Demod1.xls';
in_path2='C:\Users\Desktop\Run1 Demod2.xls';
in_path3='C:\Users\Desktop\Run1 Demod3.xls';
out_path='C:\Users\Desktop\Run1\DataAnalysis.xls';

if(j==1)
    f=fopen(char(out_path),'a+');

    fprintf(f,'%s\t%s\t%s\t%s\t%s\t%s\t%s\t%s\t%s\t%s\t%s\t%s\t%s\t%s\t%
    s\t%s\t%s\t%s\t%s\t%s\n','Cell Number','T entry','T in','T
    middle','T exit','Z baseline@1MHz','Z peak@1MHz','Theta
    baseline@1MHz','Theta peak@1MHz','Z baseline@100k','Z
    peak@100k','Theta baseline@100k','Theta peak@100k','Z
    baseline@10k','Z peak@10k','Theta baseline@10k','Theta peak@10k','Z
    baseline@1k','Z peak@1k','Theta baseline@1k','Theta peak@1k');
    fclose(f);
end

data=dlmread(in_path,'\t');
data1=dlmread(in_path1,'\t');
data2=dlmread(in_path2,'\t');
data3=dlmread(in_path3,'\t');
Z_mag=data(:,1);
Z_phase=data(:,2);
t=data(:,6);
Z_mag1=data1(:,1);
Z_phase1=data1(:,2);
t1=data1(:,6);
Z_mag2=data2(:,1);
Z_phase2=data2(:,2);
t5=data2(:,6);
Z_mag3=data3(:,1);
Z_phase3=data3(:,2);
```

```
t3=data3(:,6);
figure(1);
plot(t,Z_mag);
disp('Please select lower left and upper right corners of boxes (in that
order)');
disp('for all cells you wish to analyze and then press enter');
[x,y]=ginput;

for i=1:2:numel(x)
    clc;
    if(i>1)
        clear X;
        clear Y;
    end
    figure(2);
    h1=subplot(1,1,1);
    plot(t,Z_mag);
    set(h1,'XLim',[x(i) x(i+1)]);
    clc;
    disp('Please select 5 points on Figure 2 (top left) corresponding to
    times where');
    disp('1. Cell starts deformation to enter channel');
    disp('2. Cell completely enters channel');
    disp('3. Cell is in middle of channel');
    disp('4. Cell completely exits channel');
    disp('5. No cell');
    disp('Next select two points corresponding to baseline and peak
    values in all other plots');
    disp('and then press enter');
    [X,Y]=ginput;
    f=fopen(char(out_path),'a+');
    fprintf(f,'%s\t',char(strcat('Cell',int2str(j))));

    for p=1:1:length(t)
        if t(p)>X(5);
            i_b=p-1;
            break;
        end
    end

    Y(6)=-180-Z_phase(i_b);
    Y(8)=Z_mag1(i_b);
    Y(10)=-180-Z_phase1(i_b);
    Y(12)=Z_mag2(i_b);
    Y(14)=-180-Z_phase2(i_b);
    Y(16)=Z_mag3(i_b);
    Y(18)=-180-Z_phase3(i_b);

    for k=1:1:length(t)
        if t(k)>X(3);
            i_c=k-1;
            break;
        end
    end
```

```
    Y(7)=-180-Z_phase(i_c);
    Y(9)=Z_mag1(i_c);
    Y(11)=-180-Z_phase1(i_c);
    Y(13)=Z_mag2(i_c);
    Y(15)=-180-Z_phase2(i_c);
    Y(17)=Z_mag3(i_c);
    Y(19)=-180-Z_phase3(i_c);

    fprintf(f,'%6.4f\t%6.4f\t%6.4f\t%6.4f\t%10f\t%10f\t%2.2f\t%2.2f\t%10
    f\t%10f\t%2.2f\t%2.2f\t%10f\t%10f\t%2.2f\t%2.2f\t%10f\t%10f\t%2.2f\t
    %2.2f\n',[X(1) X(2) X(3) X(4) Y(5) Y(3) Y(6) Y(7) Y(8) Y(9) Y(10)
    Y(11) Y(12) Y(13) Y(14) Y(15) Y(16) Y(17) Y(18) Y(19)]);
    fclose(f);
    j=j+1;
end
```

## Bioelectrical parameters (Microfluidics)

Using the impedance magnitudes and phase angles in four frequencies to extract individual cell bioelectrical parameters.

```
clear;
clc;

%-------------------------------------------------------------
%                      Read Experimental Values
fn1='C:\Users\Desktop\DataAnalysis.xls';
rD=xlsread(fn1);
out_path='C:\Users\Desktop\DataAnalysis_Parameters.xls';

file=fopen(char(out_path),'a+');
fprintf(file,'%s\t%s\t%s\t%s\t%s\t%s\t%s\t\t%s\t%s\t%s\t%s\t%s\n','Cell
Number','Qdl','ndl','Rsp','Qpar','npar','RsquareBaseline','Rint','Qm','n
m','Rcyt','RsquarePeak');
fclose(file);

%-------------------------------------------------------------
%                        List of frequencies used
freq=[1e3; 1e4;  1e5; 1e6];

%-------------------------------------------------------------
%              Extract baseline and peak values of impedance
k=1;
for i=1:1:size(rD,1)
    for j=5:4:size(rD,2)
        Zb_mag(i,k)=rD(i,j);
        Zp_mag(i,k)=rD(i,j+1);
        k=k+1;
    end
    k=1;
end

for i=1:1:size(rD,1)

    %-------------------------------------------------------------
    %                    Curve fitting for Baseline
```

```
    Zb=transpose(Zb_mag(i,:));
    ftype_baseline=fittype('abs((((j*Cdl*2*pi*f)^-ndl+Rsp*1e12)^-
    1+(j*4.185e-14*2*pi*f)^0.845)^-1)','independent',
    {'f'},'dependent',{'Zb'},'coefficients',{'Cdl','ndl','Rsp'});

    foptions_baseline=fitoptions('Method','NonlinearLeastSquares','Algor
    ithm','Trust-Region','DiffMaxChange', 1e-15,'DiffMinChange',1e-
    15,'MaxFunEvals',2e3,'MaxIter',2e3,'TolX',1e-15,'TolFun',1e-
    15,'Lower',[1e-14,0.6,6e-7],'Upper',[1e-13,1,5e-6],'Startpoint',[1e-
    14,0.1,1e-6]);
    [fobjb gofb]=fit(freq,Zb,ftype_baseline,foptions_baseline);
    Cdl(i)=fobjb.Cdl;
    ndl(i)=fobjb.ndl;
    Rsp(i)=fobjb.Rsp*1e12;
    Cpar(i)=4.185e-14;
    npar(i)=0.845;
    Rsquareb(i)=gofb.adjrsquare;

    %-------------------------------------------------------------
    %                      Curve fitting for Peak
    Zp=transpose(Zp_mag(i,:));
    ftype_peak=fittype('abs((((j*Cdl*2*pi*f)^-ndl+0.7*Rsp+((Rint*1e12)^-
    1+((j*2*pi*f*Cm)^-nm+Rcyt*1e12)^-1)^-1)^-1+(j*4.185e-
    14*2*pi*f)^0.845)^-1)','problem',{'Cdl','ndl','Rsp'},'independent',
    {'f'},'dependent',{'Zp'},'coefficients',{'Rint','Cm','nm','Rcyt'});

    foptions_peak=fitoptions('Method','NonlinearLeastSquares','Algorithm
    ','Trust-Region','DiffMaxChange', 1e-15,'DiffMinChange',1e-
    15,'MaxFunEvals',2e3,'MaxIter',2e3,'TolX',1e-15,'TolFun',1e-
    15,'Lower',[9e-8,1e-14,0.7,4e-8],'Upper',[2e-6,1e-13,1,4.75e-
    7],'Startpoint',[1e-6,1e-14,0.1,1e-7]);
    [fobjp gofp]=fit(freq,Zp,ftype_peak,foptions_peak,'problem',{Cdl(i),
    ndl(i), Rsp(i)});
    Rint(i)=fobjp.Rint*1e12;
    Cm(i)=fobjp.Cm;
    nm(i)=fobjp.nm;
    Rcyt(i)=fobjp.Rcyt*1e12;
    Rsquarep(i)=gofp.adjrsquare;

    %-------------------------------------------------------------
    %                      Print Values in Spreadsheet
    file=fopen(char(out_path),'a+');
    fprintf(file,'%u\t%e\t%e\t%e\t%e\t%e\t%e\t\t%e\t%e\t%e\t%e\t%e\n',[i
    Cdl(i) ndl(i) Rsp(i) Cpar(i) npar(i) Rsquareb(i) Rint(i) Cm(i) nm(i)
    Rcyt(i) Rsquarep(i)]);
    fclose(file);
end
```